Characterization and simulation of fluorescent silicon carbide: a study of donor-acceptor-pairs and intrinsic defects

Wei, Yi

Publication date:
2019

Document Version
Publisher's PDF, also known as Version of record

Doctoral thesis

Characterization and simulation of fluorescent silicon carbide:

a study of donor-acceptor-pairs and intrinsic defects

Yi Wei
韦祎

April, 2019, Kongens Lyngby

DTU Fotonik
Department of Photonics Engineering

DTU Fotonik
Department of Photonics Engineering
Technical University of Denmark

Ørsteds Plads
Building 345A, room 067
2800 Kongens Lyngby, Denmark
Phone +45 4525 6634
ywei@fotonik.dtu.dk
www.fotonik.dtu.dk

Preface

This thesis was prepared at the Department of Photonics Engineering, Technical University of Denmark (*i.e.*, DTU Fotonik) in partial fulfillment of the requirements for the degree of Doctor of Philosophy. The work presented here was carried out in the period from 1st September, 2015 to 31st December, 2018, at DTU Fotonik. A three month external research stay was spent at Materials Department 6, Electronic Materials and Energy Technology, Friedrich-Alexander University of Erlangen-Nürnberg, Germany. The project was financed by Innovation Fund Denmark through the "A new type of white light-emitting diode using fluorescent silicon carbide " (LEDSiC) project (grant no. 4106-00018B), and supervised by Assoc. Prof. Dr. Haiyan Ou at DTU Fotonik.

Acknowledgements

I am greatly indebted to Assoc. Prof. Haiyan Ou, my principal supervisor, for offering me the valuable opportunity to roam the world of silicon carbide. As the supervisor, she always provides insightful guidance and warm encouragement with patience and dedication. Thank you for being an excellent supervisor.

An sincere gratitude to Dr. Abebe Tilahun Tarekegne, as we have had a wonderful and fruitful cooperation during the last one and half year. You always have very clear physical images about the mechanisms behind the experimental results. Much thanks to your splendid viewpoints on silicon carbide research.

I am also grateful to Prof. Dr.-Ing. Peter Wellmann and his group from University of Erlangen-Nürnberg (FAU), who offered me the great opportunity to work on the new characterization techniques for silicon carbide during my three-month external stay in Germany. I would also like to thank my colleagues Dr. Ulrike Künecke, Philipp Schuh, and Martin Wilhem in FAU for their disinterested help.

A special thanks Assoc. Prof. Mikael Syväjärvi and Dr. Valdas Jokubavicius from IFM, Linköping University for growing silicon carbide samples for my research. Also, deep thanks to Assoc. Prof. Jianwu Sun from the same institute for a meaningful conversation about silicon carbide research by phone.

A warm thanks to Prof. Satoshi Kamiyama from Meijo University, Japan, for his inspiring insights on silicon carbide research during our very limited discussion.

I am also thankful to Dr. Ahmed Fadil for his precious help on FDTD simulations about localized surface plasmons, and Dr. Weifang Lu for the fruitful discussion on silicon carbide based nanoprocessings and characterizations.

I would also like to thank Dr. Kaiyu Wu from DTU Nanotech for his selfless assistance with Raman spectroscopy, and Dr. Peter David Girouard from DTU Fotonik for the support on manuscript revision.

Huge thanks to my colleagues in our research group including Asst. Prof. Yiyu Ou, Dr. Li Lin, Yi Zheng and Xiaodong Shi for their supports.

I also wish to acknowledge all the members of the assessment committee of my thesis including: Prof. Peter Uhd Jepsen (Chairman of the committee, Deputy Head of Department, DTU Fotonik), Assoc. Prof. Brian Julsgaard from Institut for Fysik og Astronomi, Aarhus University, and Assoc. Prof. Jianwu Sun from IFM, Linköping University. I am sincerely grateful for your dedicated efforts on reviewing my thesis and arranging the time to participate my defense.

A special thank to our research group leader, Prof. Paul Michael Petersen, for being the master of my thesis defense and graduation ceremony.

It is hard to find words to express my gratitude to my parents and parents-in-law, who always believe me and give me strength, thank you for all the love and support. Even though there are large distances between us, we are always feeling close.

Last but not least...I want to thank my dear Xu, you made my life so wonderful and meaningful. It is because of your unconditional love and tireless encouragement that I can keep concentrating on my Ph.D studies without hesitation and fear.

Yi Wei (韦祎)
April 10^{th}, 2019

Abstract

Fluorescent silicon carbide (f-SiC) is an emerging luminescent material capable of displaying broadband and strong orange-yellowish light thanks to its extraordinarily high density of donor-acceptor-pairs (DAPs) introduced by the co-doping of nitrogen (N) and boron (B). This thesis describes the luminescent properties of f-SiC material by both theoretical and experimental approaches. The correlations between the radiative/non-radiative centers within the band gap of f-SiC introduced during its crystal growth and the particular luminescent behaviors have been established.

DAP recombination is the major contributor of the photoluminescence (PL) in f-SiC where the non-equilibrium electrons/holes on the N-induced donor levels and the B-induced acceptor levels, respectively, can have radiative recombination. In this thesis, several non-radiative recombination regimes corresponding to the inactive donors and the intrinsic defects are revealed to compete with the DAP recombination in f-SiC. For instance, by combining the results of the thermally stimulated luminescence (TSL) measurements on f-SiC with the related TSL simulations, it is discovered that part of non-equilibrium electrons are trapped on the donors related to the hexagonal sites where these electrons are not enrolled in the spontaneous emission (*i.e.*, PL). On the other hand, by measuring the temperature-dependent PL intensity spectra on f-SiC, the existence of a new B-induced deeper acceptor level (D^*-center) other than the well-known D-center (together called double D-centers) is confirmed. The D^*-center is found to account for the dominating redshifted PL of f-SiC at low temperature. Meanwhile, the huge gap between the luminescence intensities of n-type and p-type f-SiC at elevated temperatures is explained by a two-step thermal activation procedure which involves the double D-centers and an hole trap with its energy level staying between those of the former two centers. Moreover, on the basis of the results from the time-resolved PL and static PL measurements at room temperature where the results are explained using a negative-U center related carrier dynamics model together with a steady-state DAP recombination model, it is believed that the fast non-radiative recombination channels involved with the intrinsic negative-U centers close to the conduction band minimum capture the majority of the non-equilibrium carriers, which causes the low internal quantum efficiency of f-SiC. Since f-SiC is anticipated to replace yellow phosphor for novel white light emitting diode (LED), the optimized thickness and optical incident power regarding to f-SiC material are investigated by measuring its PL quantum yield by using an integrating sphere. It is found that excessive incident power mainly contributes to the ultrafast non-radiative recombination, *i.e.*, Auger recombination.

The research outputs reported in this thesis have revealed that there still exists

the possibility for the improvement of the luminescence efficacy of f-SiC, where the crystal growth conditions including dopants concentrations as well as thickness control of epilayer can be further optimized in order to reduce the densities of intrinsic defects and enhance DAP recombination in f-SiC.

Resumé

Fluorescerende siliciumcarbid (f-SiC) er et materiale, der er i stand til at udsende bredbånd og intenst orange-gulligt lys pga. den ekstraordinært høje koncentration af donor acceptor-par, der introduceres ved doping med nitrogen (N) og bor (B). Denne afhandling beskriver både teoretisk og eksperimentelt de luminicerende egenskaber af f-SiC. Sammenhængen mellem de radiative / ikke-radiative centre i f-SiC under krystalvækst beskrives.

Donor acceptor rekombination er den største bidragsyder til fotoluminescensen (PL) i f-SiC, hvor ikke-ligevægtselektroner/huller på henholdsvis N-inducerede donorniveauer og B-inducerede acceptor-niveauer har radiativ rekombination. I denne afhandling beskrives flere ikke-radiative rekombinationsregimer svarende til de inaktive donorer og de egentlige defekter der kan konkurrere med donor acceptor-rekombinationen i f-SiC. Ved at kombinere resultaterne af de termisk stimulerede luminescensmålinger (TSL) på f-SiC med de relaterede TSL-simuleringer, er det opdaget, at en del af ikke-ligevægtselektroner er indfanget i donorer relateret til de hexagonale områder, hvor elektroner ikke er involveret i den spontane emission. Ved at måle de temperaturafhængige PL-intensitetsspektre på f-SiC, kan et B-induceret dybere acceptor-niveau (D^*-center) bekræftes. D^*-centeret er fundet at være ansvarlig for den dominerende rødlige PL af f-SiC ved lav temperatur. Endvidere forklares store forskelle mellem luminescensintensiteterne af n-type og p-type f-SiC, ved forhøjede temperaturer, ved en to-trins termisk aktiveringsprocedure, der involverer dobbelte D-centre og en hul tilstand med dets energiniveau mellem de af de to tidligere centre. På baggrund af resultaterne fra de tidsopløste PL og statiske PL målinger ved stuetemperatur, hvor resultaterne forklares ved anvendelse af en negativ-U-center-relateret ladningsbærermodel sammen med en stationær donor acceptor-rekombinationsmodel, beskrives det; at de hurtige ikke-radiative rekombinationskanaler involveret med de iboende negative U-centre tæt på ledningsbåndets minimum indfanger flertallet af ikke-ligevægt ladningsbærerne, hvilket forklarer den lave interne kvante-effektivitet af f-SiC. Da f-SiC potentielt kan erstatte gul fosfor i fremtidens nye hvide lysdioder (LED), undersøges den optimale tykkelse og den optimale optiske effekt i f-SiC ved at måle PL-kvanteudbyttet i en integreret kugle. Det konstateres, at den forhøjede effekt bidrager til ultrahurtige ikke-radiative rekombination, dvs. Auger-rekombination.

De forskningsresultater, der er beskrevet i denne afhandling, har vist, at der stadig findes forbedringsmuligheder for luminescenseffektiviteten i f-SiC, herunder doteringskoncentrationer samt tykkelsesvariation af det epitaksiale lag, som yderligere kan optimeres for at reducere tæthederne af intrinsiske defekter samt forbedre donor acceptor rekombination i f-SiC.

Publication List

Articles in peer-reviewed journals included in this thesis:

1. **Wei, Y.,** Tarekegne, A. T., & Ou, H. (2019). Double D-centers related donor-acceptor-pairs emission in fluorescent silicon carbide. *Opt. Mater. Express,* 9(1), 295–303. DOI: 10.1364/OME.9.000295

2. **Wei, Y.,** Tarekegne, A. T., & Ou, H. (2018). Influence of negative-U centers related carrier dynamics on donor-acceptor-pair emission in fluorescent SiC. *Journal of Applied Physics,* 124(5), 054901. DOI: 10.1063/1.5037167

Peer-reviewed journal article outside the scope of the thesis:

1. **Wei, Y.,** Fadil, A., & Ou, H. (2017). Localized Surface Plasmon on 6H SiC with Ag Nanoparticles. *Materials Science Forum,* 897, 634–637. DOI: 10.4028/www.scientific.net/MSF.897.634

Conference contributions:

1. **Wei, Y.,** Künecke, U., Wellmann, P., & Ou, H. (2017). *Detection of effective recombination centers in fluorescent SiC using thermally stimulated luminescence.* Abstract from 5$^{\text{th}}$ international workshop on LED and Solar Applications, Kgs. Lyngby, Denmark. [oral presentation + poster session]

2. Tang, K., Ma, X., can der Eijk, C., Ou, H., & **Wei, Y.** (2017). *Liquid Phase Epitaxial Growth of Al-doped f-SiC for White Light-Emitting Diodes.* Abstract from 5$^{\text{th}}$ international workshop on LED and Solar Applications, Kgs. Lyngby, Denmark.

3. **Wei, Y.,** Künecke, U., Jokubavicius, V., Syväjärvi, M., Wellmann, P., & Ou, H. (2017). *Low Temperature Photoluminescence of 6H fluorescent SiC.* Abstract from E-MRS Spring Meeting 2017, Strasbourg, France. [oral presentation]

4. **Wei, Y.,** Künecke, U., Wellmann, P., & Ou, H. (2017). *Thermally Stimulated Luminescence in 6H Fluorescent SiC.* Abstract from 2017 International Conference on Silicon Carbide and Related Materials , Washington D.C., United States. [poster session]

5. **Wei, Y.,** Fadil, A., & Ou, H. (2016). *Localized Surface Plasmon on SiC with Ag Nanoparticles.* Paper presented at 11$^{\text{th}}$ European Conference on Silicon Carbide and Related Materials, Halkidiki, Greece. [oral presentation]

List of Figures

List of Tables

Contents

CHAPTER 1

Introduction

1.1 Background

White light-emitting diodes (LEDs), with constantly improved robustness and luminescence efficacy, have been extensively implemented in almost all industrial sectors as well as all aspects of personal lives. Compared to traditional white light solutions (*e.g.*, incandescent light bulbs), white LEDs have several advantages, for instance, they are more energy efficient, environmentally friendly (no mercury or other hazardous elements included), as well as do not require warm-up period. However, there is a dilemma regarding the design of white LEDs. The higher color rendering index (CRI) can be achieved by using a near ultraviolet (NUV) LED to pump the three-color phosphors (red, green, and blue), *i.e.*, NUV LED + RGB phosphors solution, however, the efficiency of the red phosphor is quite lower compared to the other two phosphors[1]. On the other hand, the most prevailing white LED solution could only induce lower CRI. This solution combines a nitride-based blue-LED chip coated with a yellow phosphor layer, *i.e.*, blue LED + yellow phosphor solution, where one of the most commonly used yellow phosphors is made of cerium-doped yttrium aluminum garnet, *i.e.*, (YAG):Ce[1]. In fact, the low CRI as well as low luminescence efficacy corresponding to the blue LED + yellow phosphor solution is due to the degradation issue of the yellow phosphor[2–5]. Besides, the research and development costs are quite high[2, 3] in order to achieve uniform coating of yellow phosphor on blue LED chip, let alone the issues regarding the cost and supply of the rare earth (RE) elements in yellow phosphors, *e.g.*, cerium in (YAG):Ce. Hence a breakthrough regarding further improvement of the efficiency and robustness of yellow phosphor is expected if one still would like to adhere the development on the blue LED + yellow phosphor solution. Fortunately, a new type of inorganic yellow phosphor grown by Kamiyama *et al.*[2], *i.e.*, the donor and acceptor co-doped fluorescent silicon carbide (f-SiC), contains no RE elements and has no degradation issues making it become quite promising for replacing (YAG):Ce in future white LEDs. By getting heavily nitrogen-boron (N-B) co-doped, f-SiC can be applied as a passive wavelength conversion medium, where strong orange-yellowish light emission with large full width at half maximum (FWHM) can be generated by optically pumping f-SiC via NUV light source (*e.g.*, a nitride-based NUV LED chip). It is also worthy to notice that, SiC is regarded as a better platform for the integration of nitride-based NUV LED chip compared to the prevalent sapphire substrate. In addition, another type of f-SiC which is N-Al co-doped is anticipated to emit blue-greenish light by NUV light source pumping[3]. It was then proposed by Kamiyama *et al.*[4] that a new type

of white LED with high CRI white light emission can be achieved by growing the stacking structure which contains a nitride-based NUV LED chip, a N-B as well as a N-Al co-doped f-SiC layers. Note that since N-Al co-doped SiC doesn't show PL at room temperature (RT), in the time frame of this project, f-SiC usually refers to N-B co-doped SiC. Since SiC is an indirect band gap material, the efficiency regarding donor-acceptor-pair (DAP) recombination is expected to be quite low. Two methods have been proposed to enhance the intensities of the DAP recombination events in f-SiC, *i.e.*, increase the density of DAP and the sample thickness. Luckily, the above-mentioned two methods have been successfully implemented in the epilayer growth of f-SiC thanks to the advent of fast sublimation growth process (FSGP) method developed by Syväjärvi *et al.*[6], which makes the current f-SiC have N-B co-doping beyond 10^{18} cm^{-3}. In addition, with FSGP method, it is also easy to achieve sufficient epilayer thickness since the growth rate of FSGP can be up to 200 $\mu m \cdot h^{-1}$[7]. Furthermore, the densities of the 1-D (*i.e.*, micropipe), 2-D (*i.e.*, stacking fault) and 3-D[8] (*i.e.* polytype switch, carbon inclusion and silicon droplet) defects in f-SiC have been drastically decreased to the negligible levels[6, 9] by applying the FSGP method for the growth of f-SiC epilayers. Meanwhile, the source SiC material for FSGP is prepared via the modified physical vapor transport (M-PVT) technique developed by Wellmann *et al.*[8, 10, 11], where the stable nitrogen doping and low dislocation densities in the source SiC material have been realized.

1.2 Motivation

Although the luminescence intensity of f-SiC has been greatly enhanced by the micro- and nano-processing[12–14] as well as much effort has been made[3, 4, 14, 15] toward the realization of f-SiC based white LED, the room for improvement regarding to the luminescence efficacy of f-SiC is limitted by its internal quantum efficiency (IQE), which is dominated by the efficiency of DAP recombination in f-SiC. However, the capacities about how the N-induced donors and B-induced acceptors are able to enroll in the radiative recombination separately are still not clear yet. On the other hand, in spite that the crystal quality of f-SiC has been largely improved by applying the sublimation growth methods including FSGP | M-PVT, it is still inevitable to form the 0-D defect (*i.e.*, point defects) during the sublimation growth of SiC especially under high co-doping condition[8, 16, 17]. In f-SiC, the point defects include vacancies, interstitials, and antisites related to silicon | carbon atoms, which could induce deep levels[18] within the band gap of SiC. These deep levels are the active channels for non-radiative recombination which competes with DAP dominated radiative recombination channels in f-SiC[19]. In fact, there still lacks of the theoretical study about how the carriers trapping processes corresponding to the point defects induced non-radiative centers would affect the DAP recombination in f-SiC. In addition, for the device fabrication of the white LED based on f-SiC, the investigation about of how the pumping power of NUV LED and the thickness of f-SiC epilayer would influence the luminescence efficacy of f-SiC is needed. Therefore, our general motivation of this

research is to study the potential to improve the efficiency of f-SiC after considering the defects in the material, and the luminous efficacy after considering the sample thickness and pumping power.

1.3 Scope of this work

This thesis investigates the luminescence mechanism of f-SiC in three aspects. The first one is to study how the nitrogen-induced donors and boron-induced acceptors would separately affect the DAP recombination process. The next one is to demonstrate the influence from the intrinsic point defects related non-radiative centers on the efficiency of DAP recombination. The last one is to determine the luminescence efficiency of f-SiC in correlation with the incident power and the thickness of f-SiC.

Chapter 2 briefly introduces the fundamentals of SiC material including its crystal structures, electrical and optical properties, where these basic knowledges are essential for the analysis of the experimental characterization results and launching numerical simulations of f-SiC. In addition, the basic physical parameters of all the f-SiC samples employed in this research are summarized.

Chapter 3 introduces the experimental techniques and setups including:

- The thermally stimulated luminescence (TSL) measurement system for the research in Sec. 4.1.
- The temperature-dependent photoluminescence (PL) measurement system for the research in Sec. 4.2.
- The experimental facilities related to time-resolved photoluminescence (TRPL) based on the time-correlated single photon counting (TCSPC) solution for the research in Chapter 5.
- The design and methodology of the integrating sphere based photoluminescence quantum yield (PL-QY) determination system for the research in Chapter 6.

Chapter 4 are divided into two parts. The first part (Sec. 4.1) investigates the non-radiative behavior corresponding to the nitrogen-induced donors on the hexagonal sites of f-SiC by implementing a classic TSL model to analyze the related experimental results. In addition, the "finger prints" of the impurities induced shallow centers shown in the TSL measurement results are also discussed.

The second part (Sec. 4.2) of Chapter 4 demonstrates the existence of a new boron-induced deeper acceptor level (D^*-center) different from the D-center in f-SiC. The D^*-center is correlated to the dominant DAP recombination at low temperature ranges in f-SiC with a PL peak around 1.90 eV. A hole-trap with an energy level that lies between the D^*-center and D-center is predicted to exist. A two-step thermal ionization involving the hole-trap is proposed to explain the evolution of both D^*-center and D-center related temperature-dependent DAP recombination.

Chapter 5 quantitatively demonstrates how the dominating non-radiative center in 6H f-SiC, *i.e.*, the E_1/E_2 center which possess negative-U properties, could affect the

non-radiative recombination regime in f-SiC in parallel with the DAP recombination process. The rapid luminescence decay in f-SiC is explained by applying a negative-U centers related carrier dynamics model. A steady-state DAP recombination model is also implemented to reveal how the DAP related process could be affected by the presence of negative-U centers. Moreover, the carrier dynamics of a commercial N-B co-doped n-type 6H SiC substrate is also studied in order to compare with f-SiC, where an additional trapping center is found other than E_1/E_2 defects in the bulk material.

Chapter 6 illustrates the experimental design and related numerical algorithms for the determination of the PL-QY of f-SiC samples. The influence of epilayer thickness and incident power on the PL-QY of f-SiC are discussed.

CHAPTER 2

General properties of SiC and growth of 6H f-SiC

Silicon carbide (SiC) is a wide-bandgap semiconductor material where its unit cell is composed of silicon-and-carbon bilayers. It is essential to understand the basis of its crystal structure as well as fundamental electrical | optical properties, since they are the cornerstone for the further research based on SiC. In this chapter, the basic knowledge related to the crystal structure, electrical and optical properties of SiC are summarized. The growth techniques corresponding to 6H fluorescent silicon carbide (f-SiC) are also reviewed. Finally, the basic physical parameters of all the f-SiC samples included in this research are listed.

2.1 Crystal structure

SiC is a binary-covalent-compound semiconductor, where only the stoichiometry of 50% Si-atom and 50% C-atom is allowed. Eq. (2.1) shows the ground state electronic structures of neutral Si- and C-atom.

$$\begin{aligned} \text{Si},\ 14e^- &:\ 1s^2 2s^2 2p^6 3s^2 3p^2 \\ \text{C},\ 6e^- &:\ 1s^2 2s^2 2p^2 \end{aligned} \tag{2.1}$$

Where SiC is formed via Si and C being bonded tetrahedrally with four covalent bonds by sharing the four valence electron pairs in sp^3-hybrid orbitals. In pure SiC, each Si-atom bonds with four neighboring C-atom, and vice versa. SiC is known as one of the typical materials which can form various crystal structures by only changing the stacking sequence (*i.e.*, the changing in one dimension) without altering the chemical composition. This character is called *polytypism*[20–24]. For SiC, different *polytypes* are formed by various site occupation in a *hexagonal close-packed* (HCP) lattice system along the *c*-axis. The site occupation in the HCP system can be futher explained schematically in Fig. 2.1 where the stacking sequence along the [0001] direction (*c*-axis) is shown.

Here, each C-atom bonds tetrahedrally to Si-atoms where three of the four Si-atoms lie on the same (0001) plane and form the bilayer with the C-atom, and the bond links the C-atom with the fourth Si-atom is in parallel with the *c*-axis. Here we label the location of the C-atom in the bilayer configuration which forms a hexagonal

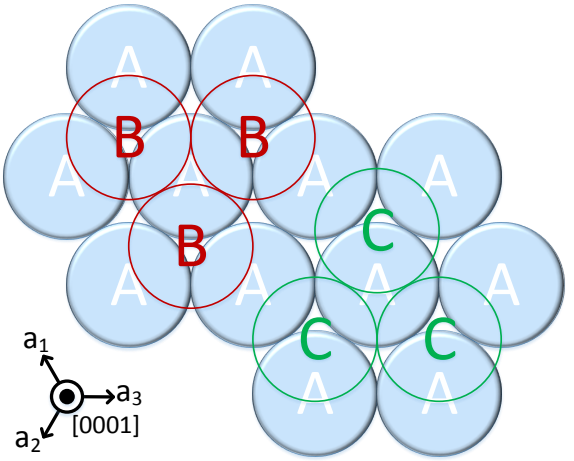

Figure 2.1: Different sites occupation scenarios for the C-atom in the Si-C bilayer configuration of the HCP system in the [0001] plane.

structure as "A". Then there are two types of lattice site for the C-atom of the next bilayer towards [0001] direction labelled by "B" and "C". As the high bond energy of the Si-C bond can ensure the stable stacking structure between two close bilayer configurations, it is possible to form different multi-layered-stacking structures. This makes SiC crystallize in more than 200 polytypes. Even though there are numerous polytypes of SiC, only few of them are reproducible and available for further material processing and device fabrication. At present, the most common polytypes of SiC for electrical, optical and quantum researches are 3C-SiC (cubic), 4H- and 6H-SiC (hexagonal), where 6H-SiC and 3C-SiC are also called α-SiC and β-SiC, respectively. Fig. 2.2 shows the unit cells and principal axes of (a) cubic SiC, *e.g.*, 3C-SiC; and (b) hexagonal SiC, *e.g.*, 4H- and 6H-SiC.

For cubic SiC, the three fundamental vectors a_1, a_2 and a_3 are identical in length. Note that the structure of 3C-SiC is also known as the *zincblende* structure. Normally four principal axes are applied for hexagonal SiC, *i.e.*, a_1, a_2, a_3, and c. Note that when identifying a plane or a direction for hexagonal SiC, only three of the four principal axes are needed. This is because the sum of the reciprocal intercepted with the three axes on the (0001) plane, *i.e.*, a_1, a_2 and a_3, is zero, where a_1, a_2 and a_3 are divided by 120° with each other. The fourth principal axes of hexagonal SiC, *i.e.*, the c-axis, is perpendicular to the (0001) plane. The schematic diagrams demonstrating the lattice periodicities of 3C-, 4H- and 6H-SiC are shown in Fig. 2.3.

3C-SiC is the only polytype of SiC which has the pure cubic crystal structure and often referred as β-SiC. As its tetrahedral bonding has to be maintained, only three orientations denoted by A, B and C are allowed for the stacking of the Si-C bilayer

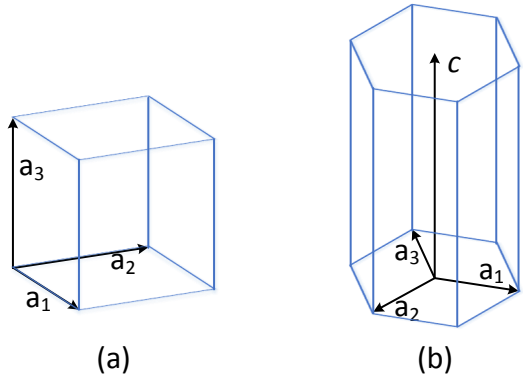

Figure 2.2: Unit cells and principal axes of (a) cubic and (b) hexagonal SiC.

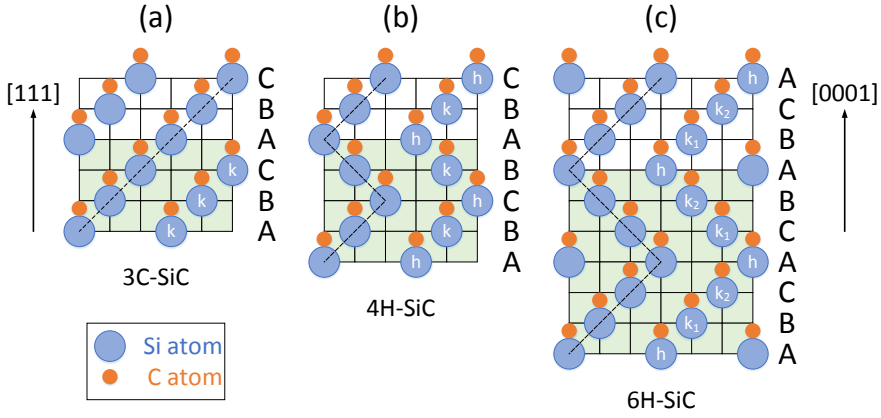

Figure 2.3: Schematic diagrams of the lattice periodicities of (a) 3C- (b) 4H- and (c) 6H-SiC. Note that the shadow areas designate the dimension of the unit cells along [111] (for 3C) or [0001] (for 4H and 6H), respectively. The dashed lines indicate the route for Si-C bilayer stacking for each polytypes.

with the stacking sequence of "ABCABC...". This stacking sequence agrees well with the notation of cubic SiC, *i.e.*, 3C, where "3" designates its number of bilayers in one lattice period along the [111] direction. In addition, the sites related to A, B, and C in 3C-SiC are all cubic sites which can be uniformly designated as the "k" sites.

On the other hand, the polytypes of SiC other than 3C-SiC are generally called α-SiC. One of the α-SiC with the stacking of the Si-C bilayer in the sequence of "ABAB..." is 2H-SiC. As 2H-SiC consists of only hexagonal structure, its *hexagonality*, *i.e.*, the portion of the hexagonal bonds, is 100%. In addition, the structure of 2H-SiC is often named as *wurtzite* structure. For 4H-SiC, its stacking sequence is represented by "ABCBABCB..." with four bilayers in one lattice period along [0001] direction. There are equal number of cubic and hexagonal bonds in 4H-SiC, namely its hexagonality is 50%. The hexagonal sites can be uniformly designated as "h" sites. Whereas the stacking sequence of 6H-SiC is designated by "ABCACBABCACB..." with six bilayers in one lattice period along [0001] direction. The ratio of the number of cubic and hexagonal bonds in 6H-SiC is fixed at 2:1 indicating the hexagonality is around 33%. Note that in 6H-SiC, all the "A" sites are hexagonal sites, while the two nonequivalent quasi-cubic sites "B" and "C" are normally denoted by "k_1" and "k_2" sites, respectively. For 4H- and 6H-SiC, we can see that the hexagonal and cubic sites are different in the locations of their second-nearest neighbors, which leads to different crystal fields[25]. In this way, the energy levels of the dopants, impurities and defects become site-dependent where the related characteristic is called "site-effect"[25–27]. Some fundamental crystal properties of 3C-, 4H- and 6H-SiC are summarized in Tab. 2.1.

			Lattice constant			
Polytype	SG	SG no.	a (å)	c (å)	E_g	Hex.
3C	T_d^2-F43m	216	4.36	-	2.36 eV	0.0%
4H	C_{6v}^4-P6$_3$mc	186	3.080	10.082	3.23 eV	50.0%
6H	C_{6v}^4-P6$_3$mc	186	3.082	15.100	3.02 eV	33.3%

Table 2.1: Crystal properties of 3C-, 4H- and 6H-SiC, note that "SG" designates the abbreviation of "space group", the values of E_g at RT are given, and "Hex." refers hexagonality.

The space group (SG) of the cubic SiC is T_d^2 whereas the SG for either 4H- or 6H-SiC is C_{6v}^4. In general, we can see that less hexagonality could result in smaller band gap (E_g). Tab. 2.2 summarizes the standard atom coordinates of 3C-, 4H- and 6H-SiC. By implementing the SG and lattice constants from Tab. 2.1 and the related atom coordinates from Tab. 2.2 into VESTA, *i.e.* a 3D visualization program for crystal structures[28], the obtained ball-stick models for 3C-, 4H- and 6H-SiC are shown in Fig. 2.4.

Fig. 2.5 introduces four major planes in a hexagonal SiC structure. The (0001) plane consists of the Si-atoms which bond tetrahedrally with the Si-C bilayer along the c-axis ($\langle 1000 \rangle$ direction). Hence (0001) plane is also called "Si-face". On the

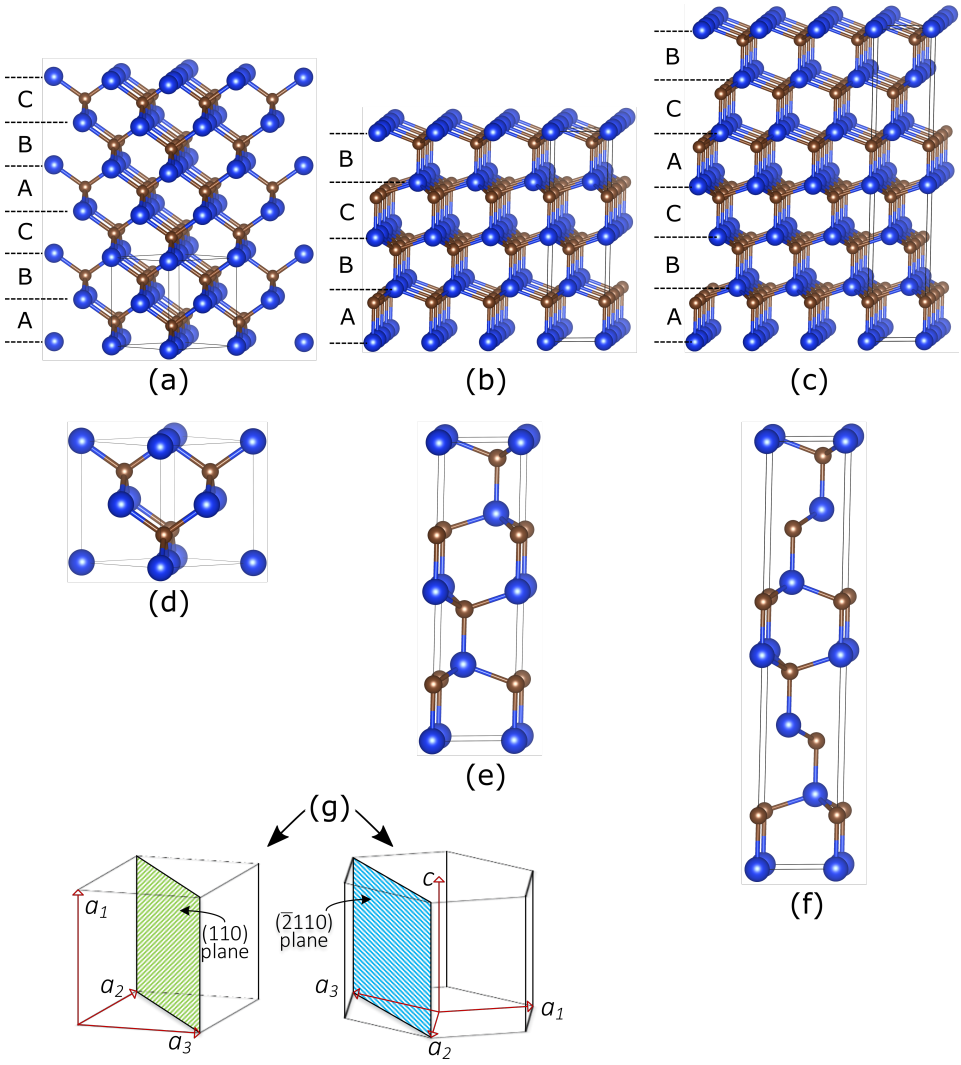

Figure 2.4: 3D ball-stick structures for (a) 3C-, (b) 4H- and (c) 6H-SiC. (d) to (f) are the unit cells for 3C-, 4H- and 6H-SiC, separately. The structures of 3C-SiC and 4H/6H-SiC are presented in the (110) and ($\bar{2}$110) plane, respectively, where the related planes are indicated in (g).

Polytype	Site	Element	Symmetry	X	Y	Z	Ref.
3C	C	C	-43m	1/4	1/4	1/4	[29]
	Si	Si		0	0	0	
4H	Si1	Si	3m.	1/3	2/3	1/4	[30]
	Si2			0	0	0	
	C1	C		1/3	2/3	0.4354	
	C2			0	0	0.1896	
6H	Si1	Si	3m.	0	0	0	[31]
	Si2			1/3	2/3	1/6	
	Si3			2/3	1/3	0.3329	
	C1	C		1/3	2/3	0.0412	
	C2			2/3	1/3	0.2080	
	C3			0	0	0.3746	

Table 2.2: Standard atom coordinates of 3C-, 4H- and 6H-SiC.

contrary, the $(000\bar{1})$ plane which is also called "C-face" consists of the C-atoms which bond tetrahedrally with the Si-atoms on the "Si-face". In addition, the $(1\bar{1}00)$ plane is also known as "M-face". Normally, SiC wafers are grown on (0001) plane while being off-axis towards the $\langle 11\bar{2}0\rangle$. The plane perpendicular to $\langle 11\bar{2}0\rangle$, *i.e.*, the $(11\bar{2}0)$ plane, is also known as the "A-face".

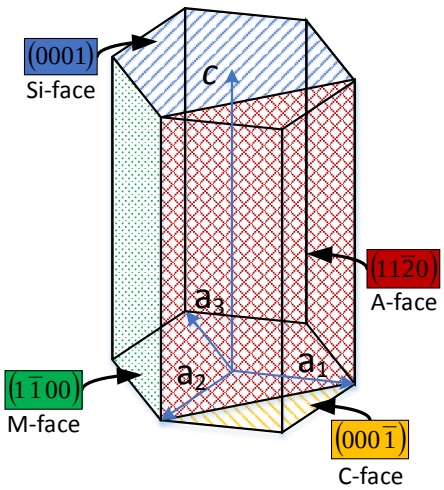

Figure 2.5: Four major planes of a hexagonal SiC structure.

2.2 Electrical and optical properties

2.2.1 Carrier density

The basics of the carrier densities calculations in semiconductor physics introduced in this subsection are mainly derived from Ref. [32]. The density of state equals to the number of discrete states at a certain energy level that electrons (e^-) or holes (h^+) can occupy, i.e., the number of states per volume per energy. The effective density of states in conduction band (N_c) / valence band (N_v) of SiC can be calculated by Eq. (2.2), where the values of M_c, m_e^* and m_h^* of 3C-, 4H- and 6H-SiC are summarized in Tab. 2.3. Note that M_c is the number of the conduction band minima in the first Brillouin zone in SiC. The density-of-state effective mass of electron, *i.e.*, m_{de}^*, is represented by the effective mass of the density of states in one valley of conduction band.

$$\begin{aligned} N_c &= 2M_c \left(\frac{2\pi m_e^* k_b T}{h^2} \right)^{3/2} \\ N_v &= 2 \left(\frac{2\pi m_h^* k_b T}{h^2} \right)^{3/2} \end{aligned} \tag{2.2}$$

Polytype	m_e^*	m_h^*	M_c	Ref.
3C	$0.35m_0$	$0.60m_0$	3	
4H	$0.39m_0$	$0.82m_0$	3	[33–36]
6H	$0.71m_0$	$0.91m_0$	6	

Table 2.3: Density-of-state effective mass of electron (m_{de}^*) and hole (m_{dh}^*), and the number of the conduction band minima (M_c) of 3C-, 4H- and 6H-SiC. Note that m_0 denotes the mass of free electron.

The intrinsic carrier concentration represented by Eq. (2.3) refers to the free carrier (e^- or h^+) concentration of the undoped semiconductor.

$$n_i = \sqrt{N_c N_v} \exp\left(-\frac{E_g}{2k_b T} \right) \tag{2.3}$$

The Fermi level is considered as the energy level that can be occupied by e^- with the probability of 50% at thermodynamic equilibrium. For the intrinsic semiconductor, the intrinsic Fermi energy (E_i) can be expressed by Eq. (2.4) where E_c and E_v are the energy level of the conduction band minimum and valence band maximum, respectively.

$$E_i = \frac{E_c + E_v}{2} + \frac{1}{2} k_b T \ln\left(\frac{N_v}{N_c} \right) \tag{2.4}$$

It is essential to know that the product of free electron density (n_0) and free hole density (p_0) equals to the square of the intrinsic carrier concentration. This conclusion is called *the mass action law* which is expressed in Eq. (2.5).

$$n_0 \cdot p_0 = N_c N_v \exp\left(\frac{E_v - E_c}{k_b T}\right) = n_i^2 \tag{2.5}$$

Doped semiconductor contains impurities, *i.e.*, the foreign atoms being implanted into the intrinsic crystal structure intentionally or unintentionally. The energy level(s) induced by the impurities normally stay inside the band gap. If the impurities give off e^- to the conduction band, they are called *donors*. Whereas they are called *acceptors* when giving off h^+ to the valence band. The donor energy level is filled with e^- and stay neutral prior to being ionized. The ionization of the donor causes the donor level to release the e^- into the conduction band where the donor level is now positively charged. On the other hand, the acceptor energy level is filled with h^+ prior to being ionized. The ionization of the acceptor causes the acceptor level to release the h^+ into the valence band. The acceptor level is negative charged now and equivalent to accepting an e^- from the valence band, therefore it is called acceptor. If the majority carriers are contributed by donor impurities, the semiconductor is n-type and e^- becomes the majority carrier. Otherwise, the semiconductor is p-type and h^+ becomes the majority carrier if acceptor impurities contribute most of the free carriers. It is noticed that the Fermi energy level (E_F) becomes different from E_i when the semiconductor is doped, where E_F can be expressed by Eq. (2.6) and Eq. (2.7) for the case of n-type and p-type semiconductors, respectively.

$$E_F = E_i + k_b T \ln\left(\frac{n_0}{n_i}\right) = E_c + k_b T \ln\left(\frac{n_0}{N_c}\right) \tag{2.6}$$

$$E_F = E_i - k_b T \ln\left(\frac{p_0}{n_i}\right) = E_v - k_b T \ln\left(\frac{p_0}{N_v}\right) \tag{2.7}$$

Here we simplify the condition where only one donor level and acceptor level are taken into consideration for a doped semiconductor. Considering the balance of the total charge density, one can have:

$$p_0 + N_d^+ = n_0 + N_a^- \tag{2.8}$$

Where N_d is the concentration of the donor impurity, and N_d^+ is the density of the positively charged donors. And N_a is the concentration of the acceptor impurity, and N_a^- is the density of the negatively charged acceptors. For a non-degenerate semiconductor where its E_F is being separated by at least $3k_bT$ away from either the conduction band minimum or the valence band maximum, one can apply *Fermi-Dirac* distribution function to rewrite Eq. (2.8) into Eq. (2.9) as shown below.

$$p_0 + \frac{N_d}{1 + g_D \exp\left(\frac{E_F - E_d}{k_b T}\right)} = n_0 + \frac{N_a}{1 + g_A \exp\left(\frac{E_a - E_F}{k_b T}\right)} \tag{2.9}$$

Where E_d and E_a are the energy level of the donor and the acceptor, respectively. g_D and g_A are the degeneracy factor of the donor and the acceptor, separately. For n-type semiconductor where $N_d > N_a$, the hole density p_0 is negligible and the acceptors are considered to be fully ionized since E_F is expected to be above the energy levels of all the acceptors. Hence by giving: $p_0 \approx 0$ and $N_a^- \approx N_a$, Eq. (2.9) can be simplified to the form of Eq. (2.10) for n-type semiconductor.

$$\frac{N_d}{1 + g_D \exp\left(\frac{E_F - E_d}{k_b T}\right)} = n_0 + N_a \tag{2.10}$$

By referring the second half of Eq. (2.6), one can rewrite Eq. (2.10) without E_F by considering the derivation shown in Eq. (2.11).

$$\begin{aligned}\left[g_D \exp\left(\frac{E_F - E_d}{k_b T}\right)\right]^{-1} &= \frac{1}{g_D} \exp\left(\frac{E_d - E_F}{k_b T}\right) \\ &= \frac{1}{g_D} \exp\left(\frac{E_d - E_c}{k_b T}\right) \exp\left(\frac{E_c - E_F}{k_b T}\right) \\ &= \frac{1}{g_D} \exp\left(\frac{E_d - E_c}{k_b T}\right) \frac{N_c}{n_0}\end{aligned} \tag{2.11}$$

Where the last line of Eq. (2.11) can be further simplified by considering an auxiliary variable N_n^* expressed by Eq. (2.12).

$$N_n^* = \frac{N_c}{g_D} \exp\left(\frac{E_d - E_c}{k_b T}\right) \tag{2.12}$$

As a consequence, Eq. (2.10) is changed to the form of Eq. (2.13).

$$\frac{N_d}{1 + \frac{n_0}{N_n^*}} = n_0 + N_a \tag{2.13}$$

Similarly, for p-type semiconductor where $N_a > N_d$, it is reasonable to assume that $n_0 \approx 0$ and $N_d^+ \approx N_d$ since E_F is expected to stay below the energy levels of all donors. Therefore Eq. (2.9) can be simplified to the form of Eq. (2.14).

$$\frac{N_a}{1 + g_A \exp\left(\dfrac{E_a - E_F}{k_b T}\right)} = p_0 + N_d \tag{2.14}$$

Here we take the relation shown in the second half of Eq. (2.7) into consideration, then Eq. (2.14) can be rewritten into a new form without E_F by considering the derivation shown in Eq. (2.15).

$$\begin{aligned}\left[g_A \exp\left(\frac{E_a - E_F}{k_b T}\right)\right]^{-1} &= \frac{1}{g_A}\exp\left(\frac{E_F - E_a}{k_b T}\right) \\ &= \frac{1}{g_A}\exp\left(\frac{E_F - E_v}{k_b T}\right)\exp\left(\frac{E_v - E_a}{k_b T}\right) \\ &= \frac{1}{g_A}\frac{N_v}{p_0}\exp\left(\frac{E_v - E_a}{k_b T}\right)\end{aligned} \tag{2.15}$$

Where the last line of Eq. (2.15) can be further simplified by considering an auxiliary variable N_p^* expressed by Eq. (2.16).

$$N_p^* = \frac{N_v}{g_A}\exp\left(\frac{E_v - E_a}{k_b T}\right) \tag{2.16}$$

Hence Eq. (2.14) is now turned to the form of Eq. (2.17).

$$\frac{N_a}{1 + \dfrac{p_0}{N_p^*}} = p_0 + N_d \tag{2.17}$$

The solutions for Eq. (2.13) and Eq. (2.17) are given by Eq. (2.18) and Eq. (2.19), respectively.

$$n_0 = -\frac{N_n^* + N_a}{2} + \sqrt{\frac{(N_n^* + N_a)^2}{4} + N_n^*(N_d - N_a)} \tag{2.18}$$

$$p_0 = -\frac{N_p^* + N_d}{2} + \sqrt{\frac{(N_p^* + N_d)^2}{4} - N_p^*(N_d - N_a)} \tag{2.19}$$

2.2.2 Band gap narrowing

When determining E_g of a specific SiC sample, the narrowing of the band gap needs to be taken into account if the SiC sample is heavily doped. Persson *et al.*[37] have developed a model to calculate the band gap narrowing of both n- and p-type SiC.

The model is presented as the function of ionized impurity concentration where the methodology for the model development is based on a zero-temperature Green's function formalism. The energy shift of the conduction band minimum (ΔE_c) and the valence band maximum (ΔE_v) of the n-type SiC are expressed by Eq. (2.20) and Eq. (2.21), respectively. The values of the parameters in Eq. (2.20) and Eq. (2.21) for 3C-, 4H- and 6H-SiC are summarized in Tab. 2.4.

$$\Delta E_c = A_{n,c}\left(\frac{N_d^+}{10^{18}}\right)^{1/3} + B_{n,c}\left(\frac{N_d^+}{10^{18}}\right)^{1/2} \tag{2.20}$$

$$\Delta E_v = A_{n,v}\left(\frac{N_d^+}{10^{18}}\right)^{1/4} + B_{n,v}\left(\frac{N_d^+}{10^{18}}\right)^{1/2} \tag{2.21}$$

for n-type (meV)	3C-SiC	4H-SiC	6H-SiC
$A_{n,c}$	-17.22	-17.91	-23.31
$B_{n,c}$	-2.57	-2.20	2.26
$A_{n,v}$	25.05	28.23	26.57
$B_{n,v}$	8.01	6.24	0.43

Table 2.4: Parameters[37] for the calculation of ΔE_c and ΔE_v of n-type 3C-, 4H- and 6H-SiC using Eq. (2.20) and Eq. (2.21).

Whereas the energy shift of the conduction band minimum (ΔE_c) and the valence band maximum (ΔE_v) of the p-type SiC are expressed by Eq. (2.22) and Eq. (2.23), respectively. The values of the parameters in Eq. (2.22) and Eq. (2.23) for 3C-, 4H- and 6H-SiC are summarized in Tab. 2.5. Note that a third fitting parameter is added in Eq. (2.23) for 4H- and 6H-SiC for precision improvement.

$$\Delta E_c = A_{p,c}\left(\frac{N_a^-}{10^{18}}\right)^{1/4} + B_{p,c}\left(\frac{N_a^-}{10^{18}}\right)^{1/2} \tag{2.22}$$

$$\Delta E_v = A_{p,v}\left(\frac{N_a^-}{10^{18}}\right)^{1/3} + B_{p,v}\left(\frac{N_a^-}{10^{18}}\right)^{1/2} + C_{p,v}\left(\frac{N_a^-}{10^{18}}\right)^{1/4} \tag{2.23}$$

The aforementioned calculation method is applied for the estimation of the band gap narrowing at absolute zero (0 K) where the resulted narrowed band gap at 0 K (E_{g0}) due to impurities doping can be expressed by Eq. (2.24).

$$E_{g0} = E_{g0}^I + (\Delta E_c - \Delta E_v) \tag{2.24}$$

Where E_{g0}^I is the band gap of intrinsic SiC at 0 K and equals to 2.40 eV, 3.29 eV and 3.10 eV for 3C-, 4H- and 6H-SiC, respectively. The band gap further decreases with rising temperature due to thermal expansion, where the band gap at

for p-type (meV)	3C-SiC	4H-SiC	6H-SiC
$A_{p,c}$	-16.18	-16.15	-21.77
$B_{p,c}$	-0.52	-1.07	0.10
$A_{p,v}$	26.36	-35.07	-27.88
$B_{p,v}$	-4.28	6.74	4.60
$C_{p,v}$	-	56.96	50.13

Table 2.5: Parameters[37] for the calculation of ΔE_c and ΔE_v of p-type 3C-, 4H- and 6H-SiC using Eq. (2.22) and Eq. (2.23).

elevated temperature ($E_g(T)$) is given by the empirical Varshni relation[38] as shown in Eq. (2.25).

$$E_g(T) = E_{g0} - \frac{aT^2}{T+b} \tag{2.25}$$

Where the fitting parameters a and b for all SiC polytypes are[25] ($a = 8.2 \times 10^{-4}$ eV.K^{-1} and $b = 1.8 \times 10^3$ K).

2.2.3 Absorption coefficient of 6H-SiC

Absorption coefficient (α) of a material is used to quantify how quickly an incident light beam gets attenuated as it penetrates through the sample. The penetration depth, *i.e.*, the depth where the intensity of the light beam decays to $1/e$ of its value at the incident surface, is actually equals to $1/\alpha$. Since α is an essential parameter for the determination of the injection level (g) which is crucial for the research related to the lifetimes of the DAP recombination (Chapter 4) and carriers trapping by the negative-U centers (Chapter 5). It is important to know the value of the interband absorption coefficient of 6H-SiC with $\mathbf{E} \perp \mathbf{c}$ configuration which is the condition of the laser excitation in our lab. Sridhara *et al.*[39] have measured the temperature-dependent absorption coefficients for 3C-, 4H- and 6H-SiC thick films. The related experimental setup consists of a homemade dual beam absorption apparatus system with several types of pumping lasers where the $\mathbf{E} \perp \mathbf{c}$ configuration was applied. The wavelength range of the measurements is from 3900 Å (∼3.179 eV) to 2968 Å (∼4.177 eV). The intraband absorption coefficients of 6H-SiC were measured by Dubrovskii *et al.*[40]. Therein, an absorption band of n-type 6H-SiC under $\mathbf{E} \perp \mathbf{c}$ condition was found to peak at around 2.0 eV. Similarly, we also found the peak of the absorbance at nearly the same photon energy (∼1.97 eV) on two strong n-type 6H f-SiC samples, *i.e.*, SN-1 and SN-2(the detailed parameters related to those two samples will be introduced latter in this chapter), as shown in Fig. 2.6. The absorption spectra were measured by an integrating sphere (the detailed experimental setup by applying the integrating sphere will be introduced in Chapter 3). One explanation for this absorption peak is provided by Limpijumnong *et al.*[41]. By applying *first-principles* calculations, they proved that the peak around 2.0 eV of the optical-absorption band

of n-type 6H-SiC is caused by the e^- transition from c_1 band to c_4 band at **M** point (as shown in Fig.4(d) in Ref. [41]) within the conduction band after absorbing the incident photons.

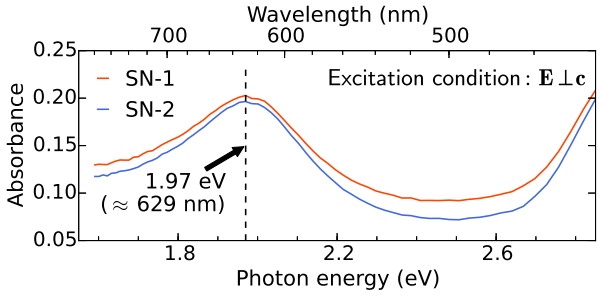

Figure 2.6: Absorption spectra of two strong n-type sample SN-1 & SN-2 under $\mathbf{E} \perp \mathbf{c}$ condition.

2.3 Growth of f-SiC

2.3.1 Growth of f-SiC epilayer by FSGP technique

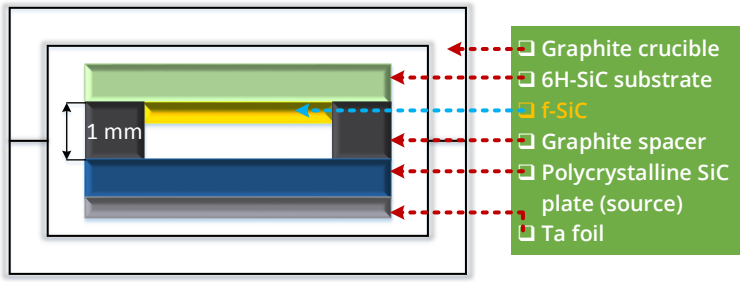

Figure 2.7: Schematic illustration[42] of f-SiC growth setup using FSGP technique (cross-sectional view).

As Murata *et al.*[43] have experimentally demonstrated the trend where the emission efficiency related to DAP recombination in N-B co-doped n-type 6H f-SiC could be further improved by letting both N_d and N_a be higher than 10^{18} cm^{-3}. Fast Sublimation Growth Process (FSGP)[6] is up to now one of the few epilayer growth methods that can realize N_d, $N_a > 10^{18}$ cm^{-3} for N-B co-doped f-SiC. The schematic

diagram of the cross-sectional view of the f-SiC growth environment is shown in Fig. 2.7. There is only 1 mm vertical spacing between the source material and the substrate, where the purpose is to prevent the vapor species to react with the graphite walls. A polycrystalline SiC plate is chosen as the source material instead of the SiC powders, this is to reduce the density of the structural defects in the grown epilayer which is reflected by the irregularities on the surface of the source material. In addition, it is easier to control the growth process by using solid source compared to powder source, where the powder source is more likely to sublime in a non-uniform way. In this research, the SiC source plate is grown by modified physical vapor transport (M-PVT)[10] where the details about this technique will be introduced latter. The typical temperature ramp-up during the epilayer growth is around 20 $\mathrm{K} \cdot \mathrm{min}^{-1}$. The growth rate is maintained to increase slowly with 5 to 15 $\mu\mathrm{m} \cdot \mathrm{h}^{-1}$ per minute until it reaches to $\sim$100 $\mu\mathrm{m} \cdot \mathrm{h}^{-1}$. The final growth temperature is controlled approximately between 1700 °C to 1800 °C much lower than that of physical vapor transport (PVT) technique which is around 2300 °C to 2500 °C. When the growth temperature is lowered compared to PVT, the ambient pressure will also decrease enabling to maintain a high growth rate. Typical range of the ambient pressure is maintained within 0.01 to 100 Pa[7] for the stabilization of the growth rate and enhancement of the nitrogen incorporation. Note that the high concentration of both N and B over 10^{18} cm^{-3} comes from the high doping condition in the source SiC plate. While the concentration of N in the epilayer can be further enhanced by introducing nitrogen gas into the growth ambient. The 6H-SiC substrate is normally 1.4° off-axis from (0001) plane toward $\langle 11\bar{2}0 \rangle$ direction. In addition, the substrate is cleaned firstly by trichlorethylene, acetone and ethanol, and then by the solution with $H_2O : NH_3 : H_2O_2$ (5:1:1) and $H_2O : HCl : H_2O_2$ (6:1:1) sequentially. One of the challenges of applying FSGP technique is the control of 3C-SiC inclusions as there exist high probability to form 3C-SiC during the epilayer growth of 6H f-SiC. This is because that there is good phase matching between the (111) plane of 3C-SiC and the (0001) plane of 6H-SiC and the nucleation energy for 3C-SiC is quite low[44]. There are several disadvantages of 3C-SiC inclusion in 6H f-SiC. For instance, stacking faults could be created due to the increased stress induced by 3C-SiC[45]. More non-radiative recombination centers are introduced. Extra luminescence caused by 3C-SiC at infrared region would further increase the device temperature, and so on. As higher Si/C ratio could enhance the inclusion of 3C-SiC[42], the Si/C ratio can be controlled by introducing a tantalum (Ta) foil beneath the source SiC plate as shown in Fig.2.7. The Ta foil is pretreated by being annealed in a carbon-rich environment at 1850 °C for 2.5 hours. By introducing the pretreated Ta foil into the growth ambient of f-SiC, the Si/C can be lowered hence 3C-SiC can be avoided.

2.3.2 Growth of source material by M-PVT technique

As mentioned earlier, the source SiC plate for FSGP technique is grown by the M-PVT method, where the cross-sectional view of the growth cell of M-PVT is shown

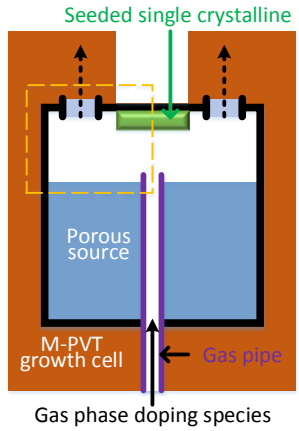

Figure 2.8: Schematic illustration[10] of seeded SiC single crystalline growth setup using M-PVT technique (cross-sectional view).

in Fig. 2.8. Compared to the conventional PVT method, an additional gas pipe is introduced into the growth cell for M-PVT method. Therein, silane (SiH_4 : H_2 with 1:10) and propane (C_3H_8) which contains Si- and C-element, respectively, are introduced into the growth ambient via the gas pipe. In this way, the gas stream of SiC is pushed to the facet of the seeded SiC which break the diffusion limitation of the conventional PVT method. Meanwhile, due to the accelerated SiC flux, the issue of source material graphitization can be solved to a large extent[10]. For n-type doping using nitrogen, an extra flow of nitrogen gas is also introduced via the gas pipe, enabling the density of nitrogen impurity in the seed SiC over 10^{18} cm^{-3}. Compared to nitrogen dopant that is contained in both gas phases source and solid source, the species contains B-element is only mixed in the porous solid source[11].

2.4 6H f-SiC samples included in the thesis

There are seven N-B co-doped 6H f-SiC samples studied in this research where three of them are p-type f-SiC (SP-1 to SP-3) and the rest four samples are n-type f-SiC (SN-1 to SN-4). Here we give the temperature-dependent free carriers concentrations (n_0 or p_0), band gaps (E_g) and position of Fermi levels (E_F) for all samples by considering the standard band diagram of the N-B co-doped 6H SiC as shown in Fig. 2.9. As we can see in Fig. 2.9, N-doping induces three nonequivalent donor levels on different lattice sites of 6H-SiC as mentioned in Fig. 2.3. ΔE_h, ΔE_{k_1} and ΔE_{k_2} denote the ionization energy of the respective donor level, where we adopt the related values from Ref. [27]. On the other hand, here we only consider one deep level induced by B-

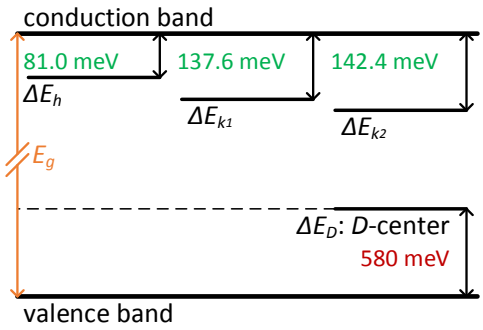

Figure 2.9: The band diagram of the perfect N-B co-doped 6H-SiC.

doping, *i.e.*, the well-known D-center with the ionization energy $\Delta E_D \approx$580 meV[46]. It is worthy to mention that we have confirmed the existence of an additional deep level induced by B-doping, *i.e.*, the D^*-center, which will be introduced in Sec. 4.2. Nonetheless, it is believed that D-center is still the only boron related deep center in 6H-SiC active at room temperature. The methodology for the calculation of the temperature-dependent n_0 (or p_0), E_g and E_F refers to Subsec. 2.2.1 and 2.2.2. The exception is that Eq. (2.13) has to be rewritten into the form of Eq. (2.26) since we have three different donor levels in 6H-SiC, where $N_{d,i}$ refers to the concentration of the donor impurity on each lattice site.

$$\sum_i \frac{N_{d,i}}{1 + g_D \frac{n_0}{N_c} \exp\left(\frac{E_i}{k_b T}\right)} = n_0 + N_a \tag{2.26}$$

The essential parameters of these seven f-SiC samples at RT are summarized in Tab. 2.6 as shown below. Note that the f-SiC epilayers on all seven samples are grown on 250 μm thick 6H-SiC substrates (SiCrystal GmbH). The temperature-dependent n_0 (or p_0), E_g and E_F of all seven f-SiC samples are shown in Fig. 2.10. Note that the related source code written in Python for the calculation of n_0 (or p_0), E_g and E_F for all the samples can be found in Listing A (included in Appx. A). Here, for the trends of the free carrier densities (n_0 | p_0), in n-type f-SiC, we find that the free carrier density (n_0) is dependent on N_d/N_a at a low-temperature range approximately up to 200 K where $N_n^* \ll N_a$, and becomes dominated by $N_d - N_a$ at elevated temperatures where N^* is comparable to N_a. Similarly, the tendency regarding p_0 in p-type f-SiC shows dependencies on N_a/N_d and $N_a - N_d$ as well. Note that there is no crossover among the curves of the three p-type f-SiC representing the trends of p_0, since both their N_a/N_d and $N_a - N_d$ follow the ranking of SP-1 > SP-2 > SP-3. Regarding the temperature-dependent band gap narrowing in f-SiC samples, it can be seen

that the extent of the band gap narrowing is strongly dependent on the density of compensation impurity, i.e., N_a for n-type f-SiC and N_d for p-type f-SiC. As for the evolution of E_F, for n-type f-SiC, the Fermi level tends to be away from the conduction band minimum (E_c) along with the increase of n_0, where the trends of both n_0 and E_F reflect the evolution of n-type doping level with changing temperatures. For p-type f-SiC, it is found that the trend regarding the difference between Fermi level and valence band maximum (E_v) against the increasing temperature becomes more negative as the p-type doping level increases, where the physical explanation behind this phenomenon still requires further investigation.

Sample →		SN-1	SN-2	SN-3	SN-4	SP-1	SP-2	SP-3
d_{epi}	(μm)	45	45	150	250	70	46	48
N_d		9.0	9.2	2.85	2.55	0.04	3.2	6.0
N_a	($\times 10^{18}\text{cm}^{-3}$)	4.4	5.2	1.10	1.50	8.0	6.9	6.9
n_0, p_0		1.90	1.69	1.34	1.02	2.39 $\times 10^{-7}$	1.11 $\times 10^{-9}$	1.80 $\times 10^{-10}$
E_g	(meV)	2985	2983	3003	3003	3043	3001	2992
E_F		2888	2883	2897	2890	475	615	662

Table 2.6: Essential parameters for all seven f-SiC samples at RT, where d_{epi} refers to the epilayer thickness. It is also necessary to mention that all the N_d, N_a are measured by time-of-flight secondary ion mass spectroscopy (TOF-SIMS).

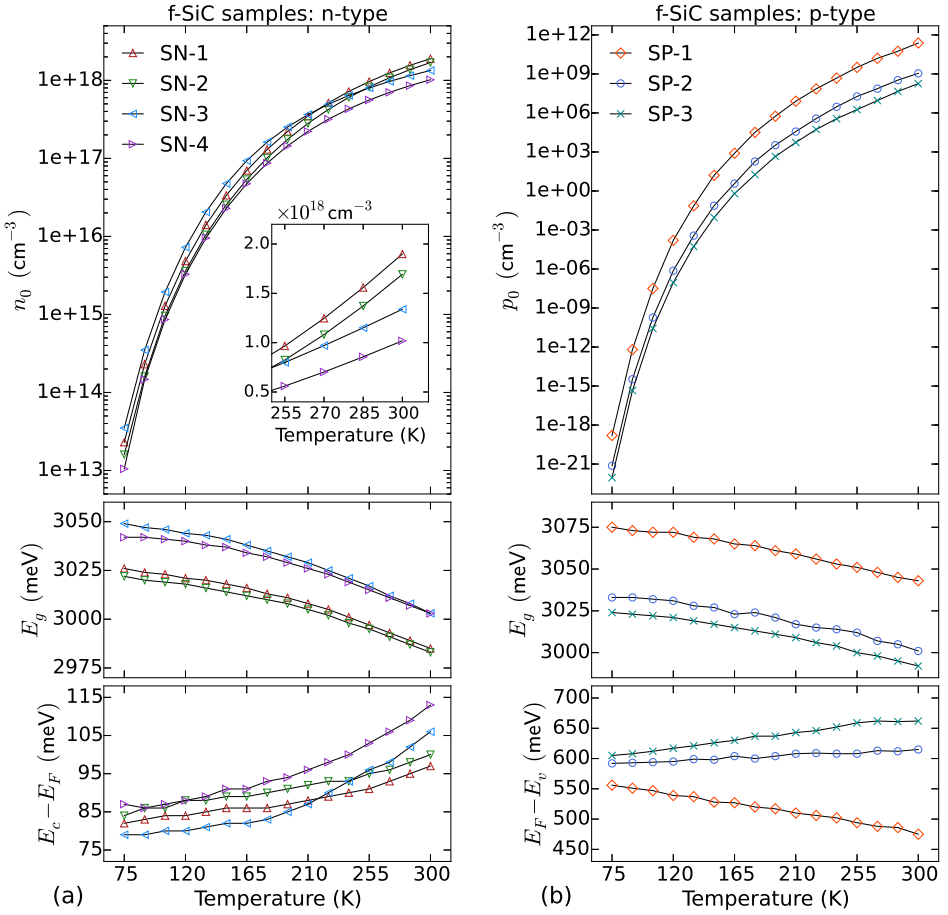

Figure 2.10: The calculated temperature-dependent free carriers concentrations (n_0 or p_0), band gaps (E_g) and position of Fermi levels (E_F) of all seven 6H f-SiC samples.

CHAPTER 3
Experimental techniques

There are various instrumentation systems which can be applied to characterize different aspects of the properties of SiC material. In this chapter, we mainly summarize the experimental techniques employed in our research on f-SiC including: a) Temperature-dependent micro-PL system; b) Thermally stimulated luminescence (TSL) measurement system; c) Time-resolved photoluminescence (TRPL) measurement system based on time-correlated single photon counting solution; d) Integrating sphere based photoluminescence quantum yield (PL-QY) measurement system.

3.1 Thermally stimulated luminescence measurement system

In this research, the aim of performing the thermally stimulated luminescence (TSL) measurements on f-SiC is to study the radiative recombination and the carriers (e^-) retrapping process related to the non-equilibrium majority carriers being captured on the shallow trapping centers, where the shallow trapping centers are normally induced by doped impurities. The details of the research will be introduced in Chapter 4.

3.1.1 Introduction to TSL

To clarify the existence of shallow traps for the majority carriers which are either below the conduction band minimum or above the valence band maximum and how they could affect the luminescence properties of 6H f-SiC, the systematic examinations of their energy levels within the band gap and temperature dependencies are necessary. Temperature dependent hall measurements could reveal energy levels but do not differentiate between different donor and acceptor levels and degree of compensation. Another disadvantage is that contact preparation is necessary, which for f-SiC is time consuming. This is also the case for other methods like deep level transient spectroscopy (DLTS), admittance spectroscopy and capacitance-voltage profiling. On the other hand, the measurement of thermally stimulated luminescence (TSL) is nondestructive and requires only thermal conductivity.

The principle and basics of TSL is summarized in Fig. 3.1, where we take the TSL measurement of an n-type semiconductor material as an example. In the beginning, the sample at a low temperature (*e.g.*, in our case, the f-SiC sample is kept at 25 K at the initial stage) is excited by X-ray source, stimulating the e^- to transit from

the top of the valence band into the conduction band and generating active h^+ at the top of the valence band. Particularly, in the highly co-doped samples such as 6H f-SiC, most of the non-equilibrium e^- and h^+ are captured by the existing donor and acceptor levels where the spontaneous emission will be immediately observed as the DAP recombination photoluminescence. Whereas the remained non-equilibrium majority carriers (*i.e.*, e^-) are trapped on the shallow trapping center meanwhile leaving the leftover non-equilibrium minority carriers (*i.e.*, h^+) on the recombination center as shown in the (a) of Fig. 3.1. During the sample being heated up with a constant heating rate, the trapped e^- is thermally stimulated and transited towards either the excited state of the trapping center or the bottom of the conduction band as shown in the (b) of Fig. 3.1. The thermally stimulated e^- can be further retrapped by the ground state of the trapping center or recombine with the h^+ at the recombination center radiatively, where the luminescence caused by the later process is known as the thermally stimulated luminescence (TSL). Note that more information specifically related to the TSL measurements on f-SiC samples (*e.g.*, available temperature ranges) will be given in Sec. 4.1.

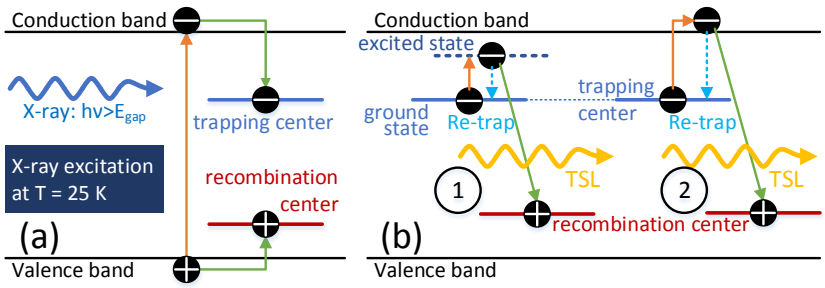

Figure 3.1: (a) X-ray excitation of the sample at 25 K; (b) Two pathways of TSL generation, where the trapped e^- can be thermally excited to 1) the excited state of trapping center or 2) the conduction band minimum then recombine with h^+ at the recombination center.

3.1.2 Experimental setup of TSL measurement system

The experimental setup of the TSL measurement is presented in Fig. 3.2, which was self-assembled during the author's external stay at University Erlangen-Nürnberg. We can see that there are generally two steps in the characterization based on TSL measurement. First, the sample is mounted on the cryostat (compressor: CTI-CRYOGENICS 8300, vacuum pump: COMBIVAC CM 31, temperature controller: LakeShore 330 Autotuning) using silver paste. The sample has to be cooled down to 25 K in a vacuum chamber. When the temperature of the sample reaches to 25 K,

it is excited by the X-ray source (Siemens NANODOR 1, set as 75 kV and 18 mA) for 6 cycles with 30 sec per cycle. Second, the cryostat starts to be heated up with the preset heating rate, the heating rate is controlled to be stable using the temperature controller with the embedded PID algorithm. The thermally stimulated photons are modulated by a chopper (Model SR540, STANFORD RESEARCH SYSTEMS, INC.) in order to eliminate the background noise then collected by a multialkali photomultiplier tube (PMT, THORN EMI Electron Tubes) with the lock-in amplifier (SR510, STANFORD RESEARCH SYSTEMS, INC.). An automated data acquisition and visualization program developed by the researchers in i-MEET, University Erlangen-Nürnberg simplifies the data processing of the TSL measurement results.

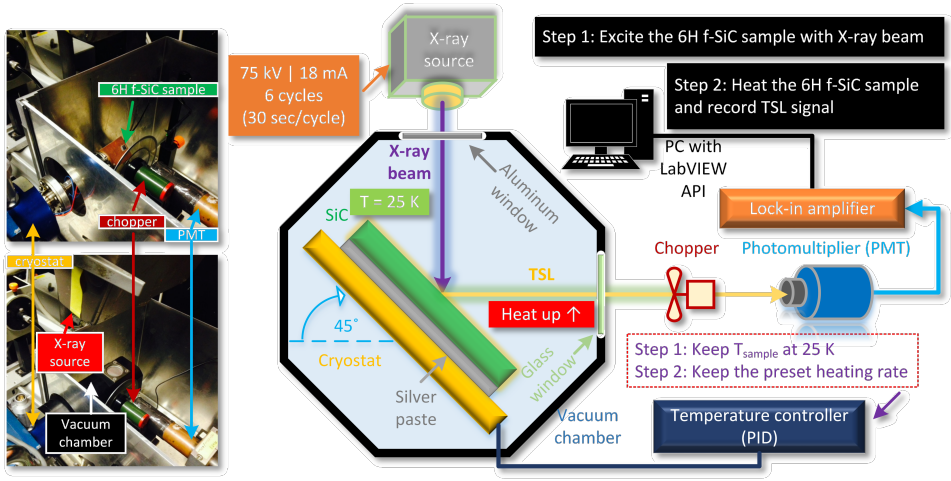

Figure 3.2: Schematic diagram of the TSL measurement system where the two steps of the experimental operation are indicated. In addition, two pictures showing some of the components of the experimental setup are placed in the top right corner.

3.2 Temperature-dependent micro-PL system

The purpose of applying the temperature-dependent micro-PL measurements on f-SiC is to investigate the double *D*-center related DAP emission which will be introduced in Chapter 4.

3.2.1 Cryostat system

The cryostat system is essential for the temperature control of the temperature-dependent micro-PL system. The related schematic diagram is shown in Fig. 3.3

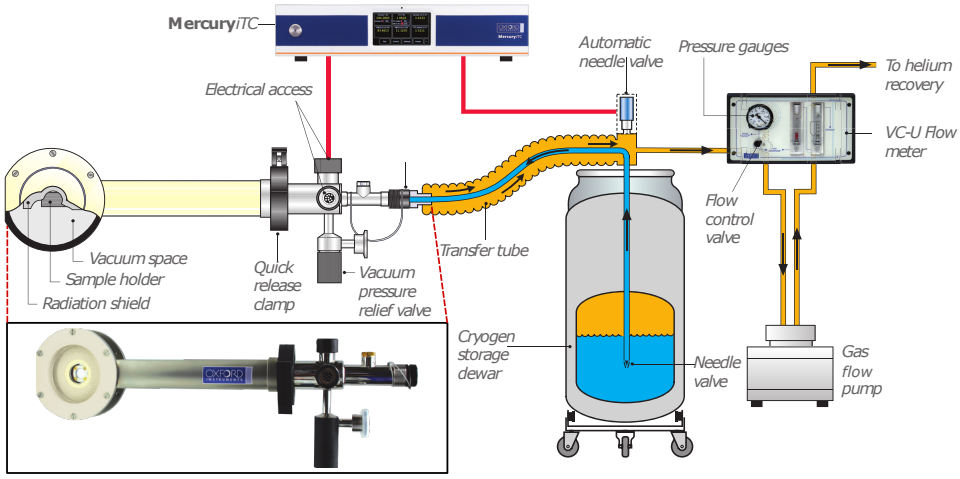

Figure 3.3: Schematic diagram of cryostat system (from: Oxford Instruments plc), the picture of the cryostat is shown in the bottom left corner.

where the whole system is purchased from Oxford Instruments plc[1]. The temperature of the sample implemented in the cryostat system can be controlled within 65 K to 310 K or within 2.2 K to 310 K with liquid nitrogen or liquid helium, respectively. In our research, the cryostat system uses liquid nitrogen. The main components of the system shown in Fig. 3.3 are summarized as followings: (a) Cryostat (MicrostatHe, the picture of the real product is shown in the bottom left corner of Fig. 3.3). (b) Temperature controller (Mercury*iTC*, with embedded proportional–integral–derivative (PID) controller). (c) Cryogen storage dewar, where the liquid nitrogen is stored. (d) VC-U flow meter (VC41 helium and nitrogen gas flow controller). (e) Gas flow pump (Elnor Motors NV). Note that the cryostat mounted with the sample needs to be evacuated down to the pressure $< 10^{-5}$ mbar before the measurement. The vacuum pump system applied for the evacuation of the cryostat is purchased from Pfeiffer Vacuum SAS. Fig. 3.4(a) shows the three main components of the vacuum pump system[2].

3.2.2 Micro-PL system

The temperature-dependent PL intensities of the f-SiC samples are measured by a micro-PL system shown in Fig.3.5. The micro-PL system consists of a continuous diode laser with $\lambda = 377$ nm and an optical spectrometer (shamrock SR-303i-A Spec-

[1] The original figure is from the official brochure of MicrostatHe available at: http://nanoscience.oxinst.com/assets/uploads/products/nanoscience/documents/Microstat-family-of-cryostats.pdf

[2] The figure is from the official manual of HiCube 80 Eco available at: https://www.idealvac.com/files/ManualsII/Pfeiffer_HiCube80_Eco.pdf

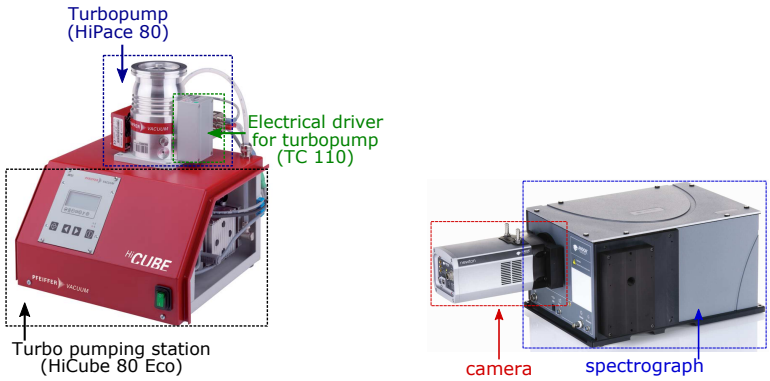

Figure 3.4: (a) Photo of the vacuum pump (from: Pfeiffer Vacuum SAS); (b) Photo of the spectrometer (from: Andor Technology Ltd).

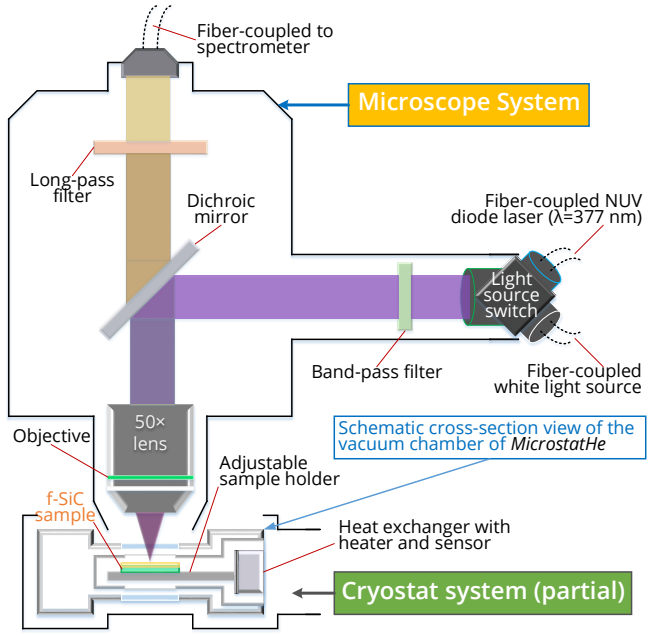

Figure 3.5: Schematic diagrams of the fiber-coupled micro-PL setup and vacuum chamber of the cryostat system mounted with f-SiC sample.

trograph, Andor Technology Ltd). Both the excitation laser beam and the PL emission are fiber-coupled to a 50× microscope lens in a front-excitation|front-detection configuration. The picture of the optical spectrometer[3] is shown in (b) of Fig. 3.4. It is worth to mention that the spectrometer could provide very precise PL signal measurement solution. To be specific, we set the spectrometer to capture the signal 40 times per second (*i.e.*, with a 40 Hz frequency) with 7.5 seconds in total, then the final PL spectrum is obtained by taking the average of the captured 300 PL spectra where the interference from the ambient noise can be minimized.

3.3 Time-resolved photoluminescence measurement based on time-correlated single photon counting solution

The purpose of the employing the TRPL measurements on f-SiC at RT in our research is to extract the information related to the carrier lifetimes of different recombination channels in f-SiC which will be discussed in detail in Chapter 5.

3.3.1 Basics of the principle of TCSPC

Typical fluorescence decay curve consists of multiple exponential decay channels, in which the lifetime of the fastest decay channel is normally hundreds of picoseconds to several nanoseconds. Time-correlated single photon counting (TCSPC) system is one of the target solutions to quantify the decay constants of the fluorescent decay profiles. The basics of the operation of TCSPC system can be divided into two steps[47, 48]:

1. During each cycle of the pulsed laser excitation on the fluorescent sample, the time interval (Δt) between the single laser pulse injection and the emission of single photon is recorded, as shown in the (a) of Fig. 3.6, where the electronics for measuring Δt in the TCSPC system acts like a stopwatch;

2. Each Δt is added to the "stack" labeled with a range of "time bins" (*e.g.*, $\Delta t \pm$ 500 ps) where the "stack" represents the number of photon counts. Each stacks with different ranges of "time bins" finally constitute the TCSPC histogram shown in the (b) of Fig. 3.6. Note that the lower limit of the "time bins" is affected by the resolution of the stopwatch-behaved electronics in TCSPC system.

One of the essential points is that one must keep the probability of detecting more than one photon per cycle is low. The precondition of maintaining single photon

[3]The picture is from the users guide of Shamrock SR-303i available at: http://www.tokyoinst.co.jp/en/product_file/file/AD10_man01_en.pdf

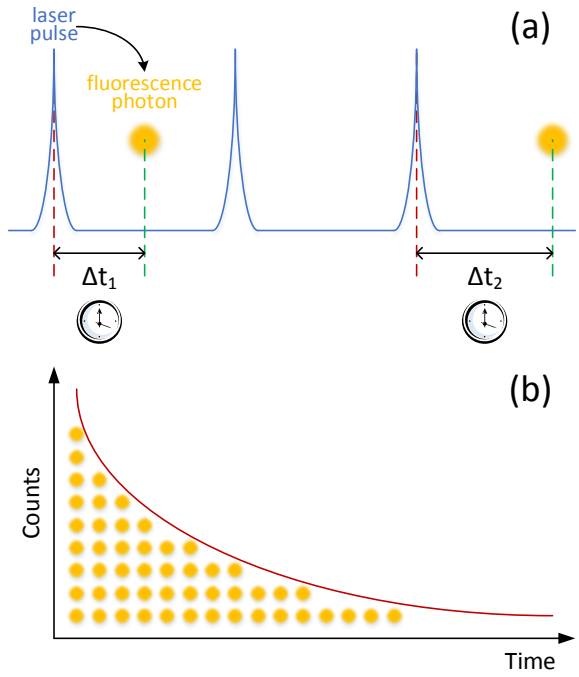

Figure 3.6: (a) Measurement of the time interval (Δt) between the laser pulse excitation and the single photon emission via TCSPC system; (b) Histogram of Δt generated by TCSPC system.

detection or empty cycle (*i.e.*, no photon detected, as shown in the second pulse shown in the (a) of Fig. 3.6) is to simply attenuate the power of the pulsed laser. On the other hand, if the number of the occurrence of the photon is more than one during one excitation cycle, the TCSPC system would only register the first photon but miss the following ones. This would cause the overestimation of the histogram with small Δt, where the related effect is called "pile-up". In addition, the electronics of the TCSPC system needs a "break" between the photon registration events, the time period for this "break" is called "dead time", where the photon emitted during the dead time cannot be registered. The issue of the pile-up and the dead time are depicted in Fig. 3.7. Normally, the time range of the TRPL decay of f-SiC is normally few hundreds of μs. In order to capture the related decay profile within long enough time period, the TCSPC system has to be operated in the long-range-mode with the time resolution of the stopwatch-behaved electronics much longer than the dead time (<2.5 ns). Therefore, the issue related to the dead time can be avoided.

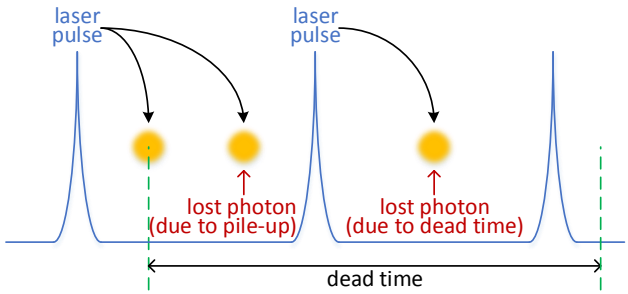

Figure 3.7: Effect of pile-up and the dead time during photon registration by TCSPC system.

3.3.2 Experimental setup of TRPL

The diagram of the experimental setup of TRPL system and the pictures of the key components are shown in Fig. 3.8. The following list summarizes the key components of the TRPL system purchased from PicoQuant GmbH: (a) Picosecond laser diode head (LDH-D-C-375) with $\lambda = 375$ nm, where the laser head can be fiber coupled; the full width at half maximum (FWHM) of the laser pulse is around 44 ps; the repetition rate can be controlled from single pulse to 80 MHz; (b) Computer controlled diode laser driver (PDL 828 "Sepia II", two channel version); (c) Hybrid photomultiplier detector assembly (PMA Hybrid 40), which is a compact single photon detector consisting of a PMT with an avalanche photon diode (APD) amplification stage. (d) TCSPC board with PCIe interface (TimeHarp 260 PICO), where the digital resolution is around 25 ps. In practice, the detection of the timing of laser pulse injection (here called t_1) is realized by the input of the synchronization signal directly from the laser head. While the detection of the timing of photon emission (here called t_2) is achieved by the PMT, and finally $\Delta t = t_2 - t_1$. Note that both timing signals are digitized by the fast electronics of TCSPC board. The resulted Δt is used to address the histogram memory on the TCSPC board where the value of the accessed cell marked with the fitted "time bin" for Δt in the histogram memory will be then increased by one. For the implementation of the TRPL setup to the PL decay measurements of f-SiC samples[49], both the injected laser pulse and the emitted photon signal are fiber-coupled to a $\times 50$ microscope lens with the configuration of front-excitation|front-detection. The radius of the laser spot (r) is measured to be $\sim$0.22 mm. After excitation, the emitted photons are filtered by a long-pass filter and then transferred to the PMT. The criteria for choosing the time range for the measurement is to recover the decay profile as complete as possible meanwhile one also has to prevent the interference from the background noise (typically 80 to 120 counts per second). The injection level g (cm^{-3}), *i.e.*, the density of the injected

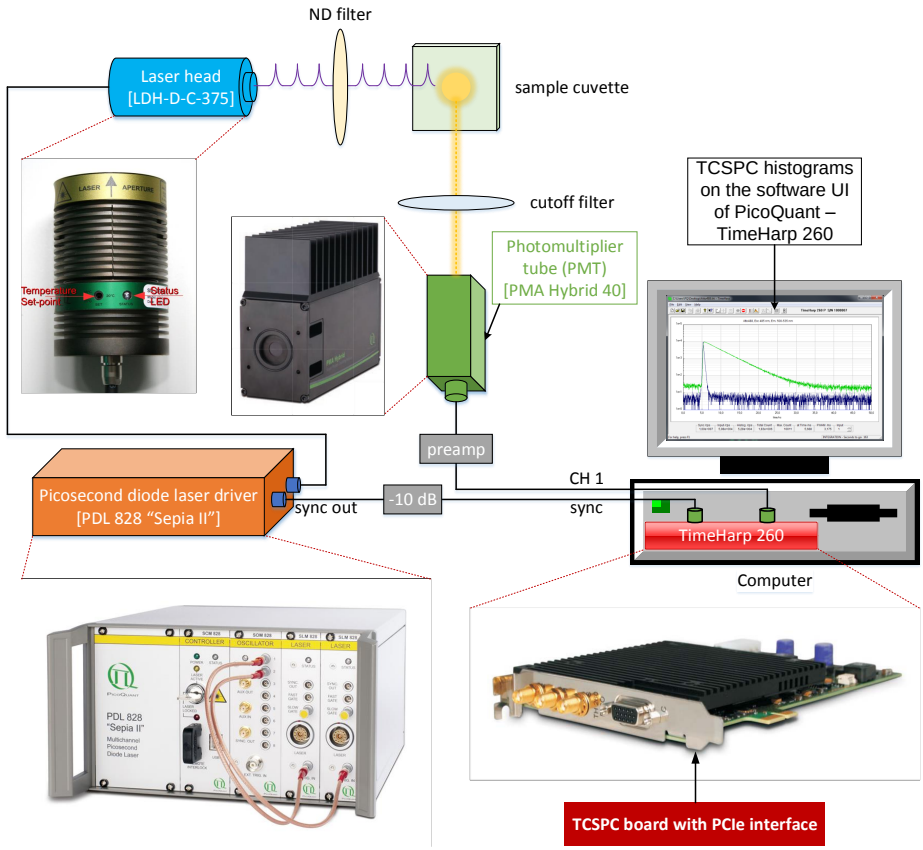

Figure 3.8: Schematic diagram of the TCSPC system.

photons per laser pulse, is an essential parameter for the negative-U center related carrier dynamics and the static DAP recombination lifetime calculation which will be introduced in Chapter 5. Note that the power of single laser pulse is independent of the repetition rate. The power of the pulsed laser beam (E_0) with a repetition rate of R_L is measured by an optical power meter (energy meter (PM100D) with silicon detector (S130VC), Thorlabs, Inc.). It is worthy to mention that during the measurement of the pulsed laser power, the laser beam is focused on the sensing area of the silicon detector. Then the photon density on the surface of the sample per single pulse I_0 (cm^{-2}) can be calculated using the values of r (the radius of laser spot), R_L (pulsed laser repetition rate) and E_0 (pulsed laser incident power) using Eq. (3.1). In Eq. (3.1), the former two parts together are aimed to get the photon energy density per single pulse on the sensing area of the silicon detector where the laser beam is

focused on, and the last part is just the reciprocal of the energy of a single photon from the laser beam.

$$I_0 = \frac{1}{R_L} \times \frac{E_0}{\pi r^2} \times \frac{\lambda}{hc} \tag{3.1}$$

In addition, the effective depth (Z_{eff}) is essential for the calculation of the injection level g [50]. Here, Z_{eff} represents the depth where the intensity of the beam intensity has just shrink to the midpoint between the original intensity and the attenuated intensity at the bottom of the thin film. Hence Z_{eff} can be obtained by applying Eq. 3.2, where the absorption coefficient α is about 400 cm^{-1} at 375 nm[39] with $\mathbf{E} \perp \mathbf{c}$ configuration as mentioned in Subsec. 2.2.3.

$$\frac{I_0 + I_0 \exp(-\alpha d)}{2} = I_0 \exp(-\alpha Z_{\text{eff}}) \quad \Longrightarrow \quad Z_{\text{eff}} = \frac{1}{\alpha} \ln\left[\frac{2}{1 + \exp(-\alpha d)}\right] \tag{3.2}$$

Finally the injection level g (cm^{-3}) can be calculated by taking the derivative of the attenuated beam intensity at Z_{eff} with respect to the depth (here represented as s) as shown in Eq. (3.3).

$$\begin{aligned} g &= \left.\frac{|\mathrm{d} I_0 \exp(-\alpha s)|}{\mathrm{d}s}\right|_{s=Z_{\text{eff}}} \\ &= \alpha I_0 \exp(-\alpha Z_{\text{eff}}) \end{aligned} \tag{3.3}$$

3.4 Integrating sphere system for photoluminescence quantum yield measurement

In this research, an integrating sphere based measurement system has been built up for the determination of the photoluminescence quantum yield (PL-QY) of the f-SiC samples, where the details related to the methodology and results of the PL-QY refer to Chapter 6.

3.4.1 Fundamentals of integrating sphere

An integrating sphere is a powerful equipment for optical flux measurement. Once the input flux strikes on the diffuse wall inside the integrating sphere, it experiences numerous diffuse reflections where the radiation of the input flux is eventually dispersed uniformly on the diffuse wall [4]. Finally, the detected integrated radiation intensity

[4] Tutorial: Integrating Sphere Fundamentals and Applications, available at: https://www.newport.com/t/integrating-sphere-fundamentals-and-applications

is proportional to that of the input flux. In this subsection, we will introduce some of the fundamentals of integrating sphere based on a related technical guide [5].

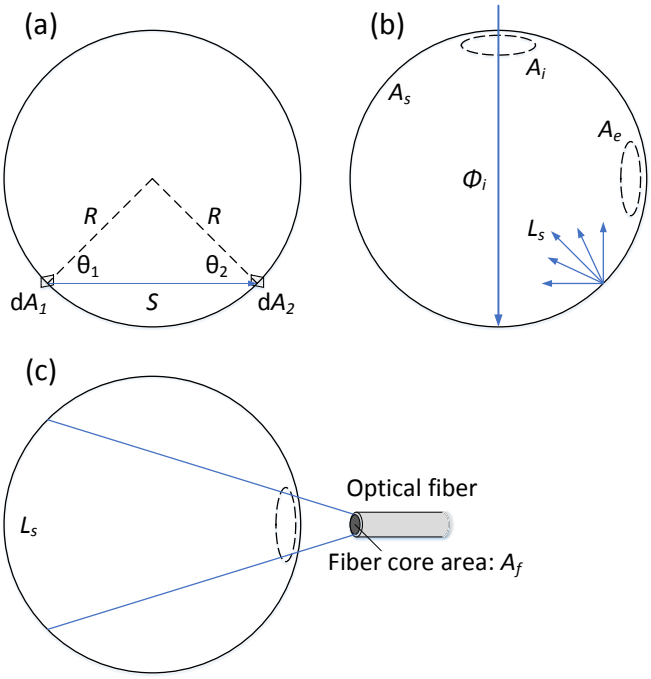

Figure 3.9: Diagrams illustrating the theory of integrating sphere in three aspects: (a) radiation exchange related to the differential diffuse areas $\mathrm{d}A_1$ and $\mathrm{d}A_2$; (b) radiance of the integrating sphere for an input flux; (c) incident flux corresponding to the optical fiber coupled input source.

First, let us consider the radiation exchange between two differential areas of the diffuse wall as shown in the (a) of Fig. 3.9. Here, we introduce a variable called the exchange factor (F_{1-2}) which denotes the fraction of energy transferred from the differential area $\mathrm{d}A_1$ to $\mathrm{d}A_2$. The original expression of F_{1-2} is given by Eq. (3.4).

$$\mathrm{d}F_{1-2} = \frac{\cos\theta_1 \cos\theta_2}{\pi S^2}\mathrm{d}A_2 \tag{3.4}$$

Since the energy transfer distance $S = 2R\cos\theta_1 = 2R\cos\theta_2$, where R is the radius of the diffuse wall sphere. One can obtain F_{1-2} by considering Eq. (3.5) shown below.

[5]Technical guide: Integrating Sphere Theory and Applications, available at: https://www.labsphere.com/site/assets/files/2551/integrating_sphere_theory_apps_tech_guide.pdf

$$F_{1-2} = \int \mathrm{d}F_{1-2} = \frac{1}{4\pi R^2} \int_{A_2} \mathrm{d}A_2 = \frac{A_2}{4\pi R^2} = \frac{A_2}{A_s} \tag{3.5}$$

Where A_s designates the total area of the diffuse wall within the integrating sphere. In fact, Eq. (3.5) indicates that the fraction of radiation energy received by element A_2 equals to A_2/A_s. This theoretically proves that the incident radiation energy does get spread uniformly on the diffuse wall as mentioned before.

When the incident light beam strikes the diffuse wall, the reflected radiation becomes the dummy light source which is normally quantified by the *radiance* (L), *i.e.*, the flux density per unit solid angle (unit: $\mathrm{W} \cdot \mathrm{m}^{-2} \cdot \mathrm{sr}^{-1}$). The radiance from a diffuse surface with the area of A within the integrating sphere is given by Eq. (3.6), where Φ_i, Ω and ρ represent the input flux, the total projected solid angle and the reflectance of the diffuse wall, respectively.

$$L = \frac{\rho \Phi_i}{A\Omega} \tag{3.6}$$

In reality, the integrating sphere is not an intact sphere but contains the input and exit ports instead. Here we assume the area of the input|exit port to be A_i and A_e, respectively as shown in (b) of Fig. 3.9. The indicent flux (unit: W) on the entire diffuse wall of the integrating sphere is given by Eq. (3.7) where $f = (A_i + A_e)/A_s$ designates the fraction of the areas of the ports.

$$\rho \Phi_i \frac{A_s - A_i - A_e}{A_s} = \rho \Phi_i (1 - f) \tag{3.7}$$

Then we can get the total incident flux after infinite times of reflection within the integrating sphere which is given by Eq. (3.8).

$$\Phi_i \sum_{k=1}^{\infty} \rho^k (1 - f)^k = \frac{\rho \Phi_i (1 - f)}{1 - \rho (1 - f)} \tag{3.8}$$

Since $\rho(1 - f) < 1$, the right part of Eq. (3.8) indicates that the ultimate flux corresponding to the entire diffuse wall sphere is actually higher than the input flux Φ_i because of the countless reflections within the integrating sphere. Accordingly, the radiance of the entire diffuse wall (*i.e.*, L_s) can be expressed by Eq. (3.9).

$$L_s = \frac{\Phi_i}{A_s \Omega} \times \frac{\rho}{1 - \rho (1 - f)} \tag{3.9}$$

Where the second part in Eq. (3.9) is unitless and often denoted as the *sphere multiplier* (M). In addition, Eq. (3.9) indicates that the radiance L_s is proportional to the sphere multiplier and inversely proportional to the dimension of the integrating sphere, *i.e.*, $L_s \propto M \cdot R^{-2}$.

Regarding to the situation where the input source beam is being coupled to an optical fiber as shown in the (c) of Fig. 3.9, the numerical aperture (NA) of the optical fiber, which quantifies its capacity of light coupling, is an important parameter for the estimation of the incident flux. The total projected solid angle (Ω) is now expressed by Eq. (3.10).

$$\Omega = \pi \left(\mathrm{NA}\right)^2 \tag{3.10}$$

Furthermore, the energy loss due to the light beam reflection at the air|fiber interface has to be taken into consideration when determining the indicent flux, where the fiber coupled incident flux (Φ_f) can be expressed by Eq. (3.11).

$$\Phi_f = L_s A_f \pi \left(\mathrm{NA}\right)^2 (1 - \mathcal{R}) \tag{3.11}$$

Where A_f represents the area of the core area of the fiber head, and $\mathcal{R}$ denotes the reflectance at the fiber head.

3.4.2 Integrating sphere system employed in this research

An integrating sphere (OL 700-71, purchased from Gooch & Housego) with diameter of 6 inch was employed in this research for the PL-QY determinations of the f-SiC samples, where Fig. 3.10 shows the photo [6] and schematic diagrams [7] of the related integrating sphere product.

This integrating sphere is originally for the purpose of spectral diffuse reflectance and transmittance measurements. With the internal surface coated with polytetrafluoroethylene (PTFE), the available wavelength range for measurement can be from 250 nm to 2.5 μm. In addition, it is specially designed to enable fiber optics for the optical coupling to the light source and spectrometer. As shown in Fig. 3.10, the light source can be fiber coupled to either reflectance | transmittance input fiber optic probe (FOP). Both the reflectance|transmittance refocusing lens attachments contains the factory-aligned lens which enable the incident light to be focused on the sample port, where the diameter of the focused beam spot on the sample port is around 3 mm. A 10° angle of incidence is designed for the reflectance input FOP aiming at minimizing the retro-reflected or near specular reflected flux losses. By tuning the beam switch knob between "sample" and "comparison" modes, the incident light beam coupled to the reflectance input FOP can be oriented directly on either the sample port or its vicinity, respectively. Note that for the measurements with light incidence from transmittance input FOP, the beam switch knob should be set to "comparison" mode in order to avoid light leakage.

[6] The photo of OL 700-71 is from the official brochure of OL 700 series available at: https://optroniclabs.com/wp-content/uploads/2014/10/700-71_73_74_B086_04-13.pdf

[7] The schematic diagrams of OL 700-71 are from the official manual (title: "OL 700-71 6-Inch Diameter Integrating Sphere Reflectance/Transmittance Attachment", manual No: M000300, Revision: D, Date: January 2010).

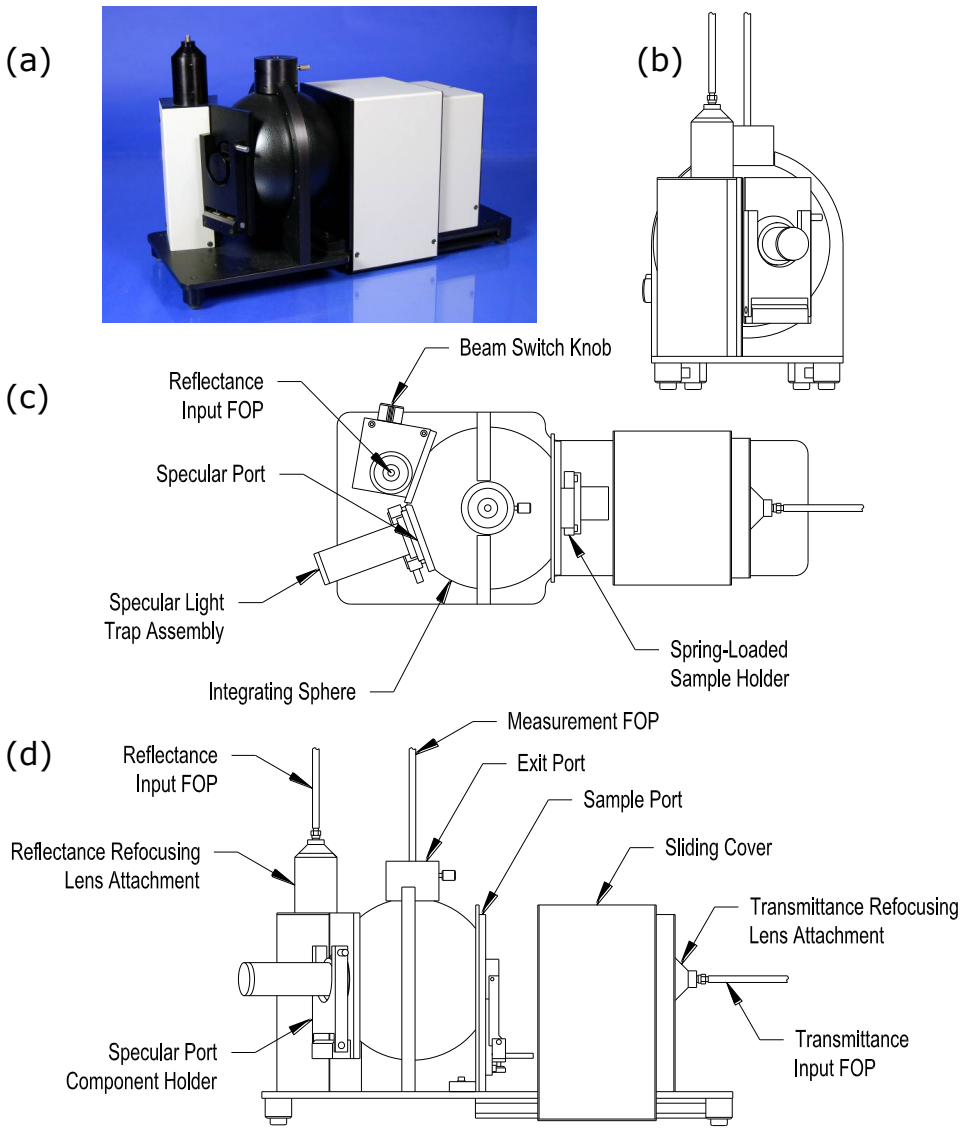

Figure 3.10: (a) photo, (b) side view, (c) top view and (d) front view of OL 700-71 6-inch diameter integrating sphere.

The integrating sphere is equipped with a certified reflectance standard (Refl-Std) of pressed PTFE powder which is packed in a 2-inch diameter holder. The 1.13-inch diameter central surface of the Refl-Std with the coated PTFE is designed to completely seal the opening of the sample port without any light leakage from the ambient. The reflectance of Refl-Std is shown in Fig. 3.11. The related reflectance data are also derived from the aforementioned official manual of OL 700-71. In this research, Refl-Std is applied for both reflectance and PL-QY measurements of SiC samples.

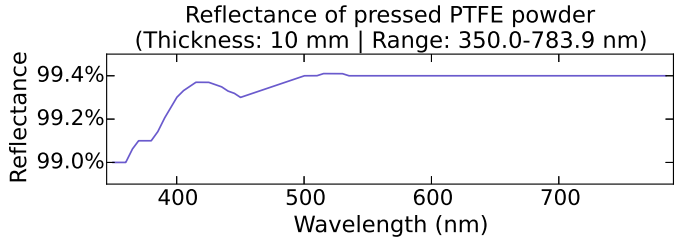

Figure 3.11: Absolute refeflectance of the 10 mm thick PTFE powder (350 nm to 783.9 nm at 0.1 nm intervals).

The detailed methodology and experimental design regarding to the PL-QY measurements based on the OL 700-71 6-inch diameter integrating sphere will be introduced in Chapter 6. The transmittance and reflectance measurements related to f-SiC are presented in Chapter 5&6, respectively. The light source for the transmittance | reflectance measurements with the integrating sphere is an xenon lamp (HPX-2000, Ocean Optics, Inc.) where the spectral range is from 185 nm to 2 μm. The photo of the HPX-2000 xenon lamp [8] is shown in Fig. 3.12. The detailed procedures corresponding to the transmittance | reflectance measurements refer to the official manual of OL 700-71 6-inch diameter integrating sphere, where 7 scans need to be acquired. Here we summarize the empirical sequence of those 7 scans in order to reduce the error of the measurements as shown in Tab. 3.1. Note that in Tab. 3.1 only the sample holder (with a ~5 mm diameter hole at the center) is placed towards the sample port for step 3 & 7.

[8] The photo is from the official installation and operation manual of HPX-2000 xenon lamp available at: https://oceanoptics.com/wp-content/uploads/hpx2000-Installation-and-Operation-Instructions.pdf

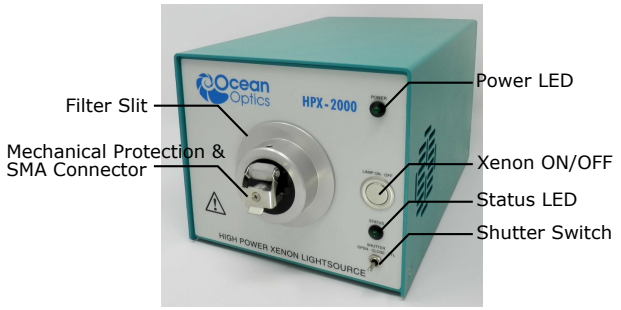

Figure 3.12: Photo of HPX-2000 high-power xenon light source.

Step no.	Spectrum name	Towards sample port	Connected FOP	Beam Switch
1	S_S	Refl-Std	Refl.	Samp.
2	S_{CS}	Refl-Std	Refl.	Comp.
3	S_B	–	Refl.	Comp.
4	S_{CL}	Sample	Refl.	Comp.
5	S_R	Sample	Refl.	Samp.
6	S_T	Sample	Tran.	Comp.
7	S_A	–	Tran.	Comp.

Table 3.1: The empirical sequence of the spectral scans for the measurements of transmittance | reflectance. The spectra names refer to the offcial manual of OL 700-71 6-inch diameter integrating sphere.

CHAPTER 4

Luminescence properties of 6H f-SiC related to doped impurities

As we have mentioned in Sec. 2.1 that the nitrogen-induced donors in 6H-SiC stay on three different lattice sites, *i.e.*, two quasi-cubic sites k_1/k_2 and hexagonal sites h, it is natural to wonder whether the contributions to DAP recombination from the donors staying on these three lattice sites are proportional to the densities of each donor in f-SiC. In other words, we are curious about whether any types of nitrogen-induced donors in our f-SiC samples show non-radiative behavior. Additionally, we also would like to check the existence of the shallow centers originated from the boron-doping in 6H f-SiC. In the first part of this chapter (Sec. 4.1), we demonstrate how we achieve the above goals by applying thermally stimulated luminescence (TSL) technique which has been introduced in Sec. 3.1 to characterize the 6H f-SiC samples followed by the numerical analysis of the TSL signals using a classic model. We reveal the non-radiative behavior regarding to the nitrogen-induced shallow donors on hexagonal lattice sites, where a part of the donors on hexagonal sites are found to keep trapping the non-equilibrium carriers instead of releasing them for the DAP recombination. In addition, we also confirm the nonexistence of boron-induced shallow acceptors as no related TSL signals are observed. As mentioned in Sec. 2.4, it is believed that the boron-induced acceptors in f-SiC by FSGP method are mainly the well-known *D*-centers staying at 0.58 eV above valence band maximum (E_v+0.58). However, there has existed the hypothesis with regard to the double-level *D*-center configuration in 6H-SiC where the second type of boron-doped acceptor level deeper than *D*-center might exist and participate in DAP recombination as well. In the second part of this chapter (Sec. 4.2), we combine the temperature-dependent photoluminescence measurements on 6H f-SiC samples together with the previous *first-principles* calculation results regarding to the lattice structures of boron-induced complexes in SiC. Our experimental results and corresponding analyses confirm the existence of the double *D*-center in 6H-SiC.

4.1 Shallow centers induced by doped impurities

4.1.1 Overview

As the shallow traps which are induced by doped impurities and have captured non-equilibrium carriers in 6H f-SiC could be easily thermally emptied to conduction band minimum[51] or valence band maximum at elevated temperatures, where the efficiency of donor-acceptor-pairs recombination can be degraded in this way. It is essential to confirm the existence of these shallow traps for further investigations. For the centers within the band gap of 6H-SiC introduced by nitrogen dopant, Ikeda *et al.*[52] have launched the photoluminescence measurements on the N-doped 6H-SiC samples at 4 K. After that, a quantum defect model was applied to extract the ionization energies related to the N-dopant induced donors which were site-dependent. The ionization energies regarding to the donor levels on hexagonal|cubic lattice site were estimated to be 100|155 meV, respectively. Latter on, Suttrop *et al.*[27] used Hall effect measurements on the N-doped 6H-SiC samples and extracted the ionization energies related to the N-induced donor levels on h, k_1 and k_2 sites as already mentioned in Sec. 2.4. On the other hand, Evwaraye *et al.*[53] applied thermal admittance spectroscopy to test the p-type B-doped 6H-SiC bulk samples, where they estimated the ionization energies of B-induced shallow acceptor levels which were about E_v+270, 310 and 380 meV corresponding to the h, k_1 and k_2 sites, respectively. Note that the deep levels induced by B-doping[46, 54] are beyond the scope of this research, where such deep centers with captured non-equilibrium h^+ are almost unable to be ionized even at RT. As mentioned in Sec. 3.1, TSL is a time-efficient and powerful technique to extract the information of shallow centers in a semiconductor material. In addition, as an indirect wide band gap semiconductor, SiC has fairly high probability to emit photons within visible spectrum range hence it is considered as available for TSL characterization[55]. Gorban and Suleimanov[1] first reported the TSL measurements on the n-type 6H-SiC crystal. They found nitrogen-induced shallow center as the e^- trap during the TSL process. Latter, several research outputs[56, 57] related to the TSL of n-type 6H-SiC were came out. However, the 6H-SiC samples employed in these researches were normally grown by Acheson process where the samples were low-compensated, *i.e.*, the density ratio between the effective donors and acceptors is far beyond or below unity, causing the very wide TSL glow curve. Since the SiC crystal quality grown by FSGP method is much better compared to the conventional growth process of SiC, and it has been reported that TSL is not only an efficient tool to study shallow traps but also a sensitive prober for the effective doping condition[58]. Accordingly, TSL technique is anticipated to reveal some new information regarding to the doped impurities in 6H f-SiC. The details of the experimental setup of the TSL measurement applied in this research have been summarized in Subsec. 3.1.2. Herein, five 6H f-SiC samples were employed in this research, *i.e.*, SP-1/3, and SN-2/3/4, where the essential parameters of these samples refer to Tab. 2.6. We tried to apply

[1] I. S. Gorban and M. Suleimanov, Sov. Phys. - Solid State **7**, 1035 (1965).

the lowest possible temperature increase rate during the TSL measurements in order to enable the real temperature of the sample to synchronize with that of the cryostat. The rate of $\sim 10\ \mathrm{K} \cdot \mathrm{min}^{-1}$ was applied for sample SP-1/3 and SN-2/3 whereas $\sim 15\ \mathrm{K} \cdot \mathrm{min}^{-1}$ was applied for sample SN-4.

4.1.2 Modelling TSL process by Halperin-Braner's method

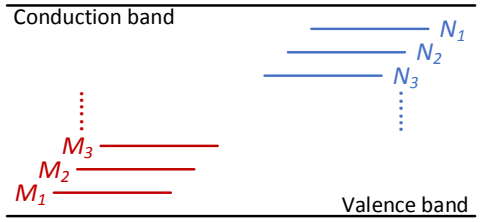

Figure 4.1: A band gap diagram of a semiconductor crystal which contains several e^- trapping centers (N_i) and h^+ trapping centers (M_i).

In this research, the fitting of the TSL glow curves was based on a simple model of TSL process developed by Halperin and Braner[59]. By revealing the influences from the two factors regarding to the symmetry of the TSL glow curve: 1) carrier retrapping probabilities and 2) ratio between the charged trapping center to the charged recombination center, it is possible to give precise estimation of the ionization energy of shallow trap by applying Halperin-Braner's model. First of all, it is assumed that several discrete localized e^-/h^+ traps are distributed within band gap. Let N_i designate the density of the e^- trap below conduction band minimum with the ionization energy of E_i and M_j designate the density of the h^+ trap above valence band maximum with the ionization energy of E_j as shown in Fig. 4.1. Based on the modelling perspective, here we add some details which supplement the brief introduction of the principle of TSL mentioned in Subsec. 3.1.1. During the excitation with $h\nu > E_g$ (*e.g.*, using X-ray source), it is believed that e^- are transferred from the valence band or from the luminescence center to the conduction band followed by being instantly trapped to the trapping center N_i. In the mean time, h^+ are being trapped at the hole trapping center M_j. By requiring that $E_i, E_j \gg 10kT$, the density of the e^- in conduction band and the h^+ in valence band can be considered negligible compared to the carriers being trapped at the corresponding trapping centers. Hence one can get the elementary charge neutrality condition as shown in Eq. (4.1).

$$\sum n_i = \sum m_j \tag{4.1}$$

$$\Delta n = \Delta m \tag{4.2}$$

Where n_i and m_j designate the number of electron | hole traps with the ionization energy of E_i | E_j occupied by electrons and holes, respectively. As the semiconductor crystal being heated up, the trapping centers may get thermally emptied and the released carriers will either be re-trapped or recombine with the carriers of the opposite sign at the recombination centers, where the radiative part of the latter process is considered as the thermally stimulated luminescence. Here we follow the assumption made by Halperin *et al.*[59] that e^- is the major carrier being thermally released. Note that this assumption fits well to the doping condition of N-B co-doped 6H-SiC. Since the shallow levels induced by B-dopant in 6H-SiC[53] are still quite deep (with respect to valence band maximum) compared to the energy levels introduced by N-doping (with respect to conduction band minimum), indicating the e^- on the shallow N-induced traps have higher chance to be thermally released than that of the h^+ being trapped on the B-induced centers, plus e^- has smaller effective mass compared to h^+. Mostly, the measured TSL glow curve of 6H f-SiC sample contains only one major glow peak which will be introduced latter, hence it is reasonable to simplify the model which now consists of only one trapping center (ionization energy: E | density: N) and one recombination center (density M). As we have neglected other trapping centers which may probably exist in reality and could capture carriers but may not relate to the TSL process, the altered carriers neutrality condition shown in Eq. (4.2) takes emphasis on the balance of the density variation of the charged traps and the charged recombination centers. In Eq. (4.2), one can have $\Delta n = n_0 - n(t)$ and $\Delta m = m_0 - m(t)$ with n_0 and m_0 being the densities of the charged trapping center and charged recombination center at the initial stage, respectively. Here we follow Stiasny *et al.*[55, 60] where they applied the Submodel II of Halperin-Braner's method, *i.e.*, the thermally released e^- being raised directly to the conduction band, for the TSL glow curves fitting of 6H-SiC. There are two considerations which should be highlighted for the modelling. First, it is believed that the probability where the thermally released e^- being re-trapped by the neighboring traps is quite small, hence this situation was neglected in the modelling. Second, the free carriers density (n_c), which represents the density of the thermally activated carriers during the TSL process, is negligible at T=25 K (the initial temperature for TSL measurements, *i.e.*, T_{init}). Hence we follow the modification made by Stiasny *et al.*[55, 60] where they have preset the differential of n_c to be zero at the initial stage. Now the modified Submodel II of Halperin-Braner's method can be presented in Eq. (4.3).

$$\begin{aligned}
\frac{\mathrm{d}n(t)}{\mathrm{d}t} &= -n(t)S(T)\exp\left(-\frac{E}{k_bT}\right) + [N - n(t)]\, n_c(t)A_n(T) \\
\frac{\mathrm{d}n_c(t)}{\mathrm{d}t} &= n(t)S(T)\exp\left(-\frac{E}{k_bT}\right) - [N - n(t)]\, n_c(t)A_n(T) - n_c(t)m(t)A_m(T) \\
\frac{\mathrm{d}m(t)}{\mathrm{d}t} &= -n_c(t)m(t)A_m(T)
\end{aligned} \tag{4.3}$$

Where $T = T_{\text{init}} + \beta t$ with β being the temperature increase rate (unit: $\text{K} \cdot \text{s}^{-1}$). As we have applied intense excitation using X-ray source on the 6H f-SiC samples as described in Subsec. 3.1.2, it is considered that the trapping centers within the X-ray active layers beneath the surface of the samples are fully charged, where $N \approx n_0$. Additionally, A_n and A_m are the capture probability (unit: $\text{cm}^3 \cdot \text{s}^{-1}$) of e^- and h^+ on the trapping center and the recombination center, respectively. The expression of A_n and A_m as shown in Eq. (4.4).

$$\begin{aligned} A_n(T) &= \langle \nu_{th,e} \rangle \sigma_n \\ A_m(T) &= \langle \nu_{th,h} \rangle \sigma_m \left(T_{\text{init}}/T \right)^2 \end{aligned} \tag{4.4}$$

Where σ_n and σ_m represent the capture cross section (unit: cm^2) of the trapping center and recombination center, respectively, where only σ_n is treated as temperature-dependent. As a matter of fact, for either the trapping center or recombination center, the relation[61] among its carrier emission coefficient (unit: s^{-1}), ionization energy, and the original capture cross section at T_{init} can be expressed by Eq. (4.5).

$$\log\left(\frac{T^{2+\alpha}}{e_{n,m}}\right) = \frac{\Delta E_{n,m}}{k_b \ln(10)} \frac{1}{T} + \log\left(\frac{1}{\sigma^0_{n,m} \gamma_{n,m}}\right) \tag{4.5}$$

Where $e_{n,m}$, $\Delta E_{n,m}$, and $\sigma^0_{n,m}$ designate the emission rate, ionization energy, and the original capture cross section at T_{init} of trapping | recombination center, respectively, and $\gamma_{n,m}$ is a temperature-independent parameter only correlated to carrier effective mass and the number of the conduction band minima (M_c). As we will introduce latter in Subsec. 4.1.3 that the energy levels of the trapping centers in our f-SiC samples are confirmed to be the nitrogen-induced donor level on the h-site which is quite shallow. Considering that the electron freeze-out effect at low-temperature range being most prominent on h-site compared to the two cubic sites, one could get $\alpha = 0$ in Eq. (4.5) for the trapping center and σ_n is treated as temperature-independent. On the other hand, it is believed that $\alpha = 2$ for the recombination center and σ_m is treated as being proportional to T^{-2}. The latter assumption is derived from Anikin *et al.*[62] where they applied this relation for the estimation of the ionization energies of the recombination centers induced by B-doping in a 6H-SiC p^+n-diode during the DLTS measurement. Where $\langle \nu_{th,e(h)} \rangle$ denotes the mean thermal velocity (unit: $\text{cm} \cdot \text{s}^{-1}$) of e^- or h^+. The expression of $\langle \nu_{th,e(h)} \rangle$ can be represented by Eq. (4.6) as shown below. Note that m^*_e and m^*_h designate the effective mass of e^- and h^+, respectively, which are already mentioned in Tab. 2.3.

$$\langle \nu_{th,e(h)} \rangle = \sqrt{3 k_b T / m^*_{e(h)}} \tag{4.6}$$

Since the value of m_0 and σ_n have no influence on the line shape of the normalized TSL glow curve, that is to say, the extraction of the ionization energy of the shallow

trap is independent of m_0 or σ_n. Hence we set $m_0 = 5\times10^{15}$ cm^{-3} and $\sigma_n = 6\times10^{-13}$ cm^2 for simplicity. In addition, the frequency factor (*i.e.*, S) denotes the probability of the re-trapping process which can be expressed by Eq. (4.7).

$$s(T) = 2\sqrt{6}\pi^{3/2} m_e^* \frac{(k_b T)^2}{h^3} \exp\left(-\frac{E}{k_b T}\right)\sigma_n \tag{4.7}$$

Next, by giving Eq. (4.4) to Eq. (4.7), one can solve Eq. (4.3) by implementing the following parameters: 1) the capture cross section (σ_m) of the recombination center at T_{init}; 2) the original density ratio (ρ) of the trapping center to the recombination center, *i.e.*, $\rho = n_0/m_0$; 3) the ionization energy of the trapping center (E). Finally, the simulated TSL glow curve can be represented in the form of $I_{\text{TSL}}(T) = -\mathrm{d}m(t)/\mathrm{d}t$.

4.1.3 "Fingerprints" of doped impurities revealed by TSL glow curves

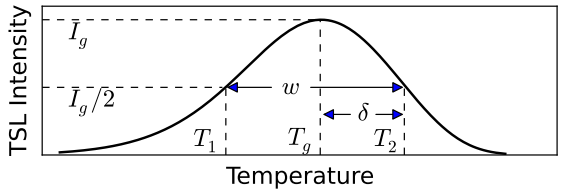

Figure 4.2: A typical TSL curve with an isolated glow peak marked with the essential parameters where: $w = T_2 - T_1$, $\delta = T_2 - T_g$. In addition, the ratio between the area to the right of T_g and the total area under the glow curve is denoted as μ_g.

Samples ⇒	SP-3	SN-2	SN-3	SN-4
β (K · s^{-1})	0.166	0.165	0.164	0.214
T_1 (K)	62.12	60.54	64.12	66.98
T_2 (K)	73.10	71.21	76.35	79.25
T_g (K)	68.17	66.74	70.67	73.24
δ (K)	4.93	4.47	5.68	6.01
w (K)	10.98	10.67	12.22	12.27
μ_g	0.45	0.41	0.48	0.51

Table 4.1: Parameters extracted from the measured TSL glow curve of each sample. Here, β designates the temperature increase rate. The implications of other parameters included in the table refer to Fig. 4.2.

The normalized TSL glow curves of sample SP-3, SN-2/3/4 are shown in the main plots of (a) to (d) in Fig. 4.3. As for SP-1 which is a strong p-type sample, there

is no TSL intensity signal within the whole temperature range, *i.e.*, from 25 K to 300 K. This is a strong indication that the TSL glow peaks observed from all the samples except SP-1 are not originated from the trapping centers at the lower half of the band gap, that is to say, these traps are not derived from *p*-type dopant. The parameters extracted from the results of the TSL measurements are summarized in Tab. 4.1. The implications of all parameters except β can refer to Fig. 4.2 where a typical isolated TSL glow curve marked with the essential indices is presented. From Tab. 4.1, we can see that the FWHM of all four samples, *i.e.*, $T_2 - T_1$, are in the range from 9 K to 13 K, indicating those samples are quite high-compensated[55], that is to say, that the difference between N_d and N_a is not significant. This observation agrees well with the TOF-SIMS measurement data shown in Tab. 2.6 where the ratios N_d/N_a of all these samples are within 0.1 to 10. What's more, this temperature range which includes all peak positions of these samples strongly suggests the prominent e^- trapping related to the shallow N-induced donor levels on the hexagonal sites[55, 60], where the fitting results regarding to the main glow peaks of these samples will be discussed later. On the other hand, one side glow peak with relatively low intensity at around 110 K to 120 K is observed from SN-3/4. According to Hartung *et al.*[63], this broad peak can be derived from the N-induced donor levels at the cubic sites with the ionization energies around 140 meV. Hence in SN-3/4, we can see that a very small portion of the donors on cubic sites could contribute to the majority carriers trappings other than DAP recombination. Normally, a glow peak within 175 K to 185K observed from 6H-SiC sample indicates the existence of the aluminum-induced shallow acceptor level ($\sim E_v + 240$ meV) [55, 60, 63, 64]. As we have concerned about whether the aluminum-dopant has been unintentionally included during the growth of f-SiC. According to the measured TSL glow curves in our research, it can be concluded that there is no remarkable inclusion related to aluminum impurity in our 6H f-SiC samples. In addition, the existence of the boron-induced shallow acceptors (typically $E_v + 330$ meV) could be reflected by a glow peak with 260 K to 300 K[65, 66]. Regarding our TSL measurement results, it is confirmed that there is no prominent involvement of boron-induced shallow acceptors in these 6H f-SiC samples. In addition, as seen in Tab. 4.1, $\mu_g > e^{-1}$ were found in all four samples, indicating that the TSL process in 6H f-SiC corresponds to bimolecular kinetics[67]. This bimolecular kinetics implies that the fluorescence decay in 6H f-SiC at the TSL-active temperature range (approximately 50 K to 100 K) cannot be described by the single exponential decay model. Instead, the carrier dynamics is more suitable to be explained by applying Becquerel's hyperbolic law where $I(t) = I_0(1 + At)^{-p}$ with $p \approx 2$ (that's why it is called bimolecular kinetics).

4.1.4 Nitrogen-induced shallow trapping center

The effective parts of the glow peaks shown in the insets of (a) to (d) in Fig. 4.3 were numerically fitted by applying the modified Halperin-Braner's method as mentioned in Subsec. 4.1.2. The simulations were executed by using Simulink (MathWorks, Inc.)

where the modified Rosenbrock method[68] with variable step was implemented. The temperature range for the simulation of SP-3 and SN-2 was 25 K to 100 K whereas the range of 25 K to 200 K was set for SN-3/4.

The results of the fitting shown in (e) to (h) of Fig. 4.3 correspond to the measured glow curves in (a) to (d), respectively. In (g) of Fig. 4.3, there is a bit mismatch between the measured|simulated glow peaks at the rising parts, this is probably due to the unfinished photoluminescence from DAP recombination[63] at the beginning of the heating process. Another mismatch was observed in either (g) or (h) of Fig. 4.3 at the descending part of the glow peak. The related reason is already given in Subsec. 4.1.3. A small amount of N-induced donors at the cubic sites participate in the e^- trapping process forming a broad but relatively low intensity glow peak around 110 K to 120 K. In this respect, the main glow peaks of sample SN-3/4 are not strictly isolated.

Parameters ⇓	SP-3	SN-2	SN-3	SN-4
E (meV)	103	101	98	101
ρ $(= n_0/m_0)$	1.08	1.10	1.00	1.00
σ_m (cm^2)	1.0×10^{-14}	1.0×10^{-14}	4.0×10^{-16}	4.0×10^{-16}

Table 4.2: TSL parameters obtained by the fitting of the glow curves using the modified Halperin-Braner's model.

Three fitting parameters (E, $\rho = n_0/m_0$ and σ_m) for the simulated TSL glow peaks of these four samples are summarized in Tab. 4.2. As we can see that the fitted ionization energies of the nitrogen-induced shallow donors at the hexagonal sites for all four samples are almost identical, where the value of ∼100 meV agrees with the one reported by Ikeda *et al.*[52]. The extracted density ratios ρ between the charged trapping centers (n_0) and the charged recombination centers (m_0) at the initial stage for all samples are found to be close to unity. This result agrees well with the trend shown in FIG 4 of Ref. [59]. To be specific, in the situation of the sample being almost thoroughly excited ($N \approx n_0$) in the light source active layer, the relation between ρ and μ_g is preferable to be described by curve-b in FIG 4 of Ref. [59], where ρ tending to unity will cause $\mu_g \Rightarrow 0.5$. We can see that SP-3 and SN-2 share the same σ_m as those two samples were grown in the same batch and so are samples SN-3/4. In fact, during the fitting work, we found that the increase of σ_m would decrease the width (w) of the calculated glow peak. This hypothesis is somehow validated by referring the fitted σ_m in Tab. 4.2 and the measured w in Tab. 4.1, where the explicit relation between σ_m and w still needs further investigation. Note that the energy level of the TSL-correlated recombination center of 6H f-SiC is still unknown. Further work should be focused on the measurement of the spectrally resolved TSL and using different excitation sources with sub-band-gap photon energies for TSL pumping in order to extract the information of the TSL-active recombination center in 6H f-SiC[55].

The calculated densities of the charged recombination centers (m), the charged

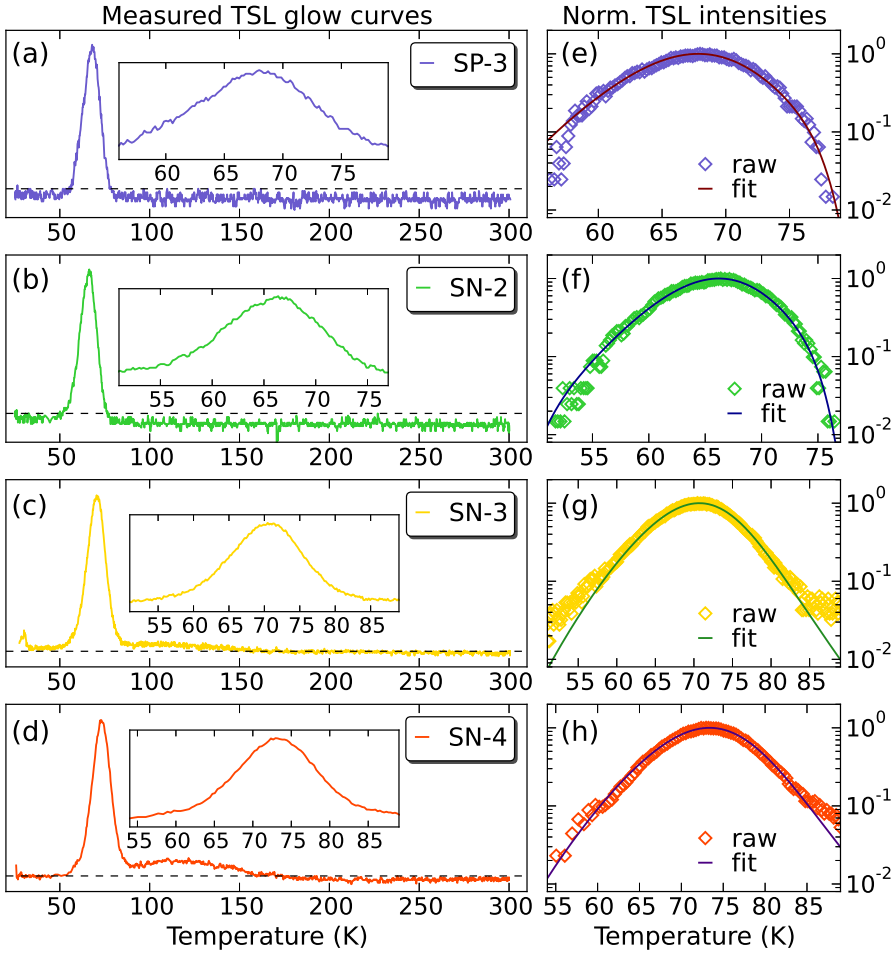

Figure 4.3: (a)-(d): the normalized TSL glow curves (with linear y-axes) of sample SP-3, SN-2/3/4, respectively. (e)-(h): the fitting results corresponding to the effective parts of the glow curves presented in the insets of (a)-(d), separately. Note that the horizontal dashed line shown in each main plot of (a) to (d) indicates the zero level of the detected TSL intensity.

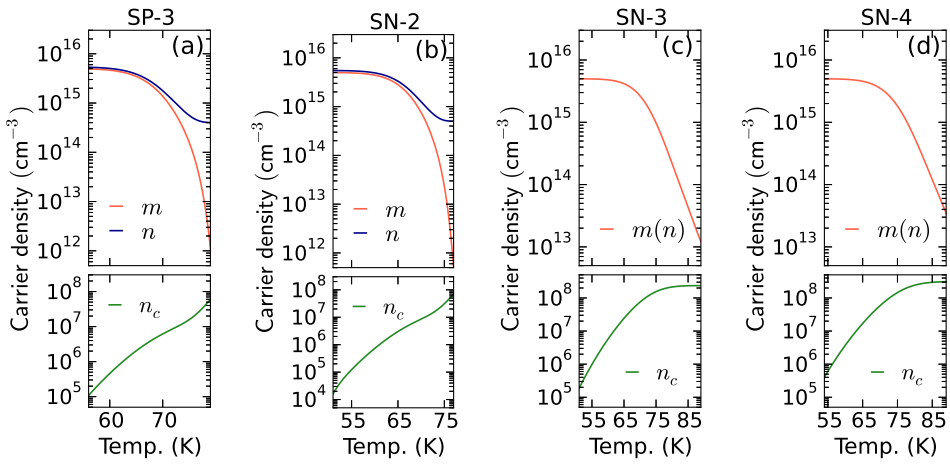

Figure 4.4: Simulated densities of the charged recombination centers (m), the charged traps (n) and the free charge carriers (n_c) related to the TSL glow curves fitting of sample (a) SP-3, (b) SN-2, (c) SN-3 and (d) SN-4. Note that the ranges of the temperature in (a) to (d) are identical with those of (e) to (h) in Fig. 4.3.

traps (n) and the free charge carriers (n_c) extracted from the TSL simulations for all four samples are depicted in Fig. 4.4. We can see that the values of m and n begin to deviate in sample SP-3 and SN-2 at elevated temperatures since the values of ρ for those two samples are not equal to unity. The density of the charged recombination center (m) available for TSL generation for either SP-3 or SN-2 has became negligible at the upper border of the TSL-active temperature range. At the same temperature point, however, the density of the charged trapping center (n) has been only decreased by one order of magnitude and its decrease rate has became much slower as seen in the (a) and (b) of Fig. 4.4. Hence it can be predicted that there still exists certain amount of charged trapping centers which will still be able to immobilize the carriers at elevated temperatures in SP-3 or SN-2. In addition, as the frequency factor (S) increases with the temperature (see Eq. (4.7)), the trapping centers having been thermally emptied still have non-negligible probabilities to re-trap the non-equilibrium carriers. On the other hand, the values of m and n keep identical in sample SN-3/4 within the TSL-active temperature range and both have become negligible at the elevated temperatures. Therefore much lower probabilities of carriers being trapped or getting re-trapped can be predicted in SN-3/4 compared to samples SP-3 and SN-2. The evidences that support our assumptions can be found in Fig. 4.5 which shows the normalized PL intensities of sample SN-2/3/4 at T=285 K (the peak intensity of the PL spectrum of SP-3 at the same temperature has been comparable to the ambient

noise). The related experimental setup for the related PL measurements refers to Sec. 3.2. In Fig. 4.5, the peak position of SN-2 is found to be red shifted compared to SN-3/4, indicating less portion of shallow donors related DAP recombination in SN-2. This agrees well with the above mentioned theoretical prediction where more portion of shallow donors in SN-2 still act as the trapping centers even at elevated temperatures compared to SN-3/4.

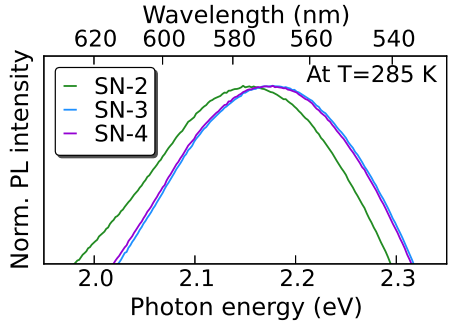

Figure 4.5: Peak positions of the PL spectra of sample SN-2/3/4 at T=285 K.

Although there exists small difference on the values of E for these four samples, as we have assumed the identical σ_n in the simulations, the deviations on the frequency factor (S) reflected by the differences on E can be negligible. This means that thermally activated carriers on the conduction band (*i.e.*, the free carriers) in all samples have the comparable probabilities to be re-trapped by the shallow trapping centers at the same temperatures. On the other hand, it is clear to get the rank of the values of n_c where: SN-4 > SN-3 > SN-2 ≈ SP-3 at the same temperature levels. Here, we can conclude that higher n_c indicates the higher chance of inducing radiative recombination (*i.e.*, the TSL process) with the same probability of being re-trapped. Fig. 4.6 shows the raw experimental TSL glow curves of all four samples, we can see that the comparison of absolute heights of the glow peaks correlates with the rank of our calculated n_c.

4.2 Identification of double *D*-center in 6H f-SiC

4.2.1 Overview

In N-B co-doped 6H-SiC at RT, we already know that the phonon replicas of DAP recombination[46] cause the broad emission with $\lambda_{\text{peak}} \approx 580$ nm (∼2.14 eV) and FWHM (nm) $\in [110, 120]$[2, 51], where N-dopant introduces three shallow donor levels on two quasi-cubic (k_1, k_2) and one hexagonal (h) lattice sites and B-dopant introduces the deep acceptor level, *i.e.*, *D*-center[46]. For 6H f-SiC at RT, however,

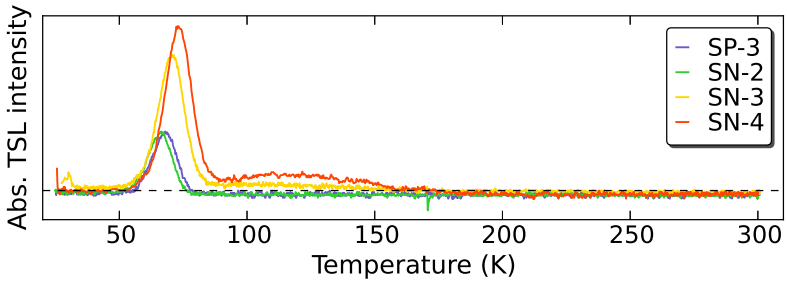

Figure 4.6: TSL glow curves of all samples with absolute linear y-axes. Note that the horizontal dashed line indicates the zero level of the detected TSL intensity.

researchers[7, 69] have observed that its emission spectrum contains another emission peak with $\lambda_{\text{peak}} \approx 640$ nm and the origin of this extra emission is still unknown. Interestingly, an extra recombination center[70] (named as D'-center) has been observed from the Photoluminescence-detected Electron Paramagnetic Resonance (PL-EPR) measurement on B-doped 6H-SiC and found to associate with D-center. Here, the D'-center is believed to stay on three different lattice sites in 6H-SiC since three g-factors were extracted from the related PL-EPR measurement results. Moreover, researchers also suggested that the low-energy flank in the PL spectrum of the B-doped 6H-SiC might be associated with the D'-center. In this section, by characterizing 6H f-SiC via the temperature-dependent PL spectroscopy, a new boron-induced acceptor level (here called D^*-center) is identified which is found to be deeper than the D-center and correspond to the DAP recombination process dominating at low temperatures with peak photon energy around 1.90 eV. We propose the lattice geometries of both D^*-center and D-center (together we call them the double D-centers) by summarizing the previous *first-principles* calculations results regarding SiC lattice structures. Moreover, the densities of the boron-induced acceptors in f-SiC samples are compared by taking their doping conditions into consideration. Additionally, a hole-trap, *i.e.*, HS2 center, is assumed to exist and stay between the energy levels of the double D-centers in our 6H f-SiC samples. Finally, a model regarding a two-stage thermal ionization of hole driven by the HS2 center is proposed to explain the two distinct trends corresponding to the PL intensities in our f-SiC samples: thermal quenching for p-type and continuous rise for n-type. Note that the research results presented in this section are derived from [71].

The samples employed in this research are SP-2/3 and SN-1. The experimental setup related to the temperature-dependent PL measurements refers to Sec. 3.2. The information related to the crystal growth and the PL characterizations of the three samples are shown in Tab. 4.3. The essential physical properties of these three samples refer to Tab. 2.6 and Fig. 2.10.

Sample ⇒	SP-2	SP-3	SN-1
N_2 pressure (mbar)	0.1	0.25	0.75
Growth rate (μm.h^{-1})	92	96	90
Max. PL intensity ($\times 10^6$ arb. unit)	0.78 (at 75 K)	0.99	1.34 (at 290 K)

Table 4.3: Basic information corresponding to the crystal growth and the PL characterizations of the three 6H f-SiC samples.

4.2.2 Origins of double *D*-centers and hole trap HS2

Figs. 4.7 and 4.8 show the normalized temperature-dependent PL intensity spectra of the three samples. It is intuitive to consider that there exist two parallel DAP recombination channels in all samples with one of them being the major recombination channel at lower temperatures while the other gradually becomes the major recombination channel at rising temperatures. It is also obvious that those two recombination channels have comparable contributions to the PL spectra at intermediate temperatures. The PL emission peak around 1.89-1.91 eV attributed to the major DAP recombination process indicates an extra boron-induced acceptor level (D^*-center) deeper than the *D*-center. Additionally, it is believed that the D^*-center can stay on different lattice sites by considering the non-smooth line shapes at the low-energy flanks of all the PL spectra, where the superposition of different emission spectra corresponding to DAP recombination with the D^*-centers on different lattice sites is expected. Moreover, it is obvious that the *D*-center is responsible for the DAP recombination at elevated temperatures with the PL emission peak around 2.10-2.14 eV.

Currently, the lattice geometries of both the *D*-center and the D^*-center have not been directly determined via experimental approach, besides, the energy level of the *D*-center is still ambiguous[46, 62, 72]. Fortunately, many attempts[73–75] have been made on the theoretical prediction of the molecular configurations of the *D*-center by using *first-principles* calculations. It is worthy to note that the theoretically predicted properties of *D*-center can be applied to all three common polytypes of SiC, *i.e.*, 3C- 4H- and 6H-SiC, as the electronic structure of the *D*-center is independent of these polytypes. In the early stage, researchers[46, 73] found that a lattice geometry combining a B-atom on Si-sublattice (B_{Si}) with a carbon vacancy (V_C), *i.e.*, a B_{Si}+V_C complex, might be the origin of *D*-center via theoretical approach. Later on, however, the aforementioned hypothesis was overturned by Aradi *et al.*[74], where their *ab initio* calculation results indicate the energy level of the B_{Si}+V_C structure to be 1.9 eV above the valence band maximum (E_v), *i.e.*, E_v+1.9 eV, meaning the more donor-like behavior for this structure. Besides, Aradi *et al.* claimed that an alternative lattice geometry combining a Si-sublattice occupied by a B-atom with the neighboring Si-antisite (Si_C), *i.e.*, the B_{Si} + Si_C complex, could stand for the electronic structure of *D*-center in 4H-SiC. In addition, Aradi *et al.* also mentioned that the above-mentioned

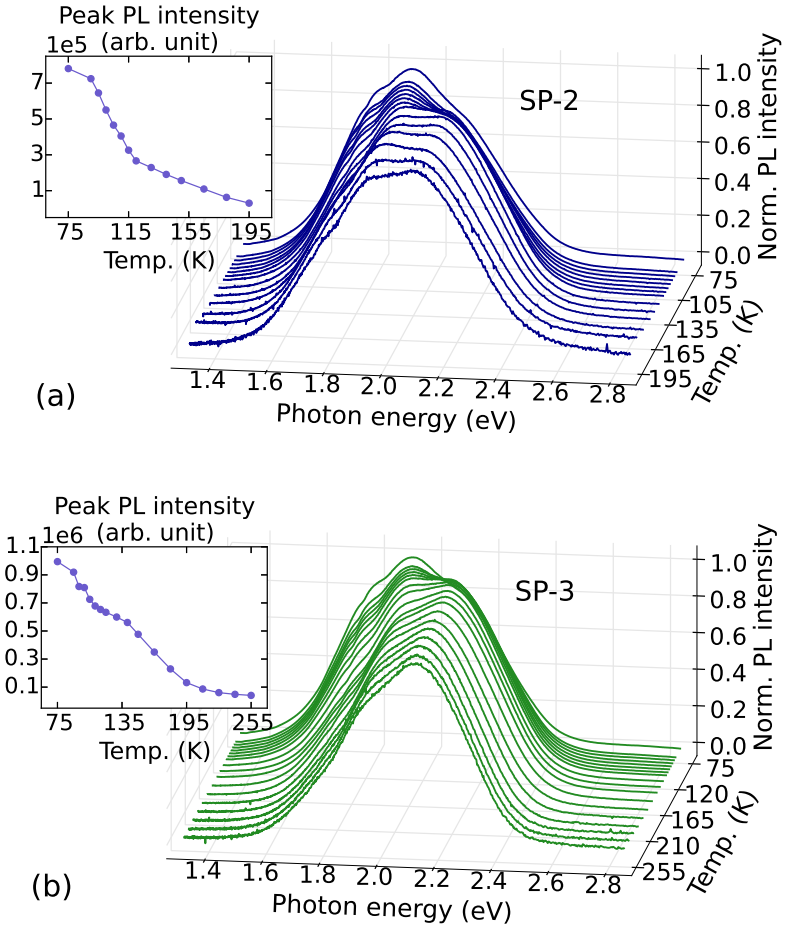

Figure 4.7: Normalized PL intensity spectra at different temperature ranges where: (a) 75-195 K for sample SP-2; (b) 75-255 K for sample SP-3. Note that the PL intensities above 195 K for SP-2 and above 255 K for SP-3 were comparable to ambient noise level. The insets show the temperature-dependent peak intensities of the PL spectra of each sample.

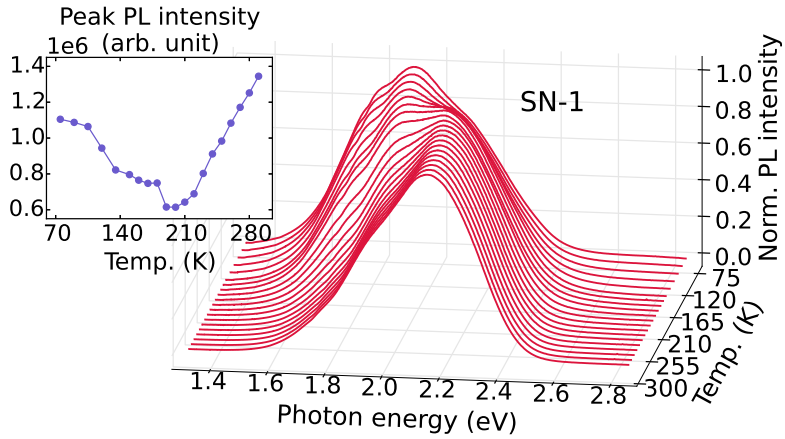

Figure 4.8: Normalized PL intensity spectra of SN-1 within 75 K to 290 K. Inset: the temperature-dependent peak intensities of the PL spectra of SN-1.

potential lattice geometry of *D*-center can only associate with cubic sites and has to be aligned parallel to the *c*-axis which result in an acceptor level of E_v+0.53 eV. Surprisingly, this theoretically predicted acceptor level agrees well with the widely accepted value by experimental determination, *i.e.*, E_v+0.58 eV[46]. On the other hand, Bockstedte *et al.*[75] predicted that the lattice geometry in 3C-SiC consisting of a B-atom occupying a C-sublattice (B_C) and the neighboring C-antisite (C_{Si}), *i.e.*, the B_C+C_{Si} complex, can induce an energy level of E_v+0.70 eV. Consequently, we attribute the B_{Si} + Si_C complex and B_C+C_{Si} to the *D*-center and the D^*-center, respectively. Meanwhile, we also consider the D^*-center to be equivalent with the previously mentioned D'-center detected by PL-EPR method[70]. There are three characteristics of the D^*-center that are quite similar to those of the D'-center. First, D^*-center is correlated to the PL emission with lower photon energies compared to *D*-center. Second, it is believed that the luminescence regime associated with D^*-center is site-dependent, as the line shapes of the PL spectra dominated by D^*-center related DAP recombination process are less smooth. Third, it is reported[70] that the D'-center also has axial symmetry along *c*-axis just like the D^*-center does. The proposed lattice geometries of the D^*-center have been shown in (a) of Fig. 4.9, where the related complex could stay on either hexagonal (h) or cubic sites (k_1 or k_2) in 6H-SiC. Likewise, the possible lattice geometries of the *D*-center in 6H-SiC are presented in (b) of Fig. 4.9, where the related complex can stay on either of the cubic sites (k_1, k_2) in 6H-SiC. In addition, the fact that the predicted energy level of the D^*-center being higher than that of the *D*-center also agrees well with the previous theory[75–77] on the lattice structure of SiC, where the acceptor level with its lattice geometry associated with B_C should be deeper compared to the lattice geometry including B_{Si}.

The temperature-dependent peak PL intensities of each f-SiC samples are shown in

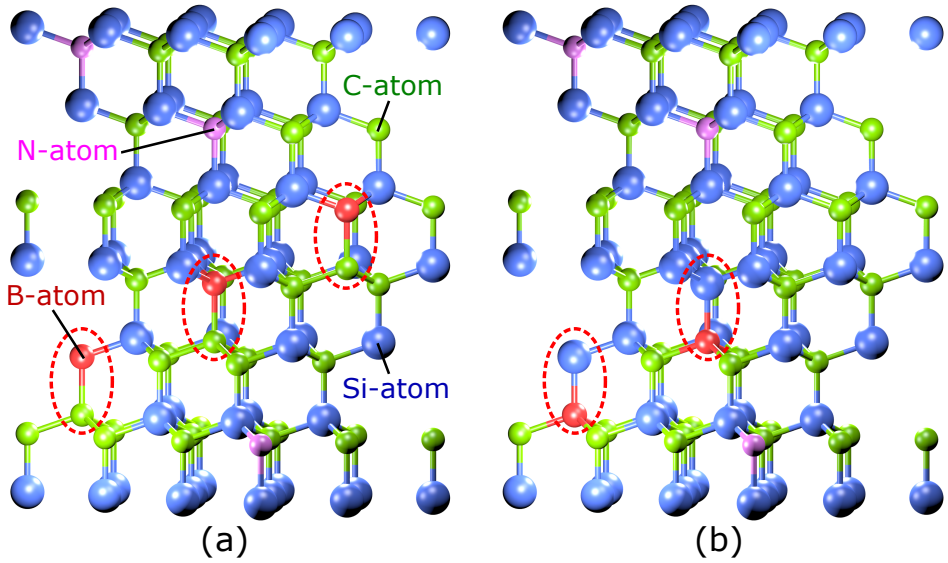

Figure 4.9: Lattice structure of: (a) the D^*-center (E_v+0.70 eV), which is associated with a C-sublattice occupied by boron (B_C) next to a carbon antisite (C_{Si}) on either cubic or hexagonal site; (b) the D-center (E_v+0.53 eV), which is associated with a Si-sublattice occupied by boron (B_{Si}) next to a silicon antisite (Si_C) on either k_1 or k_2 (cubic) site; Either of the presented molecular models of 6H-SiC contains 2×3 unit cells. N-atoms which replace the C-atoms on all cubic and hexagonal sites are also marked. The structures are presented in the $(11\bar{2}0)$ plane.

the insets of Fig. 4.7 and 4.8, where it is obvious to find that the absolute PL intensities of both p-type samples (SP-2/3) decrease with increasing temperature. Meanwhile, up til 190 K, the peak PL intensity of the strong n-type sample SN-1 drops to almost half of its original value (at 75 K) then increases continuously at temperatures higher than 190 K. It is considered that an extra hole-trap which impedes the D^*-center related DAP recombination is responsible for the consistent trends where the PL intensity keeps dropping within 75 K up to 190 K for all three samples. The HS2 center with the energy level of E_v+0.63 eV[78] is a probable candidate of this hole-trap. Since the formation of HS2 only requires carbon displacement which means the related formation energy is quite low, HS2 is believed to be the dominate hole-trap in SiC[79]. In addition, researchers[80] has observed that in 4H-SiC the density of the HS2 center starts to decrease by applying high energy electron irradiation (>170 keV), this indicates HS2 is a vacancy-interstitial pair, *i.e.*, a Frenkel pair. For the lattice geometry of HS2 which should be related to a carbon interstitial structure,

it is most likely to be the Si-C or C-C dumbbell-like atoms pair (also called split interstitial) which is aligned along ⟨100⟩ direction on the carbon site, *i.e.*, $C_{sp\langle 100\rangle}$ or $C_{spSi\langle 100\rangle}$ ('SP' refers to split), respectively. It is worthy to mention that since $C_{sp\langle 100\rangle}$ and $C_{spSi\langle 100\rangle}$ require the lowest formation energies regardless of the doping type[81], they are the dominant carbon interstitials in SiC. One of the suggested lattice geometry of HS2 center, *i.e.*, with $C_{sp\langle 100\rangle}+V_C$ complex, is shown in Fig. 4.10, where another possible geometry related to HS2 ($C_{spSi\langle 100\rangle}+V_C$) can be obtained by replacing the interstitial carbon C_I with the interstitial silicon Si_I. Moreover, previous DLTS measurement results on SiC[79] have shown that the signal representing the *D*-center overlaps with that of the HS2 center, indicating that HS2 center is very likely to participate in the double *D*-centers related DAP recombination.

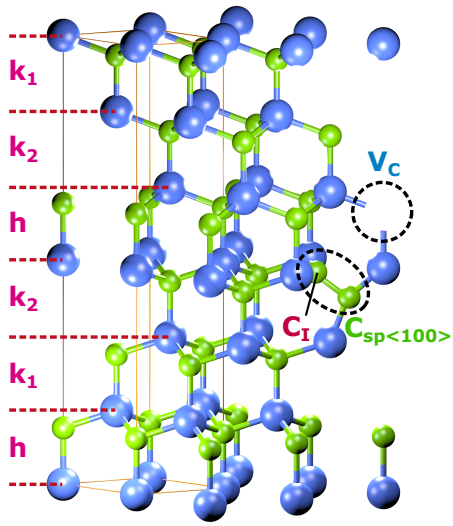

Figure 4.10: Lattice geometry of the hole-trap HS2 (E_v+0.63 eV), which consists of a carbon split interstitial $C_{sp\langle 100\rangle}$ together with carbon vacancy (V_C). The presented molecular model of 6H-SiC contains 2×2 unit cells. A unit cell of 6H-SiC crystalline is marked out associated with the corresponding stacking sequence. The structure is presented in the $(11\bar{2}0)$ plane.

Note that it is also possible for 6H f-SiC to form the the lattice structures of both *D*-center and D^*-center during the sublimation growth. To be precise, it is expected that N-atoms and B-atoms would compete for the C-site during the crystal growth, as the C-site is preferred by the N-dopant on the Si-face of the epilayer and could be occupied by the B-dopant as well, where the B-dopant can occupy Si-site[82] in the meantime. Hence the lattice geometry of B_{Si}, which is one of the components of the *D*-center complex, is more probable to be formed with higher concentration of N-dopant. In addition, the typical temperature range for the growth of f-SiC through

FSGP method, *i.e.*, 1600°C to 2000°C, will cause the Si/C ratio to be around 2 to 3 which is obviously the Si-rich condition[6, 83]. On the other hand, it is predicted by *ab initio* calculations[84] that one of the components of *D*-center complex, *i.e.*, the Si-antisite (Si_C), has higher formation probability in *n*-type SiC under Si-rich condition. To summarize, we propose a contrast on the density of the *D*-center of the three samples: SP-1 > SP-3 > SP-2, which is derived from the crystal growth condition of our 6H f-SiC samples shown in Table 4.3. From the insets of Fig. 4.7 and 4.8, we can see that the PL intensity of SN-1 shows sustainable growth after 190 K with the boosting of *D*-center related DAP recombination. In addition, the temperature where the PL intensities of SP-2 being reduced to ambient noise level (195 K) is lower compared to the situation of SP-3 (255 K), which is because of the weaker *D*-center related luminescence in SP-2 compared to SP-3. Therefore it is crucial that a quite difference between the concentrations of the N-dopant and the B-dopant should be maintained in order to form the sufficient amount of *D*-center. As for the formation of D^*-center during the growth of f-SiC epilayer via the FSGP method, previous *ab initio* calculation[84] results regarding the lattice structure of *p*-type 3C-SiC has shown that the formation energy of C_{Si} is ∼6.2 eV lower than that of Si_C. Later, the difference regarding the formation energy of C_{Si} against Si_C is predicted to be smaller in *n*-type 3C-SiC[85]. Furthermore, it is also theoretically predicted[86] that during the growth of *p*-type 4H-SiC within 1400°C and 1800°C, the B-atoms are inclined towards occupying C-sublattice (B_C) rather than occupying Si-sublattice (B_{Si}). Therefore it is reasonable to deduce that it is very likely to form a considerable amount of the D^*-center related complex (B_C+C_{Si}) in either f-SiC samples. The related evidences can be found in the insets of Fig. 4.7 and 4.8, where the strong luminescence regarding the D^*-center dominated DAP recombination can be found in all three f-SiC samples.

4.2.3 HS2-involved two-step thermal ionization

For the analysis of the three f-SiC samples' temperature-dependent luminescence properties, the differences regarding the densities among the double *D*-centers and HS2 center of each sample were the key objects for investigation. Fig. 4.11 summarizes the extracted the temperature-dependent mean PL intensities within two ranges of the photon energy, *i.e.*, 1.55-1.65 eV and 2.25-2.35 eV, respectively for all samples. We can see that the emission within the range of 1.55-1.65 eV in all PL spectra are mainly contributed by D^*-center related DAP recombination while the *D*-center dominated DAP recombination has the major contribution to the emission within the range of 2.25-2.35 eV. From Fig. 4.11(a), for the PL spectra of both *p*-type samples, we can see that PL intensities at the low-energy flanks decrease with the rising temperature. Here, at elevated temperatures, the non-equilibrium holes captured by the D^*-center could be thermally activated to the HS2 center with sufficient thermal energies. This would directly cause the non-equilibrium holes to be more likely to get trapped by the HS2 center and less likely to stay at the D^*-center, where the D^*-center related

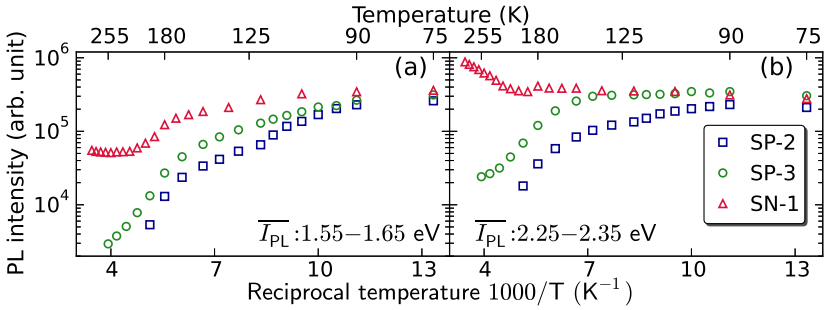

Figure 4.11: The Arrhenius plots which summarize the averaged luminescence intensities within the emitted photon energy of (a) 1.55-1.65 eV and (b) 2.25-2.35 eV for all three samples.

luminescence intensity will be weakened accordingly. One of the green dashed arrow which points to the energy level of HS2 center in Fig. 4.12 has shown the aforementioned thermal process. Moreover, for sample SN-1, it is observed that the increasing tendency regarding the *D*-center related luminescence within the green-blue emission region has caused the emission at the low energy flank to stop decreasing. Here, as the temperature keeps increasing, a further thermal activation is expected where now the non-equilibrium holes trapped at the HS2 center get the chance to be captured by the *D*-center. Another dashed green arrow pointing to the energy level of *D*-center as depicted in Fig. 4.12 has indicated the *D*-center related thermal activation process. It is reasonable to deduce that the trapped holes get higher chance to be thermally activated to the *D*-centers if the density of the *D*-center is higher. As we have concluded that more *D*-centers have been formed in SN-1 during the crystal growth compared to the other two *p*-type f-SiC, this could explain why the dominating luminescence at RT which is powered by the *D*-center related DAP recombination, is much stronger in SN-1 than in the other two *p*-type samples.

In order to have a clear picture regarding to the evolution of the D^* |*D*-centers related DAP recombination processes affected by the HS2-involved two-step thermal ionization, we further launched the numerical fitting on the temperature-dependent PL spectra for all three samples to extract the amplitudes and line shapes related to both DAP processes. To be concrete, we have applied a four-phase skew normal distributions function shown in Eq. (4.8) to fit the normalized temperature-dependent PL spectra of each sample. The reason that we did not apply the standard normal distribution function (*i.e.*, Gaussian distribution) is because of the asymmetry distribution of the DAP recombination induced luminescence intensities with respect to the photon energy or wavelength. As we have mentioned in Subsec. 4.2.2, the D^*-center related acceptors might be site-dependent in 6H-SiC, hence the first three ($i = 1/2/3$, refers to the notations shown in Eq. (4.8)) phase skew normal distributions were applied for the DAP recombination regarding to the D^*-centers on h, k_1 and k_2 sites.

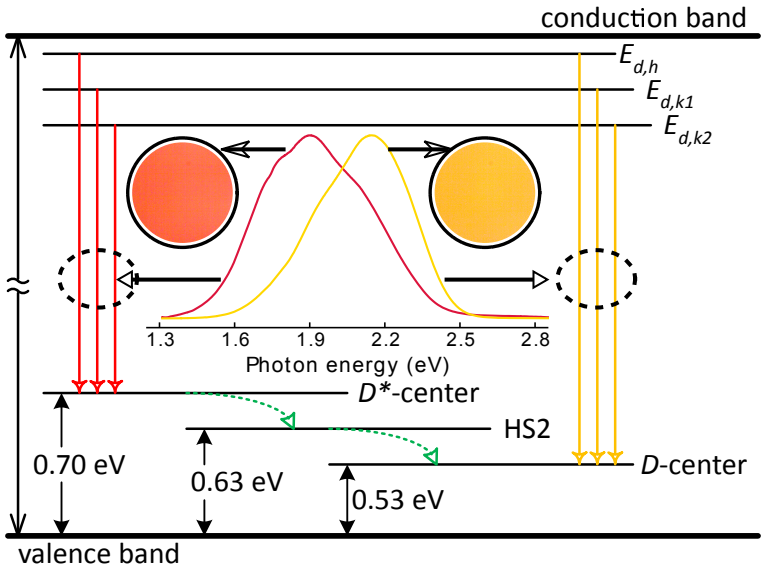

Figure 4.12: An analytical sketch showing the evolution of double *D*-centers related DAP recombination driven by HS2 center related trapping and thermal activation of holes. The inset plots two normalized PL spectra of SN-1 recorded at 75 K and 290 K, separately, where each spectrum points to the photo of the sample surface captured at the respective temperature during the PL excitation. The two green dashed arrows indicate the thermal ionization processes of the non-equilibrium holes at elevated temperatures.

In addition, the amplitude ratios between A_1, A_2 and A_3 were kept fixed during the PL spectra fitting for each sample to ensure the line shapes of the D^*-center related luminescence spectra keep unchanged. According to the temperature-dependent luminescence originated from the *D*-center related DAP recombination, a single phase (the fourth, *i.e.*, $i = 4$) skew normal distribution was applied. As shown in the inset of Fig. 4.12, the PL spectrum at 290 K representing the *D*-center dominated DAP recombination regime can be treated as a perfect single skew normal distribution curve.

$$I_{\text{norm}}(E) = \sum_{i}^{4} \frac{A_i}{\sigma_i\sqrt{2\pi}} \exp\left[-\frac{(E-\mu_i)^2}{2\sigma_i^2}\right] \left\{1 + erf\left[\frac{a_i\,(E-\mu_i)}{\sigma_i\sqrt{2}}\right]\right\} \tag{4.8}$$

The results of the numerical fitting of the normalized PL spectra using four-phase skew normal distributions function are shown in Fig. 4.13/4.14 for SP-2/3, respectively, and the results related to SN-1 are summarized in Fig. 4.15. For the PL fitting of SP-2 shown in Fig. 4.13, we can see that the relative intensity of the *D*-center

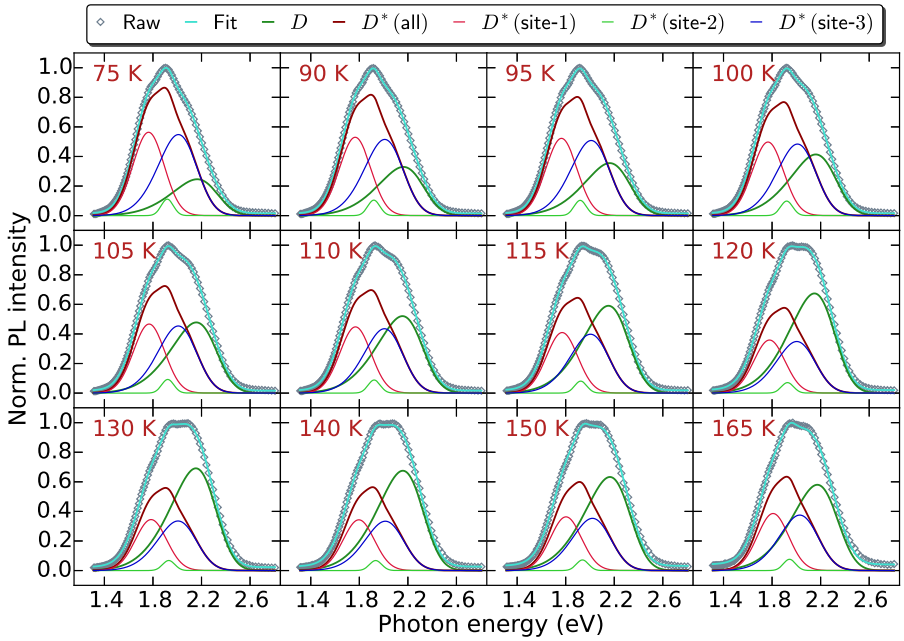

Figure 4.13: Four-phase skew normal distributions fitting of the normalized temperature-dependent PL spectra of SP-2.

related luminescence keeps increasing until 120 K. However, the D^* |*D*-center related processes make no distinct differences after 120 K. On the other hand, it is apparent to see that the relative intensities of the *D*-centers related luminescence in SP-3 and SN-1 have exceeded those of the luminescence associated with the D^*-center as shown in Fig. 4.14 for SP-3 and Fig. 4.15 for SN-1. The reason that the *D*-centers related DAP regime still cannot become dominated in SP-2 is because of the less *D*-center density compared to SP-3 and SN-1 as analyzed in Subsec. 4.2.2. Due to the limited concentration of the *D*-center in SP-2, its capacity of capturing the non-equilibrium h^+ either directly from valence band maximum or indirectly from the thermal ionization process driven by the HS2 center is thought to be quite weak.

The Arrhenius plots shown in Fig. 4.16 summarize the temperature-dependent integrated luminescence intensities originated from the two different recombination regimes. The data points presented in the figure were collected by combining the information regarding to the line shapes and the relative amplitudes of the double *D*-centers related luminescence spectra with the measured absolute PL intensities of all three samples. It can be seen that although the *D*-center related process in SP-3 has became dominated at elevated temperatures, its absolute intensity is still reducing. Compared to the situation of SN-1 shown in the (c) of Fig. 4.16, it is suggested that

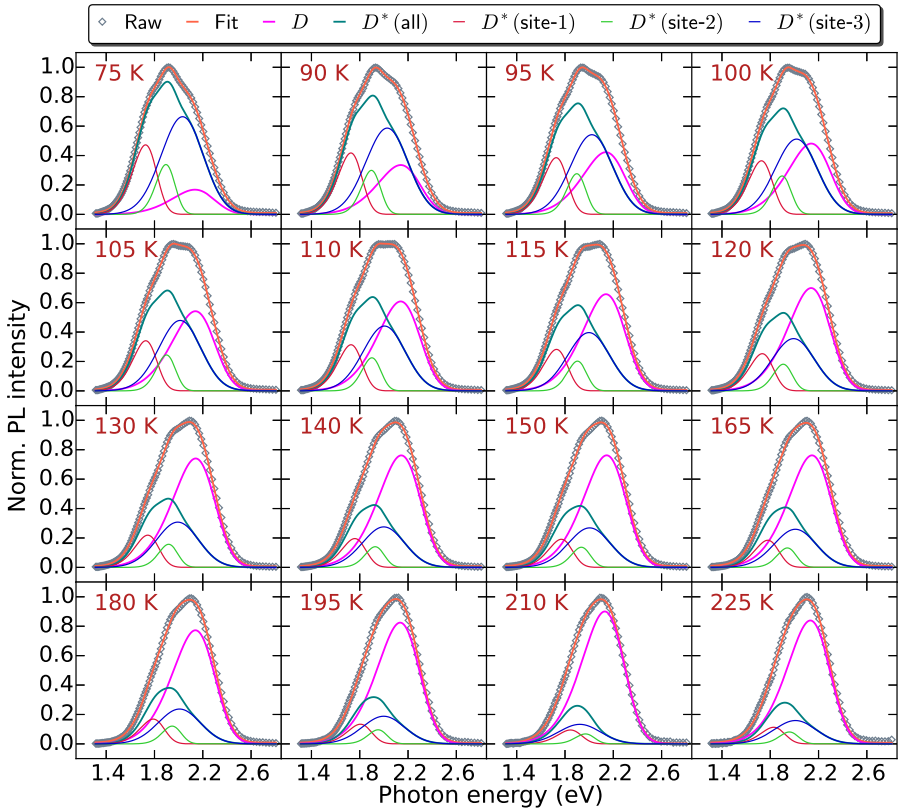

Figure 4.14: Four-phase skew normal distributions fitting of the normalized temperature-dependent PL spectra of SP-3.

less density of the *D*-center in SP-3 could result in the limited capacity of capturing the thermally activated h^+ from the HS2 center. Regarding to the deep level available for the radiative recombination in SiC, *e.g.*, the *D*-center, its capture probability of the non-equilibrium h^+ directly from the valence band is proportional to $T^{-1.5}$ due to the cascade capture process assisted by acoustic phonons[62, 87]. Therefore we believe that the booming of the radiative recombination in SN-1 is because of the increasing probability of capturing the non-equilibrium h^+ from the HS2 center rather than from the valence band maximum. A further assumption could be that the *D*-center's capture probability of the thermally activated h^+ from the HS2 center might increase with its increasing density. However, the systematic theoretical and experimental research work is still needed to study the thermal ionization and capturing of h^+ within the ternary system including the double *D*-centers and the HS2 hole trap.

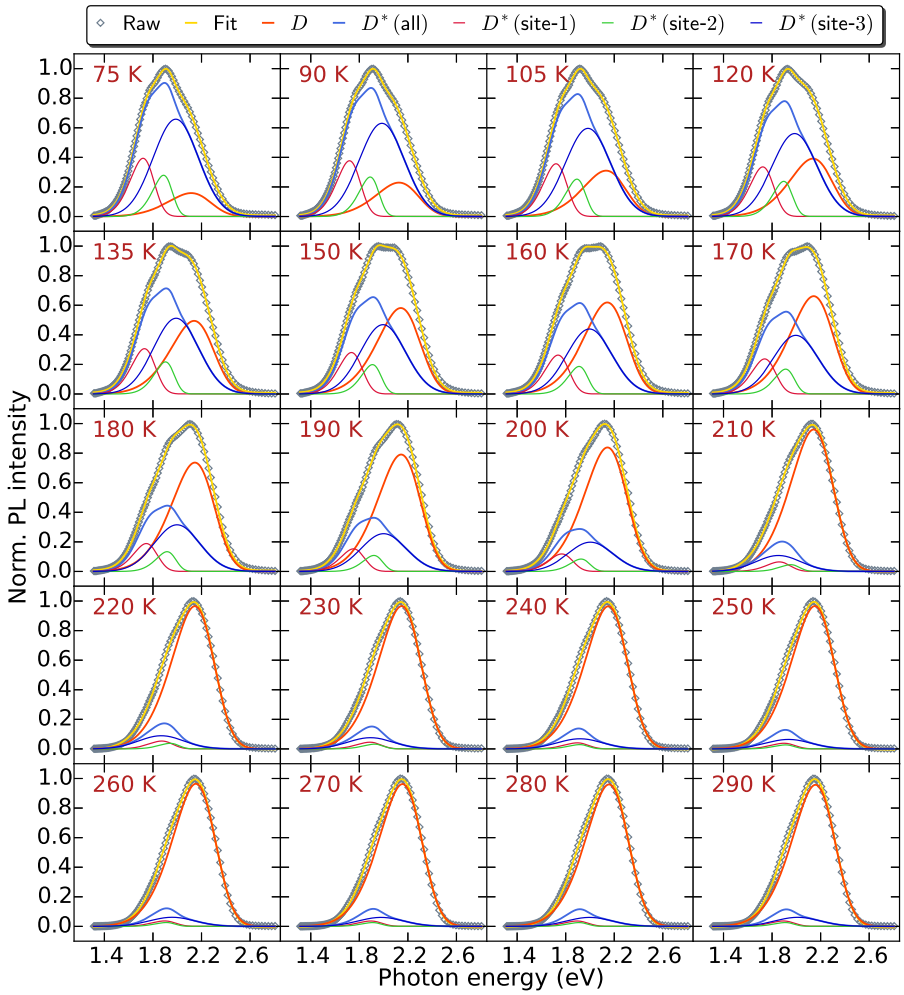

Figure 4.15: Four-phase skew normal distributions fitting of the normalized temperature-dependent PL spectra of SN-1.

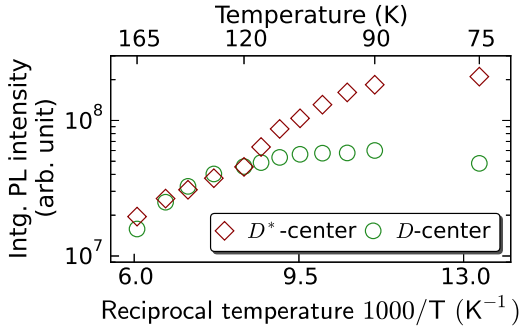

(a) SP-2

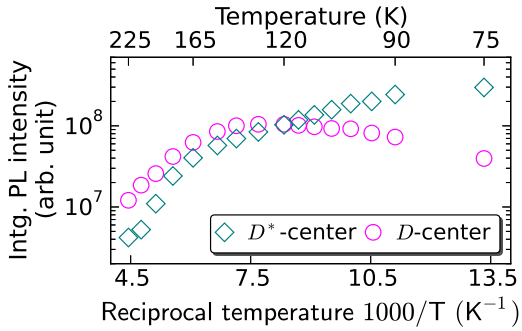

(b) SP-3

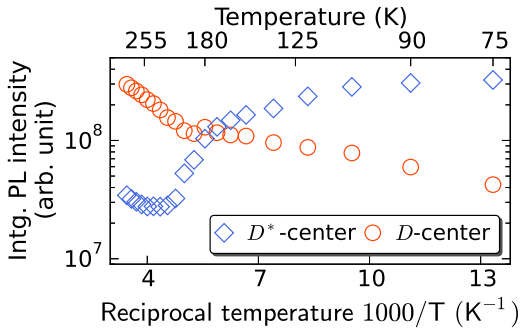

(c) SN-1

Figure 4.16: Arrhenius plots of the integrated absolute luminescence intensities corresponding to the D^* |D-centers related DAP recombination processes for (a) SP-2, (b) SP-3 and (c) SN-1. The line shapes and the relative amplitudes of the separated luminescence spectra are derived from the fitting results of the normalized PL spectra of all three samples summarized in Fig. 4.13 to 4.15.

4.3 Summary

In Sec. 4.1, we have launched the TSL measurements on the *p*-type 6H f-SiC (SP-1/3) and the *n*-type 6H f-SiC (SN-2/3/4) within 75 K to 300 K. Since the TSL were observed on all samples except the strong *p*-type sample, *i.e.*, SP-1, the shallow trapping centers related to the TSL glow peaks observed from other samples should locate at the upper half of the band gap and are induced by nitrogen-doping. By comparing the TSL glow curves of 6H-SiC from the previous research with the TSL glow curves measured here, it can be confirmed that there are no prominent inclusions of the acceptors induced by aluminum-doping. In addition, the inexistence of the shallow acceptors originated from boron-doping was also confirmed. The broad but low-intensity peaks found in SN-3/4 might be originated from the carriers trapping by the nitrogen-induced donors on cubic sites. The peak temperatures of the TSL glow curves of all samples which were identically within 65 K to 75 K indicate that all samples are high-compensated, *i.e.*, the densities of the effective donors and acceptors should be in the same order of magnitude. Another information reflected by this temperature range is that the shallow donors on hexagonal sites induced by nitrogen-doping are responsible for the TSL related processes in all samples. By applying the modified Halperin-Braner's model for the TSL glow peak fitting, we extracted the ionization energies of shallow donor levels, which were around 100 meV for all samples. The calculations revealed that the proportions of the TSL-active shallow donors in SP-3 and SN-2 are much larger than those of SN-3/4 at elevated temperatures. This would cause less portion of the shallow donors in SP-3 and SN-2 participate in the radiative DAP recombination at RT compared to SN-3/4, which might be the reason why the PL spectra of SN-2 is apparently red shifted with respect to the PL spectra of SN-3/4 at RT. In the end, it was found that the absolute TSL intensity increases with the increasing density of the thermally activated non-equilibrium electrons.

In Sec. 4.2, a strong *n*-type (SN-1), an intermediate *p*-type (SP-3), and a strong *p*-type (SP-2) f-SiC sample were characterized by temperature-dependent PL spectroscopy. The existence of a new boron-induced acceptor level, *i.e.*, D^*-center, with a higher ionization energy compared to the well-known *D*-center is confirmed. The proposed double *D*-center system in 6H-SiC agrees well with the previously reported configuration combining *D*- and D'-center which was detected by the Photoluminescence-detected Electron Paramagnetic Resonance (PL-EPR) spectroscopy. The declining tendencies regarding the luminescence at the low energy flanks in the PL spectra of all three samples, which is dominated by the D^*-center related DAP recombination, are attributed to the existence of a hole-trap, *i.e.*, the HS2 center. The lattice geometries of the double *D*-center and the HS2 center are revealed by referring the previous *first-principles* calculation results based on SiC crystal. In addition, it is also revealed that the formation of *D*-center, where the related DAP recombination is the main power driving the emission process from 6H f-SiC at RT, can be facilitated by enhancing N-doping. Moreover, it is also found that the HS2 center should stay between the *D*-center and D^*-center in the band gap of 6H-SiC. The evolution of the luminescence from both low | high energy flanks of the PL emission spectra of 6H f-

SiC which are dominated by D^*- | D-center related DAP recombination is interpreted by a two-stage thermal activation model of the non-equilibrium holes driven by the HS2 center. In order to visualize the evolution related to the competition between the D^* |D-center related DAP recombination regimes, a four-phase skew normal distributions function was applied for the PL spectra fitting, where the luminescence spectra related to those two distinct processes were resolved. The fitting results confirmed the rank of the densities of the D-centers in three samples, *i.e.*, SN-1 > SP-3 > SP-2. We suggested that the booming of the radiative recombination in SN-1 are because of the the D-center's increasing capture probability of the holes thermally activated from the HS2 center. A systematic investigation regarding to both the theory and the experiments are still needed to understand the capturing and thermal activation of holes related to the double D-center and the HS2 hole trap.

CHAPTER 5

Impact from E_1/E_2 centers on photoluminescence of 6H f-SiC at room temperature

It is well-known that the E_1/E_2 centers are the common point defects in n-type 6H-SiC. By forming the negative-U system within the lattice structure of 6H-SiC, E_1/E_2 centers are considered to be the main contributors to non-radiative recombination which limits the carrier lifetime of 6H-SiC. In this chapter, we present our comprehensive study on how the E_1/E_2 centers would affect the efficiency of the DAP recombination, which is considered as the main contributor to the PL in 6H f-SiC. The study is based on the time-resolved PL and static PL measurements of 6H f-SiC samples at RT. The experimental phenomena related to different luminescence decay channels are well-explained by a negative-U centers related carrier dynamics model together with a static PL lifetimes calculation method. Note that the research results presented in this chapter are derived from [49].

5.1 Overview

5.1.1 Brief review of E_1/E_2 centers

Originally, a model developed by Anderson[88] revealed that when two e^- become paired in the dangling bond of a defect and simultaneously couple with a large lattice relaxation, the energy gain of these two e^- may overcome the Coulomb repulsion between them. In this way, the related defect becomes the so-called negative-U center which possesses negative-U property. At early stage, the monovacancy in Si observed by Watkins *et al.*[89] has been taken as a typical example of the negative-U defect. Later on, Hemmingsson *et al.*[90] identified the negative-U properties related to the doublets called Z_1/Z_2 centers in n-type 4H-SiC by applying DLTS measurements, where the energy levels of Z_1/Z_2 centers range from $E_c - 450$ meV to $E_c - 760$ meV depending on their charge states. Soon afterwards, they observed the similar negative-U properties from the two deep levels, *i.e.*, E_1 and E_2 (together they are called E_1/E_2 centers), in n-type 6H-SiC[91] using the same experimental technique. It has been suggested[92, 93] that the Z_1/Z_2 defects in 4H-SiC and the E_1/E_2 defects in 6H-SiC might originate from the same type of point defect. A more recent research by Sasaki

et al.[94] has further solidified the aforementioned correlation between Z_1/Z_2 and E_1/E_2. In their research, Z_1/Z_2 and E_1/E_2 were observed to have almost the same generation rates by e^- irradiation and their annealing behaviors were similar as well.

For the details of the observed negative-U behavior of the E_1/E_2 centers, by characterizing the Schottky diode based on the n-type 6H-SiC[91] by DLTS the E_1/E_2 centers were found to be associated with two acceptor-like levels. To be precise, the experimental results suggested a two-stage ionization process where the transformations of the charge states of E_1/E_2 are summarized in Eq. (5.1) and (5.2) as shown below (note that $E_{1/2}$ represents to E_1 or E_2 center).

$$E^-_{1/2} \xleftarrow{e^-} E^0_{1/2} \xleftarrow{e^-} E^+_{1/2} \tag{5.1}$$

$$E^-_{1/2} \xrightarrow{h^+} E^0_{1/2} \xrightarrow{h^+} E^+_{1/2} \tag{5.2}$$

Here, the charge state $E^-_{1/2}$ which captures two e^- was found to be the ground state with the deepest energy level below the conduction band, while $E^0_{1/2}$ and $E^+_{1/2}$ were characterized as the intermediate state and metastable state, respectively. Note that the atomic structure of E_1/E_2 is still not confirmed yet. The potential candidates range from the Si/C divacancy[95] ($V_{Si}V_C$), the Si vacancy V_{Si} complexes[96], the interstitial pair of N-atom and C-atom (N_iC_i)[97], the negatively charged carbon vacancy (V_C^-)[98] to the carbon vacancy together with a carbon antisite (V_CC_{Si})[99]. Subsequently, Chen *et al.*[100] confirmed the range of the probable candidates which was narrowed down to V_C or C_i. They observed the threshold of e^- irradiation for E_1/E_2 generation on low doped 6H-SiC which was only 0.3 MeV, and such low e^- energy is only sufficient to induce V_C or C_i. A theoretical study based on *first-principles* calculations has been developed by Bechstedt and his co-workers[101, 102] which confirmed that either V_C^- or V_C^+ is a negative-U center. They found that the generation of V_C is associated with giant Jahn-Teller distortion. The dangling bonds are accompanied with the vacancy and reconstructed which can lead to the symmetry lowering of the defect. This symmetry lowering (from C_{3v} to C_{1h}) of V_C due to Jahn-Teller distortion was also observed experimentally[103] in 6H-SiC using EPR spectroscopy.

5.1.2 Motivation

Albeit E_1/E_2 centers are already widely observed by DLTS on as-grown and irradiated 6H-SiC[90, 93–95, 98, 104, 105], so far, no experimental technique based on DLTS is available for the related characterization on f-SiC. Since the fabrication of the metal-insulator-semiconductor (MIS) structured Schottky diode based on f-SiC with low leakage current is still not available due to the very high free carrier concentration[61, 106] in f-SiC at thermal equilibrium. On the other hand, for the investigation about how E_1/E_2 could influence the IQE of f-SiC which is mainly dependent on the radiative DAP recombination, the application of the non-destructive and time-efficient

(*i.e.*, no contact preparation is needed) methods, *e.g.*, TRPL and static PL measurements, are preferred. In the following part of this chapter, the process related to how the carriers trapping by E_1/E_2 centers could affect the DAP recombination in f-SiC is demonstrated quantitatively. The rapid luminescence decay detected by TRPL in f-SiC is illustrated by a negative-U centers related carriers dynamics model. By further implementing a steady-state DAP recombination model, how the DAP recombination lifetimes could be influenced by the existence of E_1/E_2 centers is revealed. In addition, the carrier dynamics of a N-B co-doped n-type 6H-SiC bulk sample is also investigated for the comparison against f-SiC. It is revealed that apart from the higher E_1/E_2 found in the bulk sample, an additional trapping center is also observed from the related experimental results.

5.1.3 Experimental

In principle, the information regarding various recombination channels in 6H-SiC whether they are radiative or non-radiative, could be obtained from the time-resolved photoluminescence (TRPL) measurements[107, 108]. For the multi-exponential photon decay curve recorded by the TRPL system, there are two parameters employed to quantify the decay process in every single channel, *i.e.*, the recombination lifetime (time constant) indicates the rate of the photon decay and the amplitude designates the "load capacity" of the non-equilibrium carriers of the channel. In this research, it is believed that the carrier dynamics regarding the 6H f-SiC is mainly driven by three recombination channels, where two of them are attributed to the E_1/E_2 centers and the left one is for DAP recombination. In order to study the efficiency regarding the steady-state DAP recombination in 6H f-SiC samples, the related static PL spectra at RT are also needed. Additionally, the contrast among the DAP recombination efficiencies of different samples was numerically analyzed, where some parameters extracted from the corresponding TRPL measurements were employed for the related analysis. We chose sample SN-1/2 for this research since they are both strong n-type samples and grown in the same batch with the identical epilayer thickness, the essential parameters of these two samples refer to Tab. 2.6. A bulk 6H-SiC sample named as 'BK' for reference (as mentioned in Subsec. 5.1.2) was purchased from TanKeBlue Ltd. with double-side-polished along the direction of $\langle 0001 \rangle \pm 0.5°$. The detailed parameters regarding sample SN-1/2 as well as BK are listed in Tab. 5.1. Sufficient numbers of sampling points were chosen for each sample (SN-1: three | SN-2: nine | BK: two) by considering their dimensions for TRPL | PL measurements. The time span for sampling the photon decay during the TRPL measurements was set to 2 ms | 20 μs for the f-SiC | bulk sample, respectively. As for the repetition rate of the laser pulse for the TRPL system, a rate of 500 Hz with 80 ns resolution and 1 h integration time was chosen for f-SiC samples, while a rate of 50 kHz with 800 ps resolution and 30 min integration time was set for bulks sample. By measuring the beam power of the pulsed laser source under the repetition rate of 500 kHz, the single pulse energy was determined as $\sim$920 nW. In addition, due to the heavy thicknesses

of all three samples, the values of Z_{eff} and g (as determined in Subsec. 3.3.2) for each sample are almost independent of sample thickness d. To maintain the identical experimental condition for both TRPL and PL measurements, the same pulsed laser source (500 kHz & ∼920 nW) was employed for PL measurements based on the same setup (mentioned in Subsec. 3.3.2) as those of TRPL measurements. In addition, for static PL measurements, an optical spectrometer (CAS 140B, Instrument Systems GmbH) with 5 s integration time and a pre-installed long-pass filter (λ_{cutoff} =420 nm, for emitting photons) was applied.

5.1.4 Computational methods

In this research, it is believed that the negative-U centers related carriers trapping competes with the emission process dominated by the DAP recombination, hence a systematic and quantitative investigation is needed in order to figure out how the above-mentioned two transient processes could result in different PL intensities of the three 6H-SiC samples. Here, the theoretical investigation consists of the negative-U centers related carrier dynamics and the steady-state DAP recombination calculation. Note that the parameters regarding each decay channels obtained from the TRPL measuremens were applied as the inputs for the above two modelings. The methodology regarding the modeling of the negative-U centers related carrier dynamics was derived from Ref. [50] with a major modification. In Ref. [50], the author came up with a carrier dynamics model based on the negative-U centers Z_1/Z_2, where the

Sample ⇒	SN-1	SN-2	BK
d (μm)	45+250		325
Dim. (cm^2)	0.8×0.5	1.2×1.2	0.5×0.5
Growth rate ($\mu m \cdot h^{-1}$)	90	80	-
N_2 pressure (mbar)	0.75	1	-
N_d ($\times 10^{18} cm^{-3}$)	9.0	9.2	5.4
N_a ($\times 10^{18} cm^{-3}$)	4.4	5.2	0.95
E_g (meV)	2985	2983	2998
E_F (meV)	2885	2880	2903
n_0 ($\times 10^{18} cm^{-3}$)	1.90	1.69	2.34
N_u ($\times 10^{12} cm^{-3}$)	2.08	3.50	172
Z_{eff} (μm)	17.33		
g (cm^{-3})	4.57×10^{11}		

Table 5.1: Essential parameters of each 6H-SiC sample. The methods for the calculations of n_0, E_g and E_F of BK refers to Subsec. 2.2.1. The determination of the total density of E_1/E_2 centers (N_u) of each sample will be introduced in Sec. 5.2. The calculation methods of the effective penetration depth (Z_{eff}) and the injection level (g) are already mentioned in Subsec. 3.3.2.

Z_1/Z_2 centers have been simplified as a single defect system. As researchers[94, 109] have confirmed that the Z_1/Z_2 centers in n-type 4H-SiC is equivalent to the E_1/E_2 centers in n-type 6H-SiC, the methodology regarding the modeling of the negative-U centers related carrier dynamics in 4H-SiC reported by Ref. [50] should be applicable for the E_1/E_2 centers related carrier dynamics simulation in 6H-SiC as well. The details corresponding to the major modification of the original carrier dynamics model where three types of negative-U center and the influence of heavy B-doping were taken into consideration for our research will be discussed in Sec. 5.2. On the other hand, our methodology for the steady-state DAP recombination calculation is expanded from Ref. [110]. Here, the author came up with a theoretical framework for predicting the DAP recombination lifetime (τ_{dap}) in steady-state for a single-donor-single-acceptor system, where the model has been extended to three types of DAP recombination including three donor levels and one acceptor level for our f-SiC samples. Based on the above classical steady-state DAP recombination model, we also added the analysis regarding how the transition probability of DAP ($W(r_{\mathrm{dap}})$) is determined by the mean DAP separation distance (r_{dap}), and how τ_{dap} is further determined by $W(r_{\mathrm{dap}})$. Moreover, we also analyzed the capture probabilities of each donor and acceptor. We will discuss the modeling of the DAP recombination lifetime in 6H-SiC further in detail in Sec. 5.3. As mentioned in Sec. 2.4, it is believed that the D-center ($E_v + 580$ meV) is the only boron-induced deep acceptor level available for radiative DAP recombination at RT. Therefore, D-center is the only acceptor level included in both the negative-U center related carrier dynamics simulation and the τ_{dap} calculation. The general parameters of N-B co-doped n-type 6H-SiC for both types of simulation are summarized in Tab. 5.2.

5.2 E_1/E_2 related carrier dynamics in 6H f-SiC

5.2.1 Principle of the carriers trapping by E_1/E_2 centers

Recently, by characterizing 6H-SiC through Laplace DLTS, Koizumi *et al.*[111] have confirmed that the E_2 center, which is one of the components in the negative-U system in 6H-SiC detected by Hemmingsson *et al.*[90, 91] before, is actually constitutive of two centers, *i.e.*, E_{2L} and E_{2H}. The subscripts ($L \mid H$ stands for "low" or "high", respectively) indicate the contrast on the emission rate where the corresponding DLTS peaks emerges during the measurements. Hence, in this research, three distinct trapping centers, *i.e.*, E_1, E_{2L}, and E_{2H}, are included in our negative-U centers related carrier dynamics simulations. Note that $E_1 \mid E_{2L,2H}$ defects are believed to stay on the hexagonal | cubic sites[98], respectively, where these three types of negative-U center are all considered as the carbon vacancy related centers[94]. The dynamic procedures regarding the negative-U centers related non-equilibrium carriers capturing in 6H-SiC are depicted in Fig. 5.1. Herein, the ground state at RT is represented by E_i^- ($i \Rightarrow 1,\ 2L,\ 2H$). This indicates that after the transient process where all the non-equilibrium carriers have been dissipated via the carriers trapping correlated to

Parameter	Symbol	Value	Reference
Activation energy (meV)			
of the charge state:			
E_1^-	$\Delta E_1^{0/-}$	390	[111]
E_{2L}^-	$\Delta E_{2L}^{0/-}$	440	[111]
E_{2H}^-	$\Delta E_{2H}^{0/-}$	430	[111]
E_1^0	$\Delta E_1^{+/0}$	260	[111]
E_{2L}^0	$\Delta E_{2L}^{+/0}$	140	[111]
E_{2H}^0	$\Delta E_{2H}^{+/0}$	180	[111]
Thermal barrier (meV)			
related to the transition of:			
$E_1^0 + e^- \rightarrow E_1^-$ transition	ε_{b1}	48	[91]
$E_2^0 + e^- \rightarrow E_2^-$ transition	ε_{b2}	70	[91]
e^- capture cross section (cm^{-2})			
related to the transition of:			
$E_1^0 + e^- \rightarrow E_1^-$	$\sigma_{1,e}^{0/-}$	3×10^{-15} $\times \exp(-\varepsilon_{b1}/(k_bT))$	[91, 111]
$E_1^+ + e^- \rightarrow E_1^0$	$\sigma_{1,e}^{+/0}$	2×10^{-15}	[111]
$E_{2L}^0 + e^- \rightarrow E_{2L}^-$	$\sigma_{2L,e}^{0/-}$	6×10^{-15} $\times \exp(-\varepsilon_{b2}/(k_bT))$	[91, 111]
$E_{2L}^+ + e^- \rightarrow E_{2L}^0$	$\sigma_{2L,e}^{+/0}$	5×10^{-16}	[111]
$E_{2H}^0 + e^- \rightarrow E_{2H}^-$	$\sigma_{2H,e}^{0/-}$	5×10^{-15} $\times \exp(-\varepsilon_{b2}/(k_bT))$	[91, 111]
$E_{2H}^+ + e^- \rightarrow E_{2H}^0$	$\sigma_{2H,e}^{+/0}$	7×10^{-16}	[111]

Table 5.2: General characteristics of the N-B co-doped n-type 6H-SiC.

E_1/E_2 centers, ideally, all the excited charge states (E_i^0 and E_i^+) would turn back to E_i^-. It is worthy to mention that we did not take the carriers emission into consideration as the related process can be negligible at RT due to large activation energies, therefore only the carriers capture processes were included in the carrier dynamics modeling. For negative-U centers involved e^- capture process, the transition from the empty state (E_i^+) to the intermediate state (E_i^0) is treated as a fast cascaded e^- capture process[87, 112], while the transition from the intermediate state E_i^0 to the ground state E_i^- is believed to be a multi-phonon assisted e^- capture process[91] where the related transition energy must be corrected with the thermal barrier when building the numerical model. In addition, in contrast to Ref. [50], the influence from the acceptor level, *i.e.*, the D-center, has to be taken into the consideration when building the model, since the three samples included in this research are all heavily boron-doped ($> 10^{17}$ cm^{-3}). By assuming that the D-center is the exclusive acceptor level being effective in our 6H-SiC samples at RT, all the non-equilibrium

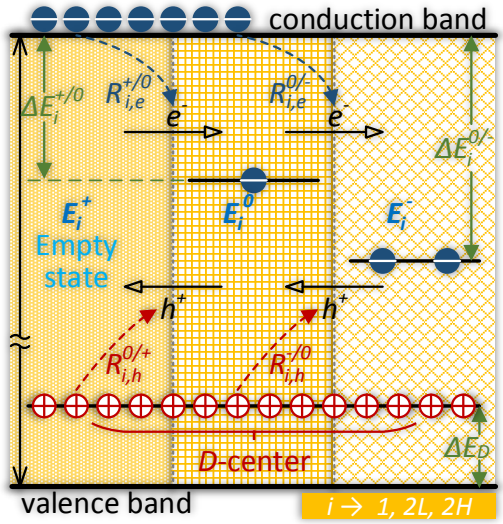

Figure 5.1: A sketch showing the dynamic procedure regarding the negative-U center involved electron | hole capture in 6H-SiC at RT. The diagram is split into three charge states, *i.e.*, E_i^+, E_i^0, and E_i^-, where the subscript i designates each constituent of the negative-U system in 6H-SiC: E_1, E_{2L} or E_{2H}. The dashed arrows indicate both electron (from conduction band) and hole (from D-center) capture process. These capture processes further correlate to the respective charge state transitions involving both $E_i^+ \rightleftharpoons E_i^0$ and $E_i^0 \rightleftharpoons E_i^-$. In addition, $\Delta E_i^{+/0}$ | $\Delta E_i^{0/-}$ represents the ionization energy of E_i^0 | E_i^- state, respectively, and ΔE_D designates the binding energy of the D-center.

h^+ would be instantaneously released to the acceptor level after the carriers injection and have very little chance to be ionized into the valence band as the related ionization energy is too high[51]. Hence we consider the D-center rather than the valence band to be the only origin of non-equilibrium h^+ participating in negative-U centers related carriers capture in our model. Table 5.2 summarizes the e^- capture cross-sections regarding both fast cascaded process and multi-phonon process and the thermal barriers for all three negative-U centers in 6H-SiC included in our model. For the characterization of an n-type semiconductor that contain defect levels, it is difficult to determine the capture cross-sections of minority carriers (holes, in this case) for the defect levels. Hence the estimations of the hole capture cross-sections for all three negative-U centers with different charge states are needed in our modeling. At the early stage, Hemmingsson *et al.*[90] have proposed that if the E_1/E_2 centers are considered being active in non-equilibrium electron-hole recombination process the

capture cross-section of h^+ for each center should have the same order or higher than that of the e^-. Afterwards, researchers[50] came up with a more specific relation between the electron | hole capture cross-sections of both the ground (E^-) and intermediate (E^0) charge states for the Z_1/Z_2 centers in 4H-SiC as shown in Eq. (5.3). After getting the reasonable range of the value of $\sigma_{i,h}^{-/0}(\sigma_{i,h}^{0/+})$, one can estimate the density of the negative-U center E_i by further extracting the related minority carrier lifetime $\tau_{u,i}$ under low injection level[113], where the density of E_i, *i.e.*, $N_{u,i}$, can be expressed by Eq. (5.4) with $\langle\nu_{th,h}\rangle$ representing the mean thermal velocity of h^+. In Eq. (5.4), we have fixed the relation for simplicity where: $\sigma_{i,h}^{-/0} = \sigma_{i,h}^{0/+} = 5 \times \sigma_{i,e}^{+/0}$. In fact, we have tried various values of k for $\sigma_{i,h} = k \times \sigma_{i,e}^{+/0}$ in our modeling with $k \in [5, 10]$, where the line shape of the normalized decay curve we simulated was found to be almost independent of k with such a narrow range.

$$\sigma_{i,h}^{-/0} \approx \sigma_{i,h}^{0/+} \approx (5 \sim 10) \times \sigma_{i,e}^{+/0} \gg \sigma_{i,e}^{0/-} \tag{5.3}$$

$$N_{u,i} = \frac{1}{\sigma_{i,h}\langle\nu_{th,h}\rangle\tau_{u,i}} \tag{5.4}$$

5.2.2 General formulation of the carrier dynamics model

The carrier capture rates corresponding to the respective charge state transitions as depicted in Fig. 5.1 in 6H-SiC can be described by Eq. (5.5) which was expanded from Eq. 9 in Ref. [50]. In Eq. (5.5), n_0 | p_0 represents the equilibrium electrons | holes concentration, respectively. The density of the time-dependent non-equilibrium electrons | holes allocated for the certain negative-U center E_i is denoted by $\delta n_i(t)$ | $\delta p_i(t)$, separately, where Eq. (5.6) designates the time-dependent total density of the non-equilibrium carriers. Eq. (5.7) refers to the expression of $n_i^{0/-}(n_i^{+/0})$ which is derived from Ref. [114]. A rough estimation of $p_i^{-/0}(p_i^{0/+})$ is expressed by Eq. (5.8).

$$\begin{aligned}
R_{i,e}^{0/-}(t) &= \sigma_{i,e}^{0/-}\langle\nu_{th,e}\rangle\Big\{\Big[n_0 + \delta n_i(t)\Big]N_i^0(t) - n_i^{0/-}N_i^-(t)\Big\} \\
R_{i,e}^{+/0}(t) &= \sigma_{i,e}^{+/0}\langle\nu_{th,e}\rangle\Big\{\Big[n_0 + \delta n_i(t)\Big]N_i^+(t) - n_i^{+/0}N_i^0(t)\Big\} \\
R_{i,h}^{-/0}(t) &= \sigma_{i,h}^{-/0}\langle\nu_{th,h}\rangle\Big\{\Big[p_0 + \delta p_i(t)\Big]N_i^-(t) - p_i^{-/0}N_i^0(t)\Big\} \\
R_{i,h}^{0/+}(t) &= \sigma_{i,h}^{0/+}\langle\nu_{th,h}\rangle\Big\{\Big[p_0 + \delta p_i(t)\Big]N_i^0(t) - p_i^{0/+}N_i^+(t)\Big\}
\end{aligned} \tag{5.5}$$

$$\begin{aligned} \delta n(t) &= \sum_i \delta n_i(t) \\ \delta p(t) &= \sum_i \delta p_i(t) \end{aligned} \tag{5.6}$$

$$n_i^L = N_c \exp\left(-\frac{\Delta E_i^L}{k_b T}\right)\Bigg|_{L\to 0/-,+/0} \tag{5.7}$$

$$p_i^L = N_a \exp\left(-\frac{E_g - \Delta E_i^L - \Delta E_D}{k_b T}\right)\Bigg|_{L\to -/0,0/+} \tag{5.8}$$

In addition, the total density of the negative-U center is described by Eq. (5.9), where $N_i^C(t)$ refers to the time-dependent density of a certain type of negative-U center E_i with a charge state of C. Likewise, the conservation of the total density of each negative-U center E_i is expressed by Eq. (5.10), where $\delta N_i^C(t)$ designates the time-dependent variation of the density of a certain type of negative-U center E_i with a charge state of C.

$$N_u = \sum_i \sum_C N_i^C(t)\Big|_{C\to -,0,+} \tag{5.9}$$

$$0 = \sum_C \delta N_i^C(t)\Big|_{C\to -,0,+} \tag{5.10}$$

As we have mentioned that all three types of negative-U center stay at the ground state (E_i^-) at RT, which indicate that the densities of the respective E_i^0 and E_i^+ states are zero. Moreover, since all three samples included in this research are strong n-type 6H-SiC samples, electrons are the majority carriers, the net density of the non-equilibrium carriers allocated to each negative-U center related recombination channel during the transient carriers injection should be in the form of $\delta n_i(t) - \delta p_i(t)$. By rethinking the process regarding the charge state transfer through electron capture described by Eq. (5.1), the above-mentioned net density of the non-equilibrium carriers for each channel is found to follow the relation shown in Eq. (5.11).

$$\delta n_i(t) - \delta p_i(t) = \delta N_i^0(t) + 2\delta N_i^+(t) \tag{5.11}$$

5.2.3 The modelling in the case of low injection level

Specifically, we further consider that our strong n-type samples were excited under low injection level where the condition is summarized in Eq. (5.12). The electron capture

rates corresponding to the charge state transitions which are originally described by Eq. (5.5) can be re-expressed in the form of Eq. (5.13) by applying Eq. (5.10), Eq. (5.11), and Eq. (5.12) into Eq. (5.5). The differential equations regarding the time-dependent forms of the non-equilibrium carriers densities (e^- and h^+) as well as the changes of each charge states for every trapping center are presented in Eq. (5.14) which are derived from Eq. (11) in Ref. [50]. At this point, we have formulated the theoretical model describing the carrier dynamics of the negative-U centers in strong n-type 6H-SiC under low injection levels which is based on Eq. (5.10) to Eq. (5.14).

$$\begin{aligned} n_0 &\gg \delta n_i(t) \\ p_0 &\ll \delta p_i(t) \\ \delta p_i(t) &\gg p_i^{0/+}, p_i^{-/0} \end{aligned} \tag{5.12}$$

$$\begin{aligned} R_{i,e}^{0/-}(t) &= \sigma_{i,e}^{0/-}\langle\nu_{th,e}\rangle\left\{n_0\left[\delta p_i(t) - \delta n_i(t) - 2\delta N_i^-(t)\right] - n_i^{0/-}\left[N_{u,i} + \delta N_i^-(t)\right]\right\} \\ R_{i,e}^{+/0}(t) &= \sigma_{i,e}^{+/0}\langle\nu_{th,e}\rangle\left\{\left(n_0 + n_i^{+/0}\right)\left[\delta n_i(t) - \delta p_i(t)\right] + \left(n_0 + 2n_i^{+/0}\right)\delta N_i^-(t)\right\} \\ R_{i,h}^{-/0}(t) &= \sigma_{i,h}^{-/0}\langle\nu_{th,h}\rangle\left\{\delta p_i(t)\left[N_{u,i} + \delta N_i^-(t)\right]\right\} \\ R_{i,h}^{0/+}(t) &= \sigma_{i,h}^{0/+}\langle\nu_{th,h}\rangle\left\{\delta p_i(t)\left[\delta p_i(t) - \delta n_i(t) - 2\delta N_i^-(t)\right]\right\} \end{aligned} \tag{5.13}$$

$$\begin{aligned} \frac{\mathrm{d}\delta n_i(t)}{\mathrm{d}t} &= -\left[R_{i,e}^{0/-}(t) + R_{i,e}^{+/0}(t)\right] \\ \frac{\mathrm{d}\delta p_i(t)}{\mathrm{d}t} &= -\left[R_{i,h}^{-/0}(t) + R_{i,h}^{0/+}(t)\right] \\ \frac{\mathrm{d}\delta N_i^-(t)}{\mathrm{d}t} &= R_{i,e}^{0/-}(t) - R_{i,h}^{-/0}(t) \end{aligned} \tag{5.14}$$

$$\begin{aligned} \tau_p(t) &= \left[-\frac{\mathrm{d}\delta p(t)}{\mathrm{d}t}\frac{1}{\delta p(t)}\right]^{-1} \\ \tau_{p,1}(t) &= \left[-\frac{\mathrm{d}\delta p_1(t)}{\mathrm{d}t}\frac{1}{\delta p_1(t)}\right]^{-1} \\ \tau_{p,2}(t) &= \left\{-\left[\frac{\mathrm{d}\delta p_{2L}(t)}{\mathrm{d}t} + \frac{\mathrm{d}\delta p_{2H}(t)}{\mathrm{d}t}\right]\frac{1}{\delta p_{2L}(t) + \delta p_{2H}(t)}\right\}^{-1} \end{aligned} \tag{5.15}$$

Furthermore, with low-injection level, it is considered that the time-dependent PL intensity, *i.e.*, $I(t)$, can be approximately proportional to the density of the non-equilibrium minority carriers, so we have $I(t) \propto \delta p(t)$ in our case. Accordingly,

one can treat the lifetime of the non-equilibrium holes as being equivalent to the PL lifetime where: $\tau_{\mathrm{PL}}(t) \cong \tau_p(t)$. Eq. (5.15) summarizes the lifetimes of the non-equilibrium h^+ for the recombination channels of each E_i.

5.3 Steady-state DAP recombination lifetime calculation model

5.3.1 Procedure of steady-state DAP recombination

The band diagram illustrating the principle of the steady-state DAP recombination model is presented in Fig. 5.2. The core of the steady-state DAP recombination model[110] is to treat the DAP as a single defect. The whole procedure of DAP recombination is consisting of a sequence of charge state transitions, where each transition is accompanied with carriers emission | capture process. The charge state S designates the number of electrons occupied by one set of DAP[115]. In this research, since we focus on strong n-type samples, the charge state S is limited to *1*, $1'$, and *2* and only the charge state transitions denoted by the dashed arrows shown in Fig. 5.2 were included in our modeling. Specifically, the charge state $1'$ stands for the excited state ready for electron-hole recombination via DAP, where DAP recombination occurs during the $1' \rightarrow$ *1* transition. The transient DAP recombination procedure in an n-type semiconductor can be described in a simple manner: after carriers injection, the minority carriers (h^+) cascade from valence band to conduction band where the charge state S undergoes the circulation of: *2* $\rightarrow 1' \rightarrow$ *1* $\rightarrow$ *2*. It is worthy to mention that this circulation is reversible, where the transition between two certain charge states is realized by the capture or emission of the same type of carriers (e^- or h^+) as indicated by the pair of opposite arrows between each two charge states in Fig. 5.2. For instance, $n_0 N_1^j C_{n1}^j$ denotes the electron capture rate of state *1* (for charge state transition: *1*→*2*), where N_1^j indicates the density of the charge state *1* with the donors staying on the j-sites and accordingly C_{n1}^j represents the related electron capture probability. Contrary to the charge state transition *1*→*2* via electron capture, the transition from *2* to *1* involves the electron emission with the corresponding emission rate denoted by $N_2^j e_{n2}^j$, where the implication of N_2^j is similar to that of N_1^j and e_{n2}^j indicates the related electron emission probability. At steady-state, for the reversible charge state transition procedure: *2* $\rightleftharpoons 1' \rightleftharpoons$ *1* $\rightleftharpoons$ *2*, the overall transition rate regarding the left-to-right direction would be equal to the overall transition rate for the right-to-left direction, that is, a dynamic balance has been reached. In addition, the ionization energies regarding all the unperturbed energy levels are summarized in Table. 5.2, where each pair of the perturbed | unperturbed energy levels are separated by the Coulomb interaction energy (U_E) of a pair of elementary charges where: $U_E = e^2/(4\pi\varepsilon_0\varepsilon_r r_{\mathrm{dap}})$[1] with r_{dap} representing the donor-acceptor distance[18, 116].

[1] ε_0 and ε_r denote the vacuum permittivity and the relative permittivity of 6H-SiC, respectively.

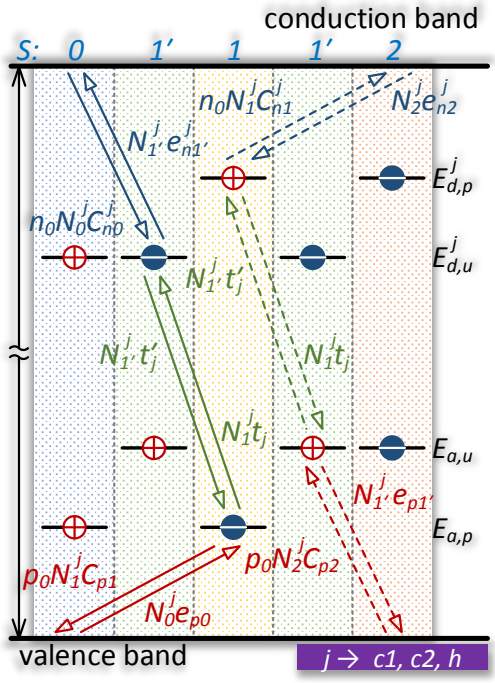

Figure 5.2: An analytical sketch showing the full process of DAP recombination. There are five charge states of DAP which are represented by S. The arrows refer to the carriers emission | capture processes marked with the related rates, where the solid | dashed arrows indicate the major recombination paths for strong p-type | n-type sample, respectively. The perturbed donor | acceptor level(s) are designated by $E_{d,p}^j$ and $E_{a,p}$, respectively, while the unperturbed donor | acceptor level(s) are designated by $E_{d,u}^j$ and $E_{a,u}$, separately. Note that the superscript j indicates the type of the lattice sites (k_1, k_2, and h) where the donors occupy.

Note that r_{dap} is a crucial parameter for estimating DAP recombination lifetimes and will be further used in the steady-state DAP recombination model.

5.3.2 General model of the steady-state DAP recombination

As depicted in Fig. 5.2, the steady-state DAP recombination rate for each type of DAP (*i.e.*, $E^j_{d,u} + E_{a,u}$ with $j \to k_1, k_2, h$) is actually equal to the corresponding net transition rate of: $1' \rightleftharpoons 1$ which can be expressed by Eq. (5.16). Alternatively, since $1'$ is the charge state ready for DAP recombination and there are two paths leading to $1'$ state, *i.e.*, $0 \to 1'$ and $2 \to 1'$, where the related transition rates are designated by $R^j_{0\to1'}$ and $R^j_{2\to1'}$, respectively, the steady-state DAP recombination rate for each type of DAP can be represented by $R^j_{0\to1'} + R^j_{2\to1'}$ as shown in Eq. (5.17).

$$R_{\mathrm{dap}} = \sum_j N^j_{1'} t'_j - N^j_1 t_j \tag{5.16}$$

$$R_{\mathrm{dap}} = \sum_j R^j_{0\to1'} + R^j_{2\to1'} \tag{5.17}$$

In addition, the expressions for $R^j_{0\to1'}$ and $R^j_{2\to1'}$ are shown in Eq. (5.18), where $R^j_{0\to1'}$ | $R^j_{2\to1'}$ is actually represented by the net rate of electron | hole capture for $0 \to 1'$ | $2 \to 1'$ transition, respectively.

$$\begin{aligned} n_0 N^j_0 C^j_{n0} - N^j_{1'} e^j_{n1'} &= R^j_{0\to1'} \\ p_0 N^j_2 C_{p2} - N^j_{1'} e_{p1'} &= R^j_{2\to1'} \end{aligned} \tag{5.18}$$

It is also worthy to mention that at steady-state there is no accumulation of $1'$ states, the net rate of $1' \to 1$ transition should be equal to the sum of the transition rate of $0 \to 1'$ and $2 \to 1'$ which can be expressed by Eq. (5.19).

$$t'_j N^j_{1'} - t_j N^j_1 = R^j_{0\to1'} + R^j_{2\to1'} \tag{5.19}$$

On the other hand, as there is no accumulation of $1'$ states which means all the available $1'$ states would transfer to 1 states simultaneously at steady-state, the net rates for $0 \to 1'$ and $1 \to 0$ should be equal for p-type sample, accordingly, the net rates for $2 \to 1'$ and $1 \to 2$ should be equal for n-type sample. The above-mentioned two boundary conditions are summarized in Eq. (5.20).

$$\begin{aligned} n_0 N^j_0 C^j_{n0} - N^j_{1'} e^j_{n1'} &= p_0 N^j_1 C_{p1} - N^j_0 e_{p0} \\ p_0 N^j_2 C_{p2} - N^j_{1'} e_{p1'} &= n_0 N^j_1 C^j_{n1} - N^j_2 e^j_{n2} \end{aligned} \tag{5.20}$$

Furthermore, the effective density of a certain type of DAP (N^j_{eff}) regardless of charge state, *i.e.*, $\sum_S N^j_S = N^j_{\text{eff}}$, can be expressed by Eq. (5.21) where N^j_{eff} is determined by the allocated injection level for DAP recombination (g_{dap}) and the Fermi level (E_F) at steady-state. The calculation of E_F refers to Subsec. 2.2.1. Note that the low injection level ($\sim \times 10^{11}$ cm^{-3}) in this research would cause the quasi-Fermi level for e^- to approximate to the static Fermi level E_F.

$$N^j_{\text{eff}} = \frac{g_{\text{dap}}}{1 + \frac{1}{g_D}\exp\left(\frac{E_g - \Delta E_j - E_F}{k_b T}\right)} \tag{5.21}$$

In order to deduce the expressions for the emission probabilities in this model, *i.e.*, $e^j_{n1'}$, e^j_{n2}, $e_{p1'}$, and e_{p0}, an approximate solution[114] is to represent each emission probability by an "assumed" temperature-dependent carrier density multiplied by a capture probability. For instance, as $e^j_{n1'}$ is related to $0 \rightarrow 1'$ transition and indicates the probability regarding "releasing" one electron by the unperturbed donor level $E^j_{d,u}$, $e^j_{n1'}$ can be approximated by getting the capture probability C^j_{n0} (related to $1' \rightarrow 0$) multiplied by a "temporary" carrier density, where this "temporary" carrier density is derived by assuming the Fermi level to stay on $E^j_{d,u}$. The assumed four "temporary" carrier densities (by treating the Fermi level as $E^j_{d,p}$, $E^j_{d,u}$, $E_{a,p}$, or $E_{a,u}$) are given in Eq. (5.22). Accordingly, the approximated expressions for all four types of emission probabilities are shown in Eq. (5.23).

$$\begin{aligned}
n^j_{d,p} &= n_0 \exp\left(\frac{E_g - \Delta E_j - E_F}{k_b T}\right) \\
n^j_{d,u} &= n_0 \exp\left(\frac{E_g - \Delta E_j - U_E(r_{\text{dap}}) - E_F}{k_b T}\right) \\
p_{a,p} &= p_0 \exp\left(\frac{E_F - \Delta E_D}{k_b T}\right) \\
p_{a,u} &= p_0 \exp\left(\frac{E_F - \Delta E_D - U_E(r_{\text{dap}})}{k_b T}\right)
\end{aligned} \tag{5.22}$$

$$\begin{aligned}
e^j_{n2} &= n^j_{d,p} C^j_{n1} \\
e^j_{n1'} &= n^j_{d,u} C^j_{n0} \\
e_{p0} &= p_{a,p} C_{p1} \\
e_{p1'} &= p_{a,u} C_{p2}
\end{aligned} \tag{5.23}$$

Moreover, t_j and t'_j represent the transition probability regarding $1 \rightarrow 1'$ and $1' \rightarrow 1$, respectively. As we have mentioned that for n-type semiconductor, a dynamic

balance would be reached regarding the reversible process: $2 \rightleftharpoons 1' \rightleftharpoons 1 \rightleftharpoons 2$, where this dynamic balance can be analytically expressed by Eq. (5.24).

$$p_0 N_2^j C_{p2} \times N_{1'}^j t_j' \times n_0 N_1^j C_{n1}^j = N_2^j e_{n2}^j \times N_1^j t_j \times N_{1'}^j e_{p1'} \tag{5.24}$$

By combining Eq. (5.22), Eq. (5.23), and Eq. (5.24), one can get the ratio between t_j' and t_j which is expressed by Eq. (5.25).

$$\frac{t_j'}{t_j} = \frac{e_{p1'} e_{n2}^j}{n_0 p_0 C_{n1}^j C_{p2}} = \exp\left(\frac{E_g - (\Delta E_j + \Delta E_D + U_E(r_{\mathrm{dap}}))}{k_b T}\right) \tag{5.25}$$

From Eq. (5.25), it can be found that $t_j' \gg t_j$ at RT, hence the net DAP transition probability can be regarded as t_j', where now t_j' can be relabeled into a more general form, *i.e.*, $W(r_{\mathrm{dap}})$. The expression of $W(r_{\mathrm{dap}})$ derived from Ref. [117] is shown in Eq. (5.26) which is applied to describe the DAP transition process assisted by strong phonon replicas. A simplified condition was applied when building up the expression of $W(r_{\mathrm{dap}})$: a donor bound with an electron and an acceptor bound with a hole are separated by a distance of r_{dap} where only the optical momentum matrix element between the states with | without electron-hole pair is taken into consideration. For 6H-SiC, the range of $W_{\max}$ has been experimentally determined in Ref. [116] which is around $(3 \sim 4) \times 10^5\ \mathrm{s}^{-1}$. In this research, we set the value of $W_{\max}$ to $3.5 \times 10^5\ \mathrm{s}^{-1}$ for simplicity. In addition, the Bohr radii of nitrogen-induced donors (with ionization energies of ΔE_j) in 6H-SiC is designated by a_0^j. The expression of a_0^j derived from Ref. [87] is shown in Eq. (5.27) where a situation regarding the capture of an exciton to a neutral donor is considered when building up the expression of a_0^j.

$$W_j(r_{\mathrm{dap}}) = W_{\max} \exp\left(-\frac{2 r_{\mathrm{dap}}}{a_0^j}\right) \tag{5.26}$$

$$a_0^j = \left(\frac{e h^2}{8\pi^2 m_e^* (\varepsilon_0 \varepsilon_r)^2} \frac{1}{\Delta E_j^3}\right)^{1/4} \tag{5.27}$$

5.3.3 The modelling in the case of extrinsic *n*-type 6H-SiC

For our strong *n*-type 6H-SiC samples, in this modeling, the DAP lifetime is essentially equal to the carrier lifetime of non-equilibrium holes, *i.e.*, $\tau_{\mathrm{dap}} = \tau_p$. Furthermore, by letting $C_{n0}^j = C_{p2} = C_p$ and $C_{n1}^j = C_{p1} = C_n^j$ for simplicity, we reconstructed Eq. (22) in Ref. [110] which is applied for the estimation of τ_{dap} under low injection level. The ultimate expression for the recombination lifetime of a certain type DAP in a N-B co-doped strong *n*-type 6H-SiC is shown in Eq. (5.28).

$$\tau_{\mathrm{dap}}^{j}=\frac{1}{n_0 N_{\mathrm{eff}}^{j} W_j(r_{\mathrm{dap}})}\times\frac{\begin{array}{c}\left[n_0 p_{a,u}\left(n_0+n_{d,p}^{j}\right)\right]C_{n,j}^{2}+\\ \left[p_{a,u}\left(p_{a,p}+n_{d,p}^{j}\right)\left(n_0+n_{d,p}^{j}\right)\right]C_p C_{n,j}+\\ \left[\left(n_0+n_{d,p}^{j}\right)C_{n,j}+p_{a,p}C_p\right]n_0 W_j(r_{\mathrm{dap}})\end{array}}{n_0 C_{n,j}^{2}+C_p C_{n,j}\left(n_{d,p}^{j}+p_{a,p}\right)} \tag{5.28}$$

In addition, it is considered that[118] the density of the donors on h sites or $k_1 \mid k_2$ sites in 6H-SiC is proportional the number of hexagonal and cubic sites, respectively, where we have: $N_h/N_c = 1:2$ (subscripts $-$ h: hexagonal $\mid$ c: cubic) for 6H-SiC. For simplicity, it is also assumed there exists an equal number of k_1 and k_2 sites in 6H-SiC. Therefore now we have the same donors on h, k_1, and k_2 sites in our modeling. Finally, one can calculate the mean DAP recombination lifetime by applying Eq. (5.29).

$$\tau_{\mathrm{dap}}=\frac{\sum_j(\tau_{\mathrm{dap}}^{j})^2}{\sum_j \tau_{\mathrm{dap}}^{j}} \tag{5.29}$$

5.4 Recombination channels in nitrogen-boron co-doped *n*-type 6H-SiC

The photon decay profiles (represented by TCSPC histograms) of sample BK and SN-1/2 characterized by the TRPL system are plotted in Fig. 5.3. Since we measured multiple points on each sample as mentioned in Subsec. 5.1.3, the scattered dots shown in each plot of Fig. 5.3 designates the averaged time-resolved photon counts. The smooth decay curve for each sample represents the multi-exponential fitting of the corresponding experimental data, where a four-phase fitting $(y_0+\sum_n^4 A_n \exp(-t/t_n))$ was applied for BK and a three-phase fitting $(y_0+\sum_n^3 A_n \exp(-t/t_n))$ was applied for the two f-SiC samples (SN-1/2).

5.4.1 Two particular decay channels in bulk 6H-SiC

In this subsection, we will discuss the origins regarding the fastest ($t_1 = 3$ ns $\mid$ $A_1 = 56.1\%$) and slowest (($t_4 = 4.801$ μs $\mid$ $A_4 = 1.2\%$)) decay channels in sample BK. For the fastest decay channel, it is suggested that the related carrier dynamics might be influenced by both Auger Recombination (AR) and Bimolecular Recombination (BR)[119]. The carrier lifetime regarding AR or BR is strongly dependent on free carriers density (*i.e.*, n_0, for n-type sample) when the injection level is quite low, *i.e.*, $g \ll n_0$. The carrier lifetime of AR can be expressed by $\tau_{\mathrm{AR}} = 1/\left(\gamma_e n_0^2\right)$, where γ_e represents the AR coefficient for electron-electron-hole recombination dominated

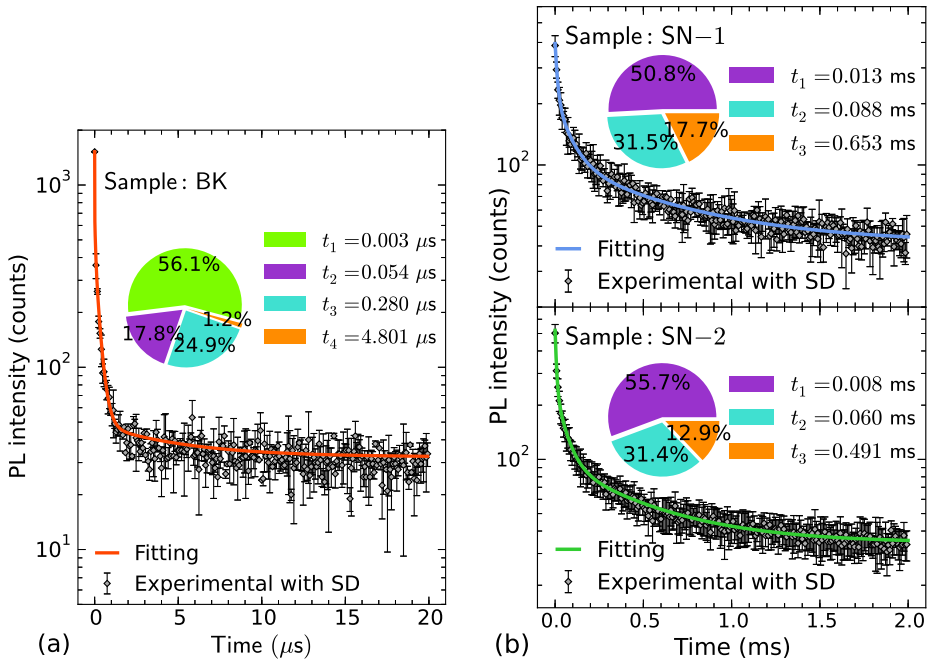

Figure 5.3: The TCSPC histograms representing the TRPL measurement results of (a) BK and (b) SN-1/2. For the measured data, the scattered dots denote the averaged time-dependent photon counts and the respective error bar indicates the standard deviation (SD). Two types of parameters, *i.e.*, the normalized amplitude (A_i) and time constant (t_i) (for each decay channel), which are extracted from the multi-exponential fittings, are summarized in the pie charts of each plots.

in *n*-type semiconductors. Note that the typical range of γ_e for 6H-SiC is around $(3.0 \pm 0.5) \times 10^{-29}$ cm^6.s^{-1}[120]. On the other hand, the carrier lifetime of BR can be expressed by $\tau_{\mathrm{BR}} = 1/(\gamma_B n_0)$, where γ_B denotes the BR coefficient typically with a range of $\times 10^{-11} \sim \times 10^{-12}$ cm^{-3}.s^{-1} for 4H-SiC[120, 121]. It is assumed that the value of γ_B for 6H-SiC should be comparable to that of 4H-SiC. Then the lifetime regarding the most decay channel in BK (channel 1) can be represented by the form of: $1/t_1 = 1/\tau_{\mathrm{AR}} + 1/\tau_{\mathrm{BR}}$[119], where the estimated and measured t_1 were found to be at the same order of magnitude. Although the estimated lifetime of the fastest decay channel in BK matches the related experimental value, further investigation is still required to confirm the origin of this recombination channel. In addition, we are still uncertain about the origin regarding the slowest decay channel in BK. Two potential explanations for the decay process in this channel have been ruled out. First, we have confirmed that the decay channel cannot be attributed to DAP recombination.

Fig. 5.4 summarizes our simulated relations between τ_{dap} and r_{dap} with 1%, 5%, and 10% to 100% (with 10% interval) of the injection level g allocated to the DAP recombination channel in sample BK, where the steady-state DAP recombination model introduced in Sec. 5.3 was implemented for the calculations. It is clear to see that the more portion of g is allocated to the DAP recombination channel, the shorter τ_{dap} is obtained. In Fig. 5.4, as we can see that τ_{dap} is predicted to be within 20 to 100 μs with 5% to 1% of g being allocated to the DAP recombination channel in BK, one can expect that the actual τ_{dap} for sample BK shall be close to 100 μs with $\sim$ 1.2% of g (see the pie chart of part (a) in Fig. 5.3) allocated to the fourth channel. Since the predicted carrier lifetime is far beyond the extracted value (4.801 μs) from the TRPL measurement results, it can be confirmed that the slowest decay channel in BK is not driven by DAP recombination. However, we do believe that there exists the decay channel in BK related to DAP recombination with the less portion of g (compared to the fourth decay channel) being allocated and accordingly the longer carrier lifetime compared to t_4, as we have obtained the weak PL spectra of sample BK (will be introduced latter in Sec. 5.5) where the N-B induced DAP recombination is found to be the dominant radiative recombination regime. The decay profile related to the DAP recombination channel in BK might become prominent in the longer term of photon decay which has exceeded the maximum time range of our TRPL system and the related TRPL intensity at the longer time points might be obscured by the background noise. On the other hand, we have also confirmed that the decay channel cannot be attributed to surface recombination. The expression of the fundamental surface recombination lifetime (τ_s)[122] is given as: $\tau_s = d^2/\left(D\pi^2\right)$ with d representing the sample thickness, and we have the diffusion constant $D = 2.5$ $\mathrm{cm}^2.s^{-1}$ for hole diffusion in 6H-SiC[123]. Hence we can estimate the shortest lifetime of surface hole diffusion in 6H-SiC to be: $\tau_s \approx 42.8$ μs, which is still an order of magnitude higher than the t_4 of sample BK.

5.4.2 Recombination channels corresponding to E_1/E_2 centers

For the implementation of the negative-U centers related carrier dynamics, we use Simulink (MathWorks, Inc.) for the execution of the simulations. All the parameters essential for triggering the carrier dynamics simulation in Simulink were inputted in a Matlab source code file (see Listing B in Appx. B. The original Simulink block diagram for the simulation is shown in Fig. B.1 (included in Appx. B). In order to have a more intuitive interpretation regarding the carrier dynamics simulation via Simulink, an additional block diagram abstracted from Fig. B.1 is also included which is shown in Fig. 5.5. From Fig. 5.5, we can see that the negative-U centers related carrier dynamics system in 6H-SiC is split into three parts which correspond to each E_i defects. The damping of the non-equilibrium electrons $\delta n_i(t)$ and holes $\delta p_i(t)$ as well as the changing regarding the *ground state* of E_i (*i.e.*, $\delta N_i^-(t)$, which is re-expressed as $\delta N_i(t)$ in Fig. 5.5 for simplicity) can be simulated in real time. By combining Eq. (5.13) and Eq. (5.14), an iterative system can be built for each E_i

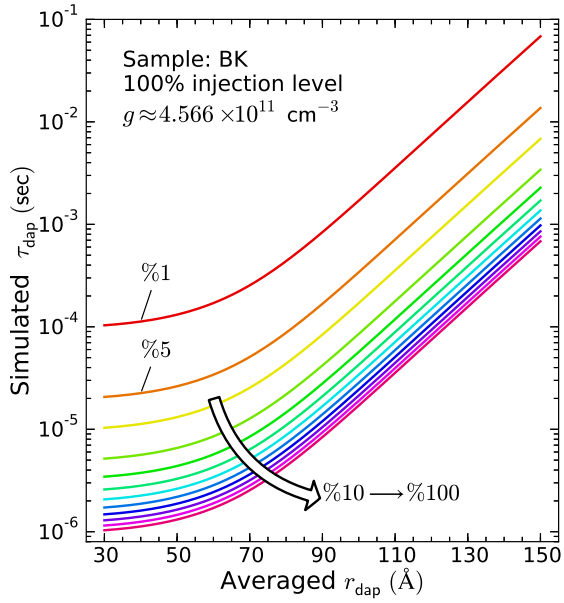

Figure 5.4: A set of calculated τ_{dap} with regard to different r_{dap} for sample BK, where the 1%, 5%, and 10% to 100% (with 10% interval) of the injection level g are allocated to the DAP recombination channel in sample BK.

related carrier dynamics. There are two inputs essential for the initialization of the model, *i.e.*, the densities of each E_i centers (*i.e.*, $N_{u,i}$, see Eq. (5.4)) and the initial densities of the non-equilibrium carriers allocated for the corresponding recombination channels ($\delta n_i(0)$, $\delta p_i(0)$). The model was numerically solved by applying the built-in Bogacki-Shampine method[124](fixed time step mode, 10 ps per step).

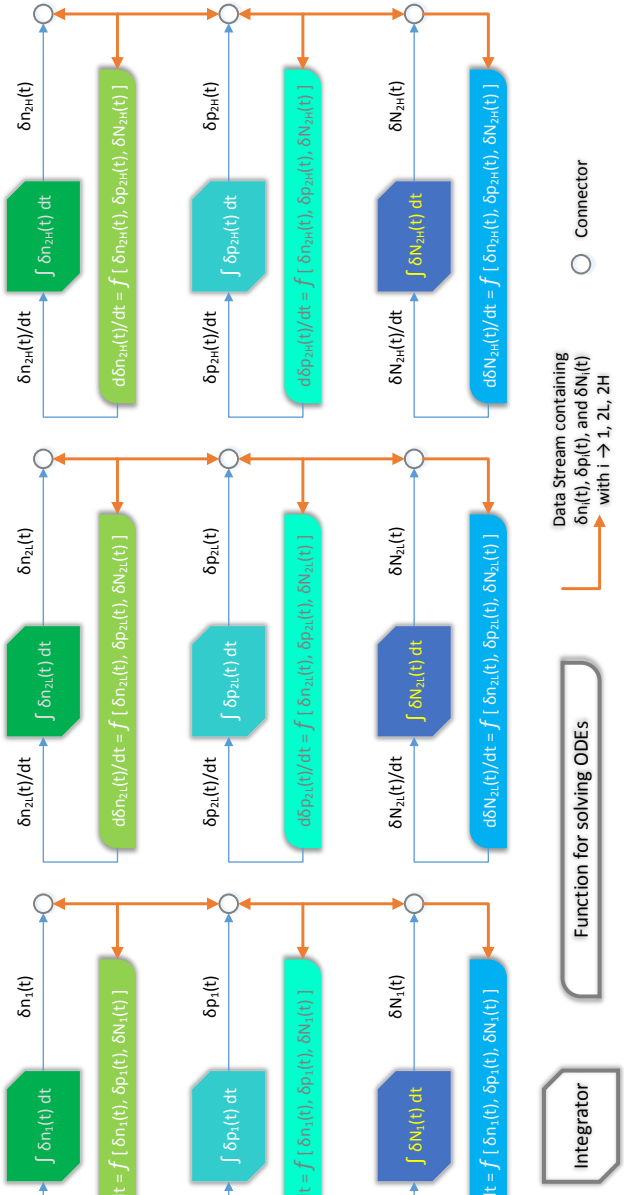

Figure 5.5: The block diagram abstracted from the complete Simulink block diagram regarding the simulation system of the negative-U centers related carrier dynamics in 6H-SiC (as shown in Fig. B.1). The system consists of three dependent parts which describe the carrier dynamics of E_1, E_{2L}, E_{2H} defects, respectively. Each part contains three integrators and the corresponding function blocks for solving the related ordinary differential equations (ODEs). It can be seen that by implementing the carrier dynamics model introduced in Sec. 5.2, the time differential of either $\delta n_i(t)$ or $\delta p_i(t)$ or $\delta N_i^-(t)$ can be expressed by the function including all themselves.

Regarding the multi-exponential fittings of the measured TRPL decay curves of sample BK and SN-1/2 shown in Fig. 5.3, we believe that there are two of recombination channels for each sample corresponding to the negative-U centers related carrier dynamics, where one of the recombination channel is for the carriers trapping by E_1 centers (hexagonal) while the other channel is for same process on E_{2L} or E_{2H} center (cubic). As pointed out by Ikeda *et al.*[54] that in 6H-SiC the ratio between the densities of nitrogen-induced donors on hexagonal- and cubic-sites might be equivalent to the ratio of between the total densities of hexagonal- and cubic- lattices, that is, $N_h : N_c \approx 1 : 2$. Likewise, it is reasonable to consider that the ratio between the densities of E_1 (on h-sites) and E_2 (on c-sites) (E_{2L} and E_{2H} together) should be roughly equal to 1:2 as well or at least the density of E_2 should be larger than that of E_1. Therefore, for those two channels corresponding to carriers trapping on E_1/E_2 centers, we suggest that the channel with larger amplitude, which indicates larger "load capacity" of non-equilibrium carriers, should correspond to E_{2L} and E_{2H} center. Furthermore, it is also assumed that E_{2L} and E_{2H} shall take over the same amount of non-equilibrium carriers for simplicity, therefore the expression for the estimation of E_{2L} and E_{2H} should be slightly different from Eq. (5.4) and we have: $N_{u,2L}, N_{u,2H} = 2/\left[(\sigma_{2L,h} + \sigma_{2H,h})\langle\nu_{th,h}\rangle\tau_2\right]$, where τ_2 denotes the time constant of E_2 related recombination channel extracted from experimental TRPL result. For sample BK, we believe its second and third decay channels are associated with negative-U centers related carriers trapping. On the other hand, there are three decay channels attributed to either of the two f-SiC samples SN-1/2, where the first and second channels for either SN-1/2 are related to the carrier dynamics of E_1/E_2 centers. In addition, the third decay channels in SN-1/2 were correlated to the DAP recombination. It is worthy to mention that we did not attribute any of the recombination channels in SN-1/2 to surface recombination process. Since researchers[125–127] have found that for f-SiC samples, under low injection levels ($g \ll N_a$), the non-equilibrium carriers would be hindered by the space charge field induced by acceptors which further makes the diffusion coefficient to be negligible. Hence the fundamental surface recombination lifetimes[122] for our f-SiC samples shall be much longer than any of the extracted lifetimes from the experimental TRPL results.

By giving the estimated densities of E_i and the initial non-equilibrium carriers densities $\delta n_i(0) \mid \delta p_i(0)$ allocated to E_i-related recombination channel, one can trigger the simulation system of negative-U centers related carrier dynamics depicted in Fig. 5.5 and gather the real time $\delta n_i(t)$, $\delta p_i(t)$, and $\delta N_i^-(t)$ as well as their differential values. In addition, the time-dependent minority carrier lifetimes $\tau_p, i(t)$ can be extracted as well by using Eq. (5.15). The simulated $\delta p_i(t)$ for each E_i are summarized in Fig. 5.6 together with the experimental decay profiles related to E_1/E_2 carrier dynamics, and Fig. 5.7 shows all the calculated minority carrier lifetimes. Recapping what we have mentioned in Subsec. 5.2.3 that at low injection level, the minority carriers density is proportional to the TRPL intensity, *i.e.*, $I(t) \propto \delta p(t)$, hence for the recombination channel dominated by E_1/E_2 carrier dynamics, the related TRPL decay profile extracted from the multi-exponential fitting should have the same line shape as that of the simulated damping of non-equilibrium holes on E_1/E_2 centers.

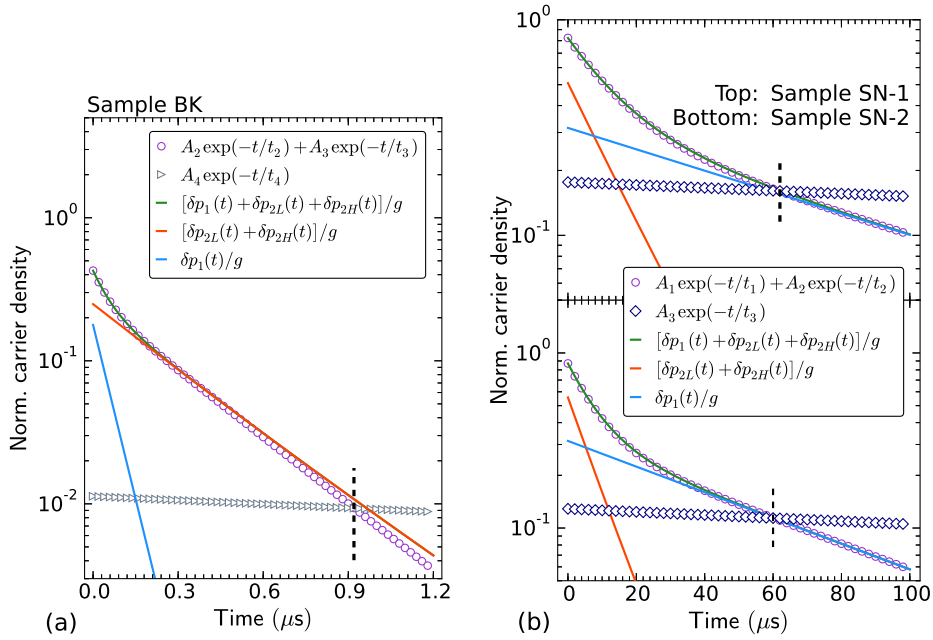

Figure 5.6: The decay profiles (extracted from experimental TRPL) and simulated minority carriers damping related to E_1/E_2 carrier dynamics. For both (a) and (b), the experimental decay profiles (with normalized amplitudes) related to the E_1/E_2 carrier dynamics, *i.e.*, the 2$^{\text{nd}}$ and 3$^{\text{rd}}$ channel in BK and the 1$^{\text{st}}$ and 2$^{\text{nd}}$ channel in SN-1/2, are designated by open circles. The open triangles in (a) represent the normalized 4$^{\text{th}}$ decay profile in BK. The open squares in (b) denote the normalized 3$^{\text{rd}}$ decay profile (DAP channel) in SN-1/2. All the related A_n and t_n were extracted from Fig. 5.3. The three curves for each sample represent the simulated time-dependent non-equilibrium hole densities corresponding to E_1-, E_2-, and the overall E_1/E_2-related carrier dynamics, respectively.

From Fig. 5.6 we can see that our calculated minority carriers damping for each sample matches quite well to the respective experimental TRPL decay profiles. Hence the results shown in Fig. 5.6 confirm that E_1/E_2 related carrier dynamics in these 6H-SiC samples is indeed responsible for the carriers trapping of the related fast decay channels, *i.e.*, the 2_{nd} and 3_{rd} channel in BK and the 1_{st} and 2_{nd} channel in SN-1/2. On the other hand, the minority carriers damping was predicted to be a bit slower compared to the corresponding fitting curve for sample BK, this might be caused by the unconfirmed defects in BK where they could be midgap centers[128] for instance. For the calculated lifetimes of the non-equilibrium holes related to different charge state transitions shown in Fig. 5.7, we can see that the hexagonal- and cubic-site related non-equilibrium h^+ lifetimes are almost time-independent indicating the constant carriers damping rates. In addition, we also calculated the hole lifetimes related to the charge state transitions of $E_i^- \rightarrow E_i^0$ and $E_i^0 \rightarrow E_i^+$ by Eq. (5.30), where Q refers to *-/0* or *0/+*. The time-dependent $\tau_p^{-/0}$ and $\tau_p^{0/+}$ for each samples are also included in Fig. 5.7. It is obvious to see that the -/0 transition (ground state $\rightarrow$ intermediate state) dominates the hole capture process, where $\tau_p^{-/0}(t)$ is almost equivalent the overall minority carrier lifetime for each sample. On the other hand, the extracted hole lifetime regarding 0/+ transition $\tau_p^{0/+}(t)$ (intermediate state $\rightarrow$ empty state) is found to be five to six orders of magnitude higher than $\tau_p^{-/0}(t)$ for each sample. As we have mentioned in Subsec. 5.2.1 that the electron capture regarding +/0 transition (empty state $\rightarrow$ intermediate state) is treated as a fast cascade process, where transition rate for +/0 process (electron capture) might be much higher than that of the opposite 0/+ process (hole capture). It is considered that the +/0 transition might hinder its opposite process, *i.e.*, the 0/+ transition to a large extent, where the density of E_i^+ might be much lower than that of E_i^0 at anytime during the whole E_1/E_2 related carriers trapping process. Therefore, the quite low efficiency regarding 0/+ transition would lead the related hole carrier lifetime, *i.e.*, $\tau_p^{0/+}(t)$, to be fairly low. In addition, it has been revealed by *first-principles* calculations on SiC[101] that for strong n-type SiC where its E_F is close to E_c, the negative-U system would prefer to keep its carbon vacancies being at neutral charge states (*i.e.*, E_i^0) at thermodynamic equilibrium.

$$\tau_p^Q = \left[\sum_i |R_{i,h}^Q| / \delta p(t) \right]^{-1} \tag{5.30}$$

5.5 Static PL intensity affected by E_1/E_2 centers

5.5.1 Comparison between f-SiC and bulk 6H-SiC

The static mean PL intensity spectra at RT for all three samples are summarized in Fig. 5.8. It is revealed that the averaged PL intensities of SN-1 and SN-2 are roughly

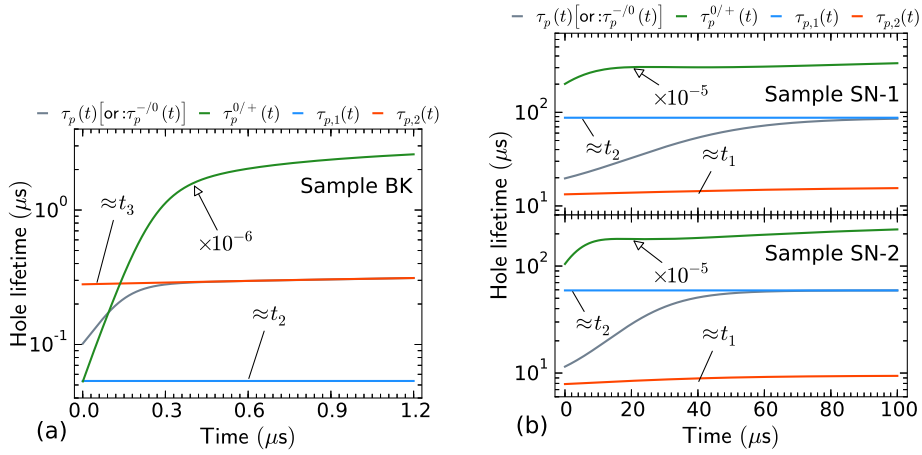

Figure 5.7: Calculated time-dependent minority carrier lifetimes for each sample including the hole lifetimes in the recombination channels related to E_1 and E_2 (E_{2L} and E_{2H} together) centers. The non-equilibrium hole lifetimes regarding the two charge state transitions, *i.e.*, -/0 and 0/+, are extracted from the carrier dynamics simulations as well.

60 and 40 times higher than that of BK, respectively. Since E_1/E_2 centers have been commonly regarded as the contributors of the non-radiative recombinations in 6H-SiC and the carrier lifetime killers[79], it is believed that the much lower PL intensity in BK is due to its much higher E_1/E_2 compared to SN-1/2, where the total E_1/E_2 density (*i.e.*, N_u) in BK is estimated to be two orders of magnitude higher than that of SN-1/2, as shown in Tab. 5.1. It is intuitive to understand why more E_1/E_2 centers would cause less PL intensity, as the increase of E_1/E_2 density in 6H-SiC will increase the "load capacity" of the related non-radiative recombination channel, which causes less non-equilibrium carriers allocated to DAP recombination channel and eventually less radiative recombination events. Here we would like to discuss the estimation of the internal quantum efficiency (IQE) of all three samples based on our experimental TRPL measurement results, where the contrast on the IQE should be similar to the contrast on the static PL intensities. We adopted a simple equation derived from Ref. [2] for the evaluation of IQE in 6H-SiC where we have: $\eta_{\text{int}} = 1/(1 + \tau_A/\tau_{\text{nr}})$ with τ_A and τ_{nr} indicating the lifetimes of non-equilibrium hole relaxation and general non-radiative recombination, respectively. Note that τ_A is essentially equivalent to the hole lifetime τ_p in this research. Since there exists two non-radiative recombination channels (channel 1&2) for f-SiC samples, we implemented $1/\tau_{\text{nr}} = 1/t_1 + 1/t_2$ as well as $\tau_{\text{dap}} = t_3$ and got the values of IQE around 1.7% and 1.4% for SN-1 and SN-2, respectively. For sample BK, as we have discussed in Subsec. 5.4.1 that its DAP lifetime must be quite long and beyond the detection limit of our experimental TRPL

setup, the contrast between the DAP lifetime and overall non-radiative lifetime for BK should be much more significant causing much lower IQE compared to SN-1/2.

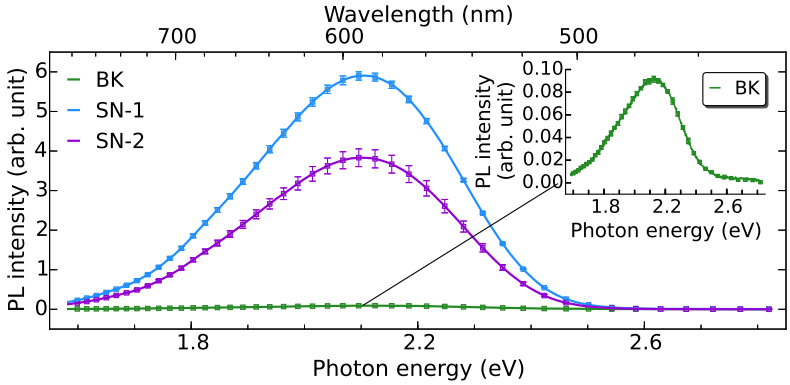

Figure 5.8: The PL intensity spectra (time-integrated) for BK and SN-1/2. The solid curves designate the averaged PL intensities for each samples. Each error bar represents the standard deviation (SD) regarding the averaged intensity of the emitted photon at a certain wavelength.

5.5.2 Comparison between the f-SiC samples

Conventionally, the decay profile regarding the photon emission via DAP recombination is modelled in a form of t^{-m}[129] instead of a single exponential decay, where m denotes the power factor (less than zero) over the decay time t. However, this model is more applicable to describe the DAP-related decay profile under high injection level with quite short DAP lifetime, where a rapid photon decay accompanied with dramatic increase of r_{dap} is expected. Instead, if we treat the DAP-related decay profile under low injection level as the part of the decay profile under high injection level with the initial time period for rapid DAP recombination has passed, *e.g.*, the time point corresponding to the inflection point of t^m has passed. Since at longer time period, exponential decay function is much more sensitive to decay time compared to power law decay function (*i.e.*, t^m), in this research, we treated the photon decay related to DAP recombination channel in 6H-SiC at low injection level as single exponential decay where the decay profile is mainly determined by its time constant, *i.e.*, DAP lifetime. A steady-state DAP recombination model which has been introduced in Sec. 5.3 was applied for the estimation of the DAP recombination lifetime of SN-1/2. The related Matlab code for the calculation of τ_{dap} regarding a certain range of r_{dap} is shown in Listing C in Appx. C. The simulated relations between τ_{dap} and r_{dap} for SN-1/2 are depicted in Fig. 5.9. By matching the measured DAP lifetime (t_3 for SN-1/2, see Fig. 5.3) to the simulated τ_{dap} which is dependent on r_{dap}, we revealed

that the average DAP separation distances (r_{dap}) are ×3.79 and ×3.54 of the average Bohr radius of donors for SN-1 and SN-2, respectively. Here, as SN-2 is revealed to have shorter r_{dap}, this indicates SN-2 has denser DAP thanks to its higher doping concentration compared to SN-1. In addition, from Eq. (5.26) we can see that the increase of r_{dap} would decrease DAP transition probability and longer τ_{dap}[116, 129], this agrees well with the comparison between SN-1/2. However, the higher DAP transition probability of SN-2 did not induce higher PL intensity compared to SN-1, this because of higher density of E_1/E_2 centers in SN-2. As shown in Fig. 5.9, it is found that SN-1 has higher normalized amplitude ($A_3 = 17.7\%$) regarding its DAP recombination channel compared to SN-2 ($A_3 = 12.9\%$), which cause SN-1 to have nearly 50% higher (see Fig. 5.8) PL intensity than that of SN-2.

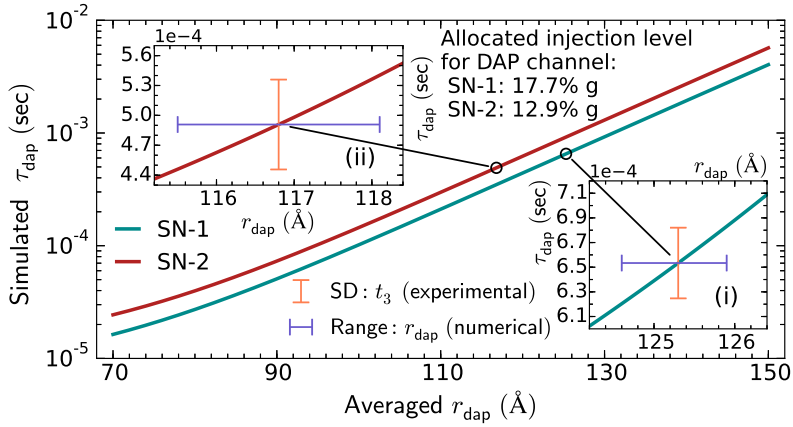

Figure 5.9: Calculated relations between r_{dap} and τ_{dap} for SN-1/2. The experimental τ_{dap} (*i.e.*, t_3 for SN-1/2 in part (b) of Fig. 5.3) are located in the main plot accompanied with the predicted r_{dap}. The standard deviations (SD) regarding the measured τ_{dap} and calculated r_{dap} for each sample are marked up in the respective insets.

5.5.3 Discussion: E_1/E_2 density vs. epilayer growth

It is commonly believed that the density of E_1/E_2 defects is strongly influenced by the C/Si ratio during the crystal growth. As Kimoto et al.[130, 131] have observed the strong decrease of the Z_1/Z_2 centers in 4H-SiC by increasing the C/Si ratio. Latter on, Huh et al.[132] have also observed the similar trend in 6H-SiC. To be specific, they observed ∼80% decrease of the density of the E_1/E_2 centers when increasing the C/Si ratio from 0.065 to 0.25. According to the FSGP method, the relation between the Si/C ratio and the growth ambient temperature on both Si-face and C-face is shown in the Figure 8 of Ref. [6]. Note that it is crucial to keep Si/C>1 by using FSGP

method in order to ensure the sufficient growth rate. Hence the C/Si ratio in this situation could be only optimized within 0.1 to 1. However, when the value of C/Si ratio tends to unity the temperature will exceed 2300°, causing the probability of graphitization being quite high. Fortunately, the graphitization can be suppressed by introducing Ta foil in the growth system[133] where the related technique has already been introduced in Subsec. 2.3.1. Another possible method for reducing E_1/E_2 density is to introduce hydrogen gas into the growth ambient[134] which could shift the stoichiometry towards higher C/Si ratio. However, there is a side-effect of increasing the C/Si ratio. As the DAP recombination is the dominant radiative recombination regime in f-SiC where its efficiency is dependent on the density of the D-center, it has been found that[74, 135] the inclusion of D-center can be decreased strongly with the increasing C/Si ratio. On the other hand, researchers have also observed the indication that the inclusion of the negative-U centers might come along with the N-doping[136]. Furthermore, despite the fact that the concentration of the nitrogen dopant in f-SiC should be kept high enough ($> 10^{18}$ cm^{-3}) to ensure the large density of DAP recombination[2], the nitrogen doping still requires further study to narrow down its range. To summarize, the growth control of f-SiC using FSGP method, *e.g.*, the C/Si ratio and the nitrogen doping, is still required to seek for the new balance between the densities of the E_1/E_2 defects and the D-center.

5.6 Post-analysis of the 6H-SiC samples

In the aforementioned experimental characterizations and modellings we have excluded the influences from other potential impurities on the 6H-SiC samples, where normally during the growth of the bulk and the epilayer (by sublimation method)-SiC several kinds of impurities can be induced, *e.g.*, Vanadium could be an effective recombination center in-SiC. In addition, as we have assigned the same value of the injection level g for both f-SiC and bulk-SiC samples, the difference on the surface roughness of the samples has been ignored. In order to confirm that our simplification for the modelling on N-B co-doped 6H-SiC is reasonable, two sets of experiment are designed for the post-analysis of our samples.

5.6.1 Investigation of additional impurities

The common impurities which are unintentionally doped in 6H-SiC include Oxygen (O), Titanium (Ti), Cobalt (Co), Vanadium (V) and Chromium (Cr). The pure O-impurity in-SiC normally could not form deep centers for non-equilibrium carrier recombination. Even for the O-related complexes in 6H-SiC, which have to be formed by intentional O^+ implantation, could not correspond to the specific PL lines[137]. On the other hand, for the epilayer of 6H-SiC sample, normally the density of O-impurity is quite low (typically $< 10^{12}$ cm^{-3})[18]. Normally, Ti-related centers induce radiative recombination, leading to strong greenish luminescence[138], where the Co-doped 6H-SiC induces two unique PL peaks at 370 nm and 413 nm, respectively[139].

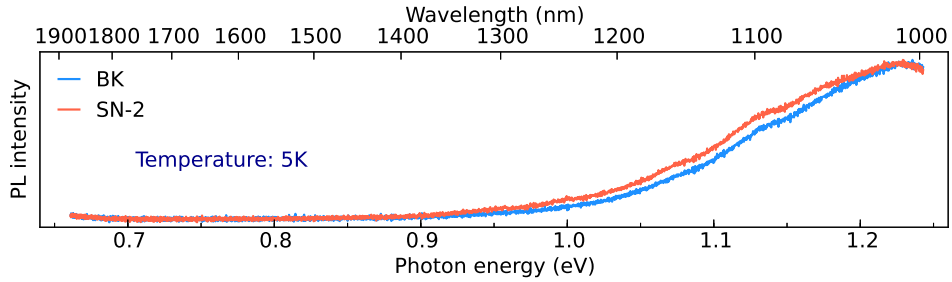

Figure 5.10: Photoluminescence intensity of sample BK and SN-2 at 5 K. A 405 nm diode laser was implemented as the excitation source. The laser power was set to 93.7 mW and the related integration time was 10 sec, indicating that the PL intensities at infrared spectral range were quite weak for both samples.

But none of them are shown in our PL. Further evidences which can prove that no prominent inclusion of V and Cr impurity in our samples were presented in Fig. 5.10, where the low temperature (T=5 K) near-infrared PL spectra of both bulk substrate and f-SiC were shown. We can see that the two zero phonon lines related to intra-center transition of V in the hexagonal and quasi-cubic sites at 0.9 eV to 1.0 eV range[140] were not presented in our PL measurement results. In addition, three strong zero phonon lines around 1.15 eV to 1.19 eV[141] caused by Cr-doping were not presented in the PL spectra of our samples either. To conclude, there is no prominent inclusion of the above mentioned five types of impurities, hence these impurities do not play an important role in the carrier dynamics in the samples included in this study. Additionally, it is worthy mentioning that the source material applied for f-SiC epilayer growth, was grown by the modified physical vopor transport (M-PVT) method[10]. As already mentioned in Subsec. 2.3.2, in the experimental setting of the M-PVT method, an additional gas pipe is implemented in the crucible to transfer the gas phase impurities for doping which reduces the unintentionally-doped impurities significantly.

5.6.2 Surface roughness test

We are aware that PL is dependent on the surface roughness by two folds: excitation power and extraction of emitted light. The following reflectance measurement results on the three samples show that differences in reflectance between BK and SN-1/2 samples due to surface roughness is much smaller than the corresponding differences of PL intensities. The measurement results related to the reflectance of all three samples were summarized in Fig. 5.11 where both the integrating sphere (in (a)) and the goniometer with an indicent angle of 10° (in (b)) were applied. Note that the incident angle for the integrating sphere system is also 10°. We can see that the reflectance of bulk substrate and f-SiC samples generally in the range of 0.24

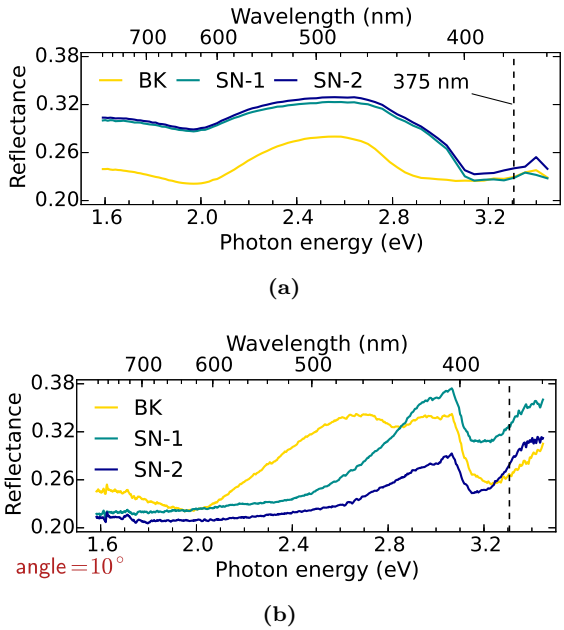

Figure 5.11: The reflectance measurement results of sample BK, SN-1&2 by using: (a) an integrating sphere (OL 700-71 6-Inch Integrating Sphere); (b) a goniometer with an incident angle of 10°. Note that the white light Xenon lamp was applied as the excitation source for both measurements.

to 0.34. We further summarized the reflectance measurement results by goniometer (incident angle: 10° to 45°) in Fig. 5.12, where the standard deviation on reflectance ($\sigma_{\text{reflectance}}$) of these three samples with different incident angles were shown. It can be seen that according to the reflectance measured by both integrating sphere and goniometer, the difference on the reflectance *at 375 nm* between BK and SN-1/2 is always kept in the same magnitude. This indicates that the surface roughness is not the dominant cause of their great differences on the PL intensity. Another evidence which can prove that the surface roughness of the 6H-SiC (BK or SN-1/2) sample would not vary so much can be also found in Ref. [142]. The article was about increasing the PL intensity of the as-grown f-SiC by forming nanopillar structure on the sample surface. After the flat sample has been processed to form nanopillars on the surface, the PL intensity has been increased by 55% but still far smaller than the contrast (i.e., >40 times difference) on the PL intensity between the f-SiC sample and the bulk substrate reported in this thesis.

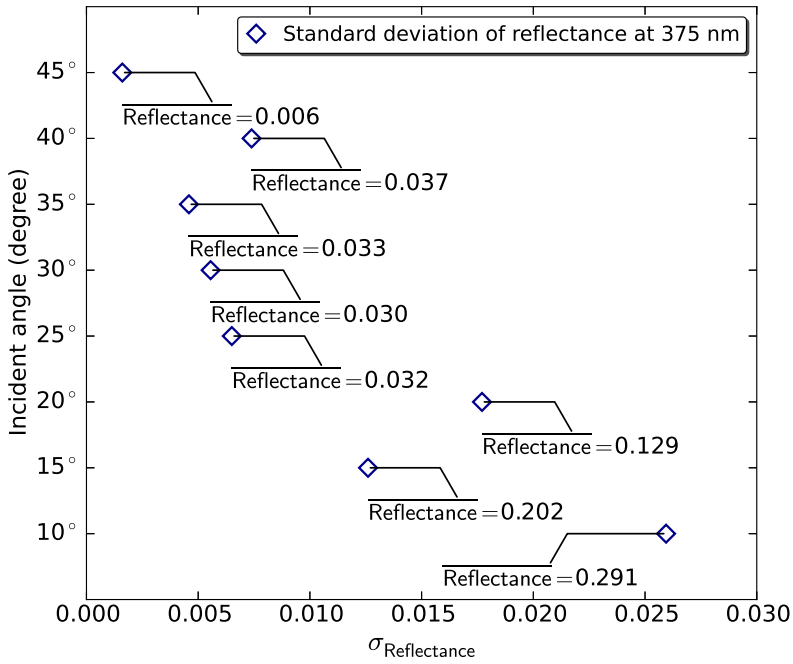

Figure 5.12: The standard deviation on reflectance ($\sigma_{\text{reflectance}}$) of sample BK, SN-1&2 with different incident angle from 10° to 45°, where the respective mean value of the reflectance ($\overline{\text{Reflectance}}$) at each incident angle has been marked.

5.7 Summary

In this research, we have launched room temperature (RT) time-resolved photoluminescence (TRPL) measurements on two fluorescent silicon carbide (f-SiC) samples SN-1/2 as well as a bulk 6H-SiC substrate (sample BK). By applying multi-exponential decay fittings on the measured photon decay curves, it is revealed that there are three | four recombination channels in SN-1/2 and BK, respectively. The simulations based on a negative-U centers related carrier dynamics model have confirmed that there are two recombination channels for each sample related to carriers trapping on E_1/E_2 centers where E_1/E_2 centers are the common negative-U centers in 6H-SiC. It is found that the density of E_1/E_2 defects in BK is two orders of magnitude higher than that of SN-1/2, which causes negligible PL intensity in BK compared to SN-1/2. A steady-state DAP recombination model is applied to study the relation between DAP separation distance (r_{dap}) and DAP lifetime (τ_{dap}) under low injection level in f-SiC samples, where the simulation results have enabled us to confirm that although SN-2 has slightly higher DAP transition probability than that of SN-1, its PL intensity is still lower because of slightly higher E_1/E_2 density compared to SN-1. This

indicates the densities of E_1/E_2 are crucial for the determination of the IQE of f-SiC samples. For sample BK, its fastest decay channel might be jointly influenced by Auger Recombination (AR) as well as Bimolecular Recombination (BR). In addition, due to the limitation of our current experimental TRPL setup, we were unable to extract the DAP lifetime of BK which is expected to be quite long. We have also discussed how to decrease E_1/E_2 density during the crystal growth of f-SiC samples. It is found that the increase of *D*-center, which is crucial for the enhancement of DAP recombination in f-SiC, is accompanied by the inclusion of E_1/E_2 defects. In addition, the density of E_1/E_2 is found to be sensitive to C/Si during the crystal growth. A further-optimized trade-off regarding the adjustment of the growth parameters of f-SiC is required for the improvement of the internal quantum efficiency (IQE).

CHAPTER 6

Photoluminescence quantum yield of 6H f-SiC

As introduced in Chapter 1, the proposed new white LED consists of the SiC bilayer, *i.e.*, the N-B co-doped and the N-Al co-doped f-SiC, integrated with the nitride-based NUV LED. By optically pumping the SiC bilayer with the nitride-based NUV LED for PL excitation, the white light emission with high CRI can be achieved by the color mixing of the orange-yellowish and blue-greenish light from N-B and N-Al co-doped SiC layer, respectively. It is worth noting that the proper control of the intensity ratio of the two PL spectra from the SiC bilayer with different DAP recombination regimes is crucial for the high CRI white light generation. In fact, the intensity ratio of those two set of PL emitting out of the device depends on two factors. One is the stacking sequence of the SiC bilayer, while the other is the photoluminescence quantum yield (PL-QY), *i.e.*, the ratio of the emitted photons to the incident photons, of the respective SiC single layer. As the N-Al co-doped SiC is still under development, it is essential to determine the PL-QY of f-SiC, where the PL-QY of N-Al co-doped SiC layer needs to match the former in turns of the bilayer stacking sequence as well as the thickness of either single layer. On the other hand, if we assign η_{NUV}, $\eta_{\text{N-Al}}$ and $\eta_{\text{N-B}}$ as the EQE of the nitride-based NUV LED, N-Al co-doped SiC and f-SiC, respectively, the EQE of the device is the product of those three efficiencies, *i.e.*, $\eta_{\text{device}} = \eta_{\text{NUV}} \times q_1 \times \eta_{\text{N-Al}} \times q_2 \times \eta_{\text{N-B}}$. Note that $q_1 \mid q_2$ indicates the portions of NUV light absorbed by each SiC layers. Here, the EQE of f-SiC ($\eta_{\text{N-B}}$) is actually represented by its PL-QY since f-SiC is the light source which needs optical pumping. Therefore knowing the PL-QY of f-SiC is of great importance for the evaluation of the upper limit of the EQE of the entire white LED device. In this chapter, we demonstrate the experimental methodology regarding to the determination of the PL-QY on *n*-type f-SiC samples. In addition, we also give the explanation for the physical mechanism corresponding to the incident power dependent PL-QY of f-SiC.

6.1 Overview

6.1.1 Determine PL-QY by integrating sphere

There are two categories for the PL-QY measurement on a fluorescent material, *i.e.*, the relative and absolute techniques[143]. For the relative technique, a standard f-SiC

sample is needed where its PL-QY is already known. It is required that the standard f-SiC should have similar excitation, absorption and emission properties as the sample to be measured. Since it is difficult to fully duplicate the experimental condition where the reference spectra of the standard f-SiC are measured in our lab, in this research, we adopt the absolute techniques for the PL-QY measurements. As f-SiC is a solid thin film sample with high refractive index, the issues of anisotropic light emission and wave-guiding effects[144] could greatly affect the accuracy of the results of PL-QY measurement. A direct solution might be mapping the light emission to the solid angle distribution where the ratio of the detected PL emission to the whole PL emission can be determined by referring the experimental conditions related to PL excitation | detection. However, this solution is quite cumbersome and not so viable where heavy workload is required and the interval of the solid angle needs to be carefully chosen. On the other hand, integrating sphere has been recognized as the standard equipment for measuring the PL-QY of solid thin films[145, 146]. By implementing integrating sphere into PL-QY measurements, all the reflected and emitted light can be collected where the concern regarding to the angular dependence of the PL emission is no longer needed. Therefore, the integrating sphere based measurement system has been widely applied in the determination of PL-QY of solid thin films[144, 146–149]. The basic theory of integrating sphere has been introduced in Subsec. 3.4.1.

6.1.2 Two-measurements approach

There are two types of methodology based on integrating sphere system for absolute determination of PL-QY[150], *i.e.*, three-measurements[144, 147, 151] and two-measurements[148, 152, 153] approaches. In fact, the two-measurements approach proposed by Johnson *et al.*[148] was derived from the three-measurements developed by de Mello *et al.*[144]. The schematic diagram of the two-measurements approach is shown in the (a) & (b) of Fig. 6.1. It involves two sets of characterizations, *i.e.*, (a) without fluorescent sample and (b) with fluorescent sample being optically pumped. While the only difference between the two-measurements and three-measurements is that the latter approach contains one more set of characterization, *i.e.*, the incident light being off the direction towards the fluorescent sample as shown in Fig. 1(b) of Ref. [144]. Leyre *et al.*[150] have theoretically proved that the values of the PL-QY determined by those two approaches are identical. In the (c) of Fig. 6.1, assuming no overlap between the excitation and emission spectrum, L_a | L_c designate the integrated luminescence intensity of the incident excitation beam recorded with|without the fluorescent sample being placed inside the integrating sphere, respectively, and P_c represents the integrated PL intensity of the fluorescent sample. Note that the above mentioned notations of the integrated luminescence intensities are adopted from de Mello *et al.*[144]. The value of the PL-QY denoted by η_{PL} with the two-measurements approach is formulated by Eq. (6.1). In addition, the evaluation of the relative uncertainty of the two-measurements approach is given by Eq. (6.2), where U_{L_a}, U_{L_c} and U_{P_c} represent the relative uncertainty of L_a, L_c and P_c, respectively.

$$\eta_{\mathrm{PL}} = \frac{P_c}{L_a - L_c} \tag{6.1}$$

$$U_{\mathrm{PL}} = \left[U_{P_c}^2 + \left(\frac{L_a}{L_a - L_c} U_{L_a} \right)^2 + \left(\frac{L_c}{L_a - L_c} U_{L_c} \right)^2 \right]^{0.5} \tag{6.2}$$

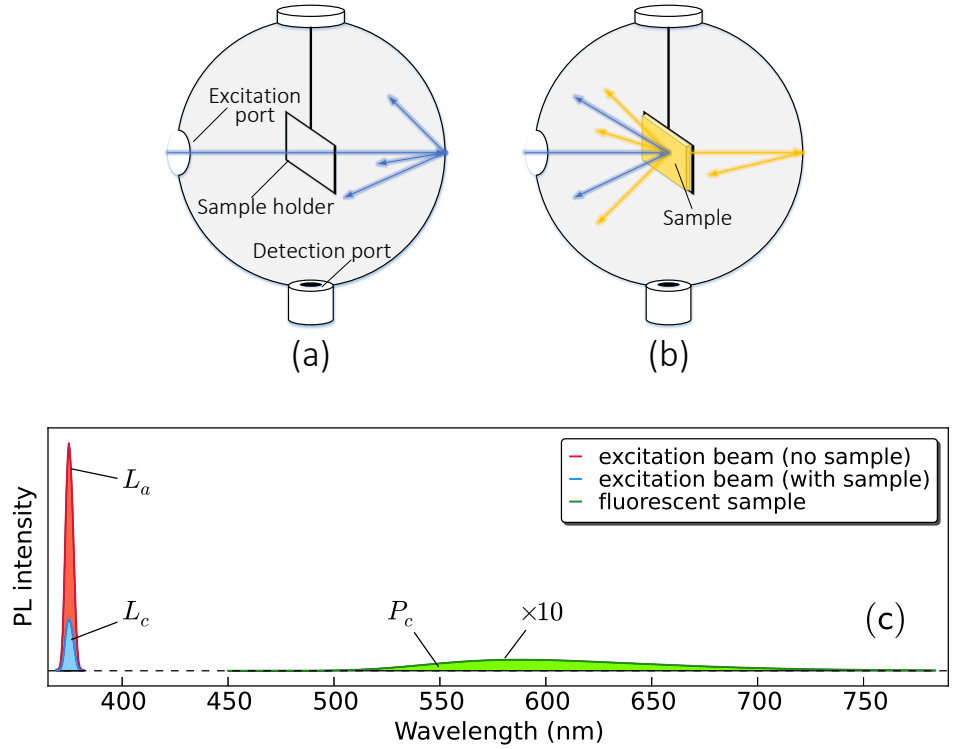

Figure 6.1: (a) without sample and (b) with sample mounted, where the sample is placed in the center of the integrating sphere. (c): three essential spectra obtained from the PL-QY measurement which are: the spectrum of laser source under the experimental configuration shown in (a), where L_a designates its integrated luminescence intensity; the spectrum of laser source using the test scheme shown in (b), where the related integrated luminescence intensity is represented by L_c; the PL spectrum of the sample with the integrated PL intensity labelled as P_c. Note that the latter two spectra are recorded simultaneously. The horizontal dashed line shown in (c) indicates the zero level of PL intensity.

The specifications related to the OL 700-71 6-inch diameter integrating sphere employed in this research for the determination of the PL-QY of the f-SiC samples have been introduced in Subsec. 3.4.2, the sample has to be placed towards the sample port on the edge of the integrating sphere. As a matter of fact, Leyre *et al.*[150] suggested that the two-measurements approach is preferred if fluorescent sample is being placed at the edge of integrating sphere. It is believed that for the extra characterization of the three-measurements approach, where the integrated source|PL intensities are designated by L_b and P_b, respectively, the P_b derived from solid thin film sample can be negligible if the following two factors are fulfilled. One factor is that the sample is placed at the edge of the integrating sphere where only one side of the sample can be excited by the diffused excitation source instead of the direct optical pumping. The other factor is that the area of the sample port, which limits the effective area of the sample capable of being excited, is quite small compared to the area of the entire diffuse wall. Regarding our PL-QY measurement setup, the sample is mounted on the edge of the integrating sphere. The effective area of the sample to be characterized is limited by the area of the port of the sample holder, where the diameter of the port is only 5 mm (∼0.2”). Therefore, we decided to adopt two-measurements approach in this research.

6.2 A solution for PL-QY determination of f-SiC

6.2.1 Experimental design

As the integrating sphere applied in our PL-QY measurements is different from the original one shown in the (a) & (b) of Fig. 6.1, we have developed a new experimental design based on the two-measurements approach where some modifications have been made. In fact, the PL emission from an fluorescent sample collected by an integrating sphere, where the sample is placed at the center of the sphere, can be divided into four aspects depending on the condition related to excitation and detection. The PL emission is considered to be collected under four conditions, *i.e.*, front-excitation-front-detection (FEFD), front-excitation-back-detection (FEBD), back-excitation-front-detection (BEFD) and back-excitation-back-detection (BEBD) as shown in Fig. 6.2. Note that we treat f-SiC sample, *i.e.*, f-SiC epilayer and 6H-SiC substrate, as a whole during PL-QY determination. Therefore the measured PL-QY can not represent the real PL-QY of the f-SiC epilayer, where the latter is expected to be lower than the former due to the absorption of excitation beam | PL emission by the substrate. Nevertheless, the evolution trend of the measured PL-QY can still represent that of the epilayer's actual PL-QY, *e.g.*, the trend along with the variation of the incident beam power. Back to the four aspects of the collected PL emission shown in Fig. 6.2, during the PL-QY determination on f-SiC samples, it was found that the luminescence intensity of PL_{BEBD} is almost undetectable. Two causes could account for this, one is the excitation beam has been largely attenuated when it reaches to the interface between f-SiC epilayer | 6H-SiC

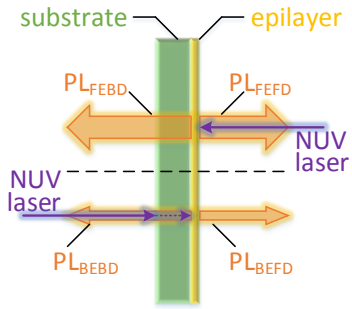

Figure 6.2: Four configurations related to the PL emission from a f-SiC sample (*i.e.*, f-SiC epilayer + 6H-SiC substrate), where the experimental configuration is derived from the PL-QY determination using an integrating sphere shown in the Figure. 6.1(b). As for the subscripts of the names of PL signals, "F", "B", "E" and "D" represent front, back, excitation and detection, respectively, where the front side of f-SiC sample refers to the side of epilayer.

substrate from backside, the other is the PL emission from the above mentioned interface has been also attenuated when it propagates through the 6H-SiC substrate. Hence there are altogether five types of luminescence spectrum required, *i.e.*, the spectra of the original and attenuated excitation beam without | with sample presented, and $\mathrm{PL_{FEFD}}$ | $\mathrm{PL_{FEFD}}$ | $\mathrm{PL_{FEFD}}$, in order to extract sample's PL-QY. Fig. 6.3 shows the experimental design based on the OL 700-71 6-inch diameter integrating sphere for the PL-QY determination on f-SiC samples in this research. Note that an optical spectrometer (CAS 140B, Instrument Systems GmbH) was connected to the measurement FOP for spectra recording, and a diode laser ($\lambda = 375$ nm, LBX-375 HPE) was used as the source of the excitation beam. It is worthy to mention that the incident beam power was calibrated by measuring it at the sample port with the power meter (as mentioned in Subsec. 3.3.2) before Step 1&4 in order to ensure the same incident power from the reflectance | transmittance FOP. The spectra recorded through the five steps of the PL-QY measurement are summarized in Tab. 6.1 with specifications. Taking the measurement results of sample SN-2 with the incident power of 5 mW based on the experimental setup shown in Fig. 6.3 as an example, the measured spectra defined in Tab. 6.1 are shown in Fig. 6.4.

6.2.2 Data processing algorithm

In Step 1, the Reflectance Standard (Refl-Std, as introduced in Subsec. 3.4.2) was installed on the sample port for measuring the original spectra of the excitation beam, where the Refl-Std was used for preventing light leakage through the sample port.

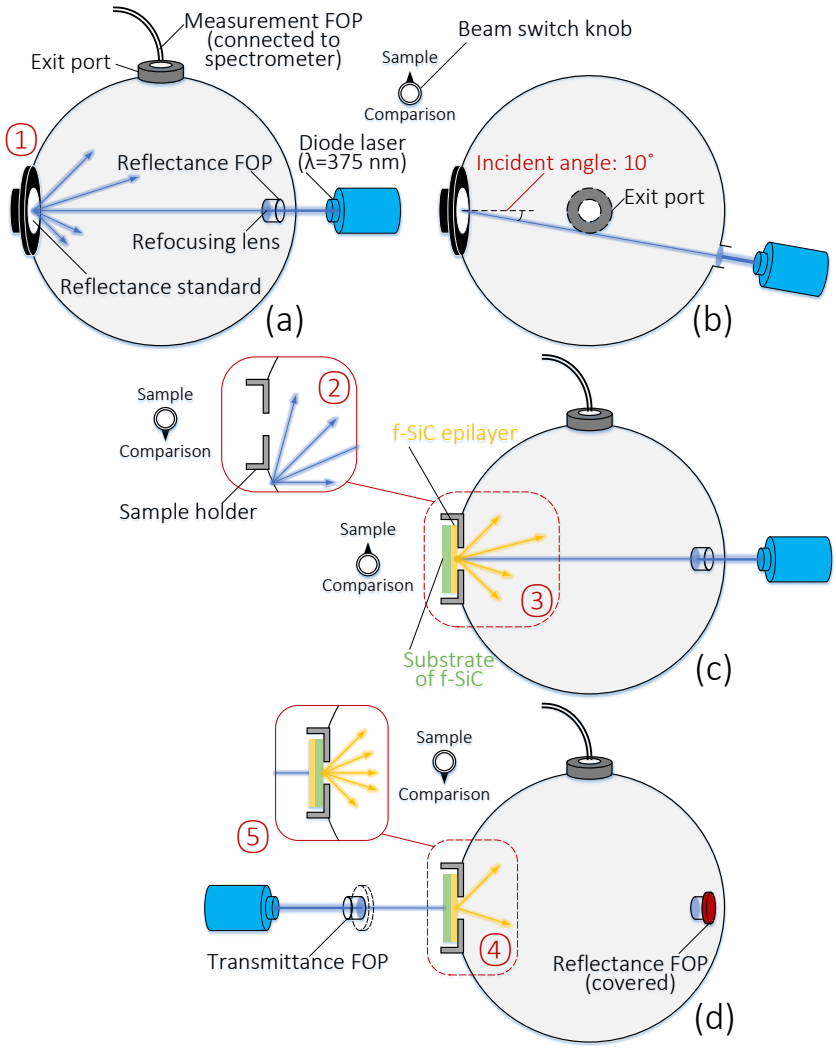

Figure 6.3: Diagram of the modified experimental procedure of PL-QY measurements on f-SiC samples. (a) Step 1: the measurement of L_a. (b) the top view of the integrating sphere during Step 1. (c) Step 2&3: the measurement of L_c and $\mathrm{PL}_{\mathrm{FEFD}}$, where the beam was directed to the vicinity of the sample port (*i.e.*, comparison mode) for Step 2;. (d) Step 4: the measurement of $\mathrm{PL}_{\mathrm{BEFD}}$; Step 5: the measurement of $\mathrm{PL}_{\mathrm{FEBD}}$, where the beam switch knob was set to comparison mode for both steps.

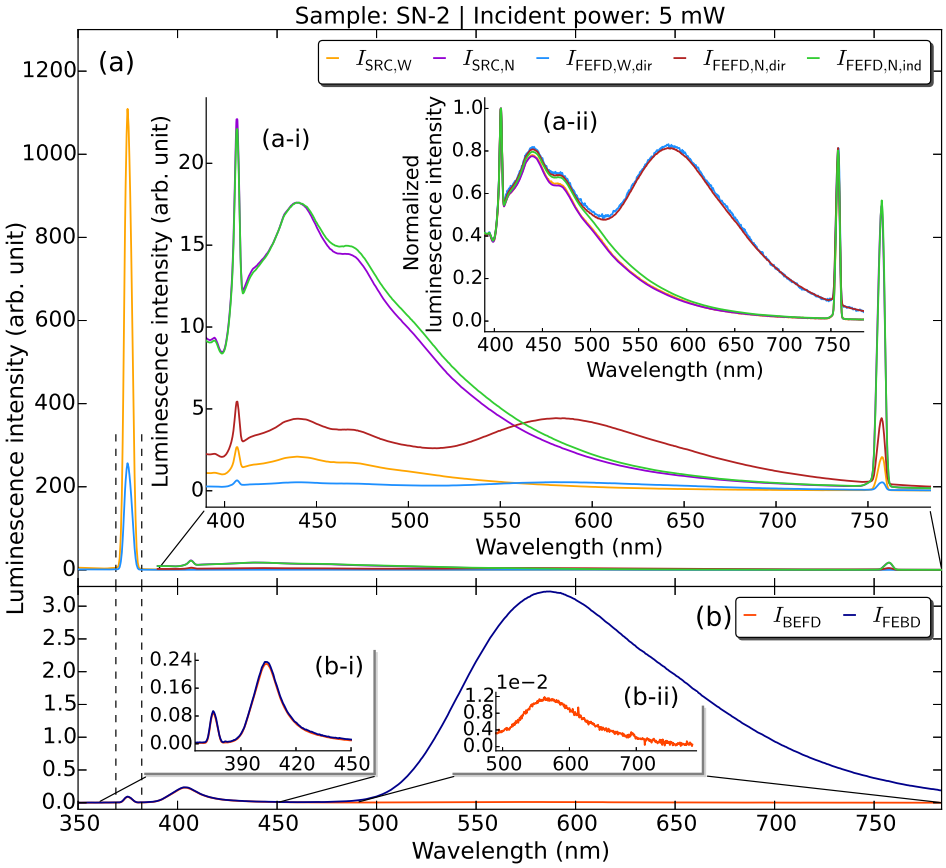

Figure 6.4: One set of spectra for the extraction of the PL-QY at certain incident power (here taking the measurement results corresponding to sample SN-2 at incident power of 5 mW as an example). According to the procedure of PL-QY measurement summarized in Tab. 6.1, the spectra recorded in Step 1-3 are presented in (a), whereas the spectra recorded in Step 4-5 are presented in (b). Note that the zoomed spectra in (a) at the predefined narrow wavelength range, *i.e.*, 390-784 nm, are presented in the inset (a-i), where the respective normalized spectra are shown in the inset (a-ii). The inset (b-i) | (b-ii) show the zoomed two spectra at 360-450 nm range and $I_{\mathrm{BEFD}}(\lambda)$ at 490-784 nm range, respectively.

Step no.	Spectrum name	Towards sample port	Range of λ	Connected FOP	Beam Switch
1	$I_{\mathrm{SRC,W}}(\lambda)$ $I_{\mathrm{SRC,N}}(\lambda)$	Refl-Std	wide narrow	Refl.	Samp.
2	$I_{\mathrm{FEFD,N,ind}}(\lambda)$	sample holder	narrow	Refl.	Comp.
3	$I_{\mathrm{FEFD,N,dir}}(\lambda)$ $I_{\mathrm{FEFD,W,dir}}(\lambda)$	f-SiC front	narrow wide	Refl.	Samp.
4	$I_{\mathrm{BEFD}}(\lambda)$	f-SiC front	wide	Tran.	Comp.
5	$I_{\mathrm{FEBD}}(\lambda)$	f-SiC back			

Table 6.1: The procedure of recording one set of spectra for the PL-QY determination on f-SiC sample using the experimental configuration shown in Fig. 6.3. Note that the "wide" and "narrow" modes under "Range of λ" refer to 350-784 nm and 390-784 nm, respectively. "W" and "N" in subscripts of spectral name are also related to the "wide" and "narrow" modes separately. "ind" and "dir" refer to the indirect and direct incidence of the excitation beam on the sample port with the sample holder mounted which correspond to the comparison mode (comp.) and sample mode (samp.), respectively. In addition, $I_{\mathrm{SRC,W}}(\lambda)$ | $I_{\mathrm{FEFD,W}}(\lambda)$ were recorded using the same parameter setting, *i.e.*, integration time, times of collection and choosing OD-filter or not, and so were $I_{\mathrm{SRC,N}}(\lambda)$ | $I_{\mathrm{FEFD,N,ind}}(\lambda)$ | $I_{\mathrm{FEFD,N,dir}}(\lambda)$.

$I_{\mathrm{SRC,W}}$ | $I_{\mathrm{SRC,N}}$ are the two spectra related to the original source beam measured in different wavelength ranges, *i.e.*, the wide mode (350-784 nm) and the narrow mode (390-784 nm), respectively. Normally, an optical density filter (OD-filter) was used when measuring $I_{\mathrm{SRC,W}}$ in order to prevent the absolute intensity of its main peak centered at 375 nm from exceeding the upper detection limit of the optical spectrometer. Here we got the expression of the integrated intensity of the original excitation spectrum (L_a) shown in Eq. (6.3), where Refl-Std(λ) refers to the reflectance spectrum of the Refl-Std.

$$L_a = \int_{369\mathrm{nm}}^{382\mathrm{nm}} \frac{I_{\mathrm{SRC,W}}(\lambda)}{\text{Refl-Std}(\lambda)} \mathrm{d}\lambda \tag{6.3}$$

In the (a) of Fig. 6.4, the spectrum of $I_{\mathrm{FEFD,W,dir}}$ which includes the spectrum of $\mathrm{PL}_{\mathrm{FEFD}}$ was also measured with the OD-filter. From the normalized spectrum of $I_{\mathrm{FEFD,W,dir}}$ shown in the (a-ii) of Fig. 6.4, we can see that by adding the OD-filter, the line shape of $I_{\mathrm{FEFD,W,dir}}$ is affected by ambient noise due to its weak intensity. In addition, the two spectra presented in the (b) of Fig. 6.4, *i.e.*, I_{FEBD} | I_{BEFD}, which reflect the information of the line shapes related to $\mathrm{PL}_{\mathrm{FEBD}}$ | $\mathrm{PL}_{\mathrm{BEFD}}$, respectively, were measured without the OD-filter. It can be expected that if the OD-filter was added during the measurements of the above mentioned two spectra, the spectrum measured in FEBD configuration would be also affected by the ambient noise while the spectrum measured in BEFD configuration would be probably beneath the lower

detection limit of the optical spectrometer. As a consequence, we decided to measure the spectra which were used for extracting the PL emission spectra without adding the OD-filter. In order to establish the correlation between the spectra measured with|without the OD-filter, a scaling ratio (SCR) expressed by Eq. (6.4) is needed. Note that the values of both components in Eq. (6.4) should be similar since the degree of attenuation resulted by the OD-filter is a constant. Accordingly, the extracted PL spectra related to the FEFD | FEBD | BEFD configuration have to be scaled down by a factor of SCR in order to calculate PL-QY. The modified expression for PL-QY is shown in Eq. (6.5) where the value of PL-QY is denoted by η_{PL}, and $P_{c,\mathrm{FEBD}}$ | $P_{c,\mathrm{FEFD}}$ | $P_{c,\mathrm{BEFD}}$ refer to the integrated PL intensities of $\mathrm{PL}_{\mathrm{FEFD}}(\lambda)$ | $\mathrm{PL}_{\mathrm{FEBD}}(\lambda)$ | $\mathrm{PL}_{\mathrm{FEFD}}(\lambda)$, respectively.

$$\mathrm{SCR} = \frac{1}{2} \times \frac{\int_{390\mathrm{nm}}^{784\mathrm{nm}} I_{\mathrm{SRC,W}}(\lambda)\mathrm{d}\lambda}{\int_{390\mathrm{nm}}^{784\mathrm{nm}} I_{\mathrm{SRC,N}}(\lambda)\mathrm{d}\lambda} + \frac{1}{2} \times \frac{\int_{390\mathrm{nm}}^{784\mathrm{nm}} I_{\mathrm{FEFD,W,dir}}(\lambda)\mathrm{d}\lambda}{\int_{390\mathrm{nm}}^{784\mathrm{nm}} I_{\mathrm{FEFD,N,dir}}(\lambda)\mathrm{d}\lambda} \tag{6.4}$$

$$\begin{aligned} \eta_{\mathrm{PL}} &= \frac{1}{\mathrm{SCR}} \times \frac{P_{c,\mathrm{FEBD}} + P_{c,\mathrm{FEFD}} + P_{c,\mathrm{BEFD}}}{L_a - L_c} \\ &= \frac{1}{\mathrm{SCR}} \times \frac{\int_{450\mathrm{nm}}^{784\mathrm{nm}} \mathrm{PL}_{\mathrm{FEBD}}(\lambda) + \mathrm{PL}_{\mathrm{FEFD}}(\lambda) + \mathrm{PL}_{\mathrm{BEFD}}(\lambda)\mathrm{d}\lambda}{L_a - L_c} \end{aligned} \tag{6.5}$$

From the inset (a-ii) of Fig. 6.4 we can see that the line shapes of the spectra of the excitation beam measured with | without the OD-filter (*i.e.*, $I_{\mathrm{SRC,W}}$ | $I_{\mathrm{SRC,N}}$, respectively) are identical, and so are the two spectra of the PL emission with FEFD configuration ($I_{\mathrm{FEFD,W,dir}}$ | $I_{\mathrm{FEFD,N,dir}}$). It is confirmed that spectra are scaled down by the OD-filter regardless of wavelength, hence it is reasonable to apply SCR for PL-QY calculation. The upper limit of the detectable wavelength (*i.e.*, 784 nm) which is also shown in Eq. (6.4)-(6.5), is actually caused by the limitation of the optical spectrometer. It is believed that the PL intensity of the f-SiC samples with wavelength shorter than the lower limits of the integrals in Eq. (6.5) (*i.e.*, 450 nm) can be negligible. In the inset (a-i) of Fig. 6.4, it is clear to see that the spectrum of the excitation beam has a tail part which consists of two sharp peaks at ∼406.4 nm and ∼757.4 nm and two broad peaks at ∼440 nm and ∼470 nm. This tail part is still distinguishable on the spectrum of $I_{\mathrm{FEFD,N,dir}}$ corresponding to the PL emission excited by FEFD configuration. Hence it is essential to split $\mathrm{PL}_{\mathrm{FEFD}}(\lambda)$ from $I_{\mathrm{FEFD,N,dir}}$. Later we will show that $\mathrm{PL}_{\mathrm{FEFD}}(\lambda)$ can be recovered by $\mathrm{PL}_{\mathrm{FEBD}}(\lambda)$. Since $\mathrm{PL}_{\mathrm{FEFD}}(\lambda)$ and $\mathrm{PL}_{\mathrm{FEBD}}(\lambda)$ are induced under the same excitation condition with the source beam incidence at air | f-SiC epilayer interface, the line shapes of those two spectra should be identical. In Step 2, the sample holder which is used for fixing f-SiC sample was installed on the sample port, where the line shape of the measured spectrum in this step ($I_{\mathrm{FEFD,N,ind}}$) is considered to represent the line shape

of the tail part of the excitation beam. Moreover, although $I_{\mathrm{SRC,N}}$ also represents the tail part of the excitation beam, the line shapes of $I_{\mathrm{SRC,N}}$ and $I_{\mathrm{FEFD,N,ind}}$ are slightly different as shown in the inset (a-ii) of Fig. 6.4. Here we believe that the line shape of $I_{\mathrm{FEFD,N,ind}}$ is more representative of the tail part of the excitation beam enclosed in $I_{\mathrm{FEFD,N,dir}}$. In Step 3, an f-SiC sample was mounted on the sample holder with the epilayer side facing towards the sample port. For $I_{\mathrm{FEFD,N,dir}}$, we have introduced that this spectrum contains $\mathrm{PL}_{\mathrm{FEFD}}(\lambda)$ which was measured without adding the OD-filter. Meanwhile, by recording $I_{\mathrm{FEFD,W,dir}}$ which was measured in wide mode with the OD-filter, one can obtain the integrated intensity of the attenuated source beam after PL excitation (L_c) as shown in Eq. (6.6).

$$L_c = \int_{369\mathrm{nm}}^{382\mathrm{nm}} I_{\mathrm{FEFD,W}}(\lambda)\mathrm{d}\lambda \tag{6.6}$$

In Step 4&5, the incident laser beam was fiber coupled to the transmittance FOP where the beam switch knob was tuned to the comparison mode for preventing light leakage. In the inset (b-i) of Fig. 6.4, the peak centered at ∼375 nm in either spectrum (*i.e.*, I_{BEFD} | I_{FEBD}) is related to the main peak of the excitation beam which has been largely attenuated. As the line shapes and the absolute intensities of the two spectra at 360-450 nm region are almost identical, it can be confirmed that another peak centered at ∼404 nm is not the part of the PL emission from f-SiC epilayer. In fact, the emergence of this peak is actually caused by the interband absorption[154] related to f-SiC's entire 6H-SiC based structure, where the strong absorption of the light with photon energy higher than the band gap of 6H-SiC is expected. In the inset (b-ii) of Fig. 6.4 shows the luminescence spectrum related to $\mathrm{PL}_{\mathrm{BEFD}}(\lambda)$. As we know that $\mathrm{PL}_{\mathrm{BEFD}}(\lambda)$ is induced by the incident beam excitation at the 6H-SiC substrate | f-SiC epilayer interface, which is different from the condition of the front side excitation with the source beam incidence at the air | f-SiC epilayer interface. The line shape of $\mathrm{PL}_{\mathrm{BEFD}}(\lambda)$ is expected to differ from that of the either PL spectrum (*i.e.*, $\mathrm{PL}_{\mathrm{FEFD}}(\lambda)$ | $\mathrm{PL}_{\mathrm{FEBD}}(\lambda)$) with the front excitation condition. Therefore the aforementioned method related to the spectrum splitting of $I_{\mathrm{FEFD,N,dir}}$ is not applicable to I_{BEFD}. Instead, a three-step process shown in Eq. (6.7) was implemented for the extraction of $\mathrm{PL}_{\mathrm{BEFD}}(\lambda)$. Firstly, a Savitzky–Golay filter[155] (SG filter) was used for smoothing I_{BEFD} within the range of 490-784 nm. Secondly, the smoothed curve was fitted by a single skew normal distribution function (Single SK-ND). Lastly, the fitting parameter obtained from the previous fitting process were implemented back to the single skew normal distribution function for the recovery of $\mathrm{PL}_{\mathrm{BEFD}}(\lambda)$ at 450-784 nm range. An example regarding to the extraction of $\mathrm{PL}_{\mathrm{BEFD}}(\lambda)$ is shown in the (a) of Fig. 6.5.

$$\begin{aligned} I_{\mathrm{BEFD}}(\lambda)\,|_{490-784\mathrm{nm}} \longrightarrow \boxed{\text{SG filter}} \longrightarrow \boxed{\text{Single SK-ND fit}} \xrightarrow{\text{fitting parameters}} \\ \xrightarrow{\text{fitting parameters}} \boxed{\text{Single SK-ND function}\,|_{450-784\mathrm{nm}}} \longrightarrow \mathrm{PL}_{\mathrm{BEFD}}(\lambda) \end{aligned} \tag{6.7}$$

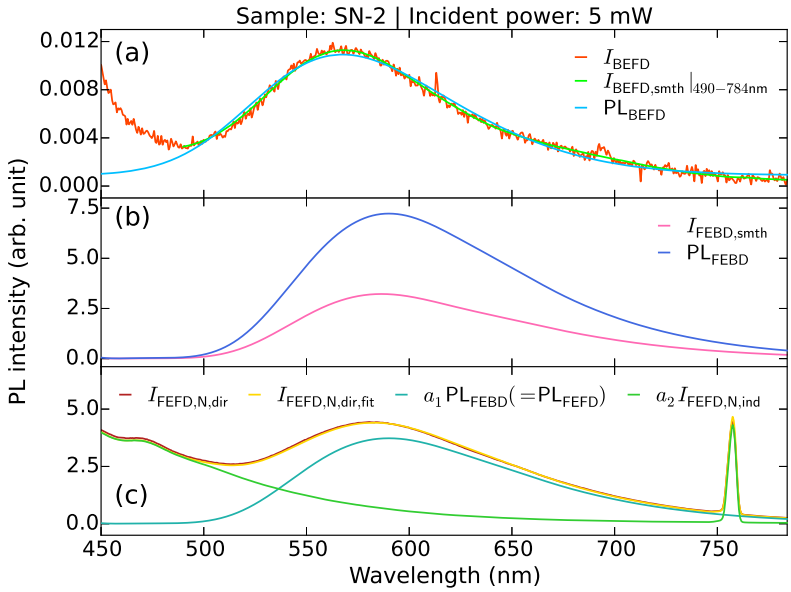

Figure 6.5: Examples of the PL spectra extraction, here taking sample SN-2 at the incident power of 5 mW for example. (a) Extraction of $PL_{BEFD}(\lambda)$ based on Eq. (6.7); (b) Extraction of $PL_{FEBD}(\lambda)$ based on Eq. (6.8)-(6.10); (c) Extraction of $PL_{FEFD}(\lambda)$ based on Eq. (6.11)-(6.12).

For Step 5, the related measured spectrum (I_{FEBD}) at the PL-active spectral region, *i.e.* 450-784 nm, is considered as the PL emission spectrum transmitted though 6H-SiC substrate, where the transmitted tail part of the excitation beam can be negligible. Here, a three-step process was developed for the extraction of $PL_{FEBD}(\lambda)$. In the first and second step, I_{FEBD} and the transmittance spectrum of 6H-SiC substrate (*i.e.*, T_{SUB}) were smoothed by the Savitzky–Golay filter at the PL-active spectral region as shown in Eq. (6.8)-(6.9). Hence $PL_{FEBD}(\lambda)$ which represents the PL emission spectrum at the interface of f-SiC epilayer | 6H-SiC substrate equals to the quotient between the smoothed I_{FEBD} and T_{SUB} as shown in Eq. (6.10). An example of the extraction of $PL_{FEBD}(\lambda)$ is shown in the (b) of Fig. 6.5. The transmittance spectra of the 6H-SiC substrate (SiCrystal, GmbH) of the three f-SiC samples SN-2 and SN-3/4 employed in this PL-QY determination experiment were measured. The same integrating sphere was applied for the related transmittance measurements where the methodology summarized in Tab. 3.1 was also implemented. The raw and smoothed transmittance spectra of the 6H-SiC substrate of SN-2 and SN-3/4 are shown in Fig. 6.6.

$$I_{\mathrm{FEBD}}(\lambda)\,|_{450-784\mathrm{nm}} \longrightarrow \boxed{\text{SG filter}} \longrightarrow I_{\mathrm{FEBD,smth}}(\lambda)\,|_{450-784\mathrm{nm}} \tag{6.8}$$

$$T_{\mathrm{SUB}}(\lambda)\,|_{450-784\mathrm{nm}} \longrightarrow \boxed{\text{SG filter}} \longrightarrow T_{\mathrm{SUB,smth}}(\lambda)\,|_{450-784\mathrm{nm}} \tag{6.9}$$

$$\mathrm{PL}_{\mathrm{FEBD}}(\lambda) = \frac{I_{\mathrm{FEBD,smth}}(\lambda)\,|_{450-784\mathrm{nm}}}{T_{\mathrm{SUB,smth}}(\lambda)\,|_{450-784\mathrm{nm}}} \tag{6.10}$$

Back to the extraction of $\mathrm{PL}_{\mathrm{FEFD}}(\lambda)$, we have confirmed that $I_{\mathrm{FEFD,N,dir}}$ can be splitted into $\mathrm{PL}_{\mathrm{FEFD}}$ and the tail part of the incident excitation spectrum. For $\mathrm{PL}_{\mathrm{FEFD}}(\lambda)$, it has been suggested that $\mathrm{PL}_{\mathrm{FEFD}}(\lambda) \propto \mathrm{PL}_{\mathrm{FEFD}}(\lambda)$ since these two spectra have the same excitation condition. Whereas $I_{\mathrm{FEFD,N,ind}}$ representing the line shape of the tail part of the excitation spectrum at FEFD mode has been measured in Step 2. Therefore we got the analytic expression of $I_{\mathrm{FEFD,N,dir}}$ at the PL-active spectral region which corresponds to the linear recombination of $\mathrm{PL}_{\mathrm{FEBD}}(\lambda)$ and $I_{\mathrm{FEFD,N,ind}}$ as shown in Eq. (6.11). By solving Eq. (6.11) using least squares regression, one can get $\mathrm{PL}_{\mathrm{FEFD}}(\lambda)$ via Eq. (6.12). An example of the extraction of $\mathrm{PL}_{\mathrm{FEFD}}(\lambda)$ is shown in the (c) of Fig. 6.5.

$$\begin{pmatrix} \mathrm{PL}_{\mathrm{FEBD}}(\lambda) & I_{\mathrm{FEFD,N,ind}}(\lambda)\,|_{450-784\mathrm{nm}} \end{pmatrix} \begin{pmatrix} a_1 \\ a_2 \end{pmatrix} = I_{\mathrm{FEFD,N,dir}}(\lambda)\,|_{450-784\mathrm{nm}} \tag{6.11}$$

$$\mathrm{PL}_{\mathrm{FEFD}}(\lambda) = a_1 \mathrm{PL}_{\mathrm{FEBD}}(\lambda) \tag{6.12}$$

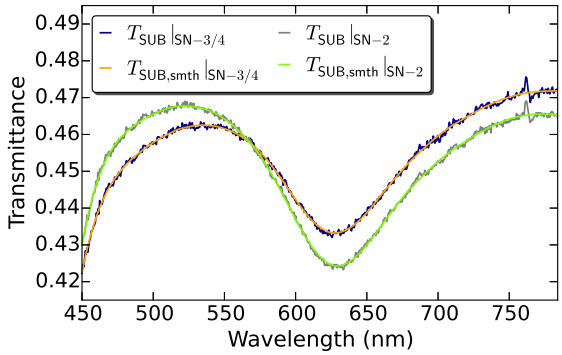

Figure 6.6: The raw and smoothed transmittance spectra of the 6H-SiC substrate of sample SN-2 and SN-3/4.

6.2.3 Relative uncertainty

Accordingly, as P_c in Eq. (6.1) is now composed of three components which corresponds to the PL excitation under FEFD, FEBD and BEFD modes. The expression of the relative uncertainty of PL-QY (*i.e.*, η_{PL}) shown in Eq. (6.2) has to be modified by following the law of propagating uncertainty[156], where the new expression of η_{PL} refers to Eq. (6.13). In Eq. (6.13), U_{FEBD}, U_{FEFD}, U_{BEFD}, U_{L_a}, U_{L_c} and U_{SCR} refer to the relative uncertainties of $P_{c,\mathrm{FEBD}}$, $P_{c,\mathrm{FEFD}}$, $P_{c,\mathrm{BEFD}}$, L_a, L_c and SCR, respectively. In addition, $\sigma_x\,|_{x=\mathrm{FEBD,FEFD,BEFD},L_a,L_c,\mathrm{SCR}}$ corresponds to the standard deviations of each variables shown in Eq. (6.13), and the expressions included in the angle brackets are related to the respective mean values.

$$
\begin{aligned}
U_{\mathrm{PL}} &= \left(U_{\mathrm{FEBD}}^2 + U_{\mathrm{FEFD}}^2 + U_{\mathrm{BEFD}}^2 + U_{L_a}^2 + U_{L_c}^2 + U_{\mathrm{SCR}}^2\right)^{0.5} \\
&= \Bigg[\left(\left\langle \frac{P_{c,\mathrm{FEBD}}}{P_{c,\mathrm{FEBD}} + P_{c,\mathrm{FEFD}} + P_{c,\mathrm{BEFD}}} \right\rangle \times \frac{\sigma_{\mathrm{FEBD}}}{\langle P_{c,\mathrm{FEBD}} \rangle}\right)^2 + \\
&\quad \left(\left\langle \frac{P_{c,\mathrm{FEFD}}}{P_{c,\mathrm{FEBD}} + P_{c,\mathrm{FEFD}} + P_{c,\mathrm{BEFD}}} \right\rangle \times \frac{\sigma_{\mathrm{FEFD}}}{\langle P_{c,\mathrm{FEFD}} \rangle}\right)^2 + \\
&\quad \left(\left\langle \frac{P_{c,\mathrm{BEFD}}}{P_{c,\mathrm{FEBD}} + P_{c,\mathrm{FEFD}} + P_{c,\mathrm{BEFD}}} \right\rangle \times \frac{\sigma_{\mathrm{BEFD}}}{\langle P_{c,\mathrm{BEFD}} \rangle}\right)^2 + \\
&\quad \left(\left\langle \frac{L_a}{L_a - L_c} \right\rangle \times \frac{\sigma_{L_a}}{\langle L_a \rangle}\right)^2 + \left(\left\langle \frac{L_c}{L_a - L_c} \right\rangle \times \frac{\sigma_{L_c}}{\langle L_c \rangle}\right)^2 + \left(\frac{\sigma_{\mathrm{SCR}}}{\langle \mathrm{SCR} \rangle}\right)^2\Bigg]^{0.5}
\end{aligned}
\tag{6.13}
$$

6.3 PL-QY of *n*-type 6H f-SiC

Power (mW)		0.25	0.5	1	2	5	8	14
SN-2	1st	6.86	6.26	5.85	5.27	4.54	4.02	3.41
	2nd	6.89	6.42	5.98	5.45	4.54	4.05	-
SN-3	1st	30.44	26.37	21.88	15.92	12.58	9.96	7.33
	2nd	29.88	26.29	22.34	16.30	12.40	10.06	-
SN-4	1st	27.04	23.88	18.68	14.11	9.34	7.35	6.15
	2nd	27.66	23.73	18.33	14.43	9.15	7.09	-

Table 6.2: The measured PL-QY (%) of sample SN-2/3/4 with different incident power.

As mentioned in Subsec. 6.2.2, the three *n*-type 6H f-SiC samples, *i.e.*, SN-2/3/4, were employed in this PL-QY determination experiment, where the basic physical

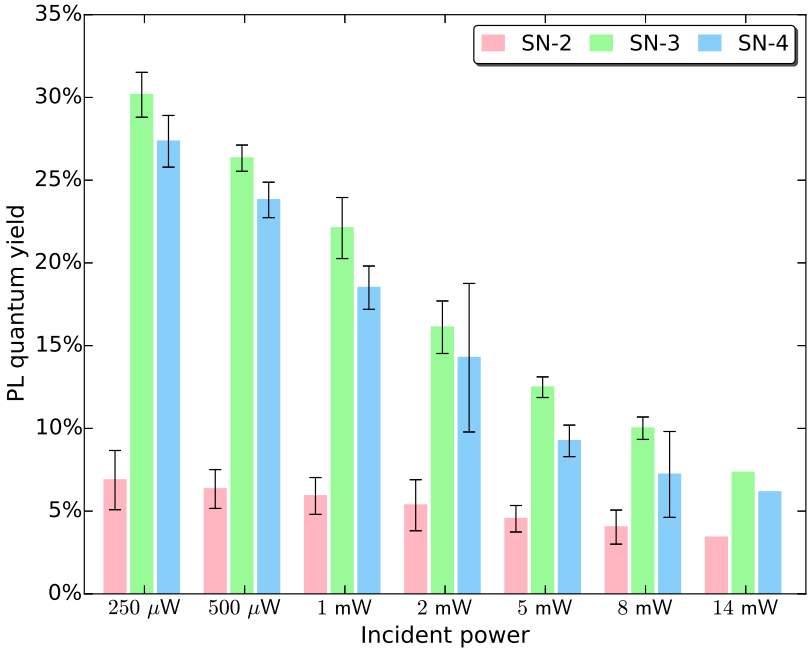

Figure 6.7: The averaged PL-QY of sample SN-2/3/4. The error bars indicate the relative uncertainties (U_{PL}) of the PL-QY measurements which were calculated using Eq. (6.13).

parameters of these three samples refer to Tab. 2.6. The PL-QY of each samples were excited under seven different incident beam power, *i.e.*, 0.25, 0.5, 1, 2, 5, 8 and 14 mW in order to study the power-dependency of f-SiC's PL-QY, where all the extracted PL-QY (η_{PL}) for the three samples are summarized in Tab. 6.2. Note that the PL-QY for all three samples were measured twice with the incident beam power from 0.25 to 8 mW, where the measurements corresponding to the beam incidence of 14 mW were only launched for once due to the unstable fiber coupled maximum output power of the laser source. The uncertainties of the measured PL-QY for each samples with specific incident power have been estimated using Eq. (6.13), where all the U_{PL} together with the respective mean values of η_{PL} are presented in Fig. 6.7. From Fig. 6.7, it is clear to see that the PL-QY of SN-2 under all incident power are lower than those of SN-3/4. On the other hand, Fig. 6.8 shows the TRPL measurement results of SN-2/3/4, where the results related to SN-2 are derived from Chapter 5. The experimental setup for the measurements on SN-3/4 are identical with that of SN-2, where three spots were characterized on both samples. Compared to SN-2, it is apparent to see that the PL decay at the initial stage of either SN-3/4 is slower, indicating the lifetimes corresponding to the decay channels of E_1/E_2 centers in SN-

3/4 are longer. Therefore, the concentrations of the E_1/E_2 centers in SN-3/4 are lower than that of SN-2 by referring to Eq. (5.4). According to the conclusion in Chapter 5, where higher density of E_1/E_2 in SiC sample will result in lower IQE, therefore the IQE of SN-2 is considered to be lower than the IQE of either SN-3/4. Here we believe that the contrast between the IQE of SN-2 and SN-3/4 is the major cause of their differences on PL-QY shown in Fig. 6.7.

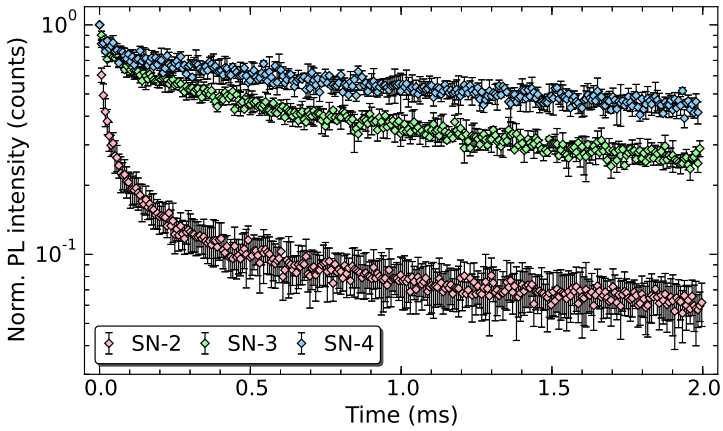

Figure 6.8: Normalized TRPL decays recorded via TCSPC histograms for sample SN-2/3/4, where the TRPL data of SN-2 are derived from Chapter 5. Each error bar indicates the standard deviation (SD) normalized by the corresponding photon count at a certain time point..

Although from Fig. 6.8 we can see that the IQE of SN-3 should be slightly lower than that of SN-4, opposite contrast on their PL-QY were obtained as shown in Fig. 6.7. It is considered that greater extent of self absorption of PL emission are expected in SN-4 due to its larger epilayer thickness (250 μm) compared to that of SN-3 (150 μm). On the other hand, sufficient epilayer thickness is also essential to ensure large medium volume for DAP recombination as concluded in Ref. [2]. At this point, we also consider that the much lower PL-QY of SN-2 compared to SN-3/4 are partially caused by the too thin epilayer of SN-2 where its volume for DAP recombination is probably insufficient. Additionally, an obvious tendency can be observed from Fig. 6.7 that the PL-QY of *n*-type 6H f-SiC sample increases with the decreasing incident power. We believe that this phenomenon is caused by the enhanced Auger recombination in f-SiC sample when the incident power density on the sample is increased[157]. It is well known that the rate of Auger recombination is proportional to the cube[158] of the total carrier densities, *i.e.*, $n_0 + \Delta n$, where Δn refers to the density of non-equilibrium carriers. As mentioned in Subsec. 3.4.2, the focused incident beam spot on the sample port of the integrating sphere has the diameter of 3 mm, by applying Eq. (3.1) to (3.3), the calculated injection level per

second on f-SiC samples corresponding to the range of the incident beam power,*i.e.*, 250 μW to 14 mW, is from 1.33×10^{18} to 7.47×10^{19} cm^{-3}. Therefore the change of the Auger recombination rate is expected to be over one order of magnitude in the PL-QY measurements. Moreover, the Auger recombination corresponding to the band-to-band transition in SiC is enhanced as the incident power increases[121, 159]. The Auger recombination coefficient related to the interband transition in SiC decreases with the increasing incident power[160, 161]. Future work about the characterization of the carrier lifetimes in f-SiC at high injection levels by using the experimental technique like time-resolved free carrier absorption[126, 160, 161] is needed in order to study how the PL-QY is degraded by Auger recombination and its carrier dynamics.

6.4 Summary

In this Chapter, we have designed the experimental scheme related to the absolute PL-QY determination on f-SiC samples, where the measurement methodology is based on a modified two-measurements approach using an integrating sphere. The algorithm corresponding to the data processing and the uncertainty estimation of PL-QY experimental results are also developed. The excitation power dependent PL-QY of the three *n*-type 6H f-SiC samples, *i.e.*, SN-2/3/4, have been measured. The measurement results have revealed that the PL-QY of f-SiC is dependent on its epilayer thickness. It is found that too thick epilayer would cause the excess self absorption of PL emission while too thin epilayer is unable to provide sufficient medium volume for DAP recombination. In addition, from the results of the PL-QY measurements, a clear tendency where the PL-QY of f-SiC sample increases with the decreasing incident power indicates strong Auger recombination in f-SiC. It is believed that this Auger recombination corresponds to the band-to-band transition which can be enhanced by increasing the incident beam power.

CHAPTER 7
Conclusion and perspective

The luminescence mechanism of nitrogen-boron (N-B) co-doped 6H fluorescent silicon carbide (f-SiC) impacted jointly by radiative and non-radiative recombination channels has been first time theoretically and experimentally investigated.

In Sec. 4.1, by applying thermally stimulated luminescence (TSL) measurements to the intermediate (SP-3) and strong (SN-2/3/4) *n*-type f-SiC samples with the related TSL modelling, it is revealed that part of the shallow donors on hexagonal sites induced by nitrogen doping are not enrolled in donor-acceptor-pair (DAP) recombination, and the fitted ionization energy of the shallow donors is around 100 meV. Meanwhile, it is found that part of the donors on hexagonal sites are not involved in DAP recombination which causes the redshift of the photoluminescence (PL) spectrum. The results of the TSL experiments also confirm the nonexistence of boron-induced shallow acceptors. In addition, there is no clear evidence from the experimental results which shows the inclusion of acceptors by unintentional aluminum doping. A future plan based on the current characterization on f-SiC using TSL technique should focus on the measurement of the spectral-resolved TSL and using different excitation sources with sub-band-gap photon energies TSL excitation pumping in order to extract the information of the TSL-active recombination center in 6H f-SiC.

In Sec. 4.2, the results of the characterizations on three f-SiC samples (SP-2/3 and SN-1) using temperature-dependent PL spectroscopy reveal the existence of a deeper boron-induced acceptor here called D^*-center compared to the well-known D-center. Here D^*-center and D-center together are called double D-centers. The existence of double D-centers confirms the previously reported D- and D'-center detected by the electron paramagnetic resonance (EPR) spectroscopy. The D^* center is correlated to the dominating DAP recombination at low temperatures with peak photon energy ∼1.9 eV compared to the D-center dominated DAP recombination at elevated temperatures peaked at ∼2.1 eV. In addition, it is found that the D^* center related DAP recombination is site-dependent, which also agrees well with the previous characterization results on SiC by using EPR technique. By taking account of the doping conditions of the three samples, it is suggested that N-doping could facilitate the formation of D-center during the epilayer growth by FSGP method. The thermal quenching regarding the D^* center related DAP recombination at elevated temperatures suggests the existence of a hole-trap, *i.e.*, the HS2 center. By referring the previous *first-principles* calculation results on SiC, the atomic structures and energy levels of the double D-centers and HS2 center have been revealed. The atomic

structures of those three centers accord well with the growth conditions of the f-SiC samples. The energy level of the HS2 center is found to stay in between that of the double *D*-centers'. Accordingly, a two-stage thermal activation model of the non-equilibrium holes related to the HS2 center is proposed to explain the evolution of the double *D*-centers related DAP recombination along with the elevated temperatures. The booming of the radiative recombination in strong *n*-type f-SiC is because of the *D*-center's increasing capture probability of the holes which are thermally activated from the HS2 center. An intensive study regarding the physical mechanism about the capturing and thermal activation of non-equilibrium holes by the system composed of the double *D*-centers and HS2 center is needed in the future. For instance, the first step would be using the EPR technique and *ab-initio* calculations to determine the hyperfine tensors of the atomic structures of the double *D*-centers and HS2 center in f-SiC samples. As the measured and the calculated hyperfine tensors can match, the atomic structures of those three centers in f-SiC can be verified which lays the foundation for further investigations.

In Chapter 5, two strong *n*-type f-SiC samples (SN-1/2) and one bulk N-B co-doped *n*-type 6H-SiC substrate are characterized by applying time-resolved photoluminescence (TRPL) and static PL measurements. In addition, the negative-U centers related carrier dynamics and steady-state DAP recombination modellings are applied to explain the experimental results. The results of the carrier dynamics modelling reveal that the density of the E_1/E_2 defects in bulk 6H-SiC is found to be two orders of magnitude higher than that of either f-SiC epilayer. It is believed that the extra non-radiative decay channel and the much higher E_1/E_2 concentration in the bulk substrate caused quite lower PL intensity as well as internal quantum efficiency (IQE) than the two f-SiC samples. For the comparison between the two f-SiC samples, the sample with higher density of E_1/E_2 centers has lower IQE compared to another sample, although the former has denser DAP which is revealed by the results derived from the steady-state DAP recombination modelling. Hence the existence of the E_1/E_2 centers is the major factor which causes the degradation of the efficiency of DAP recombination in 6H f-SiC. To further decrease the concentration of E_1/E_2 centers in 6H f-SiC during the epilayer growth by FSGP method, it is believed that control of the C/Si ratio and the nitrogen doping is still required to seek for the new balance between the densities of the E_1/E_2 defects and the *D*-center.

In Chapter 6, the absolute photoluminescence quantum yield (PL-QY) of three *n*-type f-SiC samples (SN-2/3/4) have been experimentally determined, where the related experimental setup is homemade based on an integrating sphere. The data processing algorithm for calculating the PL-QY regarding the measurement results has been developed and the related uncertainty analysis has been launched. The results show that the PL-QY of f-SiC is affected by its epilayer thickness, where too thick epilayer would cause the excess self absorption of PL emission while too thin epilayer is unable to provide sufficient medium volume for DAP recombination. In addition, a clear trend is found where the PL-QY of f-SiC increases with the decreasing incident power. This indicates strong Auger recombination in f-SiC, which corresponds to the band-to-band transition and can be enhanced by increasing the

incident beam power. A future plan about the studies on how Auger recombination degrades the PL-QY of f-SiC at elevated input power should involve the carrier lifetimes measurements at high injection levels with suitable experimental techniques, for instance, the time-resolved free carrier absorption.

To sum up, the research presented in this thesis has initiated the studies about the physical mechanisms behind the strong luminescence from fluorescent silicon carbide material, a type of 6H silicon carbide which never has such high nitrogen-boron co-doping level ($>10^{18}$ cm^{-3}) before. Although finer experimental techniques and more accurate theoretical approaches are still required to be developed for further research on f-SiC in order to get more information about the cause of the formation of non-radiative centers, where these information would help to optimize the parameters for the growth control of f-SiC. Our research has revealed several distinctive features of f-SiC compared to the conventional bulk SiC grown by physical vapor transport method, where the evolution of radiative and non-radiative recombinations in f-SiC along two dimensions, *i.e.*, temperature and injection level, has been studied in-depth. Overall, this thesis has moved one step further to the establishment of the roadmap regarding the improvement of the internal quantum efficiency (IQE) of f-SiC, where the sufficient IQE is the cornerstone of the realization of f-SiC-based white light-emitting diode.

Bibliography

[1] Y. Narukawa et al. “Phosphor-Conversion White Light Emitting Diode Using InGaN Near-Ultraviolet Chip”. In: *Jpn. J. Appl. Phys.* 41.4A (2002), p. L371. DOI: 10.1143/JJAP.41.L371.

[2] S. Kamiyama et al. “Extremely high quantum efficiency of donor-acceptor-pair emission in N- and B-doped 6H-SiC”. In: *J. Appl. Phys.* 99.9 (2006), p. 093108. ISSN: 00218979. DOI: 10.1063/1.2195883.

[3] S. Kamiyama et al. “Fluorescent SiC and its application to white light-emitting diodes”. In: *J. Semicond.* 32.1 (2011), p. 013004. DOI: 10.1088/1674-4926/32/1/013004.

[4] S. Kamiyama et al. “White light-emitting diode based on fluorescent SiC”. In: *Thin Solid Films* 522 (Nov. 2012), pp. 23–25. ISSN: 00406090. DOI: 10.1016/j.tsf.2012.02.017.

[5] H. Ou et al. “Advances in wide bandgap SiC for optoelectronics”. In: *Eur. Phys. J. B* 87.3 (2014), p. 58. ISSN: 14346028. DOI: 10.1140/epjb/e2014-41100-0.

[6] M. Syväjärvi and R. Yakimova. “3.05 - Sublimation Epitaxial Growth of Hexagonal and Cubic SiC”. In: *Comprehensive Semiconductor Science and Technology*. Ed. by P. Bhattacharya, R. Fornari, and H. Kamimura. Amsterdam: Elsevier, 2011, pp. 202–231. ISBN: 978-0-444-53153-7. DOI: 10.1016/B978-0-44-453153-7.00092-4.

[7] V. Jokubavicius et al. “Effects of source material on epitaxial growth of fluorescent SiC”. In: *Thin Solid Films* 522 (2012), pp. 7–10. ISSN: 00406090. DOI: 10.1016/j.tsf.2011.10.176.

[8] P. J. Wellmann. “Review of SiC crystal growth technology”. In: *Semicond. Sci. Technol.* 33.10 (Oct. 2018), p. 103001. ISSN: 0268-1242. DOI: 10.1088/1361-6641/aad831.

[9] M. Syväjärvi et al. “Structural improvement in sublimation epitaxy of 4H–SiC”. In: *J. Appl. Phys.* 88.3 (Aug. 2000), pp. 1407–1411. ISSN: 0021-8979. DOI: 10.1063/1.373831.

[10] P. Wellmann et al. “SiC single crystal growth by a modified physical vapor transport technique”. In: *J. Cryst. Growth* 275.1-2 (Feb. 2005), e555–e560. ISSN: 00220248. DOI: 10.1016/j.jcrysgro.2004.11.070.

[11] A. Sakwe et al. “Bulk growth of SiC - Review on advances of SiC vapor growth for improved doping and systematic study on dislocation evolution”. In: *Phys. Status Solidi Basic Res.* 245.7 (2008), pp. 1239–1256. ISSN: 03701972. DOI: 10.1002/pssb.200743520.

[12] Y. Ou et al. “Omnidirectional luminescence enhancement of fluorescent SiC via pseudoperiodic antireflective subwavelength structures.” In: *Opt. Lett.* 37.18 (2012), pp. 3816–8. ISSN: 1539-4794. DOI: 10.1364/OL.37.003816.

[13] Y. Ou et al. “Broadband antireflection and light extraction enhancement in fluorescent SiC with nanodome structures.” In: *Sci. Rep.* 4 (2014), p. 4662. ISSN: 2045-2322. DOI: 10.1038/srep04662.

[14] W. Lu et al. “White Light Emission from Fluorescent SiC with Porous Surface”. In: *Sci. Rep.* 7.1 (Dec. 2017), p. 9798. ISSN: 2045-2322. DOI: 10.1038/s41598-017-10771-7.

[15] L. Lin et al. “An adhesive bonding approach by hydrogen silsesquioxane for silicon carbide-based LED applications”. In: *Mater. Sci. Semicond. Process.* 91 (2019), pp. 9–12. ISSN: 1369-8001. DOI: https://doi.org/10.1016/j.mssp.2018.10.028.

[16] “Bulk Growth of Silicon Carbide”. In: *Fundamentals of Silicon Carbide Technology*. John Wiley & Sons, Ltd, 2014. Chap. 3, pp. 39–74. ISBN: 9781118313534. DOI: 10.1002/9781118313534.ch3.

[17] “Epitaxial Growth of Silicon Carbide”. In: *Fundamentals of Silicon Carbide Technology*. John Wiley & Sons, Ltd, 2014. Chap. 4, pp. 75–124. ISBN: 9781118313534. DOI: 10.1002/9781118313534.ch4.

[18] “Characterization Techniques and Defects in Silicon Carbide”. In: *Fundamentals of Silicon Carbide Technology*. John Wiley & Sons, Ltd, 2014. Chap. 5, pp. 125–187. ISBN: 9781118313534. DOI: 10.1002/9781118313534.ch5.

[19] S. Schimmel et al. “The role of defects in fluorescent silicon carbide layers grown by sublimation epitaxy”. In: *IOP Conf. Ser.: Mater. Sci. Eng.* 56 (2014), p. 012002. ISSN: 1757-899X. DOI: 10.1088/1757-899X/56/1/012002.

[20] W. Kleber. “Verma, Ajit Ram and P. Krishna Polymorphism and polytypism in crystals. John Wiley and Sons, Inc. New York-London-Sydney 1966. XIX+3415”. In: *Kristall und Technik* 1.4 (1966), pp. 665–666. DOI: 10.1002/crat.19660010415.

[21] C. J. Schneer. “Polymorphism in one dimension”. In: *Acta Crystallogr.* 8.5 (1955), pp. 279–285. DOI: 10.1107/S0365110X55000893.

[22] C. Cheng, R. J. Needs, and V. Heine. “Inter-layer interactions and the origin of SiC polytypes”. In: *J. Phys. C Solid State Phys.* 21.6 (Feb. 1988), pp. 1049–1063. ISSN: 0022-3719. DOI: 10.1088/0022-3719/21/6/012.

[23] P. J. H. Denteneer and W. van Haeringen. “Ground-state properties of polytypes of silicon carbide”. In: *Phys. Rev. B* 33 (4 Feb. 1986), pp. 2831–2834. DOI: 10.1103/PhysRevB.33.2831.

[24] G. R. Fisher and P. Barnes. “Towards a unified view of polytypism in silicon carbide”. In: *Philos. Mag. B* 61.2 (1990), pp. 217–236. DOI: 10.1080/13642819008205522.

[25] “Physical Properties of Silicon Carbide”. In: *Fundamentals of Silicon Carbide Technology*. John Wiley & Sons, Ltd, 2014. Chap. 2, pp. 11–38. ISBN: 9781118313534. DOI: 10.1002/9781118313534.ch2.

[26] W. J. Choyke and L. Patrick. “Exciton Recombination Radiation and Phonon Spectrum of 6*H* SiC”. In: *Phys. Rev.* 127 (6 Sept. 1962), pp. 1868–1877. DOI: 10.1103/PhysRev.127.1868.

[27] W. Suttrop et al. “Hall effect and infrared absorption measurements on nitrogen donors in 6H-silicon carbide”. In: *J. Appl. Phys.* 72.8 (1992), pp. 3708–3713. ISSN: 00218979. DOI: 10.1063/1.352318.

[28] K. Momma and F. Izumi. “VESTA3 for three-dimensional visualization of crystal, volumetric and morphology data”. In: *J. Appl. Crystallogr.* 44.6 (Dec. 2011), pp. 1272–1276. DOI: 10.1107/S0021889811038970.

[29] P. Villars and K. Cenzual, eds. *β-SiC (SiC 3C) Crystal Structure: Datasheet from “PAULING FILE Multinaries Edition – 2012” in SpringerMaterials.*

[30] P. Villars and K. Cenzual, eds. *4H-SiC (SiC 4H) Crystal Structure: Datasheet from “PAULING FILE Multinaries Edition – 2012” in SpringerMaterials.*

[31] G. C. Capitani, S. Di Pierro, and G. Tempesta. “The 6H-SiC structure model: Further refinement from SCXRD data from a terrestrial moissanite”. In: *Am. Mineral.* 92.2-3 (2007), p. 403. DOI: 10.2138/am.2007.2346.

[32] V. Zeghbroeck. *Principles of Semiconductor Devices and Heterojunctions*. Prentice Hall PTR, 2007. ISBN: 9780130409041.

[33] G. Wellenhofer and U. Rössler. “Global Band Structure and Near-Band-Edge States”. In: *Phys. Status Solidi B* 202.1 (1997), pp. 107–123. DOI: 10.1002/1521-3951(199707)202:1<107::AID-PSSB107>3.0.CO;2-9.

[34] W. R. L. Lambrecht et al. “Electronic Band Structure of SiC Polytypes: A Discussion of Theory and Experiment”. In: *Phys. Status Solidi B* 202.1 (1997), pp. 5–33. DOI: 10.1002/1521-3951(199707)202:1<5::AID-PSSB5>3.0.CO;2-L.

[35] N. T. Son et al. “Electron effective masses and mobilities in high-purity 6H–SiC chemical vapor deposition layers”. In: *Appl. Phys. Lett.* 65.25 (1994), pp. 3209–3211. DOI: 10.1063/1.112956.

[36] N. T. Son et al. “Electron effective masses in 4H SiC”. In: *Appl. Phys. Lett.* 66.9 (1995), pp. 1074–1076. DOI: 10.1063/1.113576.

[37] C. Persson, U. Lindefelt, and B. E. Sernelius. “Band gap narrowing in n-type and p-type 3C-, 2H-, 4H-, 6H-SiC, and Si”. In: *J. Appl. Phys.* 86.8 (1999), p. 4419. ISSN: 00218979. DOI: 10.1063/1.371380.

[38] Y. Varshni. “Temperature dependence of the energy gap in semiconductors”. In: *Physica* 34.1 (1967), pp. 149–154. ISSN: 0031-8914. DOI: 10.1016/0031-8914(67)90062-6.

[39] S. Sridhara et al. “Penetration depths in the ultraviolet for 4H, 6H and 3C silicon carbide at seven common laser pumping wavelengths”. In: *Mat. Sci. Eng. B-Solid* 61-62 (1999), pp. 229–233. ISSN: 09215107. DOI: 10.1016/S0921-5107(98)00508-X.

[40] G. B. Dubrovskii, a. a. Lepneva, and E. I. Radovanova. “Optical absorption associated with superlattice in silicon carbide crystals”. In: *Phys. Status Solidi* 57 (1973), pp. 423–431. ISSN: 03701972. DOI: 10.1002/pssb.2220570142.

[41] S. Limpijumnong et al. “Optical-absorption bands in the 1–3 ev range in n-type sic polytypes”. In: *Phys. Rev. B - Condens. Matter Mater. Phys.* 59.20 (1999), pp. 12890–12899. ISSN: 1550235X. DOI: 10.1103/PhysRevB.59.12890.

[42] V. Jokubavicius et al. “Morphological and Optical Stability in Growth of Fluorescent SiC on Low Off-Axis Substrates”. In: *Mater. Sci. Forum* 740-742 (2013), pp. 19–22. ISSN: 1662-9752. DOI: 10.4028/www.scientific.net/MSF.740-742.19.

[43] S. Murata et al. “Dependence of DAP Emission Properties on Impurity Concentrations in N-/B-co-doped 6H-SiC”. In: *Silicon Carbide and Related Materials 2006*. Vol. 556. Materials Science Forum. Trans Tech Publications, Aug. 2007, pp. 335–338. DOI: 10.4028/www.scientific.net/MSF.556-557.335.

[44] Y. Tairov and V. Tsvetkov. “Progress in controlling the growth of polytypic crystals”. In: *Prog. Cryst. Growth Charact.* 7.1-4 (Jan. 1983), pp. 111–162. ISSN: 01463535. DOI: 10.1016/0146-3535(83)90031-X.

[45] J. W. Sun et al. “Shockley-Frank stacking faults in 6H-SiC”. In: *J. Appl. Phys.* 111.11 (2012). ISSN: 00218979. DOI: 10.1063/1.4729064.

[46] W. Suttrop, G. Pensl, and P. Lanig. “Boron-related deep centers in 6H-SiC”. In: *Appl. Phys. A* 51.3 (1990), pp. 231–237. ISSN: 07217250. DOI: 10.1007/BF00324007.

[47] J. R. Lakowicz. *Principles of Fluorescence Spectroscopy*. Springer US, 2006, p. 954. ISBN: 978-0-387-46312-4. DOI: 10.1007/978-0-387-46312-4.

[48] D. V. O’Connor and D. Phillips. *Time-Correlated Single Photon Counting*. Academic Press, 1984, p. 298. ISBN: 978-0-12-524140-3. DOI: 10.1016/B978-0-12-524140-3.50003-4.

[49] Y. Wei, A. T. Tarekegne, and H. Ou. “Influence of negative- U centers related carrier dynamics on donor-acceptor-pair emission in fluorescent SiC”. In: *J. Appl. Phys.* 124.5 (Aug. 2018), p. 054901. ISSN: 0021-8979. DOI: 10.1063/1.5037167.

[50] P. B. Klein. “Carrier lifetime measurement in n- 4H-SiC epilayers”. In: *J. Appl. Phys.* 103.3 (2008), p. 033702. ISSN: 00218979. DOI: 10.1063/1.2837105.

[51] Y. Ou et al. “Donor-acceptor-pair emission characterization in N-B doped fluorescent SiC”. In: *Opt. Mater. Express* 1.8 (2011), p. 1439. ISSN: 2159-3930. DOI: 10.1364/OME.1.001439.

[52] M. Ikeda, H. Matsunami, and T. Tanaka. “Site-dependent donor and acceptor levels in 6H-SiC”. In: *J. Lumin.* 20.2 (Mar. 1979), pp. 111–129. ISSN: 00222313. DOI: 10.1016/0022-2313(79)90042-5.

[53] a. O. Evwaraye et al. “Boron acceptor levels in 6H-SiC bulk samples”. In: *Appl. Phys. Lett.* 71.9 (Sept. 1997), pp. 1186–1188. ISSN: 0003-6951. DOI: 10.1063/1.119620.

[54] M. Ikeda, H. Matsunami, and T. Tanaka. “Site effect on the impurity levels in 4H, 6H, and 15R SiC”. In: *Phys. Rev. B* 22.6 (1980), pp. 2842–2854. ISSN: 01631829. DOI: 10.1103/PhysRevB.22.2842.

[55] T. Stiasny and R. Helbig. “Thermoluminescence and Related Electronic Processes of 4H/6H-SiC”. In: *Phys. Status Solidi* 162.1 (1997), pp. 239–249. ISSN: 00318965. DOI: 10.1002/1521-396X(199707)162:1<239::AID-PSSA239>3.0.CO;2-K.

[56] I. Gorban, A. Gumenyuk, and Y. Suleimanov. “Energy and Kinetic Parameters of Nitrogen Impurity in Silicon Carbide Crystals”. In: *Sov. Phys. Solid State* 8.11 (1967), pp. 2746–2747.

[57] A. Halperin, E. Zacks, and E. Silberg. “The thermoluminescence (TL), phosphorescence and cryoluminescence of n-type hexagonal (6H) SiC crystals”. In: *J. Lumin.* 6.4 (1973), pp. 304–319. ISSN: 00222313. DOI: 10.1016/0022-2313(73)90026-4.

[58] T. Stiasny and R. Helbig. “Impurities in 4H and 6H SiC crystals, characterized by thermoluminescence and thermally stimulated conductivity”. In: *SILICON CARBIDE AND RELATED MATERIALS 1995* 142 (1996), pp. 389–392.

[59] A. Halperin and A. A. Braner. “Evaluation of thermal activation energies from glow curves”. In: *Phys. Rev.* 117.2 (1960), pp. 408–415. ISSN: 0031899X. DOI: 10.1103/PhysRev.117.408.

[60] T. Stiasny and R. Helbig. “The trap emptying process of low temperature thermoluminescence of 6H-SiC single crystals”. In: *J. Appl. Phys.* 79.8 (1996), pp. 4152–4156. ISSN: 00218979. DOI: 10.1063/1.361781.

[61] M. Lades. “Modeling and Simulation of Wide Bandgap Semiconductor Devices : 4H / 6H-SiC”. PhD thesis. Technische Universität München, 2000, pp. 1–156. ISBN: 3826597990.

[62] M. Anikin et al. “Investigation of the deep levels in SiC by capacitance spectroscopy methods”. In: *Sov. Phys. Semicond.* 19 (1985), pp. 69–71.

[63] W. Hartung et al. “Analysis of electronic levels in SiC: V, N, Al powders and crystals using thermally stimulated luminescence”. In: *Mater. Sci. Eng. B* 61-62 (1999), pp. 102–106. ISSN: 09215107. DOI: 10.1016/S0921-5107(98)00455-3.

[64] P. G. Baranov. “Electronic Structure of Acceptors in Silicon Carbide”. In: *Silicon Carbide, III-Nitrides Relat. Mater.* Vol. 264. Materials Science Forum. Trans Tech Publications, 1997, pp. 581–586. DOI: 10.4028/www.scientific.net/MSF.264-268.581.

[65] J. R. Jenny et al. “On the compensation mechanism in high-resistivity 6H–SiC doped with vanadium”. In: *J. Appl. Phys.* 78.6 (Sept. 1995), pp. 3839–3842. ISSN: 0021-8979. DOI: 10.1063/1.359899.

[66] H. M. Hobgood et al. “Semi-insulating 6H–SiC grown by physical vapor transport”. In: *Appl. Phys. Lett.* 66.11 (Mar. 1995), pp. 1364–1366. ISSN: 0003-6951. DOI: 10.1063/1.113202.

[67] W. Hoogenstraaten. “Electron traps in zinc sulphide phosphors”. In: *Philips Research Rept.* 13 (1958), pp. 515–693.

[68] W. H. Press et al. *Numerical Recipes 3rd Edition: The Art of Scientific Computing*. 3rd ed. Cambridge University Press, 2007. ISBN: 9780521880688.

[69] J. W. Sun et al. “Room temperature luminescence properties of fluorescent SiC as white light emitting diode medium”. In: *Thin Solid Films* 522 (2012), pp. 33–35. ISSN: 00406090. DOI: 10.1016/j.tsf.2012.02.012.

[70] S. Greulich-Weber. “EPR and ENDOR Investigations of Shallow Impurities in SiC Polytypes”. In: *Phys. status solidi* 162.1 (July 1997), pp. 95–151. DOI: 10.1002/1521-396X(199707)162:1<95::AID-PSSA95>3.0.CO;2-X.

[71] Y. Wei, A. T. Tarekegne, and H. Ou. “Double D-centers related donor-acceptor-pairs emission in fluorescent silicon carbide”. In: *Opt. Mater. Express* 9.1 (Jan. 2019), pp. 295–303. DOI: 10.1364/OME.9.000295.

[72] M. S. Mazzola et al. “Observation of the *D*-center in *6H*-SiC *p*-*n* diodes grown by chemical vapor deposition”. In: *Appl. Phys. Lett.* 64.20 (1994), p. 2730. DOI: 10.1063/1.111457.

[73] A. v. Duijn-Arnold et al. “Electronic structure of the N donor center in *4H*-SiC and *6H*-SiC”. In: *Phys. Rev. B* 64.8 (Aug. 2001), p. 085206. DOI: 10.1103/PhysRevB.64.085206.

[74] B. Aradi et al. “Boron Centers in 4H-SiC”. In: *Mater. Sci. Forum* 353-356 (Jan. 2001), pp. 455–458. ISSN: 1662-9752. DOI: 10.4028/www.scientific.net/MSF.353-356.455.

[75] M. Bockstedte, A. Mattausch, and O. Pankratov. “Boron in SiC: Structure and Kinetics”. In: *Mater. Sci. Forum* 353-356 (Jan. 2001), pp. 447–450. DOI: 10.4028/www.scientific.net/MSF.353-356.447.

[76] A. Fukumoto. “First-principles calculations of *p*-type impurities in cubic SiC”. In: *Phys. Rev. B* 53.8 (1996), pp. 4458–4461. DOI: 10.1103/PhysRevB.53.4458.

[77] P. Deák et al. “A Shallow Acceptor Complex in 4H-SiC: $Al_{Si}N_CAl_{Si}$”. In: *Mater. Sci. Forum* 433-436 (Sept. 2003), pp. 523–526. DOI: 10.4028/www.scientific.net/MSF.433-436.523.

[78] K. Kawahara, J. Suda, and T. Kimoto. “Deep levels generated by thermal oxidation in p-type 4H-SiC”. In: *J. Appl. Phys.* 113.3 (2013), p. 033705. DOI: 10.1063/1.4776240.

[79] K. Danno, D. Nakamura, and T. Kimoto. “Investigation of carrier lifetime in 4H-SiC epilayers and lifetime control by electron irradiation”. In: *Appl. Phys. Lett.* 90.20 (2007), pp. 7–10. ISSN: 00036951. DOI: 10.1063/1.2740580.

[80] L. Storasta et al. “Deep levels created by low energy electron irradiation in 4H-SiC”. In: *J. Appl. Phys.* 96.9 (2004), p. 4909. DOI: 10.1063/1.1778819.

[81] M. Bockstedte, A. Mattausch, and O. Pankratov. “*Ab initio* study of the migration of intrinsic defects in *3C*-SiC”. In: *Phys. Rev. B* 68.20 (2003), p. 205201. DOI: 10.1103/PhysRevB.68.205201.

[82] D. Larkin. “SiC Dopant Incorporation Control Using Site-Competition CVD”. In: *Phys. status solidi* 202.1 (July 1997), pp. 305–320. DOI: 10.1002/1521-3951(199707)202:1<305::AID-PSSB305>3.0.CO;2-9.

[83] P. Råback. “Modeling of the sublimation growth of silicon carbide crystals”. PhD thesis. Helsinki University of Technology, 1999, pp. 1–130. ISBN: 9529821549.

[84] C. Wang, J. Bernholc, and R. F. Davis. “Formation energies, abundances, and the electronic structure of native defects in cubic SiC”. In: *Phys. Rev. B* 38.17 (1988), pp. 12752–12755. ISSN: 01631829. DOI: 10.1103/PhysRevB.38.12752.

[85] A. Mattausch, M. Bockstedte, and O. Pankratov. “Self Diffusion in SiC: the Role of Intrinsic Point Defects”. In: *Mater. Sci. Forum* 353-356 (Jan. 2001), pp. 323–326. DOI: 10.4028/www.scientific.net/MSF.353-356.323.

[86] B. Aradi et al. “Impurity-controlled dopant activation: Hydrogen-determined site selection of boron in silicon carbide”. In: *Appl. Phys. Lett.* 79.17 (2001), pp. 2746–2748. DOI: 10.1063/1.1410337.

[87] M. Lax. “Cascade Capture of Electrons in Solids”. In: *Phys. Rev.* 119.5 (Sept. 1960), pp. 1502–1523. ISSN: 0031-899X. DOI: 10.1103/PhysRev.119.1502.

[88] P. W. Anderson. “Model for the Electronic Structure of Amorphous Semiconductors”. In: *Phys. Rev. Lett.* 34 (15 Apr. 1975), pp. 953–955. DOI: 10.1103/PhysRevLett.34.953.

[89] G. D. Watkins and J. R. Troxell. “Negative-U Properties for Point Defects in Silicon”. In: *Phys. Rev. Lett.* 44 (9 Mar. 1980), pp. 593–596. DOI: 10.1103/PhysRevLett.44.593.

[90] C. Hemmingsson et al. “Capture cross sections of electron irradiation induced defects in 6H-SiC”. In: *J. Appl. Phys.* 84.1998 (1998), p. 704. ISSN: 00218979. DOI: 10.1063/1.368125.

[91] C. G. Hemmingsson, N. T. Son, and E. Janzén. "Observation of negative-U centers in 6H silicon carbide". In: *Appl. Phys. Lett.* 74.6 (1999), p. 839. ISSN: 00036951. DOI: 10.1063/1.123401.

[92] M. Weidner et al. "Formation and annihilation of intrinsic-related defect centers in high energy electron-irradiated or ion-implanted 4H- and 6H-silicon carbide". In: *Physica B* 308-310 (2001), pp. 633–636. ISSN: 0921-4526. DOI: 10.1016/S0921-4526(01)00772-4.

[93] G. Pensl et al. "Implantation-induced defects in silicon carbide". In: *Physica B* 340-342 (Dec. 2003), pp. 121–127. ISSN: 09214526. DOI: 10.1016/j.physb.2003.09.054.

[94] S. Sasaki et al. "Major deep levels with the same microstructures observed in n-type 4H-SiC and 6H-SiC". In: *J. Appl. Phys.* 109.1 (2011), p. 013705. ISSN: 00218979. DOI: 10.1063/1.3528124.

[95] M. Gong et al. "Electron-irradiation-induced deep levels in n-type 6H-SiC". In: *J. Appl. Phys.* 85.11 (1999), pp. 7604–7608. DOI: 10.1063/1.370561.

[96] A. Kawasuso et al. "Vacancies and deep levels in electron-irradiated 6H SiC epilayers studied by positron annihilation and deep level transient spectroscopy". In: *J. Appl. Phys.* 90.7 (2001), pp. 3377–3382. DOI: 10.1063/1.1402144.

[97] T. A. G. Eberlein, R. Jones, and P. R. Briddon. "Z1/Z2 Defects in 4H—SiC". In: *Phys. Rev. Lett.* 90.22 (2003), p. 225502. ISSN: 0031-9007. DOI: 10.1103/PhysRevLett.90.225502.

[98] M. Aboelfotoh and J. Doyle. "Defect energy levels in electron-irradiated and deuterium-implanted 6H silicon carbide". In: *Phys. Rev. B* 59.16 (1999), pp. 10823–10829. ISSN: 0163-1829. DOI: 10.1103/PhysRevB.59.10823.

[99] X. D. Chen et al. "Deep level transient spectroscopic study of neutron-irradiated n-type 6H-SiC". In: *J. Appl. Phys.* 94.5 (2003), pp. 3004–3010. ISSN: 00218979. DOI: 10.1063/1.1598629.

[100] X. D. Chen et al. "Low Energy Electron Irradiation Induced Deep Level Defects in 6H-SiC: The Implication for the Microstructure of the Deep Levels E1/E2". In: *Phys. Rev. Lett.* 92.12 (Mar. 2004), p. 125504. ISSN: 0031-9007. DOI: 10.1103/PhysRevLett.92.125504.

[101] A. Zywietz, J. Furthmüller, and F. Bechstedt. "Vacancies in SiC: Influence of Jahn-Teller distortions, spin effects, and crystal structure". In: *Phys. Rev. B* 59.23 (1999), pp. 15166–15180. ISSN: 0163-1829. DOI: 10.1103/PhysRevB.59.15166.

[102] F. Bechstedt, A. Zywietz, and J. Furthmüller. "Carbon vacancy in SiC: A negative- U system". In: *Europhys. Lett.* 44.3 (Nov. 1998), pp. 309–314. ISSN: 0295-5075. DOI: 10.1209/epl/i1998-00475-5.

[103] V. Y. Bratus' et al. "Positively charged carbon vacancy in three inequivalent lattice sites of 6H-SiC: Combined EPR and density functional theory study". In: *Phys. Rev. B - Condens. Matter Mater. Phys.* 71.12 (2005), pp. 1–22. ISSN: 10980121. DOI: 10.1103/PhysRevB.71.125202.

[104] T. Dalibor et al. "Deep Defect Centers in Silicon Carbide Monitored with Deep Level Transient Spectroscopy". In: *Phys. Status Solidi A* 162.1 (1997), pp. 199–225. ISSN: 1521-396X. DOI: 10.1002/1521-396X(199707)162:1<199::AID-PSSA199>3.0.CO;2-0.

[105] Lebedev, Veinger, and Davydov. "Doping of n-type 6H-SiC and 4H-SiC with defects created with a proton beam". In: *J. Appl. Phys.* 88.2000 (2000), pp. 6265–6271. ISSN: 00218979. DOI: 10.1063/1.1309055.

[106] A. Kurtz et al. "Deep-level spectroscopy in metal-insulator-semiconductor structures". In: *J. Phys. D* 50.6 (Feb. 2017), p. 065104. ISSN: 0022-3727. DOI: 10.1088/1361-6463/aa5006.

[107] J. P. Bergman, O. Kordina, and E. Janzén. "Time Resolved Spectroscopy of Defects in SiC". In: *Phys. Status Solidi A* 162.1 (1997), pp. 65–77. ISSN: 1521-396X. DOI: 10.1002/1521-396X(199707)162:1<65::AID-PSSA65>3.0.CO;2-2.

[108] J. P. Bergman. "Carrier lifetimes in SiC, studied by time resolved photoluminescence spectroscopy". In: *Diam. Relat. Mater.* 6.10 (1997), pp. 1324–1328. ISSN: 09259635. DOI: 10.1016/S0925-9635(97)00107-6.

[109] E. Janzén et al. "Chapter 21 - Defects in SiC". In: *Defects in Microelectronic Materials and Devices*. Ed. by D. Fleetwood and R. Schrimpf. Taylor & Francis, 2008, pp. 615–670. ISBN: 9781420043761.

[110] L. W. Aukerman and M. F. Millea. "Steady-state recombination via donor-acceptor pairs". In: *Phys. Rev.* 148.2 (1966), pp. 759–765. ISSN: 0031899X. DOI: 10.1103/PhysRev.148.759.

[111] A. Koizumi et al. "E1/E2 traps in 6H-SiC studied with Laplace deep level transient spectroscopy". In: *Appl. Phys. Lett.* 102.3 (2013), pp. 2–6. ISSN: 00036951. DOI: 10.1063/1.4788814.

[112] V. Abakumov, V. Perel, and I. Yassievich. "Capture of carriers by attractive centers in semiconductors". In: *Sov. Phys. Semicond.* 12.1 (1978), pp. 1–18.

[113] P. B. Klein et al. "Lifetime-limiting defects in n - 4H-SiC epilayers". In: *Appl. Phys. Lett.* 88.5 (2006), pp. 1–3. ISSN: 00036951. DOI: 10.1063/1.2170144.

[114] W. Shockley and W. T. Read. "Statistics of the Recombination of Holes and Electrons". In: *Phys. Rev.* 87.46 (1952), pp. 835–842. ISSN: 0031-899X. DOI: dx.doi.org/10.1103/PhysRev.87.835.

[115] W. Shockley and J. T. Last. "Statistics of the charge distribution for a localized flaw in a semiconductor". In: *Phys. Rev.* 107.2 (1957), pp. 392–396. ISSN: 0031899X. DOI: 10.1103/PhysRev.107.392.

[116] S. Hagen, A. Van Kemenade, and J. Van Der Does De Bye. "Donor-acceptor pair spectra in 6H and 4H SiC doped with nitrogen and aluminium". In: *J. Lumin.* 8.1 (Sept. 1973), pp. 18–31. ISSN: 00222313. DOI: 10.1016/0022-2313(73)90032-X.

[117] D. G. Thomas, J. J. Hopfield, and W. M. Augustyniak. "Kinetics of Radiative Recombination at Randomly Distributed Donors and Acceptors". In: *Phys. Rev.* 140.1A (Oct. 1965). Ed. by Intergovernmental Panel on Climate Change, A202–A220. ISSN: 0031-899X. DOI: 10.1103/PhysRev.140.A202.

[118] A. A. Lebedev. "Deep level centers in silicon carbide: A review". In: *Semiconductors* 33.2 (1999), pp. 107–130. ISSN: 1063-7826. DOI: 10.1134/1.1187657.

[119] K. Neimontas et al. "The determination of high-density carrier plasma parameters in epitaxial layers, semi-insulating and heavily doped crystals of 4H-SiC by a picosecond four-wave mixing technique". In: *Semicond. Sci. Technol.* 21.7 (2006), pp. 952–958. ISSN: 02681242. DOI: 10.1088/0268-1242/21/7/021.

[120] N. Ramungul et al. "Carrier Lifetime Extraction from a 6H-SiC High Voltage p-i-n Rectifier Reverse Recovery Waveform". In: *Mater. Sci. Forum* 264-268 (1998), pp. 1065–1068. ISSN: 1662-9752. DOI: 10.4028/www.scientific.net/MSF.264-268.1065.

[121] A. Galeckas et al. "Auger recombination in 4H-SiC: Unusual temperature behavior". In: *Appl. Phys. Lett.* 71.22 (1997), p. 3269. ISSN: 00036951. DOI: 10.1063/1.120309.

[122] A. B. Sproul. "Dimensionless solution of the equation describing the effect of surface recombination on carrier decay in semiconductors". In: *J. Appl. Phys.* 76.5 (1994), pp. 2851–2854. DOI: 10.1063/1.357521.

[123] A. Galeckas et al. "Investigation of surface recombination and carrier lifetime in 4H/6H-SiC". In: *Mat. Sci. Eng. B-Solid* 61-62 (1999), pp. 239–243. ISSN: 09215107. DOI: 10.1016/S0921-5107(98)00510-8.

[124] L. F. Shampine and M. W. Reichelt. "The MATLAB ODE Suite". In: *SIAM J. Sci. Comput.* 18.1 (1997), pp. 1–22. DOI: 10.1137/S1064827594276424.

[125] K. Gulbinas et al. "Raman Scattering and Carrier Diffusion Study in Heavily Co-doped 6H-SiC Layers". In: *IOP Conf. Ser.: Mater. Sci. Eng.* 56 (Mar. 2014), p. 012005. ISSN: 1757-899X. DOI: 10.1088/1757-899X/56/1/012005.

[126] P. Ščajev and K. Jarašiunas. "Temperature- and excitation-dependent carrier diffusivity and recombination rate in 4H-SiC". In: *J. Phys. D* 46.26 (July 2013), p. 265304. ISSN: 0022-3727. DOI: 10.1088/0022-3727/46/26/265304.

[127] V. Grivickas et al. "Carrier lifetimes and influence of in-grown defects in N-B Co-doped 6H-SiC". In: *IOP Conf. Ser.: Mater. Sci. Eng.* 56.1 (2014), p. 012004. ISSN: 1757899X. DOI: 10.1088/1757-899X/56/1/012004.

[128] S. A. Reshanov et al. “Midgap Defects in 4H-, 6H- and 3C-SiC Detected by Deep Level Optical Spectroscopy”. In: *Mater. Sci. Forum* 457-460 (2004), pp. 513–516. ISSN: 1662-9752. DOI: 10.4028/www.scientific.net/MSF.457-460.513.

[129] A. Suzuki, H. Matsunam, and T. Tanaka. “Photoluminescence spectra of Ga-doped and Al-doped 4H-SiC”. In: *J. Phys. Chem. Solids* 38.7 (1977), pp. 693–699. ISSN: 00223697. DOI: 10.1016/0022-3697(77)90059-2.

[130] T. Kimoto et al. “Reduction of doping and trap concentrations in 4H–SiC epitaxial layers grown by chemical vapor deposition”. In: *Appl. Phys. Lett.* 79.17 (Oct. 2001), pp. 2761–2763. ISSN: 0003-6951. DOI: 10.1063/1.1413724.

[131] T. Kimoto, K. Hashimoto, and H. Matsunami. “Effects of C/Si Ratio in Chemical Vapor Deposition of 4H-SiC($11\bar{2}0$) and ($03\bar{3}8$)”. In: *Jpn. J. Appl. Phys.* 42.Part 1, No. 12 (Dec. 2003), pp. 7294–7295. ISSN: 0021-4922. DOI: 10.1143/JJAP.42.7294.

[132] S. W. Huh et al. “Residual impurities and native defects in 6H-SiC bulk crystals grown by halide chemical-vapor deposition”. In: *J. Appl. Phys.* 99.1 (Jan. 2006), p. 013508. ISSN: 0021-8979. DOI: 10.1063/1.2150593.

[133] Y. Vodakov et al. “Use of Ta-Container for Sublimation Growth and Doping of SiC Bulk Crystals and Epitaxial Layers”. In: *Phys. status solidi* 202.1 (July 1997), pp. 177–200. ISSN: 0370-1972. DOI: 10.1002/1521-3951(199707)202:1<177::AID-PSSB177>3.0.CO;2-I.

[134] Q. Li et al. “Properties of 6H–SiC crystals grown by hydrogen-assisted physical vapor transport”. In: *Appl. Phys. Lett.* 86.20 (May 2005), p. 202102. ISSN: 0003-6951. DOI: 10.1063/1.1923181.

[135] J. Zhang et al. “Electrically active defects in n-type 4H-silicon carbide grown in a vertical hot-wall reactor”. In: *J. Appl. Phys.* 93.8 (2003), pp. 4708–4714. ISSN: 00218979. DOI: 10.1063/1.1543240.

[136] I. Pintilie et al. “Formation of the $Z_{1,2}$ deep-level defects in 4H-SiC epitaxial layers: Evidence for nitrogen participation”. In: *Appl. Phys. Lett.* 81.25 (2003), pp. 4841–4843. ISSN: 00036951. DOI: 10.1063/1.1529314.

[137] T. Dalibor et al. “Oxygen in silicon carbide: Shallow donors and deep acceptors”. In: *Mat. Sci. Eng. B-Solid* 61-62 (1999), pp. 454–459. DOI: 10.1016/S0921-5107(98)00554-6.

[138] T. Kimoto et al. “Photoluminescence of Ti doped 6H-SiC grown by vapor phase epitaxy”. In: *Jpn. J. Appl. Phys.* 30.2B (1991), pp. L289–L291. DOI: 10.1143/JJAP.30.L289.

[139] Z. D. Sha et al. “Initial study on the structure and photoluminescence properties of SiC films doped with Co”. In: *Physica E: Low-Dimensional Systems and Nanostructures* 35.1 (2006), pp. 38–41. DOI: 10.1016/j.physe.2006.05.009.

[140] M. Tajima et al. “Mapping of Vanadium-Related Luminescence on SiC Wafer at Room Temperature”. In: *Jpn. J. Appl. Phys.* 36.9A (1997), p. L1185. DOI: 10.1143/JJAP.36.L1185.

[141] N. T. Son et al. “Photoluminescence and Zeeman effect in chromium-doped 4H and 6H SiC”. In: *J. Appl. Phys.* 86.8 (1999), pp. 4348–4353. DOI: 10.1063/1.371368.

[142] Y. Ou et al. “Omnidirectional luminescence enhancement of fluorescent SiC via pseudoperiodic antireflective subwavelength structures”. In: *Opt. Lett.* 37.18 (2012), pp. 3816–8. DOI: 10.1364/OL.37.003816.

[143] C. Würth et al. “Relative and absolute determination of fluorescence quantum yields of transparent samples”. In: *Nat. Protoc.* 8.8 (Aug. 2013), pp. 1535–1550. ISSN: 1754-2189. DOI: 10.1038/nprot.2013.087.

[144] J. C. De Mello, H. F. Wittmann, and R. H. Friend. “An improved experimental determination of external photoluminescence quantum efficiency”. In: *Adv. Mater.* 9.3 (1997), pp. 230–232. ISSN: 09359648. DOI: 10.1002/adma.19970090308.

[145] D. Braun et al. “Photo- and electroluminescence efficiency in poly(dialkoxy-p-phenylenevinylene)”. In: *Synth. Met.* 66.1 (Sept. 1994), pp. 75–79. ISSN: 03796779. DOI: 10.1016/0379-6779(94)90164-3.

[146] N. Greenham et al. “Measurement of absolute photoluminescence quantum efficiencies in conjugated polymers”. In: *Chem. Phys. Lett.* 241.1-2 (July 1995), pp. 89–96. ISSN: 00092614. DOI: 10.1016/0009-2614(95)00584-Q.

[147] B. L.-o. Pålsson and A. P. Monkman. “Measurements of Solid-State Photoluminescence Quantum Yields of Films Using a Fluorimeter Measurements of Solid-State Photoluminescence Quantum Yields of Films Using a Fluorimeter”. In: *Adv. Mater.* 14.5 (2002), pp. 933–935. ISSN: 0935-9648. DOI: 10.1002/1521-4095(20020517)14.

[148] A. R. Johnson et al. “Absolute photoluminescence quantum efficiency measurement of light-emitting thin films”. In: *Rev. Sci. Instrum.* 78.9 (Sept. 2007), p. 096101. ISSN: 0034-6748. DOI: 10.1063/1.2778614.

[149] N. Murase and C. Li. “Consistent determination of photoluminescence quantum efficiency for phosphors in the form of solution, plate, thin film, and powder”. In: *J. Lumin.* 128.12 (Dec. 2008), pp. 1896–1903. ISSN: 00222313. DOI: 10.1016/j.jlumin.2008.05.016.

[150] S. Leyre et al. “Absolute determination of photoluminescence quantum efficiency using an integrating sphere setup”. In: *Rev. Sci. Instrum.* 85.12 (Dec. 2014), p. 123115. ISSN: 0034-6748. DOI: 10.1063/1.4903852.

[151] L. Porrès et al. “Absolute Measurements of Photoluminescence Quantum Yields of Solutions Using an Integrating Sphere”. In: *J. Fluoresc.* 16.2 (Mar. 2006), pp. 267–273. ISSN: 1053-0509. DOI: 10.1007/s10895-005-0054-8.

[152] H. Ishida et al. “Recent advances in instrumentation for absolute emission quantum yield measurements”. In: *Coord. Chem. Rev.* 254.21-22 (Nov. 2010), pp. 2449–2458. ISSN: 00108545. DOI: 10.1016/j.ccr.2010.04.006.

[153] C. Würth et al. “Evaluation of a commercial integrating sphere setup for the determination of absolute photoluminescence quantum yields of dilute dye solutions”. In: *Appl. Spectrosc.* 64.7 (2010), pp. 733–741. ISSN: 00037028. DOI: 10.1366/000370210791666390.

[154] W. Choyke. “Optical properties of polytypes of SiC: interband absorption, and luminescence of nitrogen-exciton complexes”. In: *Silicon Carbide–1968*. Ed. by H. Henisch and R. Roy. Elsevier, 1969, S141–S152. DOI: 10.1016/B978-0-08-006768-1.50018-8.

[155] A. Savitzky and M. J. E. Golay. “Smoothing and Differentiation of Data by Simplified Least Squares Procedures.” In: *Anal. Chem.* 36.8 (July 1964), pp. 1627–1639. ISSN: 0003-2700. DOI: 10.1021/ac60214a047.

[156] I. ISO and B. OIML. “Guide to the Expression of Uncertainty in Measurement”. In: *Geneva, Switzerland* (1995).

[157] T. Hayashi et al. “Impacts of reduction of deep levels and surface passivation on carrier lifetimes in p -type 4H-SiC epilayers”. In: *J. Appl. Phys.* 109.11 (June 2011), p. 114502. ISSN: 0021-8979. DOI: 10.1063/1.3583657.

[158] M. Takeshima. “Effect of Auger recombination on laser operation in Ga 1− x Al x As”. In: *J. Appl. Phys.* 58.10 (Nov. 1985), pp. 3846–3850. ISSN: 0021-8979. DOI: 10.1063/1.335600.

[159] A. Galeckas et al. “Free carrier absorption and lifetime mapping in 4H SiC epilayers”. In: *J. Appl. Phys.* 81.8 (Apr. 1997), pp. 3522–3525. ISSN: 0021-8979. DOI: 10.1063/1.365050.

[160] P. Ščajev et al. “Fast and slow carrier recombination transients in highly excited 4H– and 3C–SiC crystals at room temperature”. In: *J. Appl. Phys.* 108.2 (July 2010), p. 023705. ISSN: 0021-8979. DOI: 10.1063/1.3459894.

[161] P. Ščajev. “Application of excite-probe techniques for determination of surface, bulk and nonlinear recombination rates in cubic SiC”. In: *Mater. Sci. Eng. B* 185.1 (July 2014), pp. 37–44. ISSN: 09215107. DOI: 10.1016/j.mseb.2014.02.006.

APPENDIX A

Python code for calculating the essential parameters of 6H-SiC

Listing A.1: The source code written in Python for calculating the temperature-dependent n_0, E_g, and E_F for all seven 6H f-SiC samples included in this thesis, where the calculated values have been presented in Fig. 2.10.

```
import numpy as np
import string

########################################
# Sample specifications
########################################

samples = {'ELS111': [ 4.0e16, 8.0e18],
           'ELS115': [ 3.2e18, 6.9e18],
           'ELS116': [ 6.0e18, 6.9e18],
           'ELS117': [ 9.0e18, 4.4e18],
           'ELS118': [ 9.2e18, 5.2e18],
           'ELS569': [2.85e18, 1.1e18],
           'ELS571': [2.55e18, 1.5e18]}

########################################
# Constants
########################################

# Plank constant [m^2.kg.s^-1]
h = 6.63e-34

# Speed of light [m.s^-1]
c = 299792458

# electron volt [J]
eV = 1.602e-19

# Boltzmann constant [m^2.kg.s^-2.K^-1]
k = 1.381e-23

# static mass of electron [kg]
m_0 = 9.11e-31

# Vacuum permittivity [F.m^-1]
sigma_0 = 8.8542e-12

```

```
# bandgap of 6H SiC
# for low temperature / undoped SiC
E_g_original = 3.10*eV

# Donor level (cubic site, k1)
E_DC1 = 0.1376*eV

# Donor level (cubic site, k2)
E_DC2 = 0.1424*eV

# Donor level (hexagonal site)
E_DH = 0.081*eV

# Acceptor level (D-center)
E_AD = 0.58*eV
#E_AD = 0.73*eV

# Effective mass of electron [kg] (C. Persson et al., JAP 1997)
# Link: http://www.iue.tuwien.ac.at/phd/ayalew/node62.html
m_e_eff = 0.71*m_0

# Effective mass of hole [kg] (N.T Son et al., PRB 2000)
# Link: http://www.iue.tuwien.ac.at/phd/ayalew/node62.html
m_h_eff = 0.90*m_0

# Ratio of cubic site at donor level
R_DC = 2/3

# Ratio of hexagonal site at donor level
R_DH = 1/3

# Relative permittivity of 6H SiC
sigma_r = 9.66

# Degeneracy factor of Donors in 6H SiC
g_D = 2

# Degeneracy factor of Donors in 6H SiC
g_A = 4

# Number of conduction band minima
M_C = 6

########################################
# Control parameters for iteration
########################################

# Number of the step for n0 calculation
# (must be a even number)
num_step = 1000000

# Function for calculation a series of
# the value of n0 regarding to
# the value of n=Nd-Na and temperature
def f_n0(n, N_D, N_A, temp):
```

```
    n0_series=list()
    for n0 in np.arange(n/num_step, n+n/num_step, n/num_step):
        # Effective density of states in conduction band [cm^-3]
        N_c    = 2*M_C*(2*np.pi*m_e_eff*k*temp/h**2)**1.5/1e6
        # Effective density of states in valence band [cm^-3]
        N_v    = 2*(2*np.pi*m_h_eff*k*temp/h**2)**1.5/1e6
        Nas_c1 = N_c/2*np.exp(-E_DC1/(k*temp))
        Nas_c2 = N_c/2*np.exp(-E_DC2/(k*temp))
        Nas_h  = N_c/2*np.exp( -E_DH/(k*temp))
        result = N_D*Nas_c1/(Nas_c1+n0)+N_D*Nas_c2/(Nas_c2+n0)+N_D*Nas_h/(
    Nas_h+n0)-N_A-n0
  n0_series.append(result)
    return n0_series

def f_p0(n, N_D, N_A, temp):
    p0_series=list()
    for p0 in np.arange(n/num_step, n+n/num_step, n/num_step):
        # Effective density of states in conduction band [cm^-3]
        N_c    = 2*M_C*(2*np.pi*m_e_eff*k*temp/h**2)**1.5/1e6
        # Effective density of states in valence band [cm^-3]
        N_v    = 2*(2*np.pi*m_h_eff*k*temp/h**2)**1.5/1e6
        N_star = N_v/4*np.exp(-E_AD/(k*temp))
        result = N_A*N_star/(N_star+p0)-N_D-p0
  p0_series.append(result)
    return p0_series

# Function for solving the neutrality equation
def find_zero(n0):
    for idx in range(num_step/2):
        if n0[idx]*n0[-1-idx] < 0: continue
        elif n0[idx]*n0[-1-idx] == 0:
            if n0[idx] == 0:
                return idx
    break
            else:
    return num_step/2-idx-1
    break
        else:
      if n0[idx]*n0[idx-1] > 0:
    if abs(n0[-1-idx]) > abs(n0[-idx]):
        return num_step/2-idx
        break
    else:
        return num_step/2-idx-1
        break
      else:
    if abs(n0[idx]) > abs(n0[idx-1]):
            return idx-1
        break
    else:
        return idx
        break

# function for intrinsic carrier concentration
# for 6H SiC with different temperature
```

```
147 def n_i(T):
148     A = -8.18214
149     B = 21.7081
150     return 10**(A*(1000/T)+B)
151 
152 # Parameters for Yarshni Equation
153 # for bandgap shrinking vs. temperature
154 aa = 8.2e-4*eV
155 bb = 1.8e3
156 
157 # function for effective E_g calculation (n-type)
158 # consider the bandgap shrinking based on:
159 # 1) doping; 2) temperature
160 def Eg_n(N_c, n_0, N_D, T):
161     N_star_c1 = N_c/2*np.exp(-E_DC1/(k*T))
162     N_star_c2 = N_c/2*np.exp(-E_DC2/(k*T))
163     N_star_h  = N_c/2*np.exp( -E_DH/(k*T))
164     N_D_plus  = N_D/(1+n_0/N_star_c1)+N_D/(1+n_0/N_star_c2)+N_D/(1+n_0/
    N_star_h)
165     delta_E_c = -23.31*(N_D_plus/1e18)**0.33+2.26*(N_D_plus/1e18)**0.5;
166     delta_E_v =  26.57*(N_D_plus/1e18)**0.25 +0.43*(N_D_plus/1e18)**0.5;
167     delta_E_g = (delta_E_c-delta_E_v)/1000*eV;
168     bandgap   = (E_g_original+delta_E_g)-aa*(T**2)/(T+bb)
169     return [bandgap, delta_E_c/1000*eV, delta_E_v/1000*eV]
170 
171 def Eg_p(N_v, p_0, N_A, T):
172     N_star    = N_v/4*np.exp(-E_AD/(k*T))
173     N_A_minus = N_A/(1+p_0/N_star)
174     delta_E_c = -21.77*(N_A_minus/1e18)**0.25+0.1*(N_A_minus/1e18)**0.5;
175     delta_E_v = -27.88*(N_A_minus/1e18)**0.33+4.6*(N_A_minus/1e18)
    **0.5+50.13*(N_A_minus/1e18)**0.25;
176     delta_E_g = (delta_E_c-delta_E_v)/1000*eV;
177     bandgap   = (E_g_original+delta_E_g)-aa*(T**2)/(T+bb)
178     return [bandgap, delta_E_c/1000*eV, delta_E_v/1000*eV]
179 
180 # Loop: Temperature [K]
181 def freeCarrierArr(sample):
182     # Create the dict of n0 at different temperature
183     n0_T=dict()
184     if sample == "ELS117" or \
185        sample == "ELS118" or \
186        sample == "ELS569" or \
187        sample == "ELS571":
188         n0_init = samples[sample][0] - samples[sample][1]
189         for T in np.arange(25, 310, 15):
190             n_dif=n0_init
191             while True:
192                 n0_ser=f_n0(n_dif, samples[sample][0], samples[sample][1], T
    )
193                 if n0_ser[0]*n0_ser[num_step/2-1] == 0:
194                     if n0_ser[0] == 0:
195                         n0_T[str(T)]=n_dif/num_step
196                         break
197                     else:
198                         n0_T[str(T)]=n_dif
```

```
                        break
                elif n0_ser[0]*n0_ser[num_step/2-1] > 0:
                    if n0_ser[0] > 0: # n_0 underrated
                        n_dif=n_dif*5
                        continue
                    else: # n_0 overrated
                        n_dif=n_dif/10
                        continue
                else:
                    index=find_zero(n0_ser)
                    n0_T[str(T)]=(index+1)*n_dif/num_step
                    break
        return n0_T
    elif sample == "ELS111" or \
         sample == "ELS115" or \
         sample == "ELS116":
        n0_init = (samples[sample][1] - samples[sample][0])/1e6
        for T in np.arange(25, 310, 15):
            n_dif=n0_init
            while True:
                n0_ser=f_p0(n_dif, samples[sample][0], samples[sample][1], T
    )
                if n0_ser[0]*n0_ser[num_step/2-1] == 0:
                    if n0_ser[0] == 0:
                        n0_T[str(T)]=n_dif/num_step
                        break
                    else:
                        n0_T[str(T)]=n_dif
                        break
                elif n0_ser[0]*n0_ser[num_step/2-1] > 0:
                    if n0_ser[0] > 0: # n_0 underrated
                        n_dif=n_dif*5
                        continue
                    else: # n_0 overrated
                        n_dif=n_dif/10
                        continue
                else:
                    index=find_zero(n0_ser)
                    n0_T[str(T)]=(index+1)*n_dif/num_step
                    break
        return n0_T
    else:
        return "No such sample!"

def physPropEntry(sample):
#    physPropDict = {"freeCarrier": np.array([np.zeros(16), np.zeros(16)]),
#                    "bandGap":     np.array([np.zeros(16), np.zeros(16)]),
#                    "fermiLevel":  np.array([np.zeros(16), np.zeros(16)])}
    print "Here comes sample: "+sample
    n0_T      = freeCarrierArr(sample)
    for t in range(19):
        temp      = t*15+25
        N_c       = M_C*2*(2*np.pi*m_e_eff*k*temp/(h**2))**1.5/1e6
        N_v       =     2*(2*np.pi*m_h_eff*k*temp/(h**2))**1.5/1e6
        key       = str(temp)
```

```
253         if sample == "ELS117" or \
254            sample == "ELS118" or \
255            sample == "ELS569" or \
256            sample == "ELS571":
257             bdg_arr   = Eg_n(N_c, n0_T[key], samples[sample][0], temp)
258       bdg       = bdg_arr[0]
259             bdg_eV    = bdg/eV
260             E_i       = (bdg_arr[0]+bdg_arr[1]+bdg_arr[2])/2+0.5*k*temp*np.
    log(N_v/N_c)
261             intri     = np.sqrt(N_c*N_v)*np.exp((-bdg)/(2*k*temp))
262             p0        = intri**2/n0_T[key]
263             delta_E_F = k*temp*np.log((n0_T[key]-p0)/intri)
264             E_F_eV    = (E_i+delta_E_F)/eV
265         elif sample == "ELS111" or \
266              sample == "ELS115" or \
267              sample == "ELS116":
268             bdg_arr   = Eg_p(N_v, n0_T[key], samples[sample][1], temp)
269             bdg       = bdg_arr[0]
270             bdg_eV    = bdg/eV
271             E_i       = (bdg_arr[0]+bdg_arr[1]+bdg_arr[2])/2+0.5*k*temp*np.
    log(N_v/N_c)
272             intri     = np.sqrt(N_c*N_v)*np.exp((-bdg)/(2*k*temp))
273             n0        = intri**2/n0_T[key]
274             delta_E_F = k*temp*np.log((n0_T[key]-n0)/intri)
275             E_F_eV    = (E_i-delta_E_F)/eV
276         else:
277             return "Error: no such sample"
278   print "temp: {0:3d}, freeCarrier: {1:6.6e}, fermiLevel: {2:4.0f}, bandGap:
      {3:4.0f}".format(temp, n0_T[key], E_F_eV*1000, bdg_eV*1000)
279     return "Done!"
280
281 sic1 = physPropEntry("ELS111")
282 print "#################################################"
283 sic2 = physPropEntry("ELS115")
284 print "#################################################"
285 sic3 = physPropEntry("ELS116")
286 print "#################################################"
287 sic4 = physPropEntry("ELS117")
288 print "#################################################"
289 sic5 = physPropEntry("ELS118")
290 print "#################################################"
291 sic6 = physPropEntry("ELS569")
292 print "#################################################"
293 sic7 = physPropEntry("ELS571")
```

APPENDIX B

Matlab code & Simulink block diagram for negative-*U* centers related carrier dynamics

Listing B.1: The Matlab code which is mainly used to generate all the essential parameters implemented to the Simulink block diagram for running the negative-*U* centers related carrier dynamics simulation. Here we take the calculation of the essential parameters for the simulation of sample SN-1 as an example.

```
format long;

%% Key parameters for tuning

% ratio between sigma_p* and sigma_n*
ratio = 5;

% proportion of E1 defects density
% assuming the densities of E2L/H are comparable
% share_E = 0.02;

% Time period for simulation [s]
Sim_Time = 1e-4;

% Sample specifications for SN-1

% Donor concentration [cm^-3]
N_D = 9.0e18;
% Acceptor concentration [cm^-3]
N_A = 4.4e18;
% Epilayer thickness [cm]
th_ep = 45e-4+250e-4;

% ExpoDecay fitted parameters
A1 = 0.422446;
t1 = 0.0133032e-3;
A2 = 0.261774;
t2 = 0.0875561e-3;
A3 = 0.146685;
t3 = 0.653474e-3;
y0 = 0.0972076;

% Equilibrium electron concentration [cm^-3]
```

```
n_0 = 1.898024e18;

% Averaged TRPL lifetime
tau_av = (A1*t1^2+A2*t2^2+A3*t3^2)/(A1*t1+A2*t2+A3*t3);

%% General physical constants

% Plank constant [m^2.kg.s^-1]
h = 6.63e-34;

% Speed of light [m.s^-1]
c = 299792458;

% electron volt [J]
eV = 1.602e-19;

% Boltzmann constant [m^2.kg.s^-2.K^-1]
k = 1.381e-23;

% static mass of electron [kg]
m_0 = 9.11e-31;

% Vacuum permittivity [F.m^-1]
sigma_0 = 8.8542e-12;

% Temperature [K]
T = 300;

%% Constants for 6H SiC

% Relative permittivity of 6H SiC
sigma_r = 9.66;

% Degeneracy factor of Donors in 6H SiC
g_D = 2;

% Degeneracy factor of Donors in 6H SiC
g_A = 4;

% Number of conduction band minima
M_C = 6;

% density-of-state effective mass of electrons [kg]
m_de = 0.71*m_0;

% density-of-state effective mass of holes (at T=300 K) [kg]
m_dh = 0.90*m_0;

% effective mass of electron [kg]
% Link: http://www.iue.tuwien.ac.at/phd/ayalew/node62.html
m_e_eff = 0.71*m_0;
% m_e_eff = 2.28*m_0;

% effective mass of hole [kg]
% Link: http://www.iue.tuwien.ac.at/phd/ayalew/node62.html
```

```
m_h_eff = 0.90*m_0;

% average thermal velocity for electron [cm/s]
v_th_n = sqrt(3*k*T/m_e_eff)*100;

% average thermal velocity for hole [cm/s]
v_th_h = sqrt(3*k*T/m_h_eff)*100;

% bandgap of 6H SiC (C. Persson, et al., Journal of Applied Physics, 1999)
% low temperature / undoped 6H SiC
E_g_original = 3.10*eV;

% Donor level (cubic site, k1) [J]
% W. Suttrop et al., J. Appl. Phys. 72, 3708 ~1992
E_DC1 = 0.138*eV;

% Donor level (cubic site, k2) [J]
% W. Suttrop et al., J. Appl. Phys. 72, 3708 ~1992
E_DC2 = 0.142*eV;

% Donor level (hexagonal site) [J]
% W. Suttrop et al., J. Appl. Phys. 72, 3708 ~1992
E_DH = 0.081*eV;

% Ratio of cubic site at donor level
R_DC = 2/3;

% Ratio of hexagonal site at donor level
R_DH = 1/3;

% Acceptor level (D-center) [J]
% W. Suttrop et al., Appl. Phys. A 51,231-237 (1990)
E_AD = 0.58*eV;

%% Carriers density in 6H SiC

% Effective density of states in conduction band [cm^-3]
N_c = 2*M_C*(2*pi*m_de*k*T/h^2)^1.5/1e6;

% Effective density of states in valence band [cm^-3]
N_v = 2*(2*pi*m_dh*k*T/h^2)^1.5/1e6;

% An auxilary constant for n_0 calculation Link: http://ecee.colorado.edu/~
    bart/book/book/chapter2/ch2_6.htm#fig2_6_6

N_star_c1 = N_c/2*exp(-E_DC1/(k*T));
N_star_c2 = N_c/2*exp(-E_DC2/(k*T));
N_star_h  = N_c/2*exp( -E_DH/(k*T));

% Ionized donor concentration [cm^-3]
N_D_plus = N_D/(1+n_0/N_star_c1)+N_D/(1+n_0/N_star_c2)+N_D/(1+n_0/N_star_h);

% Band gap narrowing (N-type) (C. Persson, et al., Journal of Applied
    Physics, 1999)
delta_E_c = -23.31*(N_D_plus/1e18)^(1/3)+2.26*(N_D_plus/1e18)^0.5;
```

```
delta_E_v =  26.57*(N_D_plus/1e18)^0.25 +0.43*(N_D_plus/1e18)^0.5;
delta_E_g = (delta_E_c-delta_E_v)/1000*eV;

% Actual band gap due to heavy dopant (AT ABSOLUTE ZERO TEMPERATURE!!!)
E_g_0 = E_g_original+delta_E_g;

% Parameters of Yarshni Equation
% From <Fundamentals of Silicon Carbide Technology
% Growth, Characterization, Devices, and Applications>
% Chapter 2, Eqn. (2.7), by T. Kimoto
aa = 8.2e-4*eV; % [J.K^-1]

bb = 1.8e3; % [K]

E_g = E_g_0-aa*T^2/(T+bb);

% Intrinsic carrier concentration in 6H SiC at room temperature [cm^-3]
n_i = sqrt(N_c*N_v)*exp((-E_g)/(2*k*T));

% equilibrium hole concentration [cm^-3]
p_0 = n_i^2/n_0;

% Difference between extrinsic Fermi level and intrinsic Fermi level [J]
delta_E_F = k*T*log((n_0-p_0)/n_i);

% Intrinsic Fermi level [J]
E_i = E_g/2+0.5*k*T*log(N_v/N_c);

% Extrinsic Fermi level [J]
E_F = E_i+delta_E_F;

%% Parameters for the intrinsic defect
% Koizumi et al., Appl. Phys. Lett. 102, 032104 (2013)

% thermal barrier of E1 defect [J]
therm_barr_1 = 0.048*eV;

% thermal barrier of E2(L/H) defect [J]
therm_barr_2 = 0.070*eV;

% -/0 trap depth of E1 [J]
E1_1 = 0.39*eV;
E1_1n = (0.39+0.048)*eV;

% 0/+ trap depth of E1 [J]
E1_2 = 0.26*eV;

% -/0 trap depth of E2L [J]
E2L_1 = 0.44*eV;
E2L_1n = (0.44+0.07)*eV;

% 0/+ trap depth of E2L [J]
E2L_2 = 0.14*eV;

% -/0 trap depth of E2H [J]
```

```
E2H_1 = 0.43*eV;
E2H_1n = (0.43+0.07)*eV;

% 0/+ trap depth of E2H [J]
E2H_2 = 0.18*eV;

% 0/- electron capture cross section of E1 [cm^2]
% sigma_n1_1 = 3e-15;
sigma_n1_1 = 3e-15*exp(-therm_barr_1/(k*T));

% +/0 electron capture cross section of E1 [cm^2]
sigma_n1_2 = 2e-15;

% 0/- electron capture cross section of E2L [cm^2]
% sigma_n2L_1 = 6e-15;
sigma_n2L_1 = 6e-15*exp(-therm_barr_2/(k*T));

% +/0 electron capture cross section of E2L [cm^2]
sigma_n2L_2 = 5e-16;

% 0/- electron capture cross section of E2H [cm^2]
% sigma_n2H_1 = 5e-15;
sigma_n2H_1 = 5e-15*exp(-therm_barr_2/(k*T));

% +/0 electron capture cross section of E2H [cm^2]
sigma_n2H_2 = 7e-16;

% -/0 hole capture cross section for E1 (estimated) [cm^2]
sigma_p1_1 = sigma_n1_2*ratio;

% 0/+ hole capture cross section for E1 (estimated) [cm^2]
sigma_p1_2 = sigma_n1_2*ratio;

% -/0 hole capture cross section for E2L (estimated) [cm^2]
sigma_p2L_1 = sigma_n2L_2*ratio;

% 0/+ hole capture cross section for E2L (estimated) [cm^2]
sigma_p2L_2 = sigma_n2L_2*ratio;

% -/0 hole capture cross section for E2H (estimated) [cm^2]
sigma_p2H_1 = sigma_n2H_2*ratio;

% 0/+ hole capture cross section for E2H (estimated) [cm^2]
sigma_p2H_2 = sigma_n2H_2*ratio;

% -/0 electron capture coefficient of E1 [cm^3.s^-1]
a_n1_1 = sigma_n1_1*v_th_n;

% 0/+ electron capture coefficient of E1 [cm^3.s^-1]
a_n1_2 = sigma_n1_2*v_th_n;

% -/0 electron capture coefficient of E2L [cm^3.s^-1]
a_n2L_1 = sigma_n2L_1*v_th_n;

% 0/+ electron capture coefficient of E2L [cm^3.s^-1]
```

```
a_n2L_2 = sigma_n2L_2*v_th_n;

% -/0 electron capture coefficient of E2L [cm^3.s^-1]
a_n2H_1 = sigma_n2H_1*v_th_n;

% 0/+ electron capture coefficient of E2L [cm^3.s^-1]
a_n2H_2 = sigma_n2H_2*v_th_n;

% 0/- hole capture coefficient of E1 (estimated) [cm^3.s^-1]
a_p1_1 = sigma_p1_1*v_th_h;

% +/0 hole capture coefficient of E1 (estimated) [cm^3.s^-1]
a_p1_2 = sigma_p1_2*v_th_h;

% 0/- hole capture coefficient of E2L (estimated) [cm^3.s^-1]
a_p2L_1 = sigma_p2L_1*v_th_h;

% +/0 hole capture coefficient of E2L (estimated) [cm^3.s^-1]
a_p2L_2 = sigma_p2L_2*v_th_h;

% 0/- hole capture coefficient of E2H (estimated) [cm^3.s^-1]
a_p2H_1 = sigma_p2H_1*v_th_h;

% +/0 hole capture coefficient of E2H (estimated) [cm^3.s^-1]
a_p2H_2 = sigma_p2H_2*v_th_h;

% density of 0/- electron state of E1 [cm^-3]
n1_1 = N_c*exp((-E1_1n)/(k*T));

% density of +/0 electron state of E1 [cm^-3]
n1_2 = N_c*exp((-E1_2)/(k*T));

% density of -/0 hole state of E1 [cm^-3]
p1_1 = N_A*exp((-E_g+E1_1+E_AD)/(k*T));

% density of 0/+ hole state of E1 [cm^-3]
p1_2 = N_A*exp((-E_g+E1_2+E_AD)/(k*T));

% density of 0/- electron state of E2L [cm^-3]
n2L_1 = N_c*exp((-E2L_1n)/(k*T));

% density of +/0 electron state of E2L [cm^-3]
n2L_2 = N_c*exp((-E2L_2)/(k*T));

% density of -/0 hole state of E2L [cm^-3]
p2L_1 = N_A*exp((-E_g+E2L_1+E_AD)/(k*T));

% density of 0/+ hole state of E2L [cm^-3]
p2L_2 = N_A*exp((-E_g+E2L_2+E_AD)/(k*T));

% density of 0/- electron state of E2H [cm^-3]
n2H_1 = N_c*exp((-E2H_1n)/(k*T));

% density of +/0 electron state of E2H [cm^-3]
n2H_2 = N_c*exp((-E2H_2)/(k*T));
```

```
307
308 % density of -/0 hole state of E2H [cm^-3]
309 p2H_1 = N_A*exp((-E_g+E2H_1+E_AD)/(k*T));
310
311 % density of 0/+ hole state of E2H [cm^-3]
312 p2H_2 = N_A*exp((-E_g+E2H_2+E_AD)/(k*T));
313
314 % E1 trap density [cm^-3]
315 E1 = 1/t2/a_p1_1;
316 % E2L+E2H trap density [cm^-3]
317 E2 = 1/t1/((a_p2L_1+a_p2H_1)/2);
318
319 % Ratio between deep level and shallow level concentration
320 E1m_0 = E1;
321 E10_0 = 0; % E10 state
322 E1p_0 = 0; % E1+ state
323
324 E2Lm_0 = E2;
325 E2L0_0 = 0; % E2L0 state
326 E2Lp_0 = 0; % E2L+ state
327
328 E2Hm_0 = E2;
329 E2H0_0 = 0; % E2H0 state
330 E2Hp_0 = 0; % E2H+ state
331
332 %% injection level [cm^-3]
333
334 % Wavelength [m]
335 lambda = 375e-9;
336
337 % Pulsed laser repetition rate [s^-1]
338 f = 500e3; % refer to the repetition rate (500 KHz)
339
340 % Measured pulsed laser power [W]
341 P = 920e-9;
342
343 % Average energy per pulse [J]
344 E_av = P/f;
345
346 % Total photons of beam waist cross-section
347 N_0 = E_av/(h*c/lambda);
348
349 % Beam diameter [m]
350 r = 0.22e-3; % beam radius
351
352 % Photon density of beam waist cross-section [cm^-2]
353 I_0 = N_0/(r^2*pi*1e4);
354
355 % Absorption coefficient of 6H-SiC at lambda=375nm [cm^-1]
356 % fitted from Watanabe et al., (2014). Jpn. J. Appl. Phys.
357 alpha = 473.556;
358
359 % Effective penetration depth [cm]
360 z_eff = alpha^-1*log(2/(1+exp(-alpha*th_ep)));
361
```

```
% Effective injection level [cm^-3] (http://www.pveducation.org/pvcdrom/
    generation-rate)
g = alpha*I_0*exp(-alpha*z_eff);

%% Parameters for the ODEs

% Equilibrium carrier concentration at conduction band [cm^-3]
n_d_0 = n_0;

% Initial non-equilibrium electron concentration for center E1 [cm^-3]
delta_n_1 = A2/(A1+A2+A3)*g;

% Initial non-equilibrium hole concentration for center E1 [cm^-3]
delta_p_1 = A2/(A1+A2+A3)*g;

% Initial non-equilibrium electron concentration for center E2L [cm^-3]
delta_n_2L = A1/(A1+A2+A3)/2*g;

% Initial non-equilibrium hole concentration for center E2L [cm^-3]
delta_p_2L = A1/(A1+A2+A3)/2*g;

% Initial non-equilibrium electron concentration for center E2H [cm^-3]
delta_n_2H = A1/(A1+A2+A3)/2*g;

% Initial non-equilibrium hole concentration for center E2H [cm^-3]
delta_p_2H = A1/(A1+A2+A3)/2*g;

%%%%%%%%%%%%%%%%%%%%%%%%%%%%%%
% 1. Gain for delta_n

% Gain of delta_n in expression for delta_n (for E1)
n_n_1 = a_n1_1*n_d_0-a_n1_1*E10_0-a_n1_2*n_d_0-a_n1_2*n1_2-a_n1_2*E1p_0;

% Gain of delta_n in expression for R_p1 of delta_p (for E1)
p_n_1a = -a_p1_1*p1_1;
% Gain of delta_n in expression for R_p2 of delta_p (for E1)
p_n_1b = a_p1_2*p_0+a_p1_2*p1_2;

% Gain of delta_n in expression for E1m
e1m_n = -a_n1_1*n_d_0+a_n1_1*E10_0-a_p1_1*p1_1;

% Gain of delta_n in expression for delta_n (for E2L)
n_n_2L = a_n2L_1*n_d_0-a_n2L_1*E2L0_0-a_n2L_2*n_d_0-a_n2L_2*n2L_2-a_n2L_2*
    E2Lp_0;

% Gain of delta_n in expression for R_p1 of delta_p (for E2L)
p_n_2La = -a_p2L_1*p2L_1;
% Gain of delta_n in expression for R_p2 of delta_p (for E2L)
p_n_2Lb = a_p2L_2*p_0+a_p2L_2*p2L_2;

% Gain of delta_n in expression for E2Lm
e2Lm_n = -a_n2L_1*n_d_0+a_n2L_1*E2L0_0-a_p2L_1*p2L_1;

% Gain of delta_n in expression for delta_n (for E2H)
```

```
n_n_2H = a_n2H_1*n_d_0-a_n2H_1*E2H0_0-a_n2H_2*n_d_0-a_n2H_2*n2H_2-a_n2H_2*
    E2Hp_0;

% Gain of delta_n in expression for R_p1 of delta_p (for E2H)
p_n_2Ha = -a_p2H_1*p2H_1;
% Gain of delta_n in expression for R_p2 of delta_p (for E2H)
p_n_2Hb = a_p2H_2*p_0+a_p2H_2*p2H_2;

% Gain of delta_n in expression for E2Hm
e2Hm_n = -a_n2H_1*n_d_0+a_n2H_1*E2H0_0-a_p2H_1*p2H_1;

%%%%%%%%%%%%%%%%%%%%%%%%%%%%%
% 2. Gain for delta_p

% Gain of delta_p in expression for delta_n (for E1)
n_p_1 = a_n1_2*n_d_0+a_n1_2*n1_2-a_n1_1*n_d_0;

% Gain of delta_p in expression for R_p1 of delta_p (for E1)
p_p_1a = a_p1_1*p1_1-a_p1_1*E1m_0;
% Gain of delta_p in expression for R_p2 of delta_p (for E1)
p_p_1b = -a_p1_2*p_0-a_p1_2*E10_0-a_p1_2*p1_2;

% Gain of delta_p in expression for E1m
e1m_p = a_n1_1*n_d_0-a_p1_1*E1m_0+a_p1_1*p1_1;

% Gain of delta_p in expression for delta_n (for E2L)
n_p_2L = a_n2L_2*n_d_0+a_n2L_2*n2L_2-a_n2L_1*n_d_0;

% Gain of delta_p in expression for R_p1 of delta_p (for E2L)
p_p_2La = a_p2L_1*p2L_1-a_p2L_1*E2Lm_0;
% Gain of delta_p in expression for R_p2 of delta_p (for E2L)
p_p_2Lb = -a_p2L_2*p_0-a_p2L_2*E2L0_0-a_p2L_2*p2L_2;

% Gain of delta_p in expression for E2Lm
e2Lm_p = a_n2L_1*n_d_0-a_p2L_1*E2Lm_0+a_p2L_1*p2L_1;

% Gain of delta_p in expression for delta_n (for E2H)
n_p_2H = a_n2H_2*n_d_0+a_n2H_2*n2H_2-a_n2H_1*n_d_0;

% Gain of delta_p in expression for R_p1 of delta_p (for E2H)
p_p_2Ha = a_p2H_1*p2H_1-a_p2H_1*E2Hm_0;
% Gain of delta_p in expression for R_p2 of delta_p (for E2H)
p_p_2Hb = -a_p2H_2*p_0-a_p2H_2*E2H0_0-a_p2H_2*p2H_2;

% Gain of delta_p in expression for E2Hm
e2Hm_p = a_n2H_1*n_d_0-a_p2H_1*E2Hm_0+a_p2H_1*p2H_1;

%%%%%%%%%%%%%%%%%%%%%%%%%%%%%
% 3. Gain for delta_E1m

% Gain of delta_E1m in expression for delta_n
n_e_1 = 2*a_n1_1*n_d_0+a_n1_1*n1_1-a_n1_2*n_d_0-2*a_n1_2*n1_2;

% Gain of delta_E1m in expression for R_p1 of delta_p
p_e_1a = -a_p1_1*p_0-2*a_p1_1*p1_1;
```

```
% Gain of delta_E1m in expression for R_p2 of delta_p
p_e_1b = 2*a_p1_2*p_0+a_p1_2*p1_2;

% Gain of delta_E1m in expression for E1m
e1m_e = -2*a_n1_1*n_d_0-a_n1_1*n1_1-a_p1_1*p_0-2*a_p1_1*p1_1;

%%%%%%%%%%%%%%%%%%%%%%%%%%%%%%
% 4.1 Gain for delta_E2Lm

% Gain of delta_E2Lm in expression for delta_n
n_e_2L = 2*a_n2L_1*n_d_0+a_n2L_1*n2L_1-a_n2L_2*n_d_0-2*a_n2L_2*n2L_2;

% Gain of delta_E2Lm in expression for R_p1 of delta_p
p_e_2La = -a_p2L_1*p_0-2*a_p2L_1*p2L_1;
% Gain of delta_E2Lm in expression for R_p2 of delta_p
p_e_2Lb = 2*a_p2L_2*p_0+a_p2L_2*p2L_2;

% Gain of delta_E2Lm in expression for E2Lm
e2Lm_e = -2*a_n2L_1*n_d_0-a_n2L_1*n2L_1-a_p2L_1*p_0-2*a_p2L_1*p2L_1;

% 4.2 Gain for delta_E2Hm

% Gain of delta_E2Hm in expression for delta_n
n_e_2H = 2*a_n2H_1*n_d_0+a_n2H_1*n2H_1-a_n2H_2*n_d_0-2*a_n2H_2*n2H_2;

% Gain of delta_E2Hm in expression for R_p1 of delta_p
p_e_2Ha = -a_p2H_1*p_0-2*a_p2H_1*p2H_1;
% Gain of delta_E2Hm in expression for R_p2 of delta_p
p_e_2Hb = 2*a_p2H_2*p_0+a_p2H_2*p2H_2;

% Gain of delta_E2Hm in expression for E2Hm
e2Hm_e = -2*a_n2H_1*n_d_0-a_n2H_1*n2H_1-a_p2H_1*p_0-2*a_p2H_1*p2H_1;

%%%%%%%%%%%%%%%%%%%%%%%%%%%%%%
% 5. Constants

% Constant in expression for delta_n (for E1)
const_n_1 = -a_n1_1*n_d_0*E10_0+a_n1_1*n1_1*E1m_0-a_n1_2*n_d_0*E1p_0+a_n1_2*
    n1_2*E10_0;

% Constant in expression for R_p1 of delta_p (for E1)
const_p_1a = -a_p1_1*p_0*E1m_0+a_p1_1*p1_1*E10_0;
% Constant in expression for R_p2 of delta_p (for E1)
const_p_1b = -a_p1_2*p_0*E10_0+a_p1_2*p1_2*E1p_0;

% Constant in expression for E1m
const_e1m = a_n1_1*n_d_0*E10_0-a_n1_1*n1_1*E1m_0-a_p1_1*p_0*E1m_0+a_p1_1*
    p1_1*E10_0;

% Constant in expression for delta_n (for E2L)
const_n_2L = -a_n2L_1*n_d_0*E2L0_0+a_n2L_1*n2L_1*E2Lm_0-a_n2L_2*n_d_0*E2Lp_0
    +a_n2L_2*n2L_2*E2L0_0;

% Constant in expression for R_p1 of delta_p (for E2L)
const_p_2La = -a_p2L_1*p_0*E2Lm_0+a_p2L_1*p2L_1*E2L0_0;
```

```
% Constant in expression for R_p2 of delta_p (for E2L)
const_p_2Lb = -a_p2L_2*p_0*E2L0_0+a_p2L_2*p2L_2*E2Lp_0;

% Constant in expression for E2Lm
const_e2Lm = a_n2L_1*n_d_0*E2L0_0-a_n2L_1*n2L_1*E2Lm_0-a_p2L_1*p_0*E2Lm_0+
    a_p2L_1*p2L_1*E2L0_0;

% Constant in expression for delta_n (for E2H)
const_n_2H = -a_n2H_1*n_d_0*E2H0_0+a_n2H_1*n2H_1*E2Hm_0-a_n2H_2*n_d_0*E2Hp_0
    +a_n2H_2*n2H_2*E2H0_0;

% Constant in expression for R_p1 of delta_p (for E2H)
const_p_2Ha = -a_p2H_1*p_0*E2Hm_0+a_p2H_1*p2H_1*E2H0_0;
% Constant in expression for R_p2 of delta_p (for E2H)
const_p_2Hb = -a_p2H_2*p_0*E2H0_0+a_p2H_2*p2H_2*E2Hp_0;

% Constant in expression for E2Hm
const_e2Hm = a_n2H_1*n_d_0*E2H0_0-a_n2H_1*n2H_1*E2Hm_0-a_p2H_1*p_0*E2Hm_0+
    a_p2H_1*p2H_1*E2H0_0;

%%%%%%%%%%%%%%%%%%%%%%%%%%%%%
% 6. Gain for (delta_n)^2

% Gain of (delta_n)^2 in expression for delta_n (for E1)
n_nn_1 = a_n1_1-a_n1_2;

% Gain of (delta_n)^2 in expression for E1m
e1m_nn = -a_n1_1;

% Gain of (delta_n)^2L in expression for delta_n (for E2L)
n_nn_2L = a_n2L_1-a_n2L_2;

% Gain of (delta_n)^2L in expression for E2Lm
e2Lm_nn = -a_n2L_1;

% Gain of (delta_n)^2H in expression for delta_n (for E2H)
n_nn_2H = a_n2H_1-a_n2H_2;

% Gain of (delta_n)^2H in expression for E2Hm
e2Hm_nn = -a_n2H_1;

%%%%%%%%%%%%%%%%%%%%%%%%%%%%%
% 7. Gain for delta_n*delta_p

% Gain of delta_n*delta_p in expression for delta_n (for E1)
n_np_1 = a_n1_2-a_n1_1;

% Gain of delta_n*delta_p in expression for R_p2 of delta_p (for E1)
p_np_1b = a_p1_2;

% Gain of delta_n*delta_p in expression for E1m
e1m_np = a_n1_1;

% Gain of delta_n*delta_p in expression for delta_n (for E2L)
n_np_2L = a_n2L_2-a_n2L_1;
```

```
572
573 % Gain of delta_n*delta_p in expression for R_p2 of delta_p (for E2L)
574 p_np_2Lb = a_p2L_2;
575
576 % Gain of delta_n*delta_p in expression for E2Lm
577 e2Lm_np = a_n2L_1;
578
579 % Gain of delta_n*delta_p in expression for delta_n (for E2H)
580 n_np_2H = a_n2H_2-a_n2H_1;
581
582 % Gain of delta_n*delta_p in expression for R_p2 of delta_p (for E2H)
583 p_np_2Hb = a_p2H_2;
584
585 % Gain of delta_n*delta_p in expression for E2Hm
586 e2Hm_np = a_n2H_1;
587
588 %%%%%%%%%%%%%%%%%%%%%%%%%%%%%
589 % 8. Gain for (delta_p)^2
590
591 % Gain of (delta_p)^2 in expression for R_p2 of delta_p (for E1)
592 p_pp_1b = -a_p1_2;
593
594 % Gain of (delta_p)^2 in expression for R_p2 of delta_p (for E2L)
595 p_pp_2Lb = -a_p2L_2;
596
597 % Gain of (delta_p)^2 in expression for R_p2 of delta_p (for E2H)
598 p_pp_2Hb = -a_p2H_2;
599
600 %%%%%%%%%%%%%%%%%%%%%%%%%%%%%
601 % 9. Gain for delta_p*delta_e1m
602
603 % Gain of delta_p*delta_e1m in expression of R_p1 of delta_p
604 p_pe_1a = -a_p1_1;
605 % Gain of delta_p*delta_e1m in expression of R_p2 of delta_p
606 p_pe_1b = 2*a_p1_2;
607
608 % Gain of delta_p*delta_e1m in expression of E1m
609 e1m_pe = -a_p1_1;
610
611 %%%%%%%%%%%%%%%%%%%%%%%%%%%%%
612 % 10. Gain for delta_n*delta_e1m
613
614 % Gain of delta_n*delta_e1m in expression of delta_n
615 n_ne_1 = 2*a_n1_1-a_n1_2;
616
617 % Gain of delta_n*delta_e1m in expression of E1m
618 e1m_ne = -2*a_n1_1;
619
620 %%%%%%%%%%%%%%%%%%%%%%%%%%%%%
621 % 11.1 Gain for delta_p*delta_e2Lm
622
623 % Gain of delta_p*delta_e2Lm in expression of R_p1 of delta_p
624 p_pe_2La = -a_p2L_1;
625 % Gain of delta_p*delta_e2Lm in expression of R_p2 of delta_p
626 p_pe_2Lb = 2*a_p2L_2;
```

```
627
628 % Gain of delta_p*delta_e2Lm in expression of E2Lm
629 e2Lm_pe = -a_p2L_1;
630
631 % 11.2 Gain for delta_p*delta_e2Hm
632
633 % Gain of delta_p*delta_e2Hm in expression of R_p1 of delta_p
634 p_pe_2Ha = -a_p2H_1;
635 % Gain of delta_p*delta_e2Hm in expression of R_p2 of delta_p
636 p_pe_2Hb = 2*a_p2H_2;
637
638 % Gain of delta_p*delta_e2Hm in expression of E2Hm
639 e2Hm_pe = -a_p2H_1;
640
641 %%%%%%%%%%%%%%%%%%%%%%%%%%%%
642 % 12.1 Gain for delta_n*delta_e2Lm
643
644 % Gain of delta_n*delta_e2Lm in expression of delta_n
645 n_ne_2L = 2*a_n2L_1-a_n2L_2;
646
647 % Gain of delta_n*delta_e2Lm in expression of E2Lm
648 e2Lm_ne = -2*a_n2L_1;
649
650 % 12.2 Gain for delta_n*delta_e2Hm
651
652 % Gain of delta_n*delta_e2Hm in expression of delta_n
653 n_ne_2H = 2*a_n2H_1-a_n2H_2;
654
655 % Gain of delta_n*delta_e2Hm in expression of E2Hm
656 e2Hm_ne = -2*a_n2H_1;
```

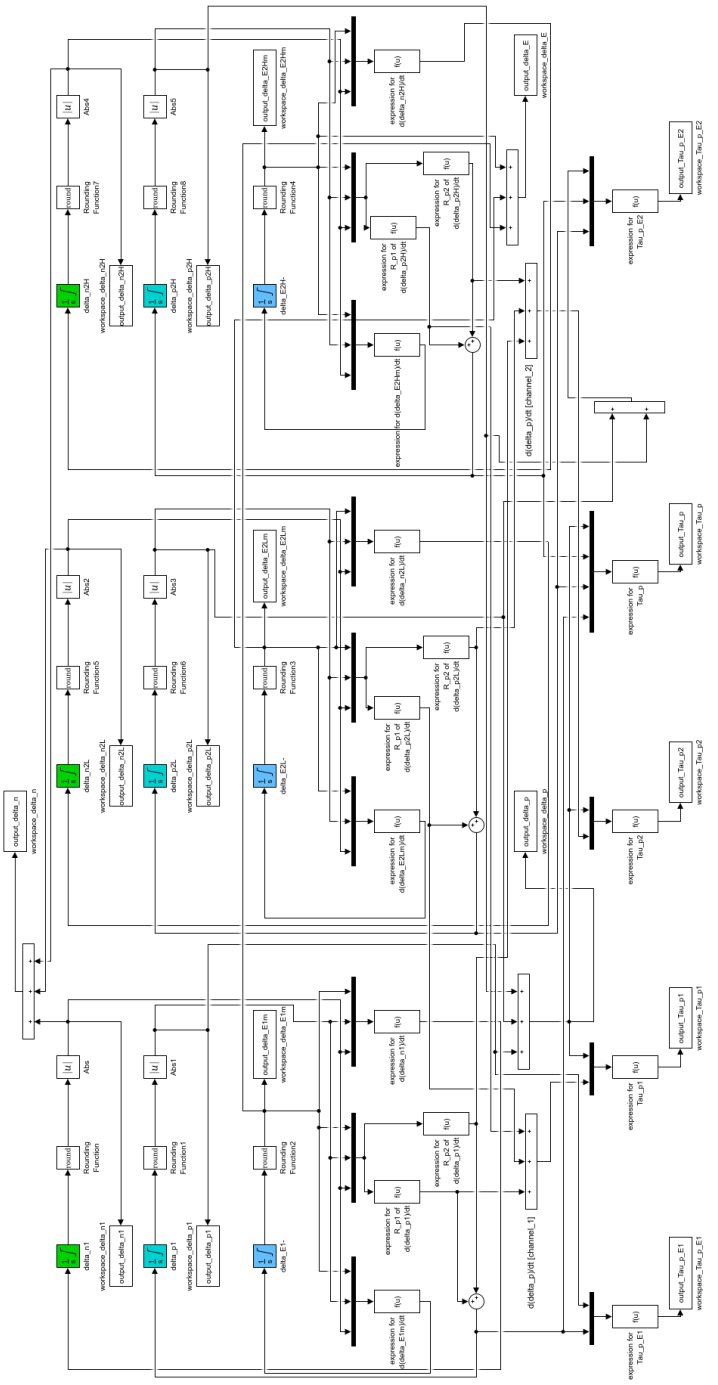

Figure B.1: The screenshot of the block diagram in Simulink which shows the simulation system of the negative-U centers related carrier dynamics in 6H-SiC. The simulation system is consist of three independent parts which are related to the negative-U centers on the h-, k_1-, and k_2-sites in 6H-SiC.

APPENDIX C

Matlab code for steady-state DAP recombination lifetime calculation

Listing C.1: The Matlab code for DAP recombination lifetime calculation. Here we take the calculation for sample SN-2 as an example.

```
format long;

%% Sample specifications

% ELS118
% Donor concentration [cm^-3]
N_D = 9.2e18;
% Acceptor concentration [cm^-3]
N_A = 5.2e18;
% Epilayer thickness [cm]
th_ep = 45e-4+250e-4;

% ELS118 - ExpoDecay fitted parameters for fast decay part
A1 = 0.4808;
t1 = 0.00788771e-3;
A2 = 0.271422;
t2 = 0.0591963e-3;
A3 = 0.111185;
t3 = 0.49128e-3;
y0 = 0.0610742;

% ELS118 - equilibrium electron concentration [cm^-3]
n_0 = 1.692365e18;

%% General physical constants

% Plank constant [m^2.kg.s^-1]
h = 6.63e-34;

% Speed of light [m.s^-1]
c = 299792458;

% electron volt [J]
eV = 1.602e-19;

% Boltzmann constant [m^2.kg.s^-2.K^-1]
```

```
k = 1.381e-23;

% static mass of electron [kg]
m_0 = 9.11e-31;

% Vacuum permittivity [F.m^-1]
sigma_0 = 8.8542e-12;

% Temperature [K]
T = 300;

%% Constants for 6H SiC

% Relative permittivity of 6H SiC
sigma_r = 9.66;

% Degeneracy factor of Donors in 6H SiC
g_D = 2;

% Degeneracy factor of Donors in 6H SiC
g_A = 4;

% Number of conduction band minima
M_C = 6;

% density-of-state effective mass of electrons [kg]
% m_de = 2.34*m_0;
m_de = 0.71*m_0;

% density-of-state effective mass of holes (at T=300 K) [kg]
m_dh = 0.90*m_0;

% effective mass of electron [kg]
% Link: http://www.iue.tuwien.ac.at/phd/ayalew/node62.html
m_e_eff = 0.71*m_0;

% effective mass of hole [kg]
% Link: http://www.iue.tuwien.ac.at/phd/ayalew/node62.html
m_h_eff = 0.90*m_0;

% average thermal velocity for electron [cm/s]
v_th_n = sqrt(3*k*T/m_e_eff)*100;

% average thermal velocity for hole [cm/s]jj
v_th_h = sqrt(3*k*T/m_h_eff)*100;

% bandgap of 6H SiC (C. Persson, et al., Journal of Applied Physics, 1999)
% low temperature / undoped 6H SiC
E_g_original = 3.10*eV;

% Donor level (cubic site, k1) [J]
% W. Suttrop et al., J. Appl. Phys. 72, 3708 ~1992
E_DC1 = 0.138*eV;

% Donor level (cubic site, k2) [J]
```

```
% W. Suttrop et al., J. Appl. Phys. 72, 3708 ~1992
E_DC2 = 0.142*eV;

% Donor level (hexagonal site) [J]
% W. Suttrop et al., J. Appl. Phys. 72, 3708 ~1992
E_DH = 0.081*eV;

% Ratio of cubic site at donor level
R_DC = 2/3;

% Ratio of hexagonal site at donor level
R_DH = 1/3;

% Acceptor level (D-center) [J]
% W. Suttrop et al., Appl. Phys. A 51,231-237 (1990)
E_AD = 0.58*eV;

%% Carriers density in 6H SiC

% Effective density of states in conduction band [cm^-3]
N_c = 2*M_C*(2*pi*m_de*k*T/h^2)^1.5/1e6;

% Effective density of states in valence band [cm^-3]
N_v = 2*(2*pi*m_dh*k*T/h^2)^1.5/1e6;

% An auxilary constant for n_0 calculation Link: http://ecee.colorado.edu/~
    bart/book/book/chapter2/ch2_6.htm#fig2_6_6
N_star_c1 = N_c/2*exp(-E_DC1/(k*T));
N_star_c2 = N_c/2*exp(-E_DC2/(k*T));
N_star_h  = N_c/2*exp( -E_DH/(k*T));

% Ionized donor concentration [cm^-3]
N_D_plus = N_D/(1+n_0/N_star_c1)+N_D/(1+n_0/N_star_c2)+N_D/(1+n_0/N_star_h);

% Band gap narrowing (N-type) (C. Persson, et al., Journal of Applied
    Physics, 1999)
delta_E_c = -23.31*(N_D_plus/1e18)^(1/3)+2.26*(N_D_plus/1e18)^0.5;
delta_E_v =  26.57*(N_D_plus/1e18)^0.25 +0.43*(N_D_plus/1e18)^0.5;
delta_E_g = (delta_E_c-delta_E_v)/1000*eV;

% Actual band gap due to heavy dopant (AT ABSOLUTE ZERO TEMPERATURE!!!)
E_g_0 = E_g_original+delta_E_g;

% Parameters of Yarshni Equation
% From <Fundamentals of Silicon Carbide Technology
% Growth, Characterization, Devices, and Applications>
% Chapter 2, Eqn. (2.7), by T. Kimoto
aa = 8.2e-4*eV; % [J.K^-1]

bb = 1.8e3; % [K]

E_g = E_g_0-aa*T^2/(T+bb);

% Intrinsic carrier concentration in 6H SiC at room temperature [cm^-3]
n_i = sqrt(N_c*N_v)*exp((-E_g)/(2*k*T));
```

```
145
146 % equilibrium hole concentration [cm^-3]
147 p_0 = n_i^2/n_0;
148
149 % Difference between extrinsic Fermi level and intrinsic Fermi level [J]
150 delta_E_F = k*T*log((n_0-p_0)/n_i);
151
152 % Intrinsic Fermi level [J]
153 E_i = E_g/2+0.5*k*T*log(N_v/N_c);
154
155 % Extrinsic Fermi level [J]
156 E_F = E_i+delta_E_F;
157
158 %% injection level [cm^-3]
159
160 % Wavelength [m]
161 lambda = 375e-9;
162
163 % Pulsed laser repetition rate [s^-1]
164 % f = 40e6; % refer to the standard repetition rate (40 MHz)
165 f = 500e3; % refer to the repetition rate (500 KHz)
166
167 % Measured pulsed laser power [W]
168 P = 920e-9;
169
170 % Average energy per pulse [J]
171 E_av = P/f;
172
173 % Average energy per pulse [J]
174 % Standard value @40[MHz]: 1[mW], from: https://www.picoquant.com/
175 % E_av = 1e-3/40e6;
176
177 % Total photons of beam waist cross-section
178 N_0 = E_av/(h*c/lambda);
179
180 % Numerical aperture of Olympus 50x lens
181 % NA = 0.8;
182
183 % Beam diameter [m]
184 % d = 1.22*lambda/NA;
185 r = 0.22e-3; % beam radius
186
187 % Photon density of beam waist cross-section [cm^-2]
188 I_0 = N_0/(r^2*pi*1e4);
189
190 % Absorption coefficient of 6H-SiC at lambda=375nm [cm^-1]
191 % alpha = 400;
192 % fitted from Watanabe et al., (2014). Jpn. J. Appl. Phys.
193 alpha = 473.556;
194
195 % Effective penetration depth [cm]
196 z_eff = alpha^-1*log(2/(1+exp(-alpha*th_ep)));
197
198 % Effective injection level [cm^-3] (http://www.pveducation.org/pvcdrom/
    generation-rate)
```

```
g = alpha*I_0*exp(-alpha*z_eff);

% initial non-equilibrium carrier concentration [cm^-3]
% for f-SiC
delta_n = A3/(A1+A2+A3)*g; % electrons
delta_p = A3/(A1+A2+A3)*g; % holes

% range of r_dap: 70 nm to 150 nm

for r_dap = 7e-9:0.1e-9:1.5e-8

% Coulomb energy in 6H SiC in steady-state [J]
E_cou = eV^2/(4*pi*sigma_0*sigma_r*r_dap);

% Quasi-Fermi energy for electrons at t=0 [J]
E_QF_e = E_i+k*T*log((n_0+delta_n)/n_i);

% Quasi-Fermi energy for holes at t=0 [J]
E_QF_h = E_i-k*T*log((delta_p)/n_i);

% Probability of an electron occupying a donor level at t=0 (cubic1)
F_DC1 = 1/(1+1/g_D*exp((E_g-E_DC1-E_F)/(k*T)));

% Probability of an electron occupying a donor level at t=0 (cubic2)
F_DC2 = 1/(1+1/g_D*exp((E_g-E_DC2-E_F)/(k*T)));

% Probability of an electron occupying a donor level at t=0 (hexagonal)
F_DH = 1/(1+1/g_D*exp((E_g-E_DH-E_F)/(k*T)));

% Probability of a hole occupying an acceptor level at t=0 (D-center)
F_AC = 1/(1+g_A*exp((E_AD-E_F)/(k*T)));

% Reduced mass of electron-hole pair [kg] (J.Y Fan et al. APL, 2012)
miu_0 = m_e_eff*m_h_eff/(m_e_eff+m_h_eff);

% Bohr radius of electron bound exciton [cm] (M. Lax, PRB, 1960)
a_ec1 = (eV*h^2/(8*pi^2*m_e_eff*(sigma_0*sigma_r)^2)/(E_DC1/eV)^3)^0.25*100;
a_ec2 = (eV*h^2/(8*pi^2*m_e_eff*(sigma_0*sigma_r)^2)/(E_DC2/eV)^3)^0.25*100;
a_eh = (eV*h^2/(8*pi^2*m_e_eff*(sigma_0*sigma_r)^2)/(E_DH/eV)^3)^0.25*100;

% Capture probability of electron [cm^3.S^-1]
C_n_c1 = a_ec1^2*pi*v_th_n;
C_n_c2 = a_ec2^2*pi*v_th_n;
C_n_h = a_eh^2*pi*v_th_n;

% Capture cross-section of two D-centers [cm^2]
S_D=2e-14; % Mazzola et al., Applied Physics Letters (1994)

% Capture probability of hole [cm^3.S^-1]
C_p = S_D*v_th_h;

% Maximum DAP transition probability [s^-1]
% Hagen et al., (1973), Journal of Luminescence
t_1 = 3.5e+05;

```

```
% DAP transition probability of each donor level [s^-1]
% Thomas et al., (1965), Physical Review

t_1_c1 = t_1*exp(-2*r_dap/(a_ec1/100));

t_1_c2 = t_1*exp(-2*r_dap/(a_ec2/100));

t_1_h = t_1*exp(-2*r_dap/(a_eh/100));

% Carriers density of electron
% Carriers density if Fermi level is located at E_1/2' (cubic 1) [cm^-3]
n_121_C1 = n_0*exp((E_g-E_DC1-E_cou-E_F)/(k*T));

% Carriers density if Fermi level is located at E_3/2 (cubic 1) [cm^-3]
n_32_C1 = n_0*exp((E_g-E_DC1-E_F)/(k*T));

% Carriers density if Fermi level is located at E_1/2' (cubic 2) [cm^-3]
n_121_C2 = n_0*exp((E_g-E_DC2-E_cou-E_F)/(k*T));

% Carriers density if Fermi level is located at E_3/2 (cubic 2) [cm^-3]
n_32_C2 = n_0*exp((E_g-E_DC2-E_F)/(k*T));

% Carriers density if Fermi level is located at E_1/2' (hexagonal) [cm^-3]
n_121_H = n_0*exp((E_g-E_DH-E_cou-E_F)/(k*T));

% Carriers density if Fermi level is located at E_3/2 (hexagonal) [cm^-3]
n_32_H = n_0*exp((E_g-E_DH-E_F)/(k*T));

% Carriers density of hole
% Carriers density if Fermi level is located at E_3/2' (cubic) [cm^-3]
p_321 = p_0*exp((E_F-E_AD-E_cou)/(k*T));

% Carriers density if Fermi level is located at E_1/2 (cubic) [cm^-3]
p_12 = p_0*exp((E_F-E_AD)/(k*T));

% Effective electron-hole pair concentration at t=0 (for cubic 1) [cm^-3]
N_eff_C1 = delta_n*F_DC1;

% Effective electron-hole pair concentration at t=0 (for cubic 2) [cm^-3]
N_eff_C2 = delta_n*F_DC2;

% Effective electron-hole pair concentration at t=0 (for hexagonal) [cm^-3]
N_eff_H = delta_n*F_DH;

%% Let C_n0/C_p2 == C_p; C_n1/C_p1 == C_n in Aukerman et al., Phys. Rev.
    (1960)
% For n-type 6H SiC

% Carrier lifetime if only DAP recombination exists (Donor Cubic 1 -
    Acceptor Cubic) [s]
tau_dap_c1 = ((n_0^2*p_321+n_0*p_321*n_32_C1)*C_n_c1^2+...
              (n_0*p_321*p_12+n_0*p_321*n_32_C1+p_321*n_32_C1^2+p_321*n_32_C1
    *p_12)...
          *C_p*C_n_c1+(n_0^2*t_1_c1+n_0*t_1_c1*n_32_C1)*C_n_c1+n_0*p_12*
    t_1_c1*C_p)/...
```

```
305           (N_eff_C1*t_1_c1*n_0^2*C_n_c1^2+(N_eff_C1*t_1_c1*n_0*n_32_C1+
    N_eff_C1*t_1_c1*n_0*p_12)...
306           *C_p*C_n_c1);
307
308 % Carrier lifetime if only DAP recombination exists (Donor Cubic 2 -
    Acceptor Cubic) [s]
309 tau_dap_c2 = ((n_0^2*p_321+n_0*p_321*n_32_C2)*C_n_c2^2+...
310             (n_0*p_321*p_12+n_0*p_321*n_32_C2+p_321*n_32_C2^2+p_321*n_32_C2
    *p_12)...
311           *C_p*C_n_c2+(n_0^2*t_1_c2+n_0*t_1_c2*n_32_C2)*C_n_c2+n_0*p_12*
    t_1_c2*C_p)/...
312           (N_eff_C2*t_1_c2*n_0^2*C_n_c2^2+(N_eff_C2*t_1_c2*n_0*n_32_C2+
    N_eff_C2*t_1_c2*n_0*p_12)...
313           *C_p*C_n_c2);
314
315 % Carrier lifetime if only DAP recombination exists (Donor Hexagonal -
    Acceptor Cubic) [s]
316 tau_dap_h = ((n_0^2*p_321+n_0*p_321*n_32_H)*C_n_h^2+...
317             (n_0*p_321*p_12+n_0*p_321*n_32_H+p_321*n_32_H^2+p_321*n_32_H*
    p_12)...
318           *C_p*C_n_h+(n_0^2*t_1_h+n_0*t_1_h*n_32_H)*C_n_h+n_0*p_12*t_1_h*C_p
    )/...
319           (N_eff_H*t_1_h*n_0^2*C_n_h^2+(N_eff_H*t_1_h*n_0*n_32_H+N_eff_H*
    t_1_h*n_0*p_12)...
320           *C_p*C_n_h);
321
322 %tau_dap = 1/(1/tau_dap_c1+1/tau_dap_c2+1/tau_dap_h);
323 tau_dap = (tau_dap_c1^2+tau_dap_c2^2+tau_dap_h^2)/(tau_dap_c1+tau_dap_c2+
    tau_dap_h);
324
325 figure(1)
326 semilogy(r_dap, tau_dap, 'g.');
327 hold on
328 drawnow
329
330 end
331
332 grid on;
```

Acronyms

AR Auger Recombination.

BR Bimolecular Recombination.

CRI color rendering index.

DAP donor-acceptor-pair.

DLTS deep-level transient spectroscopy.

EPR electron paramagnetic resonance.

EQE External quantum efficiency.

f-SiC fluorescent silicon carbide.

FOP fiber optic probe.

FSGP fast sublimation growth process.

FWHM full width at half maximum.

IQE internal quantum efficiency.

LED light-emitting diode.

M-PVT modified physical vapor transport.

N-Al nitrogen-aluminum.

N-B nitrogen-boron.

NUV near ultraviolet.

OD-filter optical density filter.

PID proportional–integral–derivative.

PL photoluminescence.

PL-EPR Photoluminescence-detected Electron Paramagnetic Resonance.

PL-QY photoluminescence quantum yield.

PMT photomultiplier tube.

PTFE polytetrafluoroethylene.

PVT physical vapor transport.

RE rare earth.

Refl-Std Reflectance Standard.

RT room temperature.

SG space group.

TCSPC time-correlated single photon counting.

TOF-SIMS time-of-flight secondary ion mass spectroscopy.

TRPL time-resolved photoluminescence.

TSL thermally stimulated luminescence.

{2.7182818284}ϑφερτυθιοπσδφγηξκλ